Neutral Beam Etching

Thesis

Neutral Beam Etching

Ziad el Otell

Department of Physical Sciences

The Open University

A thesis submitted for the degree of

Doctor of Philosophy

November, 2013

ProQuest LLC.
789 East Eisenhower Parkway
P.O. Box 1346
Ann Arbor, MI 48106 – 1346

This thesis is dedicated to my caring mother, Claude, for the infinite support and encouragement that she gave during the long period of my studies and for the endless sleepless nights she spent worrying about me (*Ykhallilna yekke ya Emme!*), to my loving brother, Jad, for all the sacrifice he made so I can reach my goals and the never ending support he gave throughout the difficult times (*Khaye, ma fi mennak enta!*), and to my late father, Samir... Words fail to express what I want to say or describe how much I miss you, Dad. I will always cherish every moment we spent with you... I only wish you were still here and hope to make you proud with what I achieve in my life...

Thank you for *always* being there for me!

Acknowledgements

First and foremost, I would like to express my immense gratitude to my supervisors, Dr. Mark D. Bowden and Prof. Nicholas St. J. Braithwaite, for giving me the opportunity to pursue research with them, their supervision, guidance, support and patience throughout the entire period of my PhD at The Open University, especially during the last few months while I was writing my thesis. I have learnt a lot and still am learning from their inspiring expertise; I consider myself fortunate for having the chance to carry out research under their guidance.

I wish to acknowledge my scholarship sponsors, The Open University and Oxford Instruments Plasma Technology. I would like to single out Dr. Geoff Hassall (OIPT) for the creative and enjoyable discussions, in particular about probes and sliding seals, and for the enlightening two weeks training at OIPT.

I would like to acknowledge our collaborators from Imec-Belgium, Dr. Jean-François de Marneffe, Dr. Patrick Verdonck and the rest of their team members, for their cooperation that led to the study which is presented in Chapter 6. Thank you for supplying the wafers, insight and interesting discussions on low-κ materials.

It would have been impossible to do all the experiments without the technical support of our technical staff - Fraser Robertson, Chris Hall, Martin Percy and Sandra Mills. You have made my life so much easier, thank you!

I am heartily thankful for the fruitful discussions and lengthy email conversations with Dr. Vladimir Šamara, Imec-Belgium, that played a key role at the start of my PhD and the support he gave during our collaboration as well as helping with other issues on the fly. Thanks Vladimir!

Also, I am eternally indebt for all the help, discussions and thorough perspectives of Dr. Daniil Marinov. Not forgetting the endless SEM imaging sessions, lengthy *typical* Friday experiments and enduring listening to me bicker about writing the thesis and life during this phase; Спасибо Даниил!

Many thanks to my friends and colleagues at The Open university who made working at the OU enjoyable and my stay in Milton Keynes remarkably memorable - Richard Busuttil, Liam Steele, Kiz Natt, Anthony Davenport, Ewelina Szymańska, Binukumar Nair, Robert Farmer, Anna Kowalczyk, Agnieszka Stypczyńska,

Sebastien Mitea, Vytas Masteika, Yvonne Sutton, Zdeněk Mašín, Andrew Mason and many more.

To my ex-flatmate, Andrew Carter, thanks for 'loaning' me your PS3 that ruined my life and consumed good hours, and Robert Farmer, my current flatmate, cheers for enduring my nocturnal lifestyle over the last couple of months!

To the fearless crusaders and the dream team of the active social scene, on campus and elsewhere (*fMK*), I thank thee from the bottom of my ~~liver~~ heart for the fond memories and the *classic* Friday night ventures. Neil J. Murray, Ben J. Dryer, Jonathan Keelan, Calum Maccormick, James H. Tutt, Phillipa Smith, Matthew R. Soman, Daniel Weathrill, Daniele Regis, Encarni Montoya, those who cannot be named for political reasons and everyone else who partook in making all these unforgettable memories, thank you all!

Many cold weekends, travel complications and life dilemmas, per say, were easy to overcome because of the amazing friends and their endless support as well as remarkably generous hospitality - thank you George J. Nohra and Andre Daccache! Many thanks go to my overseas friends, Zaki Maalouf, Tania Tahtouh and Charbel Abu Rjaily, who ~~suffered~~ enjoyed the lengthy Skype and phone conversations, long BF3 & 4 hours and for the amazing hospitality they indulged me with when I visited them. Thank you guys for everything.

Finally, I would like to thank from the bottom of my heart all the members of Al Jabbour, Ibrahim and Maalouf, in particular my aunts Dolly and Yola, who are a core part of our family and have been always beside us, especially throughout the difficult times we have faced recently. Last but not least, I would like to deeply thank my dearest uncle, Michel Jabbour, for his impeccable sense of humor, never ending support, help and all that he has done which cannot be contained in a few dozen books... I love you all!

Abstract

The aim of this research is to better understand the behaviour of pulsed discharges and electron dynamics for the purpose of tailoring the plasma properties for neutral beam etching (NBE) applications.

A capacitively coupled plasma formed in a research system was used for a study of pulsed tailoring in an electropositive plasma. A combination of high time resolved optical diagnostics, plasma imaging and optical emission spectroscopy, and hairpin probe measurements were used to study the electron density and the energy distribution function during the ignition phase of a repetitively pulsed plasma. Two different waveforms were used to modulate the envelope of the input RF-voltages in order to control the ignition phase, by changing the increase rate of the electron density and evolution of the electron energy distribution function (EEDF). The results of this study indicate that the increase rate of the electron density and the EEDF, during operation, can be influenced and even controlled to some extent by pulse tailoring. Electron densities of the order of 10^{16} m^{-3} were obtained, and EEDFs of a highly non-Maxwellian nature were characterised during the ignition phase. Also, the ignition timescales were controlled by applying pulse tailoring from a few microseconds (typically 2 μs) to a few tens of microseconds (80 μs) for the different input waveforms.

An inductively coupled plasma in an industrial plasma etching tool was used to study pulse tailoring in electropositive and electronegative discharges. The same environment was used to create a source to from energetic negative ions which could then be extracted and neutralised. Similar diagnostic techniques, as those used in the research source, in addition to RF-probes were used to characterise the inductive source. Optical emission spectroscopy and electron density measurements showed that the plasmas, almost instantaneously, ignite in the H-mode. The EEDFs were characterised by a Maxwellian distribution with an electron temperature ranging between 1.2 up to 1.6 eV, and electron densities of the order 10^{18} m^{-3} were measured, depending on the operating conditions. This source was also used for preliminary NBE studies. Neutralisation efficiencies ranging between 70% and 95% were measured, and etch rates of 25 and 30 nm/min were found.

Finally, a novel technique was developed to monitor in-situ and in real time the plasma-induced damage on thin films, in particular low-κ dielectrics. This technique uses wafer tiles to simultaneously measure the plasma properties and plasma-induced damage on the thin films. An analytical model, based on the ion flux probe model, was used to to extract the plasma parameters and mimic the existence of thin on the probe surface, by a resistor and a capacitor connected in parallel. The model managed to extract exact values of a dummy load, while a reasonable fit could not be achieved for thins silicon dioxide films. Initial results showed that, even for a well characterised material of a known permittivity and thickness, the model could not extract absolute resistivity and capacitance. Plasmas surface interactions were deduced to be the main factor for this result, which were not included in the model used in this study. However, plasma-induced damage/changes on low-κ thins films by different plasma chemistries, such as argon and hydrogen, were qualitatively measured in real-time. The wafer probe was used to monitor the etch rate of an SF_6 plasma for low-κ thin films in real-time and in-situ. This technique could also be used to measure the neutralisation efficiency and possibly the etch rates of our NBE source in real time.

Contents

List of Figures

Nomenclature

Roman Symbols

A	Collection area of a probe
C	Capacitance
c	Speed of light in vacuum
D	Diameter
e	Charge of an electron
f_0	Resonance frequency of a hairpin probe in vacuum
f_r	Resonance frequency of a hairpin probe immersed in a plasma
I_{es}	Electron saturation current
I_g	Emission intensity
I_{is}	Ion saturation current
k_B	Boltzmann's constant
L	Length of probe
m_α	Mass of species indicated by the subscript
n_α	density of species indicated by the subscript
p	Gas pressure
P_{av}	Average input power
T_α	Temperature of species indicated by the subscript
u_B	Bohm speed

V_f Floating potential of a surface in plasma

V_P Plasma potential

Greek Symbols

$< \nu >$ Average speed

ϵ_{av} Average electron energy

$\boldsymbol{\varepsilon}$ Electric field vector

ϵ Permittivity of a dielectric

ϵ_0 Permittivity of free space

γ Secondary electron emission coefficient

λ_D Debye length

$\bar{\nu}$ Mean speed

ω_p Plasma frequency

Φ Scalar potential

σ_α Excitation cross-section

ϑ_{col} Collision frequency

Subscripts

e Electrons

g Gas particles

i Ions

s Ions in the sheath region

Other Symbols

$(\nabla f)_r$ Gradient $\frac{\partial f}{\partial r}$

Acronyms

APPJ Atmospheric pressure plasma jet

CCP Capacitively coupled plasma

ECR Electron Cyclotron Resonance

EEDF Electron energy distribution function

FAB Fast atom beam

GEC Gaseous Electronic Conference

i-CCD Intensified-charge coupled device

IC Integrated circuits

ICP Inductively coupled plasma

IEDF Ion energy distribution function

MEMS Microelectromechanical systems

NBE Neutral beam etching

OES Optical emission spectroscopy

PROES Phase resolved optical emission spectroscopy

RFEA Retarding field energy analyser

RF Radiofrequency

RIBE Reactive ion beam etching

RIE Reactive ion etching

sccm Standard cubic centimeter per minute

TRG-OES Trace-rare gas optical emission spectroscopy

ULSIC Ultra-large scale integrated circuits

ULSI Ultra-large scale integrated

Chapter 1

Introduction

The objective of this research is to explore the use of pulse methods to control and monitor the properties of low pressure electrical discharges for the purpose of optimising such plasmas for neutral beam etching (NBE). The discharges were operated in two plasma systems: a research reactor and an industrial etching tool.

This chapter introduces plasmas and some of their important properties, as well as traditional plasma etching for ultra-large scale integrated (ULSI) circuit devices. Plasma etching has been widely used for more than five decades to change the morphology of silicon wafers by patterning microscopic features. However, the dimension for these features continues to decrease, and new challenges have arisen that limit this decrease. One possible solution is neutral beam etching, first suggested by Samukawa & Mieno [1996]. In order to design an etching approach suitable for diverse etching applications; it is crucial to understand the plasma physics of pulsed discharges that underlie this approach.

This chapter is structured as follows. Section 1.1 introduces the concept of

plasma. Section 1.2 presents a general summary of some of the important plasma parameters for various applications. In section 1.3, a brief introduction about traditional plasma etching is presented and some of the current challenges are highlighted. Section 1.4 contains a brief survey of what has been done so far in the field of neutral beam etching setting, the core topic of this thesis. Finally, section 1.5 presents the research questions addressed in this thesis.

1.1 Introducing plasmas

Plasma, also known as the 4^{th} state of matter, is ionised gas containing freely and randomly moving electrons, ions, and neutral gas particles where the number of ionised species with respect to the neutrals can vastly differ from one plasma to another [Chabert & Braithwaite, 2011]. Plasma was first regarded as radiant matter, when encountered by Crookes in 1879, and it was further probed and its nature was identified by Thomson in 1897. Finally, it was labeled *plasma* by Irving Langmuir who described the spatial distribution of the charges in it and introduced the concept of the space charge layers that form at plasma boundaries. These non-neutral regions are called sheaths [Langmuir, 1928]. Elsewhere the plasma tends to be neutral.

Almost 99% of visible matter in the universe is considered to be plasma. Figure 1.1 shows several examples of the different types of naturally occurring and man-made plasma such as lightning, auroras, and the ionosphere, each constituting of a different mixture of charged particles and neutral species, which may be atomic and/or molecular. Plasma televisions and fluorescence light tubes are examples of common man-made plasmas. Plasmas found in different industrial

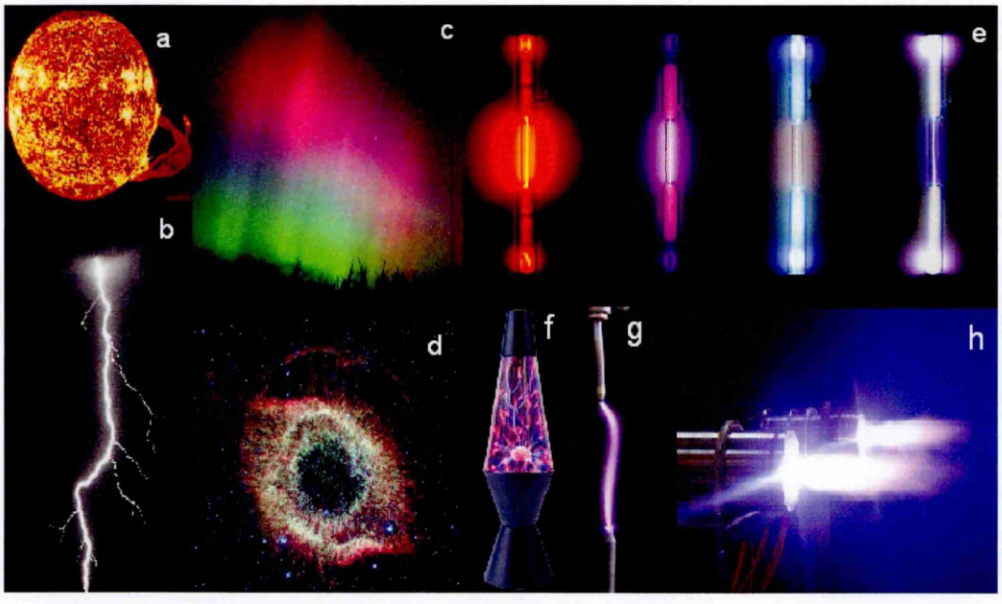

Figure 1.1: Different naturally occurring and man made plasmas found in our daily life where (a) is the sun, (b) lightning, (c) aurora, (d) nebula, (e) noble gases (Ne, Ar, Kr and Xe) light tubes, (f) decoration plasma ball, (g) spark discharge and (h) plasma welding torch [Wikipidea Images, 2010].

processes such as those used in arc welding and material processing are other examples of more specific man-made plasmas. The latter type of plasmas is the core interest of this research.

Different plasmas, figure 1.1, have different physical properties and parameters, such as ratio of charged particles to neutrals, particle densities, particles energy, electrical properties and dimensions. In some plasmas, eg. fusion plasmas, there are only ionised species while other types, eg. fluorescence light tubes, are partially ionised. In the partially ionised plasmas, the density of the ionised species can be much less than that of the neutrals, which makes the consideration of all the charged-neutral interactions a necessity. Partially ionised plasmas are the main focus of this thesis.

Plasma is a dynamic medium, due to the mobility of its particles and in particular the charged species, which interact with any externally applied electric/magnetic fields. Therefore; a steady state, stable, plasma means that it exists for a certain time interval, that it is *not* stationary, especially as the particles which constitute it are in perpetual random motion. These freely moving charges are responsible for sustaining the plasma and its different properties. A time averaged balance between the generation and loss of these charged particles signifies a steady state plasma.

In order to better understand the differences between the various types of plasmas, it is useful to understand the key plasma parameters. Some of the important plasma parameters are introduced in the following section.

1.2 Plasma parameters

As indicated in figure 1.1, different plasmas can exist over a wide range of conditions, which can lead to widely different plasma parameters. This section introduces some of the most important basic plasma parameters. Plasma parameters can be divided into particle parameters (pressure, ionisation ratios, particle densities and energies) and electric parameters (plasma potential, sheath, Debye length, and plasma frequencies). These different parameters are discussed and compared below.

1.2.1 Gas pressure

Contained in a vessel, vacuum chamber or a tube with one end open to the atmosphere, plasma can be operated over a wide range of pressures ($7.6 \leq p \leq$

38×10^5 mTorr[1]). In material processing, plasmas are usually operated at a low pressure varying from a few mTorr to a few Torr. Other plasmas, such as atmospheric pressure plasma jets (APPJ) operate at or around atmospheric pressure, as indicated by its name [Wagenaars *et al.*, 2012].

The gas density in a plasma is related to the pressure by the simple equation:

$$p = \frac{n_g m \bar{\nu}^2}{3} \tag{1.1}$$

where p, n_g, m and $\bar{\nu}$ are the gas pressure, gas particle density, particle mass and mean speed respectively. The particle mean speed is related to the gas temperature by:

$$\frac{1}{2} m \bar{\nu}^2 = \frac{3 k_B T_g}{2} \tag{1.2}$$

where k_B is Boltzmann's constant, and T_g the gas temperature. Higher pressures arise in certain plasma processes due to the increase in the heating and/or increase of the particles density, due to dissociation of molecules, which leads to an increase in the mean speed and $\bar{\nu}^2$ [Chapman, 1980]. The importance of considering the gas pressure is simply because of the fact that the higher the pressure the higher the frequency of collisions between particles. In fact, the collision frequency is expressed by:

$$\vartheta_{\text{col}} = < \nu > . n_g . \sigma_g \tag{1.3}$$

where $< \nu >$ and σ_g are the average speed of a particle and the cross-section of the collision respectively. Therefore, the pressure is a global indicator of the particles density and average velocity. Different plasmas operate at different

[1] 1 mTorr = 1.3328×10^{-3} mbar = 0.13328 Pa

pressures, and therefore they have different collision frequencies which lead to different distribution of energy between the particles.

This research concentrates on plasmas used in material processing applications which are operated at a pressure range varying from a few mTorr's up to a few Torr. Most of the important collisions in processing plasmas occur between neutral particles and charged species, therefore it is necessary to consider the different percentages of charged and neutral species.

1.2.2 Ionisation ratio

The ratio of the ion density (n_i) to gas (neutral) density is called the ionisation ratio ($n_i/(n_i + n_g)$), and in most gas discharges ($n_i/(n_i + n_g)$) $\ll 0.1$. In some high density processing reactors, this ratio can increase so that approximately 10% of the gas particles are ionised, but these situations are rare.

Most processing plasmas are considered quasi-neutral which means the density of negatively charged species is the same as that of the positively charged species. For the case of electropositive plasmas[1], this means that $n_e = n_i$. Hence, by measuring the electron/ion density the ionisation ratio can be inferred. In the case of electronegative plasmas[2], quasi-neutrality still applies such that the net charge of the plasma is equal to zero with $n_i = n_n + n_e$ where n_n is the density of the negative ions.

[1] only positive ions and electrons constitute the charged species in the plasma
[2] negative and positive ions as well as electrons constitute the charged population

1.2.3 Electron density

Most of the important reactions and collisions in a plasma take place between electrons and other particles. In fact, it is the first electron, which is accelerated within an electric field and gains enough energy to ionise another particle releasing another electron, that causes the plasma to ignite. Due to the frequent occurrence of collisions, there is a constant creation and loss of charges. When the creation and loss mechanisms of charges becomes balanced, the plasma is said have reached steady state conditions, which is characterised by a particular electron density (n_e).

In order to ionise another particle, an electron should acquire a certain minimum threshold energy. Electrons are accelerated in applied electric field to acquire this threshold energy, and the distance traveled between consecutive collisions is determined by the particle densities in the plasma volume. In material processing applications, the electron density could range in the following interval $10^{14} \leq n_e \leq 10^{18}$ m^{-3} according to the plasma source. In fact, the electron properties are of the most important key plasma parameters.

1.2.4 Electron temperature

In stable non-thermal plasma, it is impossible to determine single electron energy, due to the fact that electrons are continuously released and captured. Electrons can have different energies varying from a few hundred, $\sim$ 300 K, up to few tens of thousands Kelvins. The energy of electrons in a plasma is described by a distribution function, known as the electron energy distribution function (EEDF), which is determined by the plasma conditions.

The EEDF is characterised by the mean energy, which in the case of a Maxwellian distribution is related to the *electron temperature* (T_e). Since electrons acquire their energies via the electric field, it is suitable to use the energy and temperature unit eV. If the EEDF is a Maxwellian distribution then the average electron energy and temperature are related by following equation:

$$\epsilon_{av} = \frac{3k_B T_e}{2} \tag{1.4}$$

The electron temperature is much higher than that of other particles, typically a few eV. Therefore these plasmas are regarded as non-thermal, with the ion and neutral temperatures close to room temperature (~ 0.025 eV).

It is important to note that while T_e may be less than the threshold energy for important reactions; the distribution of electron energies means that even for relatively low average electron energy there are some electrons with sufficient energies to initiate these reactions.

1.2.5 Plasma potential

When the plasma is first ignited, the number of electrons and ions are *approximately* the same throughout the plasma region. The high mobility of electrons causes them to drift out of the plasma much faster than the ions, which creates a slight charge imbalance and gives the plasma a positive potential with respect to its surrounding. This potential is sufficient to create a small electric field that tends to force ions to leave the bulk plasma and retain electrons in the bulk of the plasma. The electrons will keep escaping from the bulk of the plasma until the plasma potential becomes high enough to exert an electric field capable

of retaining most of the electrons in the bulk of the plasma. When the plasma potential is high enough, the number of electrons leaving balances the number of ions leaving the plasma so that production and loss processes are in balance. The free charges in the plasma give it sufficient conductivity to maintain quasi neutrality while supporting the weak fields required to expel ions. The electron loss is restrained by higher fields that exist in the boundary of the plasma, the sheath.

1.2.6 Sheath

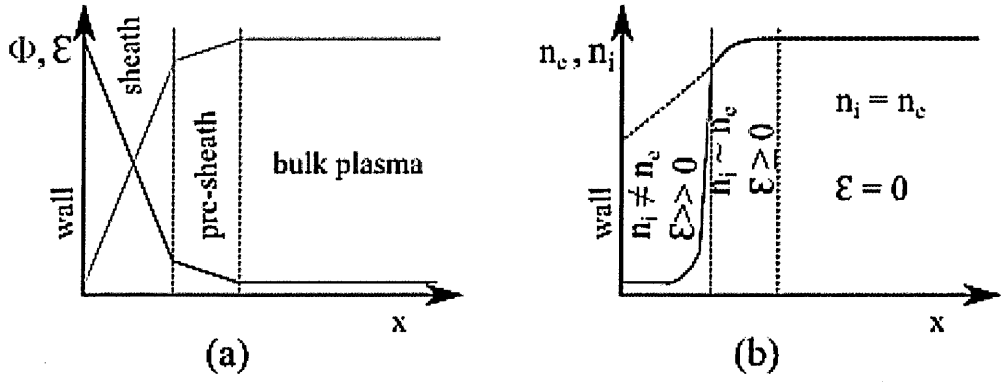

Figure 1.2: (a) is a schematic representation of the variation of the plasma potential (Φ) in blue and the electric field (ε) in green with respect to the different plasma regions. (b) the variation of the electron density (solid red line) and the ion density (dashed black line) with respect to the different plasma regions. The vertical axis shows the magnitude of each parameter, while the horizontal represents the relative distance from the wall (0) towards the bulk of the plasma.

As the plasma becomes quasi-neutral and retains most of the electrons inside its bulk while forcing ions towards nearby surfaces, a potential distribution between the plasma and nearby surfaces forms high electric field regions. These high electric fields regions separate the plasma from the nearby surfaces and are

related to the local potential by:

$$\varepsilon = -\nabla\Phi \tag{1.5}$$

where ε is the electric field and $-\nabla\Phi$ is the negative gradient of the potential (Φ). Figure 1.2 (a) shows in a simplified schematic drawing of the variation of the plasma potential as a function of the distance from the near walls of the chamber as well as the electric fields resulting from the potential.

These high electric field regions are known as sheath regions. The sheath regions mainly contain positive ions and nearly zero electron ednsity at any given instant of time, as the lifetime of electrons crossing the sheath is relatively very short compared to that of ions. However, the net electron flux at the electrodes, or near by surfaces, is equal to that of the ions. The ion and electron densities gradually change with the distance from the wall until they equal each other at the bulk of the plasma. Figure 1.2 (b) shows the different regions in a plasma with the relevant charge densities and electric fields with respect to the distance from the walls/surfaces nearby.

1.2.7 Length & time scales in plasmas

Some other important electrical plasma properties are the distance over which a substantial departure from the neutrality can be sustained, which is described by the Debye Length, and time scale of response of the charged particles to any change in electric field.

1.2.7.1 Debye length

Globally, a plasma is quasi neutral, but locally electric fields can exist. The Debye length (λ_D) is the indication of the distance over which these local electric fields can exist.

The electric charges in a plasma significantly influence one another and respond to the external electric field. The potential is a scalar value of the neighboring charges. However, since plasmas are dynamic media, due to the movement and interaction of the various species, one can assume an ion to be stationary with respect to an electron because of their different mobilities and speed, for simplicity. Therefore, the collective electric potential of a stationary ion and an electron is expressed by the following equation:

$$\phi = -\frac{\Phi_0}{r} \exp(-\frac{r}{\lambda_D}) \tag{1.6}$$

where ϕ is an electric potential at a distance r from a stationary ion; λ_D can be understood as the distance beyond which a space charge electric field is screened by the surrounding oppositely-charged particles that accumulate as all particles constantly redistribute themselves in the plasma; thereby allowing a quasi neutral plasma between electrodes at different potentials.

The expression of this characteristic length can be extracted by applying Poisson's equation, $\nabla^2\Phi = \frac{ne}{\epsilon_0}$ where n is the charge density. Then this expression becomes $\frac{d^2\Phi}{dx^2} = \frac{ne}{\epsilon_0}$ when simplified into a one dimension problem in cartesian coordinates. Multiplying both sides of the equation with $\frac{e}{k_B T_e}$ results in $\frac{d^2\eta}{d(x/\lambda_D)^2} \sim 1$,

where $\eta = \frac{e\Phi}{k_B T_e}$. The Debye length is then given by the following equation:

$$\lambda_D = \sqrt{\frac{\epsilon_0 k_B T_e}{n_e e^2}} \tag{1.7}$$

which features the electron temperature (T_e), density (n_e), charge (e), and the permittivity of free space (ϵ_0).

1.2.7.2 Plasma frequency

Plasma frequency (ω_p) is the frequency of oscillations of charged particles as they move on Debye length scales. The plasma frequency can be regarded as the maximum frequency at which the charged particles respond to changes in the plasma or to an applied electric/magnetic field. Due to the mass difference, electrons tend to have much higher mobility than ions and can respond to much higher frequencies. Therefore, in most cases, the plasma response is determined by the electron response.

The plasma frequency can be obtained in a similar way to that of the Debye length, assuming a charge with mass m passing through an electric field ε. Applying Poisson's equation, $\frac{d\varepsilon}{dx} = \frac{ne}{\epsilon_0}$, with $\frac{d^2x}{dt^2} = \frac{-e\varepsilon}{m}$ results in a second order harmonic oscillation equation, $\frac{d^2x}{dt^2} + \frac{ne^2}{m\epsilon_0}x = 0$. The plasma characteristic frequency is then given by the following equation:

$$\omega_p = \left(\frac{e^2 n}{\epsilon_0 m}\right)^{1/2} \tag{1.8}$$

where n and m correspond to the density and mass of the electrons or ions. The plasma frequency is very important for many heating mechanisms in a plasma

Table 1.1: Some plasma parameters for three different types of plasmas.

Plasma	p (mTorr)	n_i/n_g	n_e (m^{-3})	T_e (eV)	λ_D (mm)	$\omega_p(GHz)$
Fusion	Few	≥ 1	$\geq 10^{20}$	few 10^3	10 μm	10^2
Micro	7.6×10^5	$\ll 0.1$	$\geq 10^{20}$; $\leq 10^{22}$	≥ 0.1 ; ≤ 10	few μm	10^2
Processing	≤ 300	$\ll 0.1$	$\geq 10^{14}$; $\leq 10^{18}$	≤ 5	≤ 10	~ 4

especially if time varying electric fields are used to ignite the plasma. If the frequency of the electric field is much higher than the plasma frequency (ions and electron) the particles will not respond. However, by varying the input frequency of the applied field it is possible to affect either the electrons or the ions if their respective frequencies are higher than that of applied field. Table 1.1 gives some examples of these parameters for different types of plasmas.

In an industrial radiofrequency plasma, typically operated at a frequency of 13.56 MHz which is the main focus of this research, $n_e \sim 5 \times 10^{15}$ m^{-3}, $\omega_{pe} \sim$ 4 GHz and $\omega_{pi} \sim 15$ MHz are typical values for some plasma parameters.

1.3 Diverse plasma applications

Different types of plasmas are used in various applications in different fields. The choice of one particular type of plasma is totally dependent on the nature of its properties. The list below describes some of the fields that use plasmas:

- Medical field: tissue sterilisation, wound healing, tissue regeneration, treatment of melanoma skin cancer and dental cavities [Ptasinska *et al.*, 2010].
- Industrial field: Ultra-Large Scale Integrated Circuits or Very-Large Scale

Integrated Circuits (ULSIC/VLSIC) production in semiconductor manufacturing [Samukawa & Mieno, 1996], Plasma Arc Welding (PAW) for different aluminum alloys [Stava, 1993].

- Entertainment & household appliances: light sources, such as the mercury light tubes and neon signs and decorations, and plasma televisions.
- Environmental care: treatment of toxic industrial fumes and degrading pollutants in wastes [Horikoshi & Hidaka, 2002].

One of the largest applications of plasma is in the semiconductor industry, where low temperature, low-pressure plasmas are used to modify silicon wafers by either depositing new material on the wafer surface or removing material by etching patterns in the surface of the substrate. Indeed, wafers spend about 70% of their processing life time in plasma. Out of the different steps and processes where plasma is used in these industries, one particular process, *plasma etching*, is the focus of this thesis.

1.3.1 Plasma etching

Over the last few decades, the world has witnessed a revolution that has led to a remarkable miniaturisation of all electronic devices and increase in their reliability. Ranging from desktop computers to laptops, mobile phones to music players, medical equipments and household electronics; all have had vast improvements because of the IC manufacturing revolution.

All this would have been impossible without an equivalent, if not larger, improvement in the main manufacturing process of integrated circuits, *plasma etching*. Figure 1.3 shows various plasma etched patterns of sub-100 μm dimensions

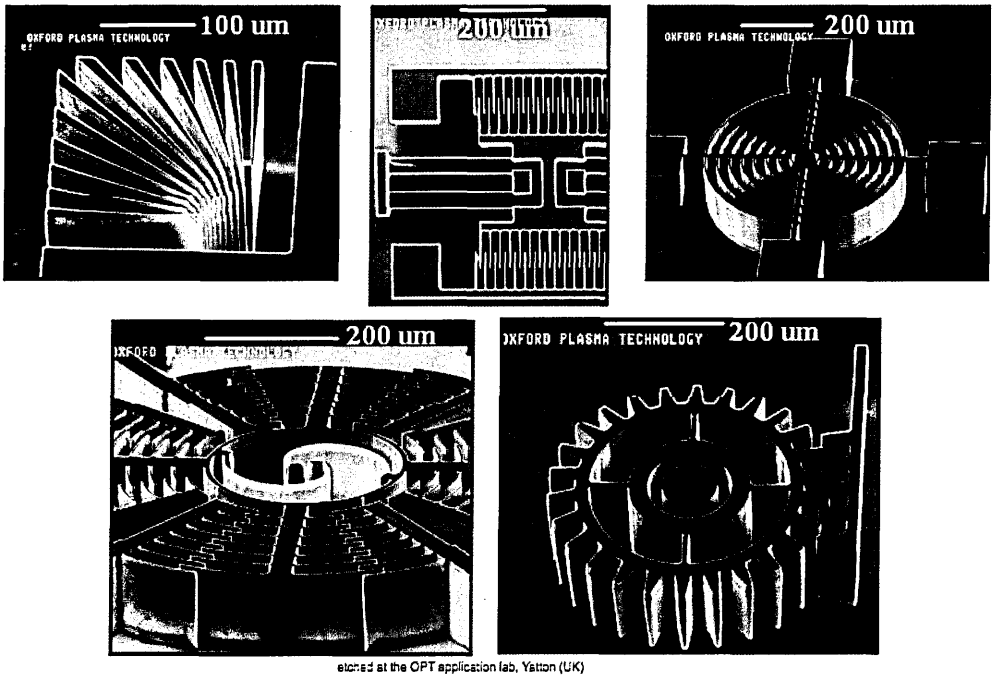

Figure 1.3: This figure shows different plasma etched patterns and their relative scales of Si for MEMS applications. The etched features are of few tens of μm. [Images are courtesy of [Oxford Instruments Plasma Technology, 2002]].

of silicon wafers produced by Oxford Instruments Plasma Technology Application Lab in the United Kingdom [Oxford Instruments Plasma Technology, 2002]. Figure 1.3 clearly shows how delicate and precise the plasma etching processes should be; especially for the micro-electromechanical systems (MEMS) applications and other semiconductor manufacturing processes that would not be possible without the large improvement in plasma etching techniques.

The most common etching methods use either wet etching[1] or reactive gas plasma (also known as dry etching). Before 1970, all semi-conductors were etched in wet-etchant manually controlled baths. Wet etching is used for etching large

[1]Wet etching is were corrosive solutions are used to imprint a pattern in a surface covered with a mask that protects certain areas while posing others.

features (order up to a few hundred microns) and when the accuracy of the etched profile is not of crucial importance. Dry etching is used for creating fine small features (sub hundred micron features) where the geometry of the etched profile is important, while advanced dry etching is used to create even finer trenches (order of few 10 nm). The aim of our research is to further understand the physics behind these advanced processes and try to adapt them to generate even finer etch dimensions.

Each of the etching processes is evaluated by the etch rate, selectivity, uniformity, directionality (isotropic or anisotropic), etched surface quality, and reproducibility. Figure 1.4 and the list below describe these parameters in more details [Pearton & Norton, 2005]:

Etch rate: is a measure of the speed that material is removed from the surface. The rate depends mainly on the type of etching, the flux or concentration of etching particles, and the speed with which the etching products are removed from the region close to the surface. For example, if the products of chemical reactions are highly volatile then etching is faster.

Selectivity: indicates the difference in etching rates for different materials. In order to remove only one particular layer and leave the underlying layer untouched (or at least not too perturbed), an etching process should have different etch rates for the different layers. The rate of etching of the layer that is going to be removed should be much higher than the rate of etching of the underlying layer. In that way, it is possible to remove only the upper layers leaving the underlying layers untouched, simply by controlling the duration of the process.

Uniformity: is an indication of how well an etching process maintains the same etch rate in both space and time. High uniformity means that all chips on a wafer will be processed in the same way.

Directionality: is essential for etching high aspect ratio features. It is defined by the ratio of horizontal etch rate over vertical etch rate. If the directionality is equal to 1, then the etching will be isotropic (i.e. the etch rate is the same in all directions), while if it is less than 1 etching is anisotropic (i.e. the etch process proceeds more quickly vertically downwards. In the ideal case, it is equal to 0 and the etching is completely directional.

Etched surface quality: indicates the smoothness of surface is after etching. This is very important for some applications, especially in ULSIC.

Reproducibility: indicates how well the same etch process can be performed over long periods of times, and large number of wafers. This is a crucial property for all industrial applications.

Simplicity, low cost, low damage to the wafer, high selectivity, and high throughput are some of the advantages of wet etching. However, with the increase in the demand for ULSIC/VLSIC which means increase in circuit density on the wafers, it became crucial to have a high-resolution pattern etching.

The main limitations of wet etching is its isotropic nature making it incapable of achieving sub-micron etching features. Hence although more expensive and lower output, dry etching was favored for ULSIC. Providing high resolution etching (patterning sub-micron features) due to its anisotropic etching nature, plasma etching became more significant in the semi-conductor manufacturing

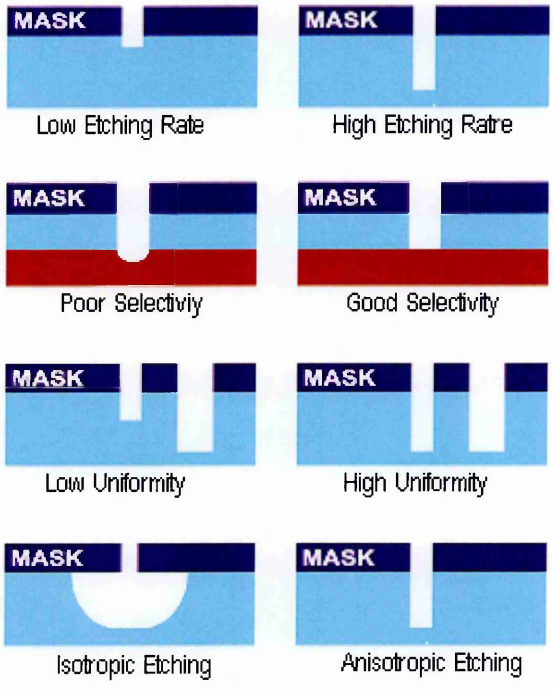

Figure 1.4: Illustration of some etching parameters.

fields over wet etching and was more and more implemented [Pearton & Norton, 2005]. Table 1.2 summarises some of the different types of dry etching used in ULSIC [Pearton & Norton, 2005]. All the mentioned techniques use the plasma as a source of energetic particles that later on initiate the chemical or physical reaction with the wafer according to the characteristics of the used technique.

ECR (Electron resonance cyclotron), ICP (Inductively coupled plasma), and CCP (Capacitively Coupled Plasma) are the main plasma sources for all the different etching techniques mentioned in table 1.2. ECR uses microwave electric fields and steady magnetic fields to create very energetic electrons which ignite the plasma. ICP uses a radiofrequency coil located outside of the vacuum chamber creating a rotationally symmetrical radiofrequency field that couples inductively

Table 1.2: Some dry etching techniques and their characteristics [Pearton & Norton, 2005].

Characteristic	**Mechanism**	**Directionality**	**Pressure** (*Torr*)
Ion Milling	Physical	Anisotropic	$\leq 1 \times 10^{-4}$
RIE (Reactive-Ion Etching)	Ion-assisted energy driven chemical etch	Anisotropic	$0.1 - 5$
RIBE (Reactive-Ion Beam-Etching)	Chemical & physical sputtering	Anisotropic	1×10^{-4}

with the electrons and so ionising the gas. Finally; CCP, the simplest design of all, is made of two parallel metallic plates, with one as a table for the wafer (could be biased, i.e. a separate DC/RF voltage can be applied to it) and the other is the radiofrequency powered electrode. The plasma is generated between the electrodes by ionising the gas in between the plates.

1.3.1.1 Some disadvantages of traditional plasma etching

Along with the need for sub-micron etching patterns, high density plasma sources (such as ICP & ECR) are key technologies for the necessary etch precision [Samukawa *et al.*, 2002]. These techniques have many advantages which involve high density plasma at lower pressure, higher degrees of ionisation, and more controllable ion energies that can be obtained by other techniques [Samukawa & Mieno, 1996]. These techniques can successfully generate etch profiles of the orders of a few tens of nanometers, but many problems arise when trying to implement them to generate sub-10 nm etch profiles.

The main disadvantages of these technologies are related to the damage caused by the charge build up of positive ions and electrons on different surfaces or by the

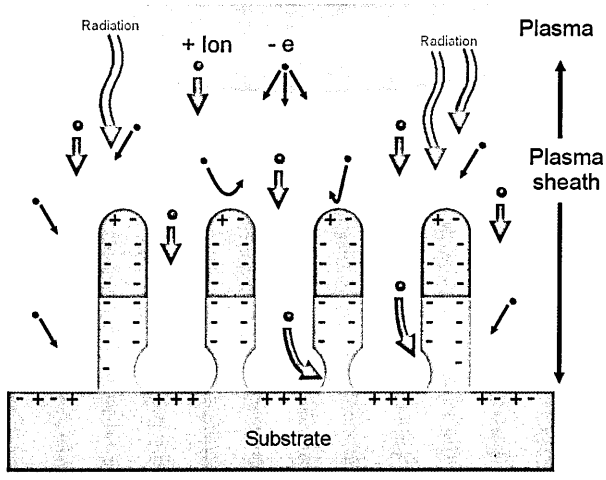

Figure 1.5: This figure illustrates the different species that exit from the plasma towards the target substrate. The species are ions, high energetic electrons, and photons with energies ranging from UV to soft X-ray. This illustration also shows the charge build up process which results in the under cuts of the substrate.

radiation damage caused by ultra-violet during etching [Mizutani & Nishimatsu, 1988; Samukawa *et al.*, 2002]. Figure 1.5 shows the damage and under-cuts due to the charge build up and photo-resist damage due to radiation from the plasma. These are clearly serious problems leading to dielectric defects as ULSIC/VLSIC device integration increases, since the insulator thickness must be scaled down. These disadvantages degrade the electrical characteristics and limit the etching parameters to the order of a few tens of nanometers. Clearly these problems need to be addressed, in order to reach sub-10 nm etching and avoid device damage due to under cuts and radiation.

In summary, traditional plasma etching is suitable for current device requirements where the features have 22-nm dimensions. However, traditional plasma etching is not compatible to meet the requirements of future devices with sub 10-nm features. One possible solution, of many suggested techniques to overcome

these problems, is to shield the substrate from the radiation and charged species by using energetic neutral particles to etch the substrate avoiding the problem of radiation damage, charge build up, and under-cuts. This technique is known as *Neutral Beam Etching* (NBE).

In order to understand the physics taking place in a neutral beam etching source, we must probe the plasma physics occurring in such a source under different operation conditions (gas mixtures and power modes). Understanding how the plasma parameters change with the operation conditions will lead to a better control over which species are extracted from the plasma and their energies. This in turn will lead to a better control over the etching profiles.

1.4 Neutral beam etching

Over the last forty years, groups that have worked and developed neutral beam etching techniques considered different plasma source designs. These designs were different in the mechanisms that generated, neutralised, and extracted the energetic particles. The following list summarises the different aspects that these groups approached:

1. Ion creation mechanism (thus, the convenient plasma source)
2. Convenient ion extraction technique
3. Convenient acceleration mechanism for the ions
4. An efficient way of neutralising these energetic ions

Neutral beam etching has been around since the early 1970s, but it was known as *Fast Atom Beam* (FAB) etching. The first FAB source, a cold-cathode ion

source using a saddle-field configuration with twin anode rods, was proposed by A. H. McIlraith (1972). Various modified sources have since been investigated, including a cylindrical cathode source and a spherical cathode source. These sources have been used to prepare specimens for electron microscopy, to prepare field electron/ion emitters, and as a vacuum ultraviolet sources for photoelectron spectroscopy [Shimokawa & Kuwano, 1994]. The particle flux emitted from a neutral-particle source, however, has been much less than the flux emitted from a magnetron ion source. Due to the small flux of neutrals, the etching rates are very slow compared with other etch techniques. This has prevented FAB sources from being used in practical plasma-processing applications. In addition, such fundamental characteristics as beam current, beam neutralisation coefficient, and energy distribution have not been clarified for FAB sources.

One of the early neutral-beam setups was presented by Mizutani & Nishimatsu [1988] which is shown in figure 1.6. This system produced ions in an ECR plasma source. The extraction of the ions from the bulk of the plasma was done by two sets of multi-aperture electrodes situated below the plasma. The extracted ion beams were allowed to propagate a few centimeters before reaching a set of retarding grids. The energetic neutral particles were produced by charge exchange reactions between the ion beam particles and background gas in the zone between the multi-aperture electrode and retarding grids [Eccles *et al.*, 1986; Mizutani & Nishimatsu, 1988]. Figure 1.6 shows the setup that was used in this study along with the plasma source, ion extraction grids and retarding grids before the substrate. The retarding grids were used to repel ions which had not been neutralised from reaching the substrates.

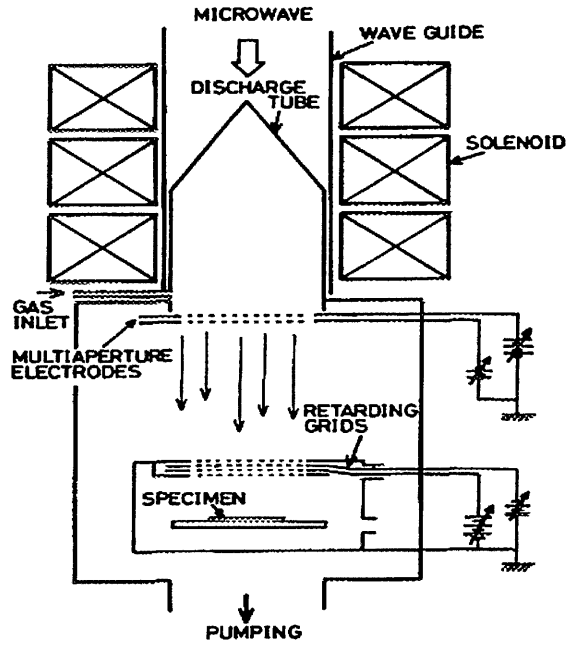

Figure 1.6: Schematic representation of one of the earliest Neutral Beam sources used by Mizutani & Nishimatsu [1988]. This setup uses ECR as plasma source for ion generation, multi-aperture electrodes for ion extraction, and a set of retarding grids for shielding that substrate from ions. The neutralisation mechanism depended on the charge-exchange collisions between ion beams and background gas between the sets of electrodes and retarding grids. Figure taken from Mizutani & Nishimatsu [1988].

Using the setup, shown in figure 1.6, this group demonstrated successful etching of substrates via neutral energetic particles. The etching profile greatly depended on the projectile of these particles after they were neutralised along with the total neutral flux reaching the substrate. The neutralisation efficiency clearly depended on the density of neutrals between the extraction and retarding grids. Therefore the neutralisation depended on the gas pressure in this volume. Too much background gas will lead to deviation and ultimately loss of the collimated extracted beams, and not enough background gas will lead to a very low neutral-

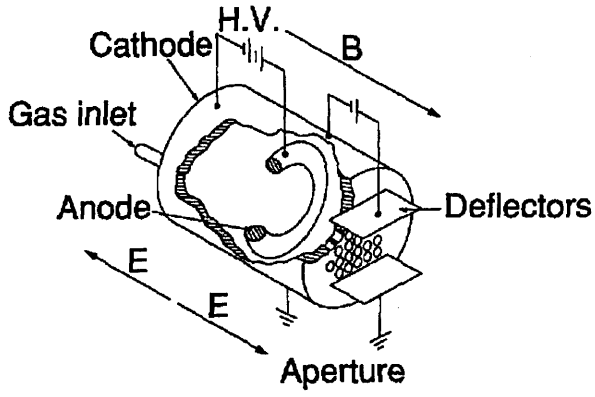

Figure 1.7: This figure shows a schematic representation of the 70 mm FAB source used by Shimokawa & Kuwano [1994], including the ring-anode which is responsible for generation the plasma and extracting the ions from it. The neutralisation depended on the neutral species found between the anode and the apertures in the graphite cathode. Deflectors were mounted after the extraction grid to deviate ions which were not neutralised from reaching the substrate. Figure takes from Shimokawa & Kuwano [1994].

isation efficiency. The specimen also sits below the retarding grid at a pressure close to that between the grids i.e. more probably collisions might occur after neutrals pass through the retarding grid. However, they were reported successful usage of neutral energetic particles to etch substrates, shielding them from ions and hence reducing charge build-up damage.

Figure 1.7 shows a setup by Shimokawa & Kuwano [1994] in which they presented a new FAB source design that had more control over some plasma characteristics by using an electromagnetic and electric field.

The setup consisted of a 70 mm long and 40 mm diameter graphite tube with a gas inlet at one end and exit apertures at the opposite containing a ring anode at the center of it. The magnetic field was to slow the loss of the electrons at the walls of the chamber. At the same time, an electron's total path from cathode

to anode is made more circuitous, thus enabling it to cause more ionisation and excitation.

The neutralisation of the energetic neutral particles was due to charge-exchange collisions with neutral gas particles or by recombination with low energy electrons. Another neutralisation effect might occur at the exit apertures. The entire tube was made of graphite (which also helps in neutralisation at the exit apertures). Most of the residual ions exiting the apertures were removed by deflectors, leaving an almost pure beam of fast atoms. The neutralisation efficiency in this setup also depended on the gas pressure and neutral particle density in the system, but the plasma source and extraction mechanism was different from the setup used by Mizutani & Nishimatsu [1988].

Although a 90% neutralisation coefficient was reported, the neutralisation of positive ions is limited to at most 60% because the charge transfer of positive ions is not efficient [Mizutani & Nishimatsu, 1988]. Therefore, these sources produced low-flux high-energy beams and were not practical for processing applications. Therefore, other ion extraction and neutralisation techniques had to be considered. These percentages can be reconciled if surface charge-exchange collisions were used instead of collisions with neutral gas particles. Surface charge-exchange collisions result in a higher neutralisation efficiency ($\sim$ 95%), as long as an appropriate surface material is used [Noda *et al.*, 2004; Samukawa, 2006].

Figure 1.8 shows a plasma source that uses different ion extraction and neutralisation techniques, presented by Panda *et al.* [2001]. They used an ICP plasma source to generate the plasma and energetic ions with a grounded aluminum grid containing high aspect ratio holes as a neutraliser grid. A tunable accelerator circuit including a tuning capacitor distributed a fraction of the power from the

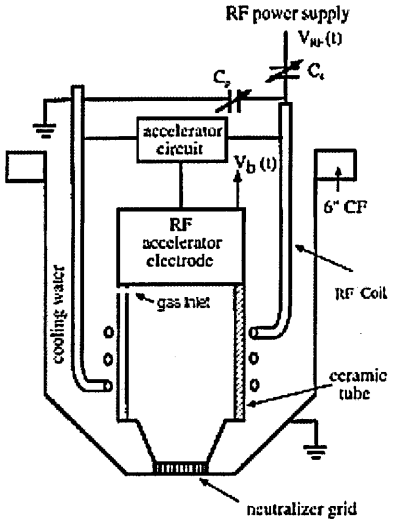

Figure 1.8: This figure shows the ICP plasma source which was used by Panda *et al.* [2001]. It shows the accelerator electrode which is responsible for extracting ions from the plasma and accelerating them towards the grounded neutraliser grid at the bottom of the setup. Figure taken from Panda *et al.* [2001].

input radiofrequency (rf) power to the rf powered accelerator electrode to control the boundary voltage (V_b) which accelerates ions out of the plasma.

The boundary voltage synchronised with the input power providing both an extraction and acceleration mechanism of the ions from the bulk of the plasma. This provided control of the ion energy and hence the neutral beam energy. The neutralisation of the energetic ions extracted from the plasma was accomplished by grasing angle surface collision with the high aspect ratio aluminum grid rather than charge-exchange collisions with neutral background gas. The periodically collapsing sheath over the grid holes causes a fraction of the ions to enter the holes with angles larger than the normal which ensured a collimated neutral beam [Panda *et al.*, 2001]. This provided a new neutralisation method that depends on charge-exchange collisions with walls of the grounded neutraliser grid.

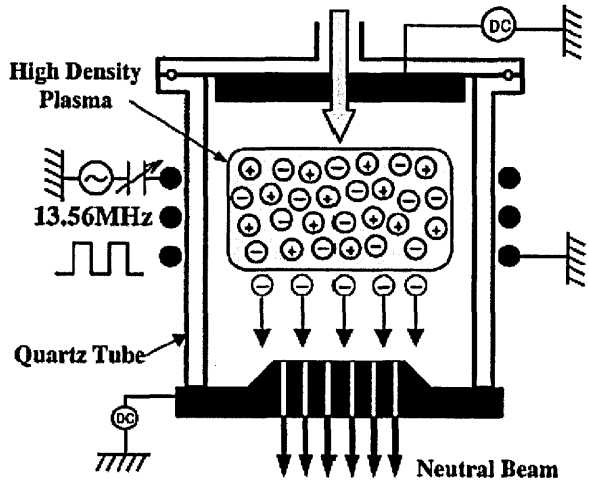

Figure 1.9: The neutral beam source that was presented by Samukawa *et al.* [2002]. This figure shows the top carbon plate which extracts and accelerates the ions and the lower carbon grid which neutralises the ions via surface collisions. Figure taken from Samukawa *et al.* [2002].

This allowed plasma operation at a much lower pressure, since there was no need for excess neutral background gas.

Other groups produced energetic (or hyperthermal) neutrals depending on charge-exchange mechanism with surfaces, by accelerating ions to a surface where they were neutralised and reflected [Panda *et al.*, 2001; Samukawa, 2006]. These groups used ECR or ICP plasma sources mainly to generate the energetic ions, while some others used DC plasma sources (similar to the setup described by Shimokawa & Kuwano [1994]).

Figure 1.9 shows another neutral-beam source consisting of an ICP source and parallel top and bottom carbon plates that was presented by Samukawa *et al.* [2002]. The ions which were generated in the high-density low-pressure plasma were extracted and accelerated when a direct current bias was applied to

the top and bottom carbon plates. This provided efficient extraction of ions and control over their energies. The neutralisation mechanism in this setup depended mainly on the grasing angle surface collision with the inside surface of the numerous apertures in the bottom carbon plate. Another main feature of this setup is that the process chamber (where the substrate is located) is separated from the plasma chamber by a carbon plate fitted at the bottom. This gives a very low pressure around the wafer and hence avoids collisions between the energetic neutrals and any background gas. Graphite plates were used because they have the lowest sputtering yield under high-energy bombardment and do not contaminate semiconductor devices. For the reasons discussed earlier about the efficiency of neutralising positive ions, another difference in this group's work is that they used electronegative gases to generate and extract energetic negative ions.

In this paper, they reported a neutralisation efficiency of negative ions of almost 100%. The differences between Samukawa *et al.* [2002]'s and Panda *et al.* [2001]'s design are the boundary control mechanics as well as the boundary materials, where the first used biased graphite grid while the latter used a grounded aluminum extraction grid. Samukawa *et al.* [2002] also added in some cases a magnet after the extraction grid to deflect any residual ions or electrons from reaching the substrate. However, they reported that they were getting the same etch results with and without the magnetic filter.

In short, they successfully generated energetic neutral beams by extracting ions, mostly negative ions produced in the afterglow discharge of an electronegative gas in an ICP/ECR low-pressure high-density plasma source, by biasing the carbon plates and neutralising them via surface-grasing collisions. Negative ions were used as they are easier to neutralise than positive ions. The DC biasing of

the carbon plates, furthermore, accelerates the ions towards the process chamber and wafer.

This design was later used extensively with minor changes in the system by the same group (Kubota *et al.* [2004]; Noda *et al.* [2004]; Samukawa [2006, 2007]; Samukawa *et al.* [2008] and Kubota *et al.* [2010]), and they have successfully proved that neutral beam etching is capable of achieving sub 10-nm etching.

In summary, several methods of generating energetic neutrals have been tested. Firstly, *volume neutralization*, which is based on the charge-exchange collisions. This neutralisation is directly proportional to the gas pressure in the chamber, which tends to be very low in processing environments. The charge exchange-collision does not change the directionality of the fast ions, however scattering due to collisions can still occur as the ions are propagating in the neutral background gas. Secondly, *surface neutralisation of ions*, which is based on the interaction of the ion beam with a solid surface. This mechanism greatly depends on the impact angle, where ions grasing the surface exit most likely in the same direction of the parent ion beam. The energy loss due to this grasing is very small compared with the initial kinetic energies of the parent ions. As the angle of impact moves closer to the normal, the surface directionality changes and the loss of energy increases as this angle gets closer to the normal. Thirdly, *simultaneous ion extraction and neutralisation*, this technique has more advantages over the others because of the larger beam flux created and the more control over the beam characteristics. This simply uses high aspect ratio grids to extract and neutralise the ions from a pulsed operated high-density low-pressure plasma source. Ions are neutralised by grasing the internal surfaces of the grids, and since it is a low pressure plasma the ion mean free paths increase. Another aspect of this technique is that the

wafer sits at a small distance downstream in a chamber below neutralising grid at a pressure ten times lower (in most cases) than the plasma source.

Furthermore, electronegative gases in low-pressure high-density plasma sources (ECR & ICP) were ignited with pulsed-modulated power to further increase the generation of negative ions and control the plasma properties. This increased the neutralisation efficiency since negative ions are much easier to neutralise.

A different mixture of gases is also used to achieve higher etch rates and passivation layers to protect the walls and prevent undercuts. However, the chemistries and physical processes that take place in the plasma formed of these gases is highly complex and it is not yet fully understood.

The main challenge is neutral beam diagnostics which are important to measure the flux, energy distribution and angular distribution (collimation) of the beam. In contrast to ion beams, neutral beam characterisation is not easy, since neutrals cannot be manipulated with electric (or magnetic) fields. Neutral beam diagnostics fall into two general categories: to measure the properties of the neutrals directly or to first ionise (a part of) the neutral beam and then characterise the resulting ions. Calorimetry may be used to directly measure the energy flux of a neutral beam. The temperature rise as a function of time of the calorimeter disc is related to the power deposited on the calorimeter. However, calorimetry provides the energy flux (i.e. particle flux times energy), and not the individual values of the neutral beam flux and energy. A common approach is to assume that the neutral beam energy distribution is the same as the energy distribution of residual ions coming out of the source, which can be readily obtained with a gridded electrostatic ion energy analyser. The neutral beam flux can then be extracted. Even if the energy distribution of the neutral beam is accurately known,

however, calorimetry provides only an approximate measure of the neutral beam flux, since the fraction of energy that neutrals actually deposit when they strike the calorimeter surface is generally unknown. It is usually assumed that all of the energy of the bombarding species is deposited on the surface. Another method to measure the neutral beam flux makes use of the secondary electron current emitted from a surface impacted by fast neutrals. Ions, electrons and photons must be prevented from striking the detector surface or else their effect must be accounted for. Even then, however, one must know the secondary electron emission coefficient, γ, of the surface as a function of energy for the particular fast neutrals [Economou, 2008].

Measurements of the angular distribution of fast neutral beams have not yet been reported. An indirect measurement was performed to the angular divergence of the residual ions emanating from the neutral beam source. Also, a rough idea of the beam divergence may be obtained by measuring the etch rate drop off as a function of distance from the neutralisation grid or by using techniques applied to ion beams [Economou, 2008].

RIE & NBE

In summary, various groups have successfully tested different approaches and systems to produce energetic neutrals. The details and efficiency of each approach was discussed earlier. However, neutral beam etching is a relatively slow process compared to RIE even with almost 100% neutralisation efficiency. But being a *gentler* process (no charging, very little VUV/UV radiation) compared with RIE, NBE may also be superior in the etching of ultra thin ($<<$ 10-nm) films, for which

the possibly lower etch rate of NBE has no significant throughput consequences. Large area (300mm diameter or more) neutral beam processing has not been demonstrated yet, but appears feasible given the viability of large area ion beam sources. From the practical point of view, pumping requirements are expected to be demanding for large wafer processing. Also, large diameter grids must have provisions for adequate heat transfer to avoid warping of the grid. Additionally, large area uniformity is a serious issue with such sources.

Most of the neutral beam sources have been presented along with the different plasma sources and various neutralisation and extraction techniques. Neutral beam etching has been proved to successfully etch ultra-fine structures which might be of great importance to some applications, but it is not yet used in industries.

Plasma etching is widely and successfully used to achieve fine etch structures (22-nm dimensions). The problems of radiation damage and undercuts arise when trying to apply these traditional techniques to achieve even smaller structures. Neutral beam etching is one of the suggested solutions that has been proved to solve these problems. However, it raises a whole new set of challenges that need to be addressed.

In order to achieve neutral beam etching, a large flux of neutrals should reach the substrate. The neutrals must also be *energetic.* Although a large neutralisation of the extracted collimated ion beams has been demonstrated, the total flux of neutrals reaching the substrate is much less than the total flux of species in a RIE technique. In neutral beam etching, ideally, there are very few, if any, free radicals or charged species that prepare and etch the substrate's surface compared to RIE,which leads to a slower etch rate. While in RIE all sorts of species

arrive to the surface enhancing, ideally, the etch rates. This makes neutral beam etching a slow process with a low etch rate. In order to compensate for this in a neutral beam etching source, a much higher flux of *energetic* neutrals should be delivered to the substrate's surface to achieve etching rates comparable with RIE. However, in some applications it is important to have ultra-fine structures, and etch accuracy is more important than speed. In such applications, because of this need, the etch rate is less important.

The efficiency of producing the energetic neutrals is related to the ion generation and extraction process which are related to the gas mixture and type of gases, plasma source, power input mode, and neutralisation techniques which are used in a neutral beam etching source. Efficient extraction and neutralisation techniques have been studied, but it was done for a small range of gases.

It is the physics of pulsed plasmas, especially when electronegative gases are used, in high-density low-pressure plasma sources we intend to probe and study in this research. A better understanding of the plasma physics which takes place in such systems will enable us to optimise its usage as a negative ion source for neutral beam etching.

1.5 Research aims

The majority of the work done so far on NBE focused on the etch properties and throughput of a specific setup for a particular application. This means that the plasma sources/chemistries were designed/chosen according to the specific application.

The *main aim* of this research is to develop and characterise a charging-

reduced etch configuration by pulse tailoring of the plasma source. This target can be divided into two complementary aims. The first is to understand the effect of pulse tailoring on the overall discharge properties and on the electron dynamics in particular. The second is to apply pulse tailoring to fine tune the plasma properties for the purpose of NBE.

◇ The first part of this research can be divided into the following:

- Developing a simple optical measurement technique with sufficient sensitivity and reliability to probe the transient ignition phase in pulsed plasmas.
- Applying pulse tailoring on a well understood plasma source to control the EEDF in the ignition phase
- Applying various optical and electrical measurement techniques to supplement the simple OES studies.
- Performing pulse tailoring in an industrial plasma source

◇ The second part of this research can be divided into:

- Designing a suitable setup for performing NBE and characterising both the plasma parameters and beam properties.
- Understanding the changes in plasma properties that arise due to the NBE setup.
- Applying pulse tailoring to the plasma source and different extraction biasing properties
- Applying NBE to pristine blank and patterned wafers.

The main focus of this research is on the areas outlined above. However, a separate collaboration with a group from IMEC - Belgium proved fruitful and scientifically interesting. The aim of this work was developing an in-situ technique to measure the effect/damage induced by plasma exposure of thin films in particular low-κ dielectrics. A new *wafer probe* technique was developed for the purposes of this study and proved its reliability and sensitivity to plasma induced changes in thin film properties. A chapter in this thesis is devoted to this study.

Chapter 2

Experimental set ups & measurement techniques

This chapter describes the plasma sources and measurement techniques used in this research. In order to address the research questions stated in the previous chapter, sufficient access to the plasma to apply the different measuring techniques is crucial. A research plasma source, which enabled easy optical and electrical access to the plasma, and an industrial plasma etching source, with limited access to the plasma, were used to study the plasma physics and carry out reactive ion etching (RIE) as well as neutral beam etching (NBE) experiments.

The research plasma source is a capacitively coupled plasma (CCP) source, Gaseous Electronic Conference (GEC) reference reactor. The industrial plasma etching source is an inductively coupled plasma (ICP) source which provided the flexibility to instal the NBE adapter. The ICP source is a PlasmaLab 80 (PL80) etching tool manufactured by our industrial partner Oxford Instruments Plasma Technology (OIPT).

This chapter is divided into four sections. Section 2.1 describes in detail the GEC reference reactor. Section 2.2 contains detailed description of the PL80 etching tool. Section 2.3 incudes a list of the different electronics and devices used during this research. Finally, section 2.4 contains a brief overview of the various plasma diagnostic techniques which were used in the course of this research.

2.1 GEC reference reactor

Plasma, once generated in a source, occupies most of the available volume due to the mobility of its particles. For this reason, the geometry of the chamber will have an effect on the overall charge distribution and most of the other plasma properties. Different materials constituting the walls of a chamber will also affect them. Hence, it was very difficult to compare plasma properties when measured by different research groups even though the plasmas were generated under the same operational conditions (same gas/mixture, pressure and power).

At the 1988 Gaseous Electronic Conference (GEC), it was agreed that there needed to be an-easy-to-model *Reference Cell* for making comparative measurements with other identical systems. A group of industrial and academic researchers then collaborated to design such a plasma source. Figure 2.1 is a schematic drawing of this reference reactor. The diagram shows the electrode dimensions and spacings, and the regions in pink indicate the volume occupied by the plasma. The design was based upon the use of water cooled, aluminum electrodes in a parallel plate configuration, a capacitively coupled system, with a showerhead gas inlet. In recent years, some researchers have retrofitted the top electrode with an inductively coupled coil so that a higher density plasma

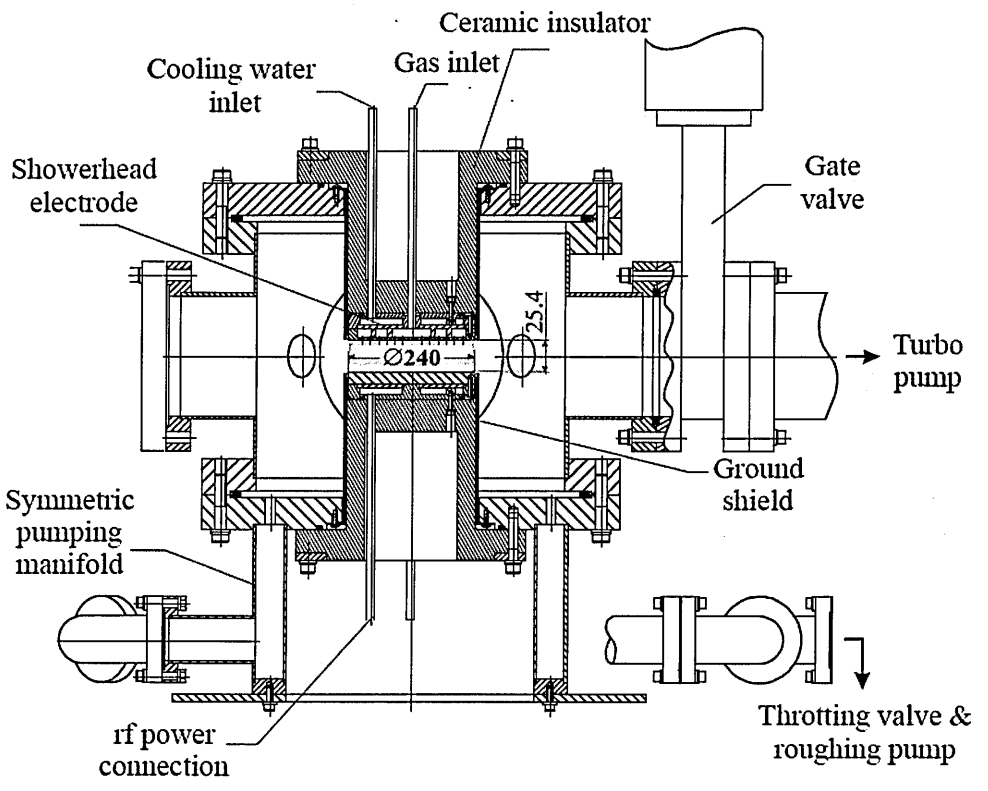

Figure 2.1: The schematic representation of the reference chamber and its dimensions with the interelectrode distance. The pink region represents the plasma in the chamber

can be obtained and the DC bias voltage across the sheath can be independently controlled by a capacitively coupled RF source. However, our system is identical to the original design, with the chamber walls and electrodes made from stainless steel.

Figure 2.2 (a) presents a sketch of a CCP GEC reference reactor with some of the external components (such as mass flow controllers and pumping system) and (b) a snapshot of an argon plasma operated in our reference reactor. The parallel electrodes are separated by 25.4 mm and have a diameter of 101.6 mm.

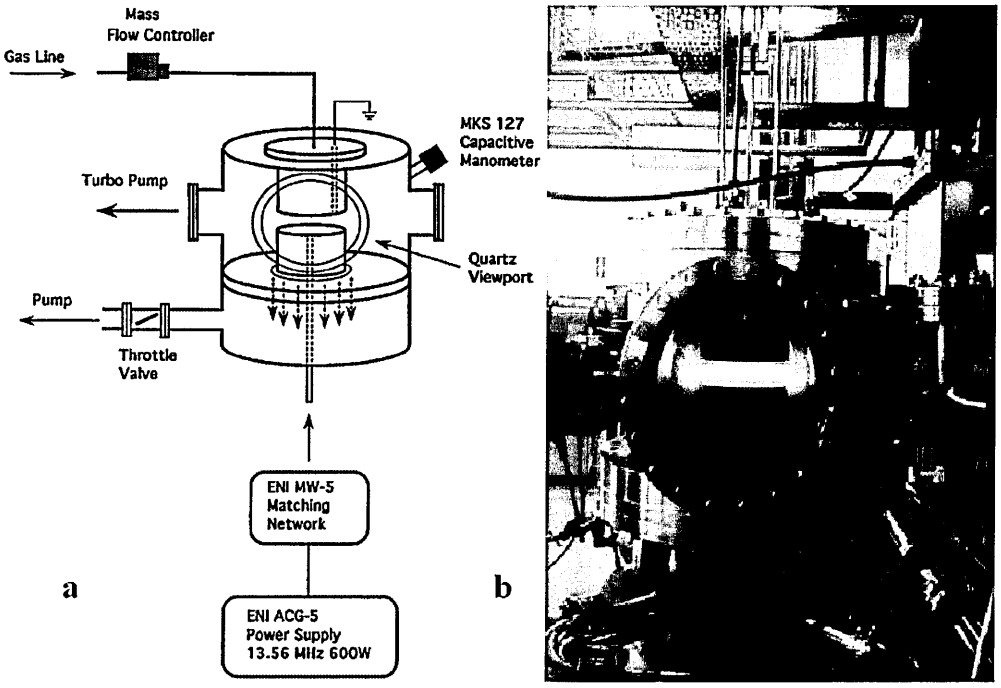

Figure 2.2: (a) schematic representation of the GEC reference reactor indicating the positions of some of the external components of this source. (b) shows a snapshot of our reactor operating with a pure argon plasma.

The flanges on the sides of the chamber provide support for electrical probes, while the quartz windows provide the means for the optical measurements.

A turbo pump (Pfieffer Vacuum, TMU 261P), with 280 L/s pumping capacity, backed by rotary pump (Leybold Ltd., TriVac D16B), with 2 L/s pumping capacity, constitute the first part of the pumping system which is attached to the side of the GEC Cell. These pumps evacuate the GEC reference cell to a base pressure around 10^{-7} mbar. This high vacuum level is needed to decrease the impurities, such as nitrogen and water molecules, in the chamber. This ensures the reproducibility of the plasma conditions, especially when the plasma is operated using noble gases that are highly sensitive to impurities and small

percentages of molecular gases. The turbo pump is then isolated from the chamber via a gate-valve and from the rotary pump by an on/off valve before the gas is flowed into the chamber to generate a plasma. The rotary pump is used to symmetrically evacuate the chamber and keep the desired gas pressure once the plasma is generated. An automated throttle valve, between the rotary pump and the chamber, is used to balance between the gas flow and pumping speed to keep the desired pressure in the chamber constant. The different gases are introduced to the chamber via mass flow controls (MKS instruments) with typically a total net flow rate of 20 sccm[1].

A 13.56 MHz sinusoidal radiofrequency source (ENI, ACG-5-01 XL) was used to generate the driving power responsible for igniting and sustaining the plasma. The output from this RF-generator passes through a matching network (ENI, MW-5D) before reaching the lower electrode. The matching network, which consists of an inductor and a set of variable capacitors, is used to couple the input power to the plasma. This configuration was used when the plasma was operated in the continuous mode.

A signal/function generator was used to in combination with this RF-generator to enable pulsing of input power. This set up was used not only to pulse but to control the rise and shape of the the input power. The signal generator was also used with a broadband amplifier (RF PowerLabs, R150C) to generate both the 13.56 MHz signal and pulse frequency when changing the shape of the input power was not needed.

[1]sccm: standard cubic centimeter

2.2 OIPT PlasmaLab80

The inductively coupled plasma source is an industrial compact etching system (PlasmaLab80 model, PL80 for short) produced commercially by our industrial partner Oxford Instruments Plasma Technology (OIPT). This system provides the necessary flexibility to modify the system from a general reactive ion etching to a neutral beam etching source, even though direct access to the plasma is very constrained. Unlike the GEC reference reactor, where the input electrode is in direct contact with the plasma (or sheath region), in this system the plasma is separated from the power source by a ceramic dielectric. The input power from a four loop copper cable is coupled inductively with the plasma inside the ceramic tube with 56 and 65 mm inner and outer diameters respectively. This coil is continuously cooled by a constant flow of deionised water. The PL80 consists of two plasma regions. The main plasma region is close to the center of the coil region while a diffused region is where the wafer resides.

Figure 2.3 (a) shows a schematic representation of the PL80 ICP source that is responsible for generating the main plasma, which is then diffused to the second region where a substrate is placed. The substrate is mounted on a table, which can be biased, below the ICP and held mechanically in position by a carbon wafer clamp. The wafer is cooled by helium[1] gas flowing from several pores in the table under the wafer. This table is connected to a matching network and second power source. It can be a operated as an independent CCP source separately or synchronously with the ICP power source. Deionized water maintains the table at a constant temperature during the operation of the plasma.

[1]Helium is used because of its high thermal conductivity, inert nature and high mobility.

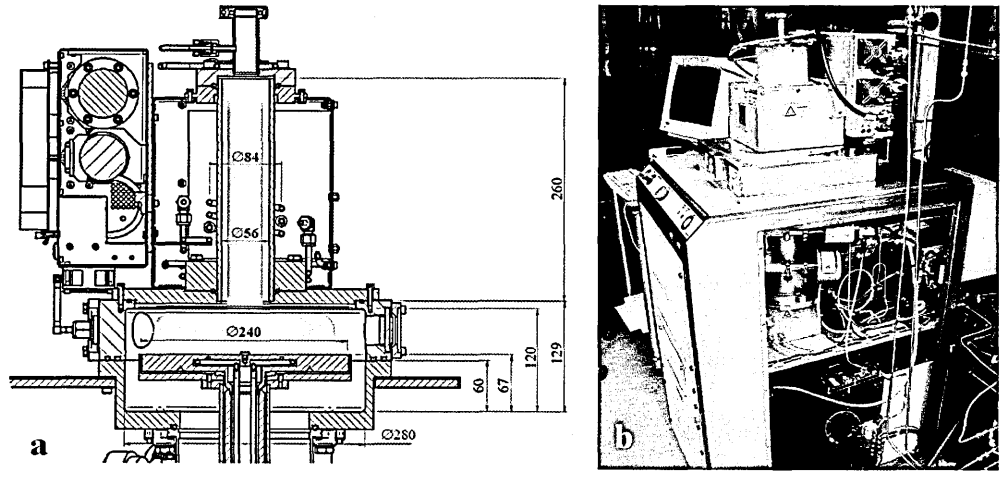

Figure 2.3: (a) shows a detailed schematic representation of the PL080, with the dimensions in mm, and the pink region designates the volume occupied by the plasma. (b) shows a picture of the PL80 in or lab and the components of the pumping system and power supplies.

An external gas pod contains all the mass flow controls for the various gases which can be used in this system. A turbo pump with 420 L/s pumping capability is positioned after an automatic throttle valve. The turbo pump is used in combination with a rotary pump to evacuate the PL80 to a base pressure of 10^{-3} mTorr and maintain the desired pressure when the plasma is ignited.

Gas flow and pressure are set via a software that controls the whole system. When operating in continuous mode, the user has only to specify basic parameters; such as power, pressure and gas mixture. The software runs automatically through the inputs of the user if the interlock chain security is switched on. The interlock chain is a health and safety feature of this system. If any failure occurs with gas pressure, gas flow, cooling water temperature or even a faulty component; this interlock chain will indicate an error and will keep any process from being carried out.

The PL80 was modified to carry out NBE according to a design adapted from Samukawa *et al.* [2002]. A detailed description of this setup is included in chapter 5.

2.3 Various electronics and components

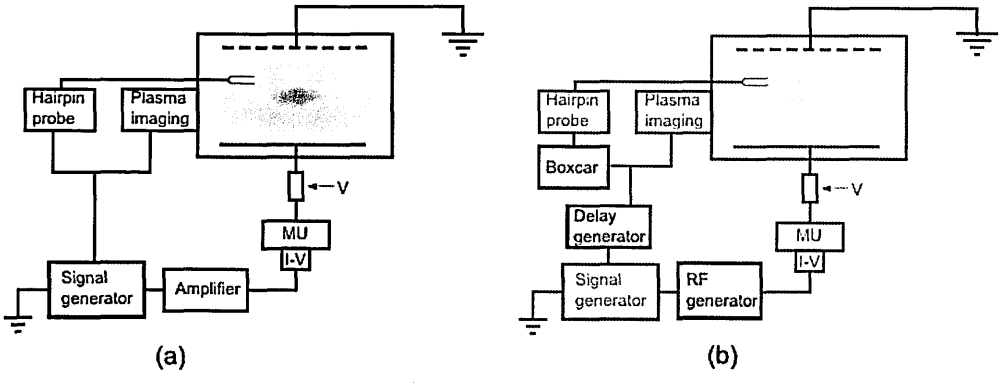

Figure 2.4: (a) shows the setup used to generate the plasma in continuous mode, matching network (MU), inline current-voltage probe (I-V), passive voltage probe (V), and two measurement systems. (b) shows the same plasma system with the extra circuit components, highlighted in red, used to operate the plasma in pulsed mode and synchronize the measurement systems.

Various electronics and sources have been used to facilitate the operation of the diagnostic systems as well as the pulsing of the input powers. Figure 2.4 presents a schematic representation of the plasma source and various electronics that were employed to operate the source and the different acquisition systems used when operating the plasma in continuous mode (a) and pulsed regime (b). Although this figure represents the GEC reactor, the same power sources and acquisition techniques were used when operating the PL80 in pulsed mode.

A signal/function generator (Agilent, 33250A) was used to pulse the dis-

charges operated in both the CCP and ICP systems. It was used mainly as the master of the circuit in order to synchronize all the acquisition techniques with the input pulses.

A boxcar system (EG&G Princton Applied Research, 4152B) was used in combination with other electronics to enable temporally resolved measurements.

A delay generator (Stanford Research Systems, DG 535) was used to control the gating and triggering of the acquisition of the hairpin probe, the plasma imaging and spectrally resolved measurements by controlling the gating of the intensifier on the i-CCD camera.

A hairpin probe was used to measure the electron density. In this system, a microwave generator (Agilent made) was used to create a sweep of frequencies ranging from 1 to 12 GHz. A circulator (AtlantaRF) and directional coupler were used in combination of the microwave generator to carry out the hairpin probe measurements.

A commercial Langmuir probe was briefly used to measurement some plasma properties in continuous and pulsed mode in the PL80.

An ion flux probe was used to measure the ion density in the diffused plasma region in the PL80. RF power supplies (OU built) and a bank of external capacitors were used to operate this probe.

An inline voltage-current (V-I) probe (Impedans Ltd) was used to measure the time resolved voltage, current, phase difference and impedance for the first four harmonics of the input power when the plasma was operated in pulsed mode. The same probe was used to measure the same parameters in addition to the input power, reflected power, and forwarded power when the plasma was operated in continuous mode.

A voltage-current probe (OU built) was also used to measure the RF-voltage at the closest physical point of the powered electrode in the GEC reactor and before the matching unit in the PL80. Details of this probe can be found in Braithwaite [1997].

Spectrally and temporally resolved measurements were carried out using a system composed of a spectrometer and an intensified-CCD. The spectrometer (Horiba, TRIAX-320) has two gratings of 300 & 1800 groove line density (mm^{-1})respectively with a 320 mm optical path and provided a resolution of 0.2 nm. An i-CCD (Andor Technology, DH 534-18F-XX) was used to perform the plasma imaging and in combination with the spectrometer to perform the spectrally and temporally resolved measurements.

Two oscilloscopes (Tektronics and LeCroy) were used to collect and average the sampling of the current and voltage measurements for the discharge of the external capacitors in the ion flux probe and the photodiode measurements.

2.4 Measurement techniques

A combination of several electrical and optical measurement techniques was used to acquire the plasma properties in both plasma sources. The same techniques were applied to the pulsed plasma studies, with some alteration to the acquisition circuits used for obtaining the temporally resolved plasma parameters. These various plasma diagnostic techniques are briefly introduced in the following sections; the reader is kindly referred to the mentioned references for further details on each technique.

2.4.1 Electromagnetic probes

The hairpin probe is a type of resonant electromagnetic probes that has been developed as a tool for measuring local electron densities. It was first used by Stenzel [1976]. It was then revisited and further improved by Piejak *et al.* [2005]. This probe depends on the physics of electromagnetic waves propagating in the plasma [Chabert & Braithwaite, 2011; Šamara *et al.*, 2012b]. A short summary of the main aspects of the hairpin probe operation is given below. A more detailed description can be found in Chabert & Braithwaite [2011]; Piejak *et al.* [2005]; Stenzel [1976].

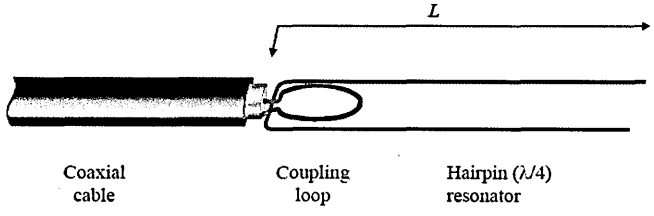

Figure 2.5: A schematic representation of the hairpin probe quarter-wavelength resonator. This figure shows the coaxial cable, inductive loop, and the U-shaped metallic wire (resonator), and L indicating the length of the probe.

Figure 2.5 shows the typical structure of the hairpin probe. The hairpin probe consists of a U-shaped wire, hence its name, which is inductively coupled by a loop of shortcircuit coaxial cable to a swept microwave source. It has a resonance whose quarter wavelength is equal to the length of the probe. The fundamental resonance frequency of the hairpin probe in a medium with uniform permittivity ϵ is given by:

$$f = \frac{c}{4L\sqrt{\epsilon}} \tag{2.1}$$

where c is the speed of light, L is the length of the probe and ϵ is the permittivity

of the medium. In case the probe was immersed in vacuum, $\epsilon = 1$, while for a weakly magnetized low-pressure plasma the permittivity is determined by the free electrons roaming in the region close to the probe. In a weakly magnetized low-pressure plasma, ϵ is given by:

$$\epsilon(\omega) = 1 - \frac{\omega_p^2}{\omega^2} \tag{2.2}$$

where

$$\omega_p = \sqrt{\frac{n_e e^2}{m\epsilon_0}} \tag{2.3}$$

is the plasma frequency ($\omega_p = 2\pi f$), n_e electron density, and e and m are the charge and mass of an electron respectively. Because the permittivity in a plasma is smaller than in vacuum, a hairpin probe immersed in a plasma will resonate at a higher frequency (determined by the plasma) from that in vacuum. By measuring this shift in the resonance frequency and applying the above equations, the electron density of the plasma surrounding the probe can be determined. The above equations and frequency shift can be combined in the following simple equation:

$$n_e/10^{16}\mathrm{m}^3 = \frac{f_r^2/\mathrm{GHz}^2 - f_0^2/\mathrm{GHz}^2}{0.81} \tag{2.4}$$

where f_r and f_0 are the probe's resonance frequency measured in the plasma and in vacuum respectively. Figure 2.6 shows typical signals produced by the hairpin when immersed in both vacuum (dashed line) and plasma (solid line). The resonance frequency of the probe is indicated in both cases where the plasma density can be determined from this shift simply by applying equation 2.4.

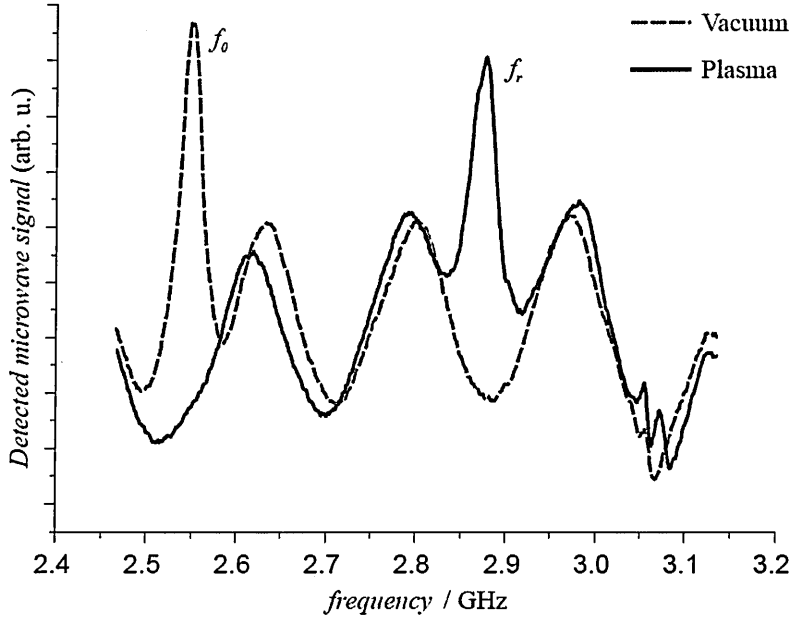

Figure 2.6: Typical hairpin probe signal in vacuum (dashed) and plasma (solid).

This technique relies on waves propagating in the plasma, hence nearby surfaces contribute to the structure of the background and standing waves. In some cases, the contribution from the nearby surfaces and standing waves completely cover the resonance frequency of the probe rendering the signal extremely noisy and not separable from the background. For such cases, there is a technique developed by Šamara *et al.* [2012b] which can be used to extract the probe's resonance frequency even in this noisy environment. A detailed description of this technique can be found in [Šamara *et al.*, 2012b].

From the practical point of view, using this hairpin probe is very straightforward and requires no complicated theories to extract the electron density. However, like any floating surface in a plasma a sheath of few λ_D forms around the wire. In some circumstances the presence of this sheath needs to be con-

sidered when determining the electron density. Piejak *et al.* [2004] developed a relation that corrects for this effect. However, when the wire radius is very small compared to the separation between the strands and the electron density of the order of 10^{16} m^{-3} this effect can be neglected.

For time resolved measurements, the same acquisition system was used together with a boxcar triggered by a delay generator, as shown in Fig. 2.4. In this case, the signal generator frequency was swept slowly compared to the discharge repetition time, so that the recorded resonance line was averaged over many discharge pulses. These signals were sampled by the boxcar integrator at the desired time of the discharge, enabling time resolved electron density measurement.

2.4.2 Electrostatic probes

Electrostatic probe techniques are well established for determining charged particle densities and electron energy distribution functions in cold plasmas. Perhaps in the electrostatic probe family the most popular and widely used is the cylindrical Langmuir probe. In a simplified description, it is a bare cylindrical strip of conducting wire immersed in the plasma. Another type of electrostatic probes is the ion flux probe. The ion flux probe is in general a small surface area, usually borrowed from one of the electrodes, and connected to an externally polarized capacitor. A brief description on the operation of both probes is presented in the following subsections. More detailed description on the Langmuir probes can be found in Chen [2009]; Godyak *et al.* [1992] and Chabert & Braithwaite [2011] and on the ion flux probe in Booth *et al.* [2000]; Braithwaite *et al.* [1996]; Chabert & Braithwaite [2011] and Šamara *et al.* [2012a].

2.4.2.1 Langmuir probes

The charged particle densities, electron temperature (T_e) and energy distribution functions (EEDFs), plasma potential (V_P) and floating potential (V_f) are determined by measuring the current drawn by the Langmuir probe for different applied voltages. In theory, this technique should work on arbitrary geometries, but the analysis becomes complicated for some geometries. Also, some geometries may lead to significant perturbation of the local plasma. For cylindrical thin probes, a small surface can produce good quality data with appropriate care. Figure 2.7 shows (a) a schematic of the Langmuir probe set up and (b) typical measured I-V curve with ion saturation current (I_{is}), V_P and V_f which denote three distinct regions in the measured curve. The first region is the ion saturation region (I_{is}), where the applied potential is negative. This region is of relatively small current formed by positive ions being attracted to the probe surface. This current is actually positive, but Langmuir probe current voltage characteristics are conventionally plotted in this inverted way so that the current appears to be negative. The potential V_f, which denotes the second region, at which the current is equal to zero (i.e. the ion and electron currents have the same amplitude and so cancel each other). It is called the floating potential because an insulated probe, which cannot draw a current, immersed in the same plasma will float at this potential value. For cold ions, in the absence of secondary electron emission, the floating potential can be calculated using the following expression:

$$V_f = \frac{k_b T_e}{2e} \ln(\frac{m_i}{2\pi m_e}) \tag{2.5}$$

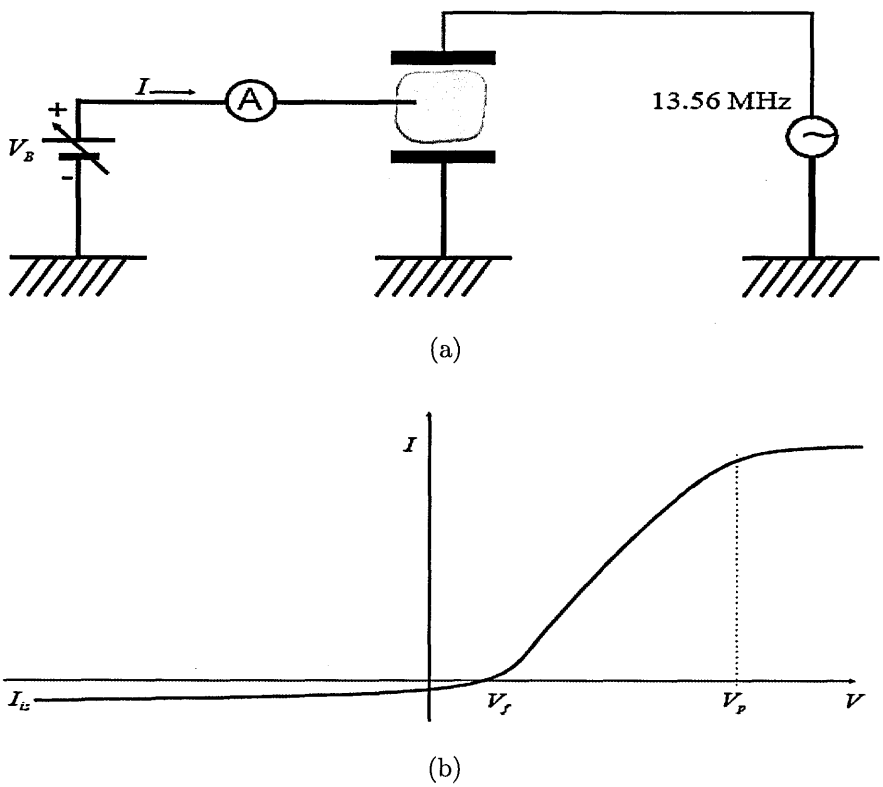

Figure 2.7: (a) is a schematic representation of the Langmuir electrostatic probe in a CCP source, and (b) is typical measured I-V data from a cylindrical Langmuir probe.

where e and m_e are the electron charge and mass respectively, m_i is the ion mass and T_e the electron temperature.

When the applied potential is less than the floating potential ($V < V_f$) electrons are repelled from the probe and the current increasingly consists of ion current, tending (at large negative potential) to a value called the ion saturation current, I_{is}, that may vary with voltage due to a change of the effective collection

area [Lieberman & Lichtenberg, 1994]:

$$I = I_{is} = -en_s u_B A \tag{2.6}$$

where n_s is the ion density in sheath (approximated as being a factor of two less than the bulk density), A is the probe area and the Bohm speed u_B, with $T_i << T_e$ given by:

$$u_B = \sqrt{\frac{ek_B T_e}{m_i}} \tag{2.7}$$

Hence, the ion saturation region I_{is} which denotes the first region, where $V << V_f$, the ion density can be measured. The second and third regions are determined by the value of the probe potential with respect to the floating potential. For $V = V_f$, the probe is said to be floating which indicates the second region. The third region is when $V_f < V \leq V_p$, where V_p is the plasma potential. Electron current saturation I_{es} is reached in the third region when $V = V_p$. As the bias voltage becomes more positive, an exponential increase in the current is observed as more and more electrons are capable of reaching the probe (Figure 2.7).

In the region between the floating and plasma potentials, the current changes exponentially with voltage, and the electron current being drawn by the probe can be expressed as a Boltzmann distribution [Lieberman & Lichtenberg, 1994] as:

$$I + I_{is} = I_{es} n_s \nu_e A \exp(\frac{V - V_p}{T_e}) \tag{2.8}$$

where $\bar{\nu}_e = \sqrt{\frac{8eT_e}{\pi m_e}}$ is the mean electron speed, I_{is} and I_{es} are the ion and electron saturation currents respectively. In this way it is possible to find electron temperature from the slope of the I-V curve in the region between the floating

and the plasma potential and then use T_e and equations 2.6 and 2.7 to find ion density.

However, analysis is difficult and there are several theories used to extract these plasma parameters from what seems as a simple measurement technique [Chen, 2009]. More information and deeper insight into the analysis and various theories used with this type of electrostatic probes can be found in Chabert & Braithwaite [2011], Chen [2009], Lieberman & Lichtenberg [1994], Godyak *et al.* [1992] and Langmuir [1928].

The vast majority of measurements are made with small ($<<$ 1 mm) diameter cylindrical probes, that are suitable for probing the EEDF in the low energy region without, in principle, excessively perturbing the system under investigation. Larger area planar probes have seen much less usage, despite the fact that they have certain advantages over cylindrical probes. The following section describes the ion flux probe, which is one type of these planar probes.

2.4.2.2 Ion flux probes

The ion flux probe is similar to a planar Langmuir probe operating in the ion saturation regime. It consists of a planar surface area, typically 1 cm^2, connected to an external capacitance which is polarised by an externally pulsed DC or RF source. Figure 2.8 shows the typical setup of the ion flux, which in this case is a small borrowed area, in blue, from the grounded electrode. The operation of the ion flux probe and analysis of its data is simpler than that of the Langmuir probe. Basically, the external capacitor is charged by electrons attracted from the plasma during the one phase of the input pulses (DC [Šamara *et al.*, 2012a] or RF [Braithwaite *et al.*, 1996]). The probe surface becomes negatively biased

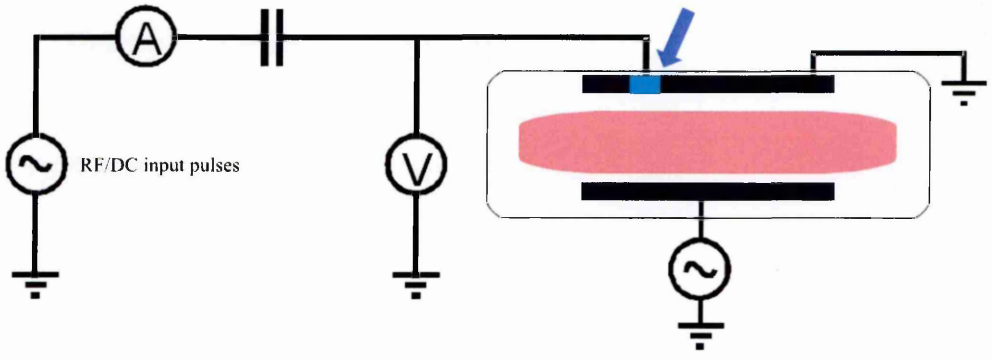

Figure 2.8: Schematic representation of the ion flux probe (indicated by the arrow) in a capacitively coupled system.

by the voltage applied through the circuit. Typically voltages of $40 - 50$ V are used to ensure that even high energy electrons are repelled from the surface initially. When the input biasing is switched off, the probe surface rises to a floating potential determined by the balance of electrons and ions impinging on its surface, whilst initially only ions are collected, discharging the capacitor linearly. Figure 2.9 shows (a) the input DC and RF pulses, and (b) the resultant charging and discharging of the capacitor due to the charged species from the plasma. The linear discharge of the capacitor is due to the ion flux impinging on the surface; the arrival of these ions shifts the surface's potential, decreasing the sheath dimension. As the sheath size diminishes and surface potential rises, electrons will be able to reach the probe. The electrons reach the probe surface at certain potentials depending on the electron temperature. If careful attention is paid to ensuring that the sheath in front of the probe is truly planar by using a guard ring to suppress edge effects, then the positive ion flux to the surface is independent of the probe potential at least for applied voltages that do not significantly perturb the plasma. In this case, when the applied voltage is sufficiently negative to repel

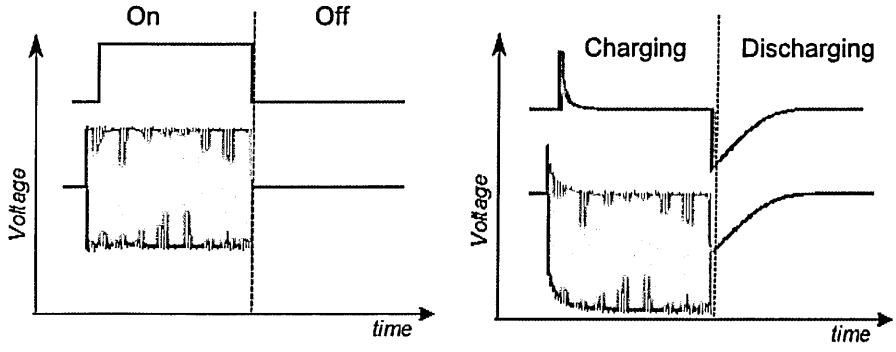

(a) (b)

Figure 2.9: (a) DC (blue) and RF (red) input pulses. (b) the measured charging and discharging phases of the external capacitor.

virtually all electrons, the net current collected saturates at a value equal to I_{is} .

The total current collected by the probe can be determined by equation 2.9, differentiating the measured voltage V_C in the discharging phase of the capacitor:

$$I(t) = C_X \frac{dV_C}{dt} \tag{2.9}$$

where C_X is the external capacitor with a known value.

Differentiating the measured voltage depends on the resolution of the measured data and may lead to very noisy outputs. Another way to acquire the collected current is by direct measurement. A resistor with low resistance, around 470 Ω, and two parallel back-to-back signal diodes can be placed between the input source and the resistor [Booth *et al.*, 2000]. The low resistance is chosen to have a small voltage drop compared to the capacitor's polarisation, and the signal diodes bypass the resistor during the 'ON' phase of the input pules. Measuring the voltage during the 'OFF' phase of the input pulses and applying $U = R \times I$ gives a direct method to acquire the collected current and avoids differentiation.

Both of these methods should give the same result as they measure the same parameter.

During the discharging of the self bias on the capacitor, the probe potential rises closer to that of the plasma. In this region although the electron flux is retarded by the probe potential, a flux of negative charge reaches the surface, offsetting a significant fraction of the positive ion flux [Booth *et al.*, 2000]. After some time, the probe attains normal floating potential where the electron flux just balances the steady positive ion flux. The effective 'tail' temperature of the EEDF can be obtained from the I-V characteristics by fitting the electron current to a Maxwellian distribution. In general a fitting is achieved to an equation of the form:

$$I = I_0[1 - \exp(e(\frac{V_{surf}(t) - V_f}{kT}))] \tag{2.10}$$

where V_f and $V_{surf}(t)$ are the probe steady floating and surface potential respectively.

There are many circumstances in which ion flux probes have advantages compared with other probes. Most probes require a reference electrode to supply the return current and close the circuit (Langmuir probes and double probes [Chabert & Braithwaite, 2011]) which is not the case for the ion flux probe. The ion flux probe completes the circuit and supplies the return current during the charging phase while it collects the current during the discharging phase.

For laboratory discharges, a planar probe located in one of the confining surfaces therefore gives a direct measurement of the ion flux to that surface. In contrast, when using cylindrical probes this parameter which is important for monitoring and controlling processing plasmas can be deduced from the char-

acteristics only by the use of one of several contradictory models. A further advantage of planar probes is that the I-V characteristic in the electron retardation region gives a good measurement of the EEDF in the important high-energy tail region. This is because the positive ion current, which must be subtracted, is constant. For cylindrical probes the ion current is some function of probe potential and must be modeled [Booth *et al.*, 1999; Braithwaite *et al.*, 1996; Chabert & Braithwaite, 2011].

Planar probes also have their disadvantages. Planar configurations necessarily involve a relatively large area so they cannot be operated close to the plasma potential, as the large current that is drawn causes severe perturbation of the plasma under investigation. This precludes measurement of the EEDF in the lower energy region [Booth *et al.*, 2000; Chabert & Braithwaite, 2011].

Despite these disadvantages, ion flux probes are well suited to the type of discharges studies in this research. They can operate in depositing/etching environments and can also give information about the thickness/etch-rate of the deposited films (only if ϵ is known) [Booth *et al.*, 2000; Šamara *et al.*, 2012a].

An adaptation of this technique was developed during this research to use a tile of wafer as the probe collecting surface area. This technique enabled us to in-situ, in almost real time, monitor the plasma-induced damage to thin films of known ϵ. This technique enabled us to acquire information in-situ about the thin films and plasma properties. A detailed description of this technique and model are introduced in chapter 6.

This section covered all the probe diagnostics that were implemented during this research. Optical diagnostics were also used and are presented in the following section.

2.4.3 Plasma imaging and spectroscopy

Measurements of plasma optical emission is a standard and powerful way of gaining information about plasma behavior. This section contains a brief overview of the hardware used in this research for plasma emission measurements. In this research, a combination of time resolved and spectrally resolved plasma imaging techniques were employed in this research to probe the highly transient ignition phase and electron dynamics in pulsed plasmas. An externally triggered intensified charge coupled device (i-CCD) camera was used as the main detector for spatially and temporally resolved measurements and, in combination with a spectrometer, to acquire spectrally resolved information. A brief description of the operation of the i-CCD and its significance is presented below, while more detailed discussions about the methodology are presented in later chapters.

An i-CCD camera operates in the same way as a standard CCD camera. The major difference is the image intensifier located in front of the CCD array that amplifies the detected light so that low intensity signals can be detected. Figure 2.10 shows the principal operation of the i-CCD. In short, the intensifier is an evacuated tube with a front window that has a photocathode coated on its inside surface, onto which the input image is projected. When a photon strikes the photocathode an electron is emitted, and this electron is drawn across the small gap towards the micro channel plate by an electric potential of the order of 150−200V. The micro channel plate is a thin disk ($<$ 1 mm thick) of honeycombed glass, and each of the honeycomb channels ($\sim 6-10$ μm) has a resistive coating. The micro channel plate has a high potential across it (500 to 1000 V) so that the photoelectron will cascade down the channel producing secondary electrons

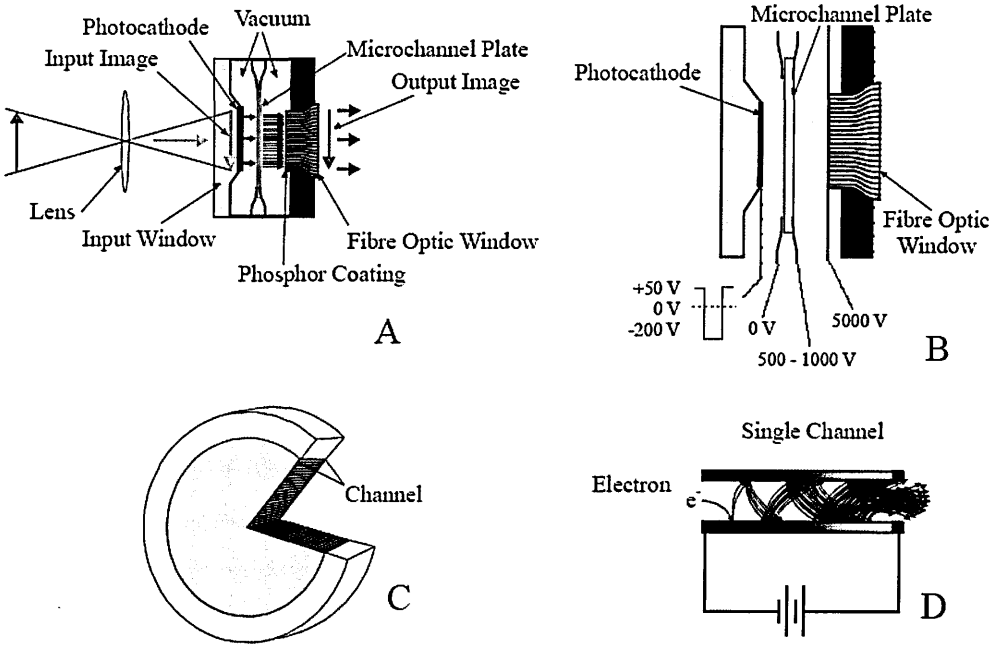

Figure 2.10: ICCD camera principle. Schematic of Second Generation Image Intensifier, (A) Sectional View, (B) Operating Voltages, (C) Micro Channel Plate and (D) Electron Amplification in Single Channel (taken from Andor i-CCD Detectors manual).

and exiting as a cloud of electrons; resultant amplifications can be up to 10^4. The cloud is finally accelerated across a small gap (0.5 mm) by a potential of several thousand volts where it strikes a phosphor coating on the inside of a fibre optic exit window. The phosphor coating emits photons that are transferred through fibre optics to a CCD and then digitised, as in regular CCDs.

The advantage of using an i-CCD camera is not only that it is capable of capturing images of very weak intensity, but by rapidly changing voltage applied to the electron multiplier, it is possible to obtain ultrafast shuttering, down to a few nanoseconds.

In order to acquire spectrally resolved measurements, the same i-CCD was

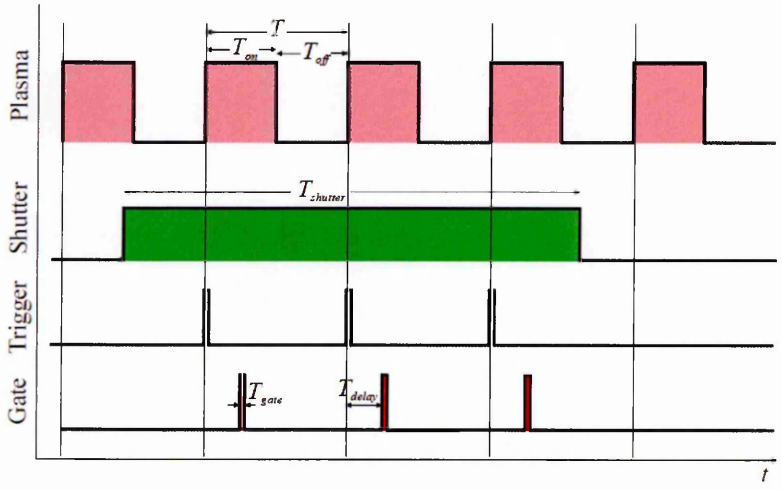

Figure 2.11: This figure shows the plasma pulses, triggering of the shutter, external trigger signal and the intensifier signal respectively.

used in combination with a spectrometer; details of the equipment can be found in section 2.3. An external delay generator was used to trigger the intensifier of the i-CCD (figure 2.4) to acquire temporal and spatial/spectral resolved measurements. The operation of the externally triggered i-CCD is presented in figure 2.11. The discharge itself operated in a pulsed mode with period T. T_{on} and T_{off} represent the plasma active and afterglow times, respectively. T_{gate} is the time that the intensifier acquires the data (8 or 75 ns typically) and T_{delay} determines the position of the acquisition with respect to the time of the plasma pulse. The shutter is open for several plasma cycles in order to accumulate more than one acquisition from the same RF period over several cycles to increase the signal to noise ratio and data quality. The intensifier is then open for few nanoseconds to sample the images from the desired time instant with respect to the plasma pulse.

The i-CCD camera system described above was used to make detailed mea-

surements of the plasma emission. A simpler arrangement was used to record the time dependence of the total emission. In this system, a photodiode with a response time of few nanoseconds was used to record the total emission from the pulsed plasma.

The electrical and optical diagnostic techniques discussed in this chapter were used to study the behavior of pulsed plasmas in both the CCP and ICP systems. Further information on the ion flux probe and plasma imaging are presented in later chapters, where measurements are presented.

Chapter 3

Pulsed capacitively coupled plasma

A general introduction about plasma parameters and plasma etching was presented in chapter 1. The new challenges and some approaches to overcome these challenges, such as neutral beam etching, were discussed in section 1.3. However, to apply neutral beam etching the discharges have to be pulsed. Therefore, it is important to understand the behavior of pulsed discharges and their properties.

Pulsed plasmas have been studied by various research groups since the early nineties [Lieberman & Lichtenberg, 1994] and have been an 'On' and 'Off' trend ever since. Nowadays, pulsed plasmas are becoming the focus not only of researchers, but also industries and chip manufacturers [Banna *et al.*, 2012; Brihoum *et al.*, 2013; Šamara *et al.*, 2010]. The increase of interest in pulsed plasmas is mainly due to the extra control parameters and flexibility attained by pulsing the discharge. This extra flexibility might be a solution for some of the etching problems faced when traditional RIE techniques are used to produce the new

generation of devices.

This chapter contains a study of the electron dynamics that take place during pulse tailoring of a capacitively coupled plasma source. Pulse tailoring is the control and shaping of input pulse parameters to modulate and change plasma properties. The main focus of this chapter is the evolution of the electron properties, especially during the breakdown phase of repetitively pulsed discharges. The breakdown phase was investigated using a combination of optical emission spectroscopy, plasma imaging and electron density measurements. The evolution of the high energy tail of the electron energy distribution function for different pulse properties was tracked by operating the discharge in a mixture of noble gases Ar, Kr & Xe and selecting emission lines from specific transitions of each of those species. The electron density was measured using a floating microwave resonator hairpin-probe. The study was carried out in a capacitively coupled Gaseous Electronic Conference reference reactor. The results of this study indicate that the EEDF during operation can be influenced, and even controlled to some extent, by pulse tailoring.

This chapter contains a focused study of the electron dynamics in a pulsed capacitively coupled discharge source and is structured as follows. Section 3.1 contains the motivation behind this study and mentions various typical optical and electrical plasma diagnostics. Section 3.2 includes a description of the experimental setup, data acquisition procedures and operational conditions. Section 3.3 contains electron density and optical emission spectroscopy measurements for two pulse sets with different input waveforms. A simple analytical model used to calculate emission intensities for certain EEDFs is also presented in section 3.3. Section 3.4 contains similar sets of measurements for input pulses having differ-

ent duty cycles and pulse frequencies. Finally, section 3.5 consists of a summary of this study and some concluding remarks.

3.1 Motivation

Processing demands are severe, and the increasing density of devices on wafers leads to ever-decreasing sizes of individual features. In order to meet these demands, it is necessary to control a range of plasma properties, such as electron temperature and density, ion flux and energy, and negative ion density. These properties in turn are responsible for the selectivity, etch rate, anisotropy, and reactive species densities [Banna *et al.*, 2012]. Separately controlling these plasma properties has proved to be challenging since many are coupled together. For example, ion flux and ion energy are strongly coupled so controlling one without affecting the other requires additional input parameters [Perret *et al.*, 2005].

Robust control over plasma properties can be obtained by changing the gas pressure or applied power; while dc biasing of the electrodes, using dual frequency capacitively coupled plasma sources [Bi *et al.*, 2011; Boyle *et al.*, 2004; Perret *et al.*, 2005] or asymmetric parallel plate radio-frequency plasma sources [Gahan *et al.*, 2012] provides more control of these parameters. Another approach is discharge pulsing which has also been used to achieve finer control of these parameters.

Power- and time-modulation [Ashida *et al.*, 1995; Booth & Cunge, 1997; Samukawa & Mieno, 1996; Šamara *et al.*, 2010] provide a way to fine tune the plasma chemistry and modify the fluxes and energies of species bombarding the substrate. Higher average electron density can be obtained by varying the duty

cycle for lower average input powers, and higher etch selectivity has been achieved when pulsing the power supplied to the plasma source [Booth & Cunge, 1997]. In electronegative plasmas, pulsing has produced high negative ion yield, by promoting dissociative electron attachment reactions in the afterglow part of the pulse where electrons rapidly cool and attach to the molecules [Ahn *et al.*, 1996]. High electron density is obtained in the active-glow phase of the pulse [Lieberman & Ashida, 1996; Samukawa, 2007]. Overall, discharge pulsing enables the tailoring of plasma parameters especially the electron energy distribution function (EEDF) and electron density, which fine tunes the plasma chemistries that promote/suppress the generation of the different species.

Control of plasma properties by discharge pulsing introduces new challenges and interesting phenomena that arise and need to be addressed. For example, in a pulsed discharge, an overshoot of electron temperature occurs at the early stages of the power-on phase before the plasma reaches steady state conditions [Booth & Cunge, 1997; Lieberman & Ashida, 1996; Šamara *et al.*, 2010]. This is important because plasma processes depend exponentially on electron temperature, and small changes in the EEDF can greatly affect the plasma chemistry. For example, in order to promote dissociative electron attachment reactions, 'cold' electrons are required in the afterglow phase while as the plasma re-ignites the overshoot in the electron temperature results in the destruction of the negative ions existing at the end of the afterglow/early ignition phase. Therefore, it is important to understand the effects of pulsing the discharge on the plasma parameters. The aim of the research reported here is to investigate the ignition/re-ignition phase of pulsed discharges, with the specific objective of gaining control of the EEDF.

Various techniques are available to characterize the discharges and measure

different plasma properties. Langmuir probes [Chen, 2009] and microwave resonator probes, such as the hair-pin probe [Piejak *et al.*, 2005; Šamara *et al.*, 2012b], are two probe diagnostic tools. Like all probe measuring techniques, they require care to ensure that the measurement technique does not alter the plasma properties especially in time resolved measurements in pulsed discharges. Extracting meaningful plasma parameters from Langmuir probes becomes increasingly difficult when acquiring time resolved measurements with tens of nanoseconds time resolution in the early ignition phase of a pulsed discharge. On the other hand, there are various non-intrusive optical sensing techniques which are used to characterize and measure plasma parameters. UV-broad band absorption, laser induced fluorescence and two-photon laser-induced florescence [Booth *et al.*, 1998, 2012], line-ratio optical emission spectroscopy (OES) [Li *et al.*, 2011a; Zhu & Pu, 2010; Zhu *et al.*, 2012], trace-rare gas optical emission spectroscopy (TRG-OES) [Chen *et al.*, 2009; Donnelly, 2004; Donnelly & Schabel, 2002], and phase resolved optical emission spectroscopy (PROES) [Gans *et al.*, 2004; Mahony & Graham, 1999; Schulze *et al.*, 2010] are examples of the most common optical measurement techniques used in highly reactive plasma sources.

In this study we probe the highly transient ignition phase of pulsed discharges and track the evolution of electron properties in a pulsed radio-frequency capacitively plasma source. This is achieved by using a combination of microwave probes, actinometry and emission imaging. The actinometry technique is a simplified version of the TRG-OES techniques reported by Donnelly [2004]; Donnelly & Schabel [2002] and Zhu & Pu [2010]. A gas mixture of argon, krypton and xenon was used to generate the discharge and specific emission lines were selected from each species to probe the evolution of high energy electrons. Emissions from

4p-4s, 5p-5s & 6p-6s transitions from Ar, Kr & Xe respectively were measured. Transitions were chosen for which the upper states are populated principally by direct electron excitation [Chen *et al.*, 2009; Chilton *et al.*, 1998, 2000; Fons & Lin, 1998]. High time resolution measurement of the evolution of the electron density was carried out by a hairpin probe.

3.2 Experimental set up

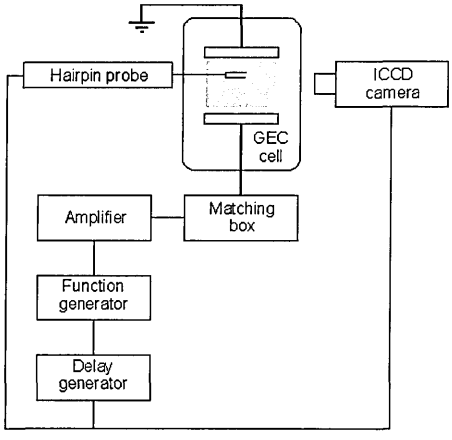

Figure 3.1: This schematic representation of the experimental system shows the various electrical and optical diagnostics.

This study was carried out in a Gaseous Electronics Conference (GEC) radio-frequency capacitively coupled plasma reference reactor with 13.56 MHz as the driving power frequency [Olthoff & Greenberg, 1995]. A detailed description of the GEC reference reactor is presented in section 2.1. Figure 3.1 shows a simplified schema of the experimental set up and acquisition tools used in this study.

3.2.1 Operational conditions

Two generator/amplifier arrangements were used to generate the plasma. The first system is powered by a waveform generator that produces the driving 13.56 MHz radio-frequency input as well as controlling the pulse frequency and duty cycles. The output of the waveform generator passes through a wide-band amplifier and a matching network before reaching the lower electrode. This setup was used to produce the set of simple rectangular wave pulses.

For the second pulse case, where the amplitude of the RF-voltage was varied within the pulse, a second circuit was used. The waveform generator was used to produce the amplitude modulation as well as pulse the frequency and duty cycle, and a RF-power source was used to produce the 13.56 MHz RF-power input. Amplitude modulated RF-pulses were then passed through the matching unit before reaching the powered electrode.

The two waveform shapes were generated at a repetition frequency of 1 kHz with 50% duty cycles. Figure 3.2 shows measurements of the RF voltage for the 1 kHz pulses. The first case is the simple rectangular wave pulse, where the RF-voltage was 'ON' for 500 μs with maximum input voltage throughout the entire active glow phase. The delay response of this generator is 2 μs. The second case has a ramped pulse shape. The RF-voltage was increased gradually for the first 250 μs and was kept constant for the rest of the active glow phase of the pulse. For this pulse case, there was a delay in the response of the generator for almost $\sim$50 μs which led to a shorter active glow phase ($\sim$450 μs). However, both cases had the same average input power. These same waveforms were also generated to at a repetition frequency of 1 kHz with a 10% duty cycle to operate the discharge.

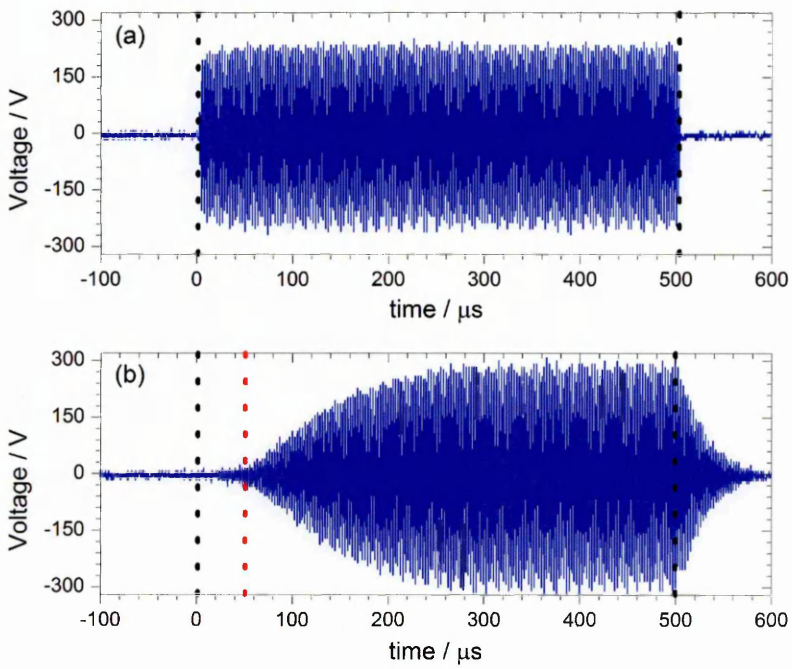

Figure 3.2: Figure (a) shows the RF voltage for the non-modulated pulses and (b) shows the RF voltage of the amplitude modulated case.

The main experiment described in this chapter used the 1 kHz pulses described above. In other experiments, the rectangular waveform shape was used also to generate a plasma at a repetition frequency of 5 kHz with 50% and 10% duty cycles.

Flow controllers were used to control the gas inflow, and an automatic throttle valve was used to maintain a constant pressure in the GEC reference reactor during the measurements. The discharge was operated with a total gas flow of 15 sccm composed of 80% argon, 10% krypton and 10% xenon, at a pressure of 100 mTorr (13.3 Pa) for all the different pulsing parameters.

3.2.2 Diagnostic tools

The RF-voltages for the two pulse cases were measured at two positions in the circuit. First, the evolution of the RF-voltage and RF-current with respect to time was recorded using an inline current probe placed before the matching network. The fundamental frequency and first four harmonics of the RF-voltage and RF-current were also recorded using the same device. Secondly, the RF-voltage delivered to the powered electrode was measured using a passive voltage probe after the matching unit at the closest physical point to the lower electrode.

A delay generator was used to synchronize and control the different optical and electrical diagnostic tools. As shown in figure 3.1, it was triggered by the waveform generator.

Time resolved electron density measurements were carried out using a hairpin probe situated 30 mm from the axis of the plasma and 15 mm above the powered electrode. A combination of the general circuit used with hairpin probes and a boxcar integrator, triggered by the delay generator, was used to acquire the temporally resolved electron density measurements. The apparatus used for the hairpin probe measurements is described in section 2.4.1. Each data point was generated by averaging 10000 acquisitions with a 74 ns measuring window per acquisition.

Temporally resolved total emission measurements were acquired using a gated intensified-CCD. Each data point was generated from 5000 acquisitions with a gate width of 74 ns where the gating was controlled by the delay generator. Spectrally resolved emission was acquired using the same setup as that of the total emission with the addition of a spectrometer. Finally, the plasma emission

was imaged using the iCCD with a lens focused at the center of the discharge, where each image was generated from 5000 acquisitions with a gate width of 74 ns.

Three emission lines were selected; one from each of argon, krypton and xenon, in order to carry out the temporally and spectrally resolved emission measurements. These selected emission lines result from the following radiative transitions $4p - 4s$, $5p - 5s$ and $6p - 6s$ of argon, krypton and xenon respectively. Those emission lines were chosen because the excited states are principally populated by direct electron excitation from the ground state atoms of these species. The life-time of those excited states is a few tens of nanoseconds ($\sim$ 30 ns) which is negligible compared with the collision frequency between the species at this pressure [Chen *et al.*, 2009; Donnelly, 2004; Donnelly & Schabel, 2002; Li *et al.*, 2011a,b; Zhu & Pu, 2010; Zhu *et al.*, 2012]. Some authors report that the Xe 828 nm emission may be contaminated by the emission from a nearby Kr line [Donnelly, 2013]. However, we examined this closely and concluded that there was no significant Kr emission in this region for our conditions, and hence our measurements at that wavelength represented only emission from the 828 nm Xe line.

3.3 1 kHz & 50% duty cycle pulses

The results from the different optical techniques and the hairpin probe measurements for the rectangular and modified pulses, with $f = 1$ kHz and 50% duty cycle, are presented and discussed in this section. The simple model of predicted emissions that was used to further interpret the measurements is also introduced.

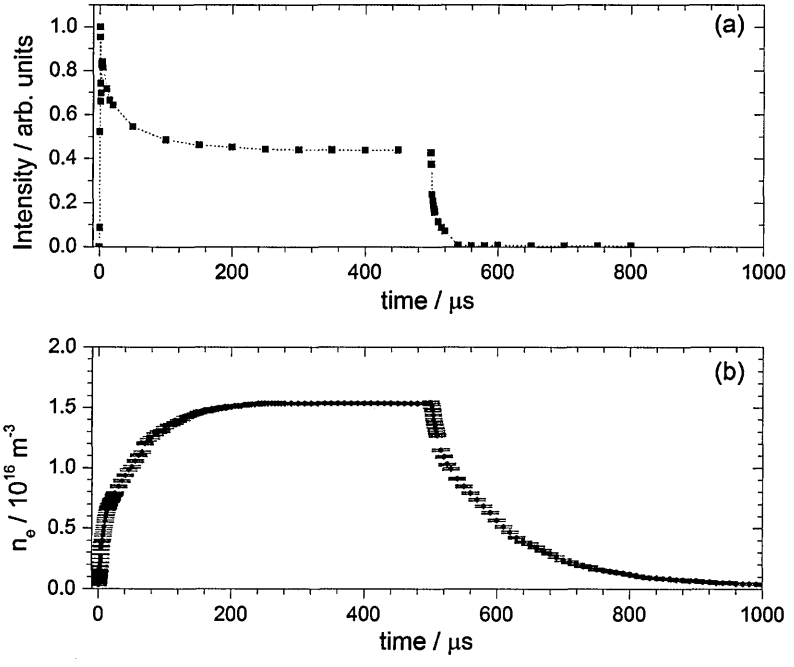

Figure 3.3: This figure shows (a) the evolution of the total emission and (b) the electron density measurement for a complete cycle of the square pulse.

3.3.1 Measurement of electron density and total light emission

The general behavior of the discharge for the two pulse cases was monitored using time-resolved measurements of electron density and plasma light emission. Figure 3.3 shows the evolution of these properties for the case of the square pulse. The emission intensity shows a distinct peak during the first few microseconds which then decreases as sharply as it rose, before settling to a much lower value throughout the rest of the active glow phase. The electron density shows a steep slope with increasing electron density for the first 20 μs. After 20 μs the electron density increases at a slower rate tending towards a constant value at 250μs,

indicating steady state conditions.

In the given regime, volume production competes with losses on electrode surfaces and chamber walls. The flux of particles at the boundary is proportional to the electron density and the square root of electron temperature. The electron production rate depends linearly on electron density and exponentially on electron temperature.

These measurements suggest the overshooting in the emission intensity is related to the response of the few electrons existing in the early ignition stage which absorb the RF-electric fields at the start of the pulse. The RF-fields at this early stage will penetrate the inter-electrode distance completely. This in turn leads to a relatively high electron temperature and production rate. Once sufficient electrons are generated, they nullify the penetration of the field throughout the inter-electrode distance leading to a decrease in the total emission and production rate of electrons. This general behavior has been observed and interpreted previously [Ashida *et al.*, 1995; Šamara *et al.*, 2010].

The hairpin probe produces reliable electron density measurements for most plasma conditions, but further interpretation is needed for low-density discharges for which significant sheaths may exist around the wires of the probe. This was investigated as follows. Figure 3.4 shows once again the temporal evolution of the measured electron density without any sheath consideration in black squares, and the electron density profile after applying a time-dependant sheath correction factor in red disks. The model developed by Piejak *et al.* [2004] was used to calculate the time-dependent sheath correction factor during the active glow phase. Since this model was developed for steady state plasmas, the instantaneous measured density was assumed to be that of a steady state plasma to calculate

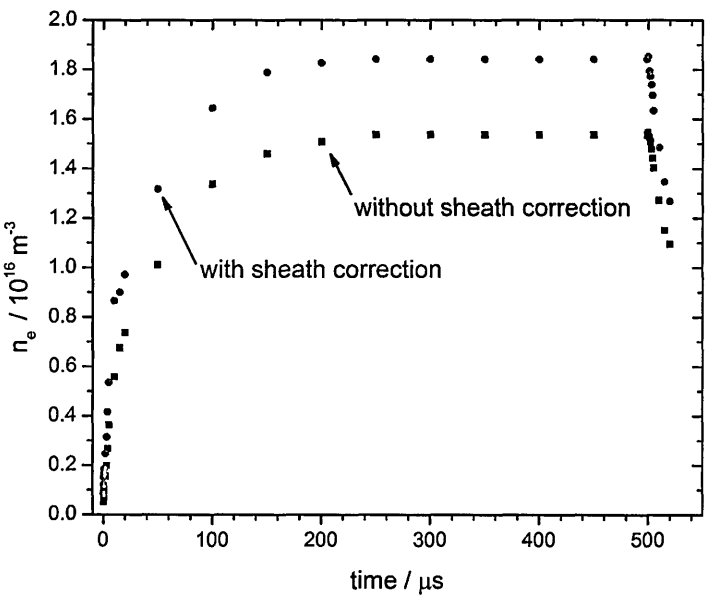

Figure 3.4: The measured electron density (black squares) and the electron density after applying the sheath correction factor (red disks) using Piejak *et al.* [2004]'s model.

a time-dependent sheath correction factor. The temporal behavior and conclusions drawn from the directly measured electron density do not change with or without including a time-dependant sheath correction factor. For this reason, the sheath correction factor was disregarded for the rest of the electron density measurements.

Figure 3.5 shows the same data for the case of the amplitude modulated (ramped) pulse shape. The emission intensity is characterized by a smooth gradual increase with no distinct features throughout the active glow phase. The electron density increases at a relatively constant rate as the applied power increases, then settles into a quasi-steady state level.

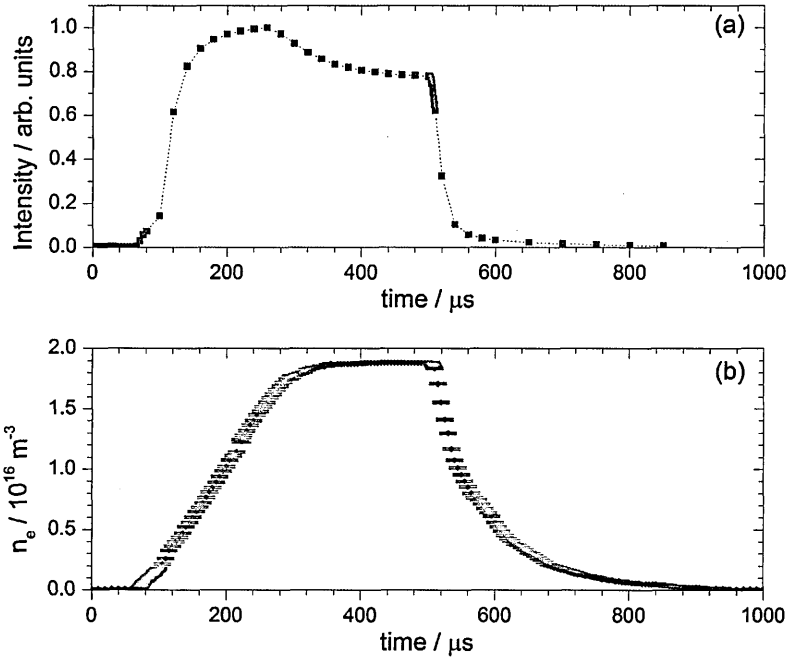

Figure 3.5: This figure shows (a) the evolution of the total emission and (b) the electron density measurement for a complete cycle of the ramped pulse.

By applying the RF-power as a waveform with ramped amplitude, the electron energy gain is more controlled so that the production-loss balance is not catastrophically disrupted at the start of the active glow. There seems to be a balance of sources and sinks throughout the entire active glow phase. This is indicated by the smooth changes in the electron production rate and light emission that accompany the gradual increase of the applied RF power.

Electron temperature was not measured directly in these experiments. It is possible to use the observed plasma emission to estimate the electron temperature in a crude way, by making assumptions about the EEDF and deriving an effective temperature from the measured emission. However, a more realistic approach to

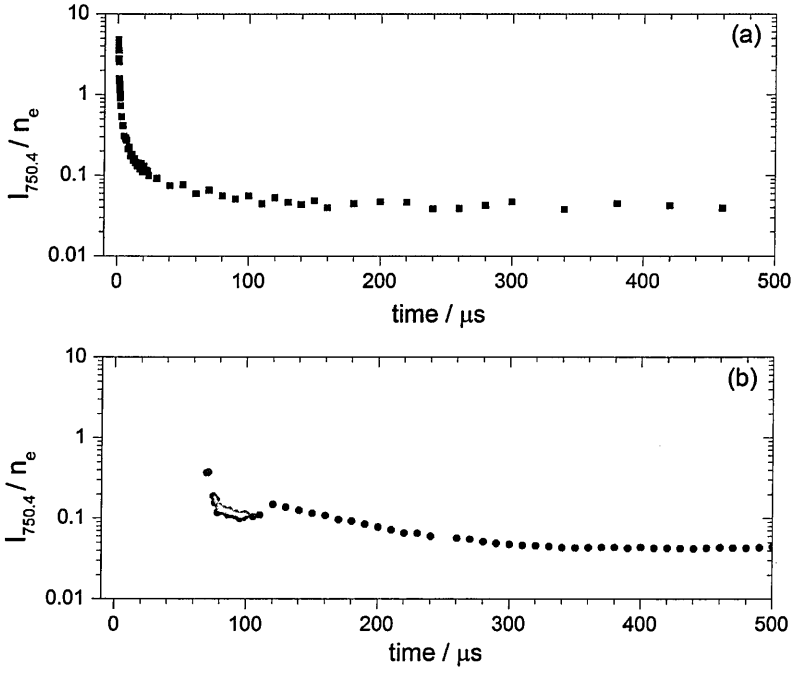

Figure 3.6: The excitation rate from the argon emission intensity measurement for (a) the square pulse and (b) the ramped pulse during the active glow phase.

gauge the ignition phase is to simply monitor the excitation rates of the argon $2p_1$ states. This can be achieved by simply dividing the the measured emission due to the relaxation of this upper state by the time resolved electron density $\frac{I_{750.4\text{nm}}}{n_e}$.

Figure 3.6 shows the evolution of excitation rate for the two pulse cases. It can be seen the the $\frac{I_{750.4\text{nm}}}{n_e}$ rises by a factor of ten more during ignition for the square pulse with respect to the ramped pulse. The EEDF is extremely unlikely to be Maxwellian during the ignition phase in both pulse cases, but this shows the combined effect of whatever energy distribution the few electrons have at the early ignition phase, and the related excitation cross-section. The ignition phase of the

square wave pulse seems not only to be much more intense, but also has a short life span which is in agreement with the total emission measurements. For the ramped pulse, there are two smaller peaks, one corresponding to the breakdown of the gas and the second appearing after few microseconds due to the increasing electron density and input RF-voltage profile. The timing of the second peak corresponds to a 'knee' seen in the total emission measurement (Fig. 3.5).

These preliminary conclusions provide some insight into the ignition behavior in this reactor but in order to understand the evolution of the EEDF during the ignition, we performed spectrally resolved measurements of plasma emission, as reported in the next section.

3.3.2 Spectrally resolved emission

This section describes the spectrally resolved emission measurements that were made to provide further information on the evolution of the EEDF, especially during the ignition phase. The first part describes the measurements. The second part presents the results of a comparison of the observed emissions with that predicted by a simple electron-excitation model of emission on these wavelengths.

Table 3.1 contains information about the three emission lines used for this experiment. These transitions were chosen because they have different threshold excitation energies and are intense enough to be observed throughout the pulse cycle. Also, the upper states are mainly populated by direct electron excitation [Chilton *et al.*, 1998, 2000; Fons & Lin, 1998], and hence their intensities reflect the number of electrons in different parts of the EEDF.

Table 3.1: Spectroscopic data for the emission lines used in this experiments. The references in the final column give the cross-sections for direct electron excitation into each state.

Gas	Emitted λ (nm)	Excitation Energy (ev)	Upper state	relaxation state	reference
Ar	750.38	13.478	$2p_1$	$1s_2$	Chilton *et al.* [1998]
Kr	758.74	11.666	$2p_5$	$1s_4$	Chilton *et al.* [2000]
Xe	828.01	9.933	$2p_5$	$1s_4$	Fons & Lin [1998]

3.3.2.1 Measurements for the two pulse shapes

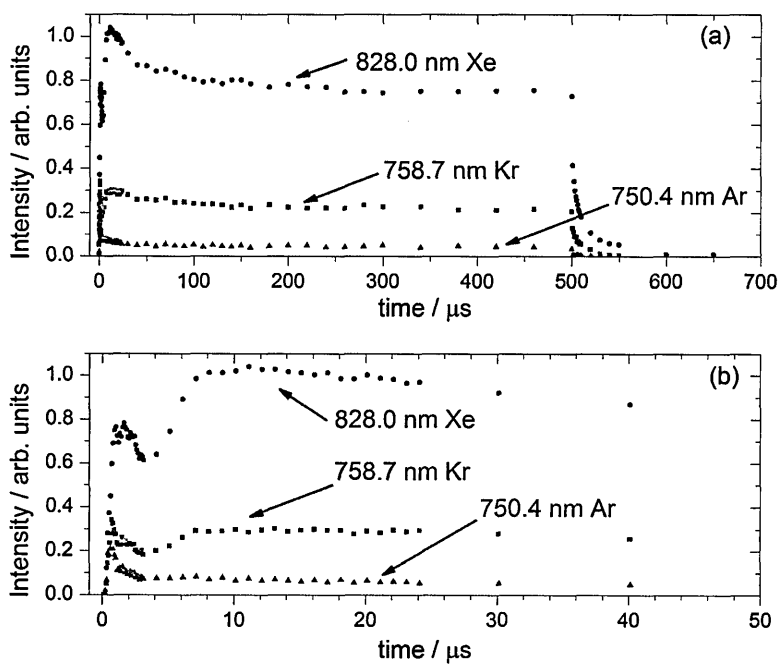

Figure 3.7: The temporal evolution of the emission intensities from each of the selected transitions for a complete cycle for the square wave pulse (a) and the first 50 μs of the pulse (b).

Figure 3.7 shows the temporal evolution of the emission from the three transi-

tions for the square pulse case. Part (a) shows the emission over the whole pulse cycle, while part (b) shows the ignition phase on an expanded time-scale. The gas mixture was Ar/Kr/Xe in ratio of 8 : 1 : 1. The Ar emission intensities in Fig. 3.7 have been reduced by a factor of 8 so that the emission from each species can be directly compared.

The data in Fig. 3.7 show an initial peak in the emission intensity for all three emission lines. However, the time dependence of each peak differs. For the case of Ar, with the highest excitation energy, there is an intense sharp peak in the first few microseconds. The emission then settles to a much lower, relatively steady value, after t= 4 $\sim$ 5 μs. For both Kr and Xe, the emission peaks in the first few microseconds but the intensity continues to change for $\sim$ 10 μs for Kr and $\sim$ 40 μs for Xe.

The general behaviour can be interpreted as indicating that the EEDF changes sharply during the first ignition phase of a few microseconds, with higher energy electrons being dominant. The differences between the time dependence of the three emission intensities indicates that the higher energy part of the EEDF stabilises first, with the lower energy electrons taking longer to come to equilibrium. Although we can not infer the EEDF itself from this data, it is likely that the EEDF in the first few microseconds is strongly non-Maxwellian, becoming Maxwellian-like as the ignition phase continues, and stabilising at $40-50$ μs into the pulse. It is worth noting that the electron density (Fig 3.3) takes $\sim$ 250 μs to stabilise, but this emission data indicates that the EEDF stabilizes over a much shorter time scale.

Figure 3.8 shows the same type of emission data recorded for the case of the ramped pulse. Part (a) shows the emission over the whole pulse, while part (b)

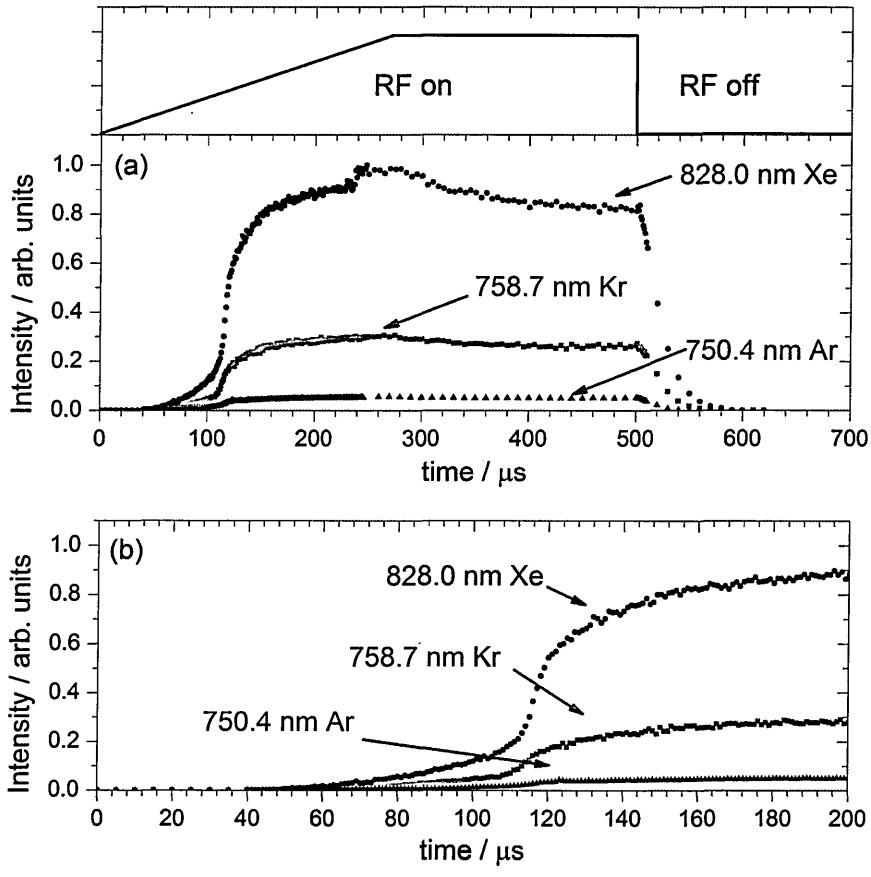

Figure 3.8: The temporal evolution of the emission intensities from each of the selected transitions for a complete cycle for the modified wave pulse (a) and the first 200 μs of the pulse (b). The trapezoid above (a) shows the RF-voltage profile for one complete cycle.

shows the early part of the pulse on an expanded time-scale. As was done for the data in Fig. 3.7, the Ar emission has been reduced by a factor of 8 so that the emission on each line can be directly compared.

In contrast to the time dependence for the square pulse case, the data in Fig. 3.8 shows no significant peaks in the ignition phase. Instead, the observed intensities for all lines change smoothly over the duration of the pulse, gradually

increasing over the first part of the pulse when the applied power is still increasing, and becoming stable just after the power becomes fixed at 250 μs. The similar dependence observed for the three lines can be interpreted as indicating that the EEDF remains relatively unchanged throughout the ignition phase and the rest of the pulse. Figure 3.8 (b) shows some weak emission from these three selected emission lines at $70 \leq t \leq 100$ μs, before the emission starts to rapidly increase. This could indicate a weak pre-breakdown phase. The absolute emission intensities are very low compared to those attained at the rest of the active glow phase.

The time- and wavelength-resolved emission data for the two pulse cases can be directly compared to give insight into the EEDF evolution for the two cases. The square pulse case is characterised by a rapidly changing ignition phase with an EEDF that is likely to be highly non-Maxwellian and contain significant numbers of high energy electrons. This short-lived phase then changes steadily until about 50 μs into the pulse, after which the EEDF is likely to be Maxwellian-like with a low average energy. The ramped pulse case is characterised by a relatively slowly changing EEDF that is likely to be always a Maxwellian-like with a low average energy. There is no short-lived rapidly changing ignition phase.

From this data, it is clear that the voltage waveform can be used to control the EEDF in these discharges and hence, to some extent, control the plasma chemistry.

3.3.2.2 Analysis using simple model

The measurements presented in the previous section indicate that the EEDF in the ignition phase is strongly affected by the applied waveform. To understand

these changes in more detail, we compared the ratios of certain measured emission lines with those predicted by a simple model of excitation and emission.

The three emission lines used in this research were selected because the emission comes primarily from direct electron excitation. With this assumption, the emission intensity for each line can be calculated using the expression:

$$I_g = n_e(t).n_g \frac{A_{ik}}{\sum A_{in}} \int \sigma_g(\epsilon) \times f(\epsilon, t) d\epsilon \tag{3.1}$$

where I_g represents the emission intensity, the subscript 'g' the particular gas species, $n_e(t)$ the electron density as a function of time, n_g the density of selected neutral species, $\sigma_g(\epsilon)$ the cross-section for direct electron excitation (fig. 3.9) and $f(\epsilon, t)$ the EEDF. The Einstein coefficient and branching factor for these emission lines is $\frac{A_{ik}}{\sum A_{in}} \sim 1$, hence, it was not included in the calculations.

Equation 3.1 was used to calculate the emission intensities for a Maxwellian distribution with average energy ϵ_{av}. These results were then used to calculate the ratio of Xe/Ar and Kr/Ar emission. These ratios are shown in Fig. 3.10. It can be seen that both ratios depend strongly on ϵ_{av} for $\epsilon_{av} \leq 3 - 5$ eV but the dependence is much weaker for higher ϵ_{av}.

This dependence can be understood in terms of the sensitivity of the emission intensities to the 'tail' of the EEDF. For an EEDF with low ϵ_{av}, emission will be dominated by the EEDF in the $10-13$ eV region where the different emission lines have their excitation thresholds. Hence, the emission ratios will vary strongly with ϵ_{av}. For higher ϵ_{av}, however, the emission will have a significant contribution from the EEDF at electron energies in the $15-25$ eV range, where all three transitions have similar excitation probabilities. While the variation in the emission ratios

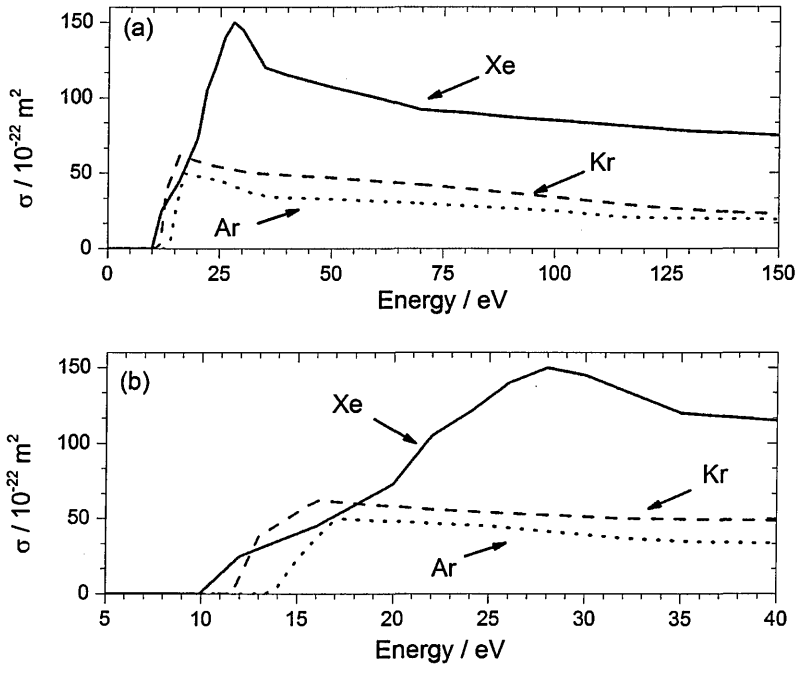

Figure 3.9: The cross-sections for the elastic direct electron excitation of the selected emission lines from Ar, Kr and Xe as a function of the electron energy (eV) [Chilton *et al.*, 1998, 2000; Fons & Lin, 1998]. Graph (a) shows the cross-sections for the elastic direct electron excitation over a wide range while graph (b) shows the region near the threshold energies on an expanded scale.

for higher ϵ_{av} will depend on the shape of the cross-section for the higher energies, the difference between cross-sections at those energies is minor compared with the $10-13$ eV region and so the emission ratios only depend weekly on ϵ_{av} for higher ϵ_{av}.

The calculated ratios shown in Fig. 3.10 can be compared with the ratios that were measured experimentally, shown in Fig. 3.11. Part (a) shows the ratios for the square pulse case while part (b) shows them for the case of the ramped pulse. It can be seen that the numerical value of the experimentally-determined

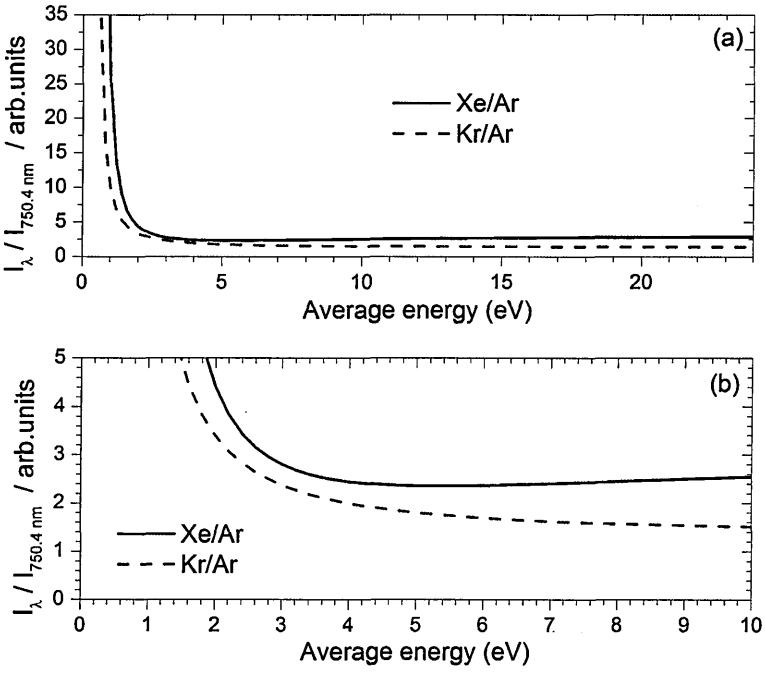

Figure 3.10: The calculated emission ratios from krypton and xenon with respect to argon as a function of the average energy of a Maxwellian EEDF. Graph (a) shows the ratio calculated for a wide range of average energy while graph (b) shows the ratio over the energy range expected for for a capacitively coupled RF discharge.

emission ratios are similar for both pulse types in the main part of the pulse. This is consistent with conclusions, drawn from other results, that the main parts of each pulse have similar electron densities and EEDFs. The first part of the pulses, however, are very different, as a result of the different ignition phases already noted earlier. Figure 3.11 can be divided into three major parts. The first is the ignition phase of the first few micro-seconds, the second where the relative emission rates seem to reach a constant value, and finally the overshoot at the start of the afterglow.

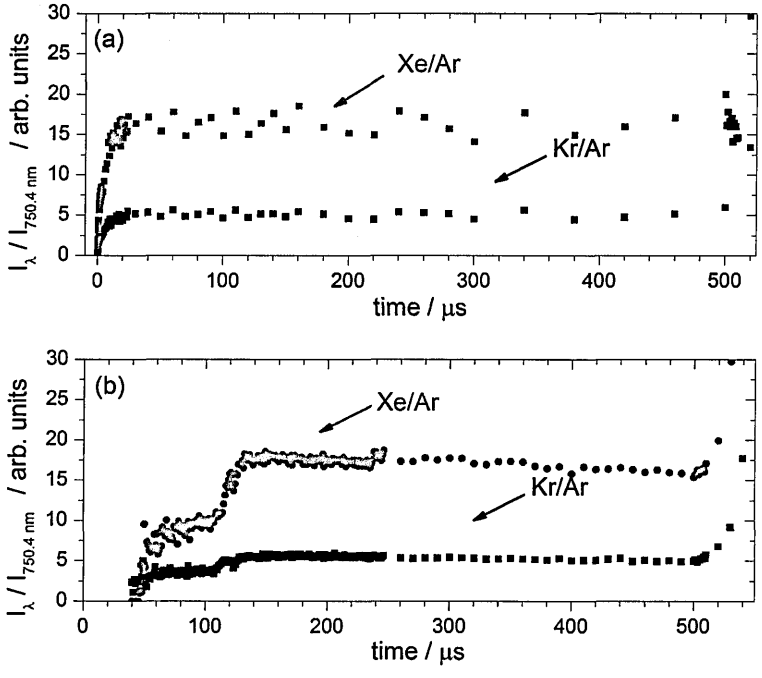

Figure 3.11: The ratio of emission lines for the two cases (a) square wave pulse and (b) ramped pulse.

The case for the square modulated pulse, figure 3.11 (a), shows a steep rapid increase from about zero to a constant value in about the first 20 μs where a knee like feature is clear. This is attributed to the fact that there is no change occurring in the emission from these species after 20 μs where the electron energy distribution tends to become a stable Maxwellian-like function. The steep increase in the ratios is due to the emission peaks from the three species indicating the presence of highly energetic electrons. The second phase is between $20 < t \leq 500$ μs where the electron average energy tends to cool down from the peak value reached at the early ignition phase to $\sim$ 3 eV, or less, with a Maxwellian-like distribution as the steady state conditions are reached later in

the active-glow phase. The third stage is the overshoot in the ratios at the onset of the afterglow, which indicates a rapid cool down of electron energies and sharp decrease from the emission intensities.

For the ramped pulse, figure 3.11 (b), in the early ignition phase there is a smooth increase of the ratios of both krypton and xenon with respect to argon. The ratios of the emission lines seem to show a weak pre-breakdown phase at $70 \leq t \leq \mu$s. The difference between the relative emission of both species is constant throughout the ignition phase until just before the start of the afterglow phase. However, after 110 μs there seems to be an increase in both relative emission lines shown as a distinct step for the Xe/Ar ratio, although the relative increase is minuscule for the Kr/Ar ratio. At this time the electron density (Fig. 3.5) is linearly increasing and the effective electron temperature is constant. This suggests that the increase in the Xe/Ar emission ratio is mostly due to the electrons in the bulk of the EEDF.

During the early ignition phase, the relative emission ratios of the ramped pulse are different from those from the square wave pulse. After $\sim$ 300 μs the emission ratios seem to attain the same levels in both pulse cases. The absolute measured values (figure 3.11) are not consistent with the calculated ratios (figure 3.10). This indicates that the simple model used to calculate emissions from these levels needs more refining where other parameters should be included (such as population of the emitting state via non-ground state levels) if absolute comparisons are desired. A better estimate of the emission, in particular during the ignition phase, would require more complicated non-Maxwellian energy distribution functions to be considered.

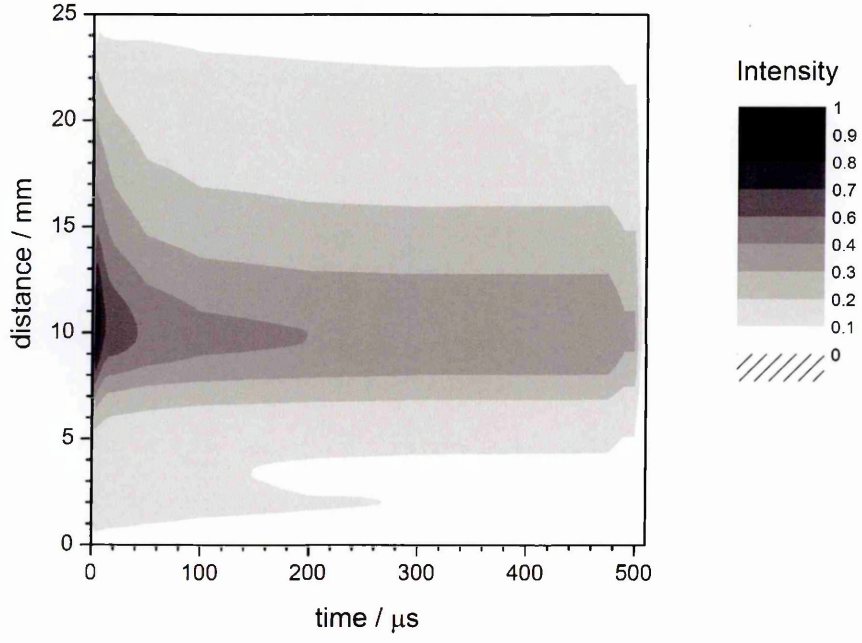

Figure 3.12: This figure shows the spatial distribution of the plasma for the square wave pulse for a complete cycle. The vertical axis is across the azimuthal direction between the electrode planes, and the horizontal axis is the time axis.

3.3.3 Spatially-resolved emission measurement

Further insight into the EEDF evolution in these discharges can be gained by observation of the spatial distribution of the plasma emission. An imaging system was used to record the distribution of light emission for the two types of pulsed discharges studied in this research. This data was used to draw conclusions about the EEDF in the active glow period in general and the ignition phase in particular.

Figure 3.12 shows the spatial distribution of the emission between the electrodes for the active glow period of the square pulse discharge. The figure shows

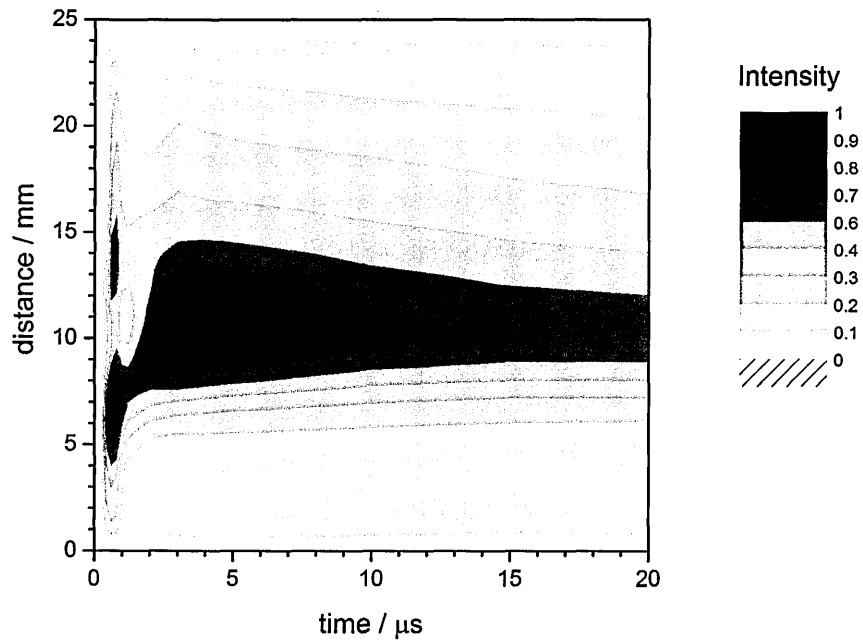

Figure 3.13: Spatial distribution of the plasma for the square wave pulse during the ignition phase in the first 20 μs of the pulse.

that the emission is most intense in the first 50 μs, before settling into a relatively stable distribution for the period t= 50−500 μs. This is consistent with the global emission presented earlier and shown in Fig. 3.3. However, the distribution shown in Fig. 3.12 shows that the emission in the first ten microseconds comes from a widespread region of the plasma volume compared with the situation after 50 μs. The 50 − 500 μs period, in contrast, shows emission coming mainly from the plasma centre. The relatively emission free-regions in front of each electrode for this time period indicate the stable sheath regions.

Figure 3.13 shows the same spatially resolved emission for just the ignition

phase. The expanded scale shows the change in the spatial distribution of the emission that takes place in this period. It can be seen that the initial emission peak in Fig. 3.3 arises from atoms distributed right across the plasma volume. This indicates that high energy electrons must exist throughout the plasma volume during this initial ignition phase. The distribution of emission changes after the first few microseconds, with emission-free sheath regions beginning to form and the emission becoming localised in the plasma centre.

The emission data supports the conclusions drawn from the electron density and spectrally resolved emission measurements presented in sections 3.3.1 & 3.3.2. This data is entirely consistent with an ignition phase characterised by a rapidly changing EEDF with a high average energy, with the high energy electrons existing throughout the plasma volume. This short lived initial ignition phase is then followed by a longer phase in which the EEDF continues to change until 50 μs into the pulse. After this time, emission is localised between the two sheaths and the EEDF is stable with a low electron average energy.

Figure 3.14 shows the spatial distribution of the light emission between the electrodes for the active glow period of the ramped pulse discharge. The figure shows a gradual increase of the emission intensity during the first 250 μs, before settling into a relatively stable distribution for the period t= $300 - 500$ μs. This is consistent with the global emission presented in Fig. 3.5. However in contrast with the square pulsed discharge, the emission is always most intense in the centre of the plasma, and the relatively emission-free regions in front of each electrode indicate the stable sheath regions throughout the entire active glow period.

Figure 3.15 shows the same emission data with an expanded time-scale that just shows the ignition phase. The expanded scale reveals the gradual change

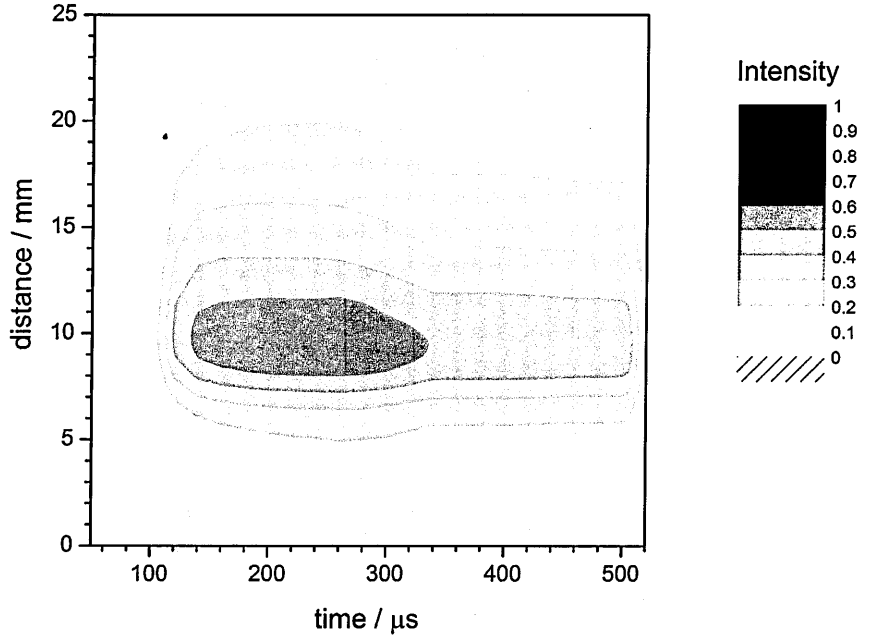

Figure 3.14: Spatial distribution of the plasma for the modulated wave pulse for a complete cycle.

in the spatial distribution of the emission that takes place in this period (t= $85 - 150$ μs). The initial low emission intensity arises from atoms distributed in the centre of the plasma volume. The distribution of the emission gradually changes with time but is always peaked near the plasma centre. Clear emission-free regions are formed indicating stable sheath regions throughout the entire active glow period. Also, it supports the assumptions made earlier about a weak pre-breakdown phase at $70 \leq t \leq 110$ μs.

It can be deduced from the spatial distribution measurements of both pulse cases that their ignition phases have a different time and electron energy de-

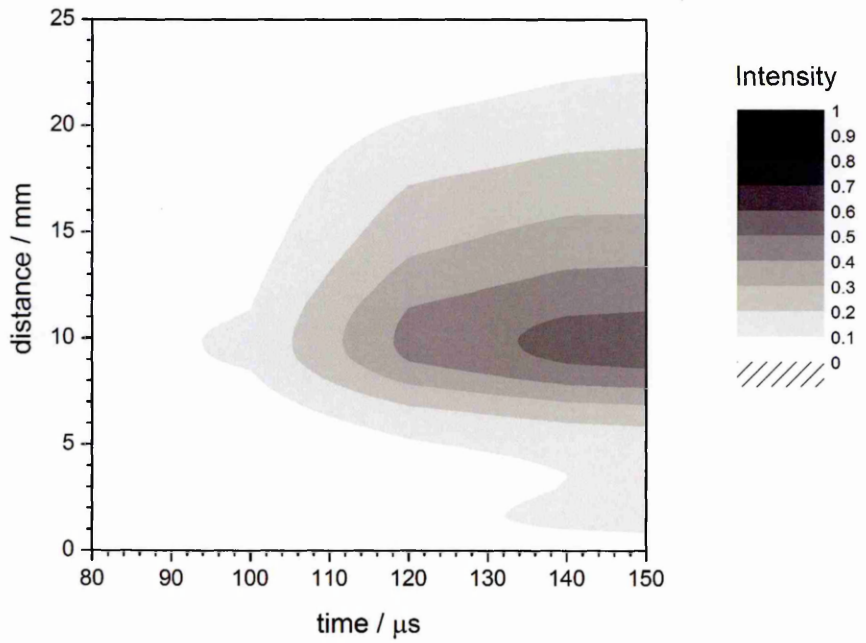

Figure 3.15: Spatial distribution of the plasma for the modified wave pulse during the ignition phase in the first 150 μs of the pulse.

pendence. The ignition phase of the square pulsed discharge is characterised by a rapidly evolving phase with electrons having high average energy widespread through the entire plasma volume which settle in few tens of microseconds. However, the ignition phase of the ramped pulse is characterised by low average energy electrons localised in the centre of the plasma which take about 250 μs to settle.

These measurements are consistent with the electron density and spectrally resolved measurements presented in the previous sections. It is clear that by changing the RF-voltage waveform we can control the timescale of the ignition phase as well as the EEDF that controls the plasma chemistries during this phase.

3.4 Other pulsing conditions

Time resolved OES and electron density measurements were performed for various pulsing conditions. While spatiotemporal imaging was not performed for these conditions, it is interesting to consider these results briefly. The first set of measurements is for a pulse frequency of 1 kHz with a 10% duty cycle for both waveforms presented in the previous section. The second set of measurements is for a pulse frequency of 5 kHz with 10% and 50% duty cycles for the rectangular waveform. Ar, Xe, and Kr gases with a ratio of 8:1:1 were used to generate the discharge at a pressure of 100 mTorr for all the pulsing conditions.

3.4.1 1 kHz & 10% duty cycle pulses

The general behavior of the discharge for the two pulse waveforms was monitored using time-resolved measurements of electron density and plasma light emission. These measurements are presented in fig 3.16 for the rectangular waveform and fig 3.17 for the modified waveform with 1 kHz pulsing frequency and 10% duty cycle.

Figure 3.16 shows the total light emission (black squares) and the electron density (blue disks) for the rectangular pulse with 1 kHz frequency and 10% duty cycle. The total light emission peaks in the first 2 μs and decreases for the rest of the active glow phase (2-100 μs) following a trend similar to the first 100 μs for the 1 kHz 50% duty cycle case, fig 3.3 (a). The oscillations in the decreasing total light emission can be attributed to aliasing. This occurred because the gating of the i-CCD was equal to 50 ns which is almost equal to two thirds of an RF-cycle ($\sim$ 74 ns). Although undesirable, this effect does not influence the general

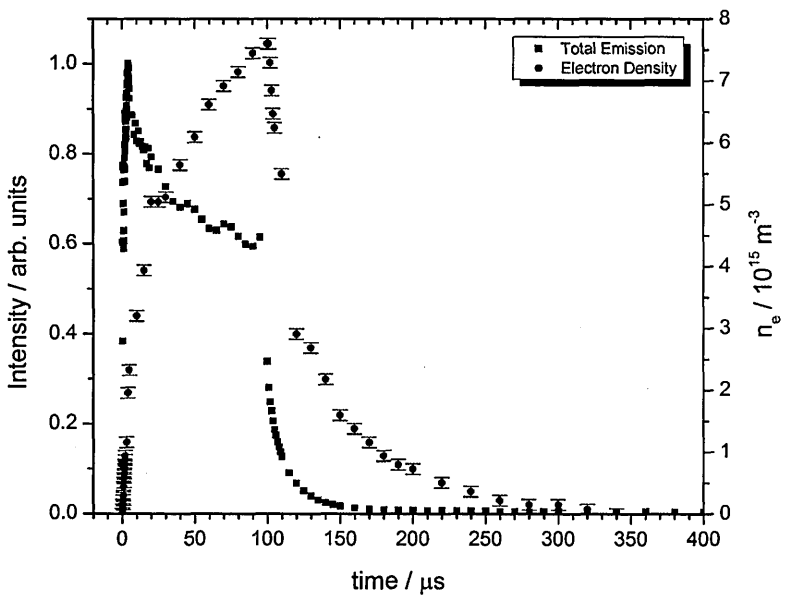

Figure 3.16: The temporal evolution of the total emission intensity (black squares) and electron density (blue disks) for a 1 kHz rectangular waveform with a 10% duty cycle.

conclusions we can draw from these measurements.

The total emission decays quite rapidly during the first few μs of the afterglow. The total emission is exponentially dependent on the electron temperature, which drops rapidly during the first few microseconds in the afterglow. The electron density shows a steep slope with increasing density during the first 20 μs, after which the density continues to increase at a slower rate for the remainder of the active glow phase. The behavior of the electron density seems to be similar to that in the first 100 μs for the 1 kHz 50% duty cycle case, fig 3.3 (b). The electron density decays exponentially during the afterglow reaching a virtual zero value after 340 μs. The electron density after 340 μs actually decreases to a value

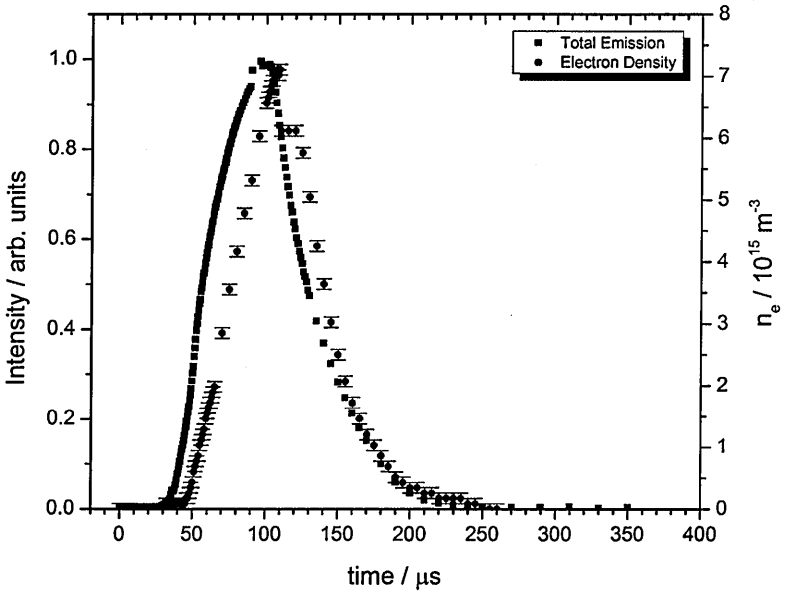

Figure 3.17: The temporal evolution of the total emission intensity (black squares) and electron density (blue disks) for a 1 kHz modified waveform with a 10% duty cycle.

lower than the sensitivity range of the hairpin probe. Assuming $n_e(t_{afterglow}) = n_{e0} \times \exp(\frac{-t}{\tau})$ where n_{e0} is maximum electron density attained during the active glow phase and τ is the decay constant rate in the afterglow. The decay constant is then 28 μs in this case.

Fig 3.17 shows the total light emission (black squares) and the electron density (blue disks) for the modified pulse with 1 kHz frequency and 10% duty cycle. The total emission shows a gradual increase with the absence of any peaks in the active glow phase. The emission during the active glow phase profile is relatively similar to that in the first 100 μs for the 1 kHz 50% duty cycle case, fig 3.5 (a). During the afterglow phase, the light emission seems to exponentially decay at a relatively

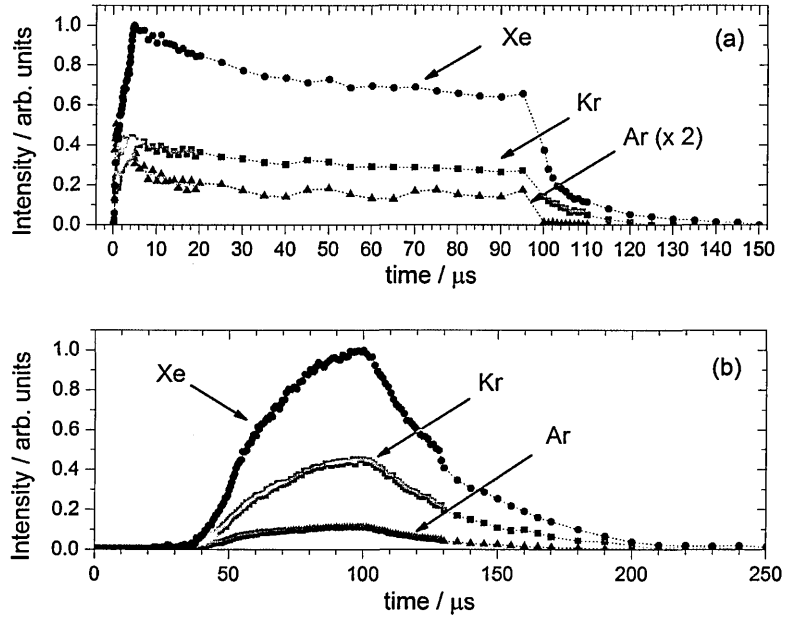

Figure 3.18: Spectrally and temporally resolved emission for the 1 kHz 10% duty cycle (a) rectangular waveform and (b) modified waveform. In (a) the emission from Argon is multiplied by two to show the peak in the early stages of the ignition.

slower rate than all the previous conditions. It actually takes about 100 μs to extinguish, longer than all previous conditions, in which the light emission reaches zero after $\sim$ 50 μs.

The electron density shows an almost linear increase during the entire active glow phase. This linear behavior is also similar to the evolution of the electron density in the first 100 μs in the modified waveform case with a frequency of 1 kHz and 50% duty cycle. During the afterglow, the electron density decays exponentially with a decay rate of 32 μs, also assuming $n_e(t_{afterglow}) = n_{e0} \times \exp(\frac{-t}{\tau})$.

Figure 3.18 shows the evolution of the emission lines from Ar, Kr and Xe

(f=1 kHz, 10% duty cycle) (a) for the rectangular pulse and (b) for the modified waveform pulse.

The intensity of the argon emission line, fig. 3.18 (a), rapidly peaks at $t = 2$ μs and then decreases and settles around 10 μs. Kr & Xe emission intensities rapidly increase as well and peak at $t = 4$ μs. The Kr emission line then tends to a constant value at $t = 20$ μs while the Xe emission line peaks at $t = 40$ μs. The ignition phase and time dependance of the emission behavior is similar to the case of 1 kHz 50% duty cycle, shown previously in fig. 3.7 (b). For the case of the modified waveform, all the emission lines, fig. 3.18 (b), simultaneously show a gradual increase with no distinguishable peaks during the early ignition phase similar to the case presented in fig. 3.8 (b). Emission from Ar almost tends to a constant value around $t = 40$ μs before gradually deceasing during the afterglow ($t > 100\mu$s). Emission from Kr & Xe gradually increases during the entire active glow phase. The emission from these lines stops at 170 μs for Ar and and at 210 μs for both Kr & Xe. Xe has the longest emission time during the afterglow ($\sim 30\mu$s). However, in this case emission from Xe takes about a 100 μs to stop. The long life time of these emissions indicates that the plasma is still on. This is so because these emission lines occur from the relaxation of excited states populated mostly by direct electron impact with a ground state atom. Measuring the RF-voltage output close to the powered

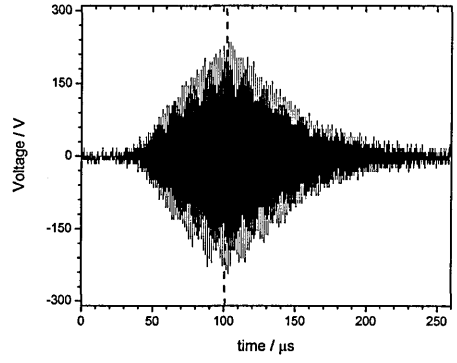

Figure 3.19: RF voltage output of the modified waveform with $f = 1$ kHz and 10% duty cycle near the powered electrode.

electrode sheds some light on this behavior.

Figure 3.19 shows the RF-voltage near the powered electrode for the modified pulse with 1 kHz and 10% duty cycle. The dotted black line shows where the trigger signal stops. It also shows that the RF-voltage decays at a slow rate, keeping the plasma ignited for longer than 100 μs. Hence, all the emissions take longer to decay to zero and the electron density decreases gradually following the decay of the RF-voltage.

3.4.2 5 kHz pulse frequency

A further set of measurements was made using a higher pulse frequency, while keeping the gas composition and pressure unchanged. The pulse frequency was set to 5 kHz, giving a period of 200 μs, with two duty cycles 10 & 50%. This pulse frequency ensured that the afterglow was sufficiently long for the electron density to decrease to a measurable relatively low value. The rectangular waveform was used for these pulsing conditions.

Similar to the previous studies, the general plasma behavior was monitored by measuring the total plasma emission and electron density for both duty cycles. Figure 3.20 shows the time resolved total plasma emission (black squares) and electron density (blue disks) for the pulsing frequency of 5 kHz and 50% duty cycle.

Interestingly, the total plasma emission shows two peaks during the early ignition phase before gradually decreasing during the rest of the active glow phase. The first peak appears at $t = 1.5\mu$s and the second at $t = 10$ μs. The first emission peak attains a relative value of almost 60% of the maximum measured value of

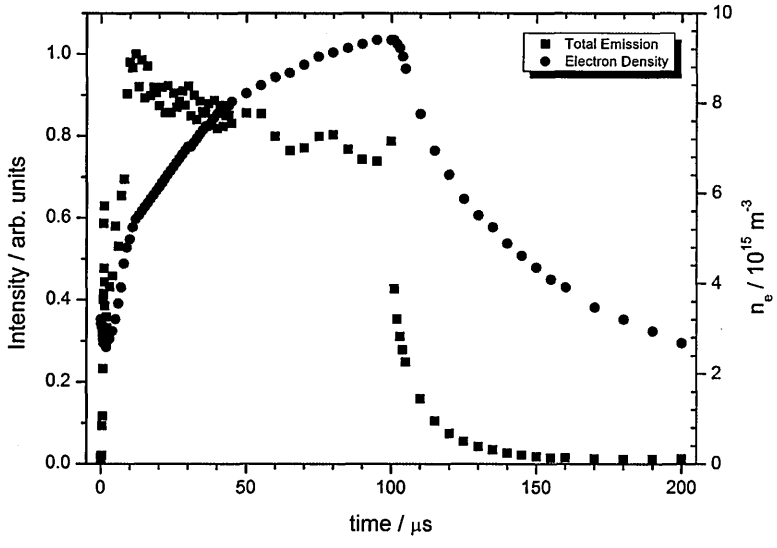

Figure 3.20: The temporal evolution of the total emission intensity (black squares) and electron density (blue disks) for a 5 kHz rectangular waveform with a 50% duty cycle.

the second peak.

The electron density shows a 'virtual' decrease in the first two microseconds, increases rapidly until $t \sim 15\mu$s and at a slower rate for the rest of the active glow phase. The electron density decay rate is about 36 μs during the afterglow. The electron density is equal to 2.5×10^{15} m^{-3} at the end of the afterglow. This remaining electron density influences the conditions of the ignition phase when the next burst of RF-voltage starts. The 'virtual' decrease in the electron density, at the beginning of the pulse, is due to the fact that the electrons heat up rapidly due to absorption of the sudden RF-voltage during the early ignition phase. This decrease in the density is not real as the density is gradually increasing, but this dip in the profile profile is because of the electrons gain a lot of energy at this

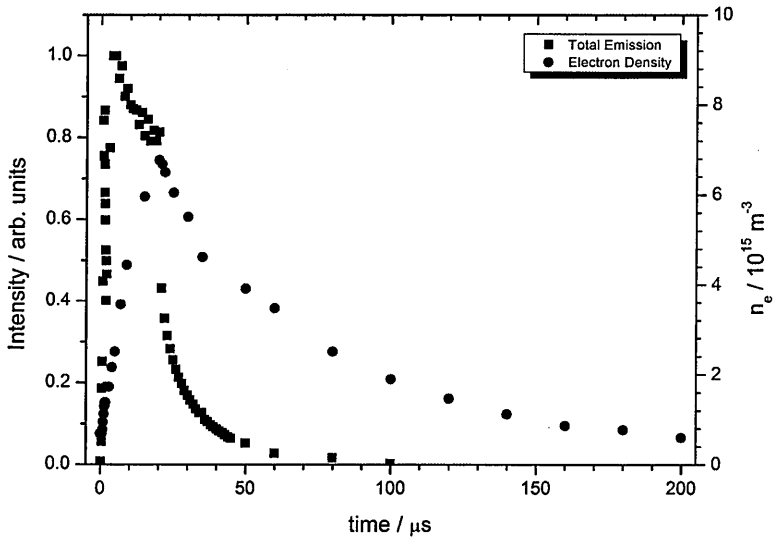

Figure 3.21: The temporal evolution of the total emission intensity (black squares) and electron density (blue disks) for a 5 kHz rectangular waveform with a 10% duty cycle.

early stage of the pulse and escape the volume surrounding the hairpin probe. It is as if the sheath expands and occupies almost all the area between the strands of the probe. This behavior was not observed in the previous measurements simply because the electron density at this time was lower than the sensitivity range of the hairpin probe. This also explains the first emission peak as the emission depends exponentially depend on the electron temperature. The emission peak decreases to about 40% of the second emission peak. This could be attributed to the fluctuations of the electron temperature and increase in the electron density as a response to the input RF-voltage.

Figure 3.21 shows the temporal behavior of the plasma emission (black squares) and electron density (blue disks) for the rectangular waveform pulse with 5 kHz

pulsing frequency and 10% duty cycle.

The total plasma emission shows a peak in the ignition phase around $t = 5$ μs, and gradually decreases during the rest of the active glow. It is not clear if there are double emission peaks during the active glow phase from the total plasma emission. This could be due to the time scale of these events and the duration of the active glow phase.

The electron density shows a monotonic rapid increase during the active glow phase without any 'virtual' decrease in the early ignition stage. The electron density decay rate time is equal to 54 μs during the afterglow, and the density reaches a value of 0.2×10^{15} m^{-3} at the end of this phase. This electron density sets up the conditions for the ignition phase when the next burst of RF-voltage starts and is very close to sensitivity limit of the hairpin probe. The lack of this 'virtual' decrease could be related to the sensitivity of the hairpin probe at this electron density range.

Figure 3.22 shows the temporal evolution of the selected emission lines from Ar, Kr & Xe for (a) 50% and (b) 10% duty cycles of the rectangular waveform pulses with $f = 5$ kHz.

For the 50% duty cycle, fig. 3.22 (a), shows a double peak in the ignition phase similar to the total plasma emission. The first peak appears at $t = 1.5$ μs, decrease at $t = 2$ μs and then all emissions increase forming the second peak at $t =\sim 11$ μs. After this time all emissions seem tend to a constant value. Oscillations in the Ar emission line could be attributed to the aliasing that occurs because of the gate width of the i-CCD (50ns).

For the 10% duty cycle, fig. 3.22 (b), shows a similar temporal behavior of the emission lines as they peak at $t = 1.5$ μs, decrease at $t = 2$ μs and then all

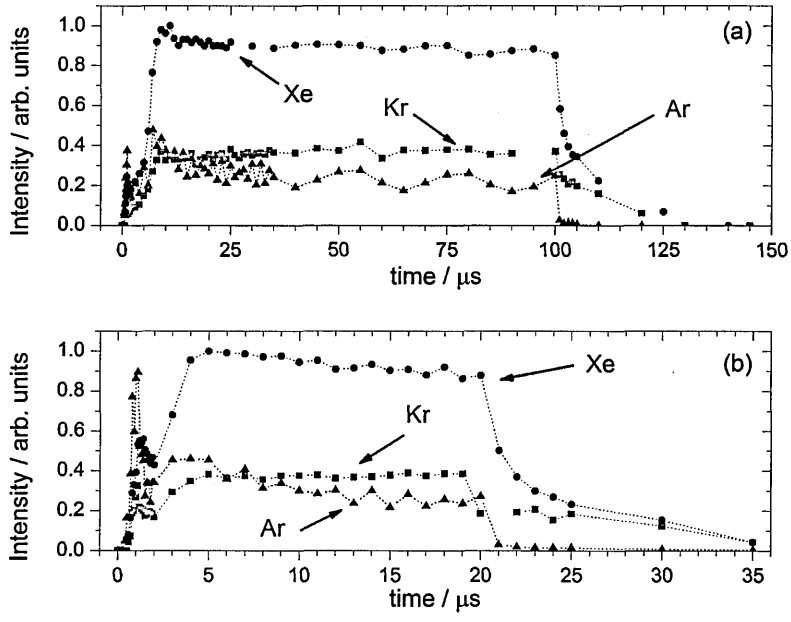

Figure 3.22: Spectrally and temporally resolved emission for rectangular waveform with 5 kHz pulsing frequency with (a) 50% and (b) 10% duty cycles.

emissions increase forming the second peak at $t =\sim 5$ μs. A double peak in the spectrally resolved emissions can be seen which was not as obvious from the total plasma emission. The Ar emission, which has the highest excitation threshold, seems to reach a constant value around $t = 8$ μs.

These measurements give further insight into the general plasma dynamics and behavior for a wider range of conditions. The conclusions from these brief measurements are in agreement with those reached from the detailed study presented in section 3.3.

3.5 Conclusions

In this chapter, we have presented a study that aimed to characterise the ignition phase of pulsed RF-discharges, with particular emphasis on understanding the evolution of the EEDF during this phase. This was achieved through electron density measurements combined with spectrally- and spatially resolved emission measurements.

We successfully applied pulse tailoring, by using different RF-waveforms, to alter the plasma properties and control the ignition phase in a capacitively coupled discharge. This technique is relatively simple and straightforward to apply compared to other approaches, such as double frequency RF-sources, used to tailor certain plasma properties. These results indicate that the EEDF during operation can be influenced and even controlled to some extent by pulse tailoring. This technique can be used to fine tune plasma chemistries, as they are highly sensitive to the details of the EEDF.

For the case of square wave pulse excitation, ignition is characterised by a highly transient phase that is very different from the discharge conditions throughout the remainder of the pulse. Electron density measurements show that electron production is relatively high in this phase, while the spectrally resolved emissions show that the EEDF is characterised by high energy electrons with a strongly non-Maxwellian distribution. The spatially resolved measurements indicate that these electrons are present throughout the discharge volume. For the case of the ramped pulse, the discharge ignition is characterised by a much gentler ignition phase in which the EEDF does not change significantly. Spectrally and spatially resolved measurements support this conclusion.

The results presented here demonstrate the significant effect that pulse tailoring can have on the EEDF, without greatly affecting properties such as plasma density. A similar approach in reactive plasmas should allow the control certain plasma chemistries through the enhancement of some reactions and suppression of others. Related studies are planned for etching chemistries such as $Ar/SF_6/O_2$.

Although in this study it was not possible to directly correlate observed emission with specific EEDFs, this combination of time-resolved electron and emission measurements enabled the identification of the different ignition processes and different ignition time-scales and their dependence on the shape of the applied voltage waveform. This approach should be applicable to other pulsed discharges, especially over the time periods in which extremely rapid transient behavior is dominant and conventional measurement techniques are difficult to apply and interpret. Further refinement of the approach should be possible through the development of time-dependent collisional-radiative models.

Chapter 4

Inductively coupled plasma study

Inductively coupled plasma sources are widely used for a variety of processing applications because of their high plasma density, low ion bombarding energy and the ability to separately control the ion bombarding energy [Ashida *et al.*, 1995, 1996]. Plasma processing requirements are becoming more strict and challenging as the device features of ICs are shrinking. This requires precise control over plasma properties such plasma density, electron temperature, radical reactivity, ion flux & energy, neutral-to-ion flux ratio and dissociation rate [Banna *et al.*, 2012]. The precise control largely relies on separately controlling these plasma properties to meet the challenges of etching sub-30 nm features.

Separately controlling plasma properties requires a certain flexibility in operating the plasma, which is not available in tradition plasma sources and continuous operational regimes. Pulsed plasmas are one of the suggested approaches to acquire this control due to the extra control 'knobs' they introduce, such as pulse frequency and duty cycle. Pulsed plasmas were widely studied in academia in the early nineties [Ashida *et al.*, 1995, 1996; Overzet & Leong-Rousey, 1995],

and have become of interest for both academia and industry over the last decade [Banna *et al.*, 2012; Brihoum *et al.*, 2013; Šamara *et al.*, 2010].

In this chapter we aim to characterise our ICP source in continuous and pulsed regimes, and in particular to probe the transient ignition phase in the pulsed regime. This chapter can be outlined as follows: section 4.1 contains different electrical and optical measurements of several discharges operated in a continuous mode which characterise our plasma source. Section 4.2 includes various measurements performed for pulsed discharges, where general plasma behavior was monitored for a wide range of parameters and detailed study was performed for specific sets of conditions. Finally, section 4.3 consists of the conclusions reached from the different measurements and studies which were performed on both continuous and pulsed discharges.

4.1 Plasma behavior for continuous operation

This section describes a series of measurements made in the PL80 ICP source when it was operated in continuous mode. The aim of these measurements is to characterise this source. A detailed description of the PL80 ICP source was presented in section 2.2. The measurement techniques used in this chapter were introduced in section 2.4 and the OES method was discussed in detail in section 3.3.2. Figure 4.1 shows a simplified schematic representation of the PL80 ICP source. The blue arrow represents the only port of access to the center of the bulk plasma in the coil region, via a small port in the vacuum flange at the top of the ICP source.

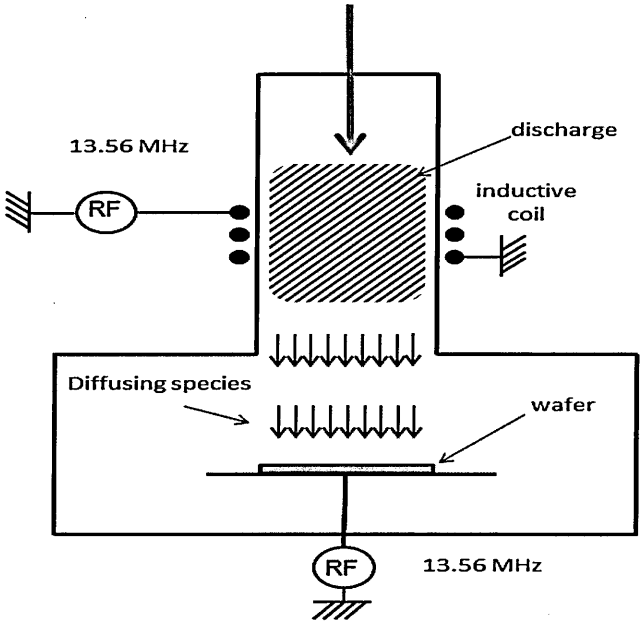

Figure 4.1: A schematic representation of the PL80 ICP source showing the main plasma region (close to the powered coil) and the diffused plasma region (species diffused to the wafer) and the power sources. The blue arrow indicates the only available access port to the bulk plasma.

4.1.1 Charged species density measurements

The electron density was measured using a hairpin probe resonator. Ion density was measured separately using a Langmuir probe, using a calculation based on the ion saturation region of the I-V characteristic. A planar Langmuir probe was used to carry out these measurements and was kept at a constant bias of -40 V.

Electron density was measured for different pressures and powers using a hairpin probe that was introduced into the system in a vertical position, indicated by the blue arrow in figure 4.1. Many problems had arisen in initial attempts to use a probe in this discharge, especially at relatively high powers ($P > 100$ W).

The problems, which included boiling and outgassing of the epoxy used to

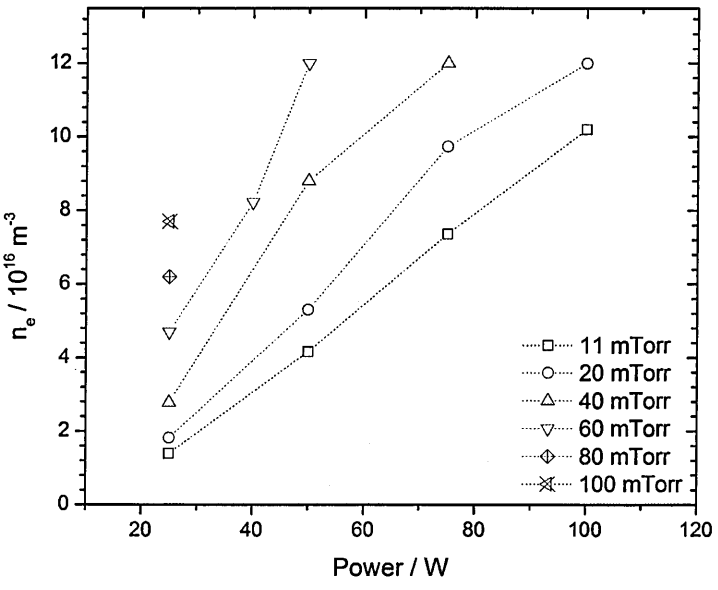

Figure 4.2: Electron density measurement in argon plasma for different gas pressures. The probe was situated 10 cm above the coil center.

seal the probe, were caused by the high electron density and perhaps the high gas temperature in the center of the source. Changes in the probe design and construction allowed successful measurements. A temporary solution was to position the hairpin probe 10 cm above the center of the coil region and perform fast measurements.

Pure argon gas was used to generate the discharge at a constant flow rate of 30 sccm while the pressure and input power were varied. Figure 4.2 shows the measured electron density for the various pressures as a function of input power. The electron density seems to increase with input power and pressure. For pressures of 60 and 100 mTorr the resonance frequency of the hairpin probe

was higher than the range of the circulator used in the hairpin probe circuit. Therefore, for these pressures there are fewer data points than the rest. For the 100 mTorr discharge, the measured plasma density was equal to 7×10^{16} m^{-3} for the lowest input power of 25 W. The electron density seems to be higher than 7×10^{16} m^{-3} for 11, 20 and 40 mTorr for input power greater than 75 W, while it is higher than that for 60 and 100 mTorr for lower input powers ($\sim$ 40 W). No sudden increase in the electron density can be seen as a the input power is increased. Typically, a sudden increase in the density occurs in ICP discharges due to the transition from E- to H-mode. E-mode is when the ICP source operates mostly in a capacitive mode with relatively low electron density (maximum $\sim$ 9×10^{16} m^{-3}), while the H-mode is the inductive mode and is characterised with densities higher than that.

Electron density was measured for an Ar/Kr/Xe plasma with 8:1:1 ratio. The discharge was operated at 20 and 100 mTorr with a total gas flow of 30 sccm. The hairpin probe was situated 12 cm above the coil center to allow higher input powers. Electron density was measured for $25 \leq P \leq 250$ W for the Ar/Kr/Xe plasma, but in argon for $25 \leq P \leq 100$ W. Figure 4.3 shows the electron density measurement for both pressures as a function of input power. The electron density seems to increase in the same manner as for the case of pure argon for the power range of $25 \leq P \leq 100$ W, attaining relatively similar values. Spectroscopic measurements require the addition of Kr & Xe gases to the discharge, as was done in the research described in chapter 3. Measurements showed that the addition of these gases to the ICP discharge had almost no effect on the electron density.

A small step increase in the electron density can be noticed at $P = 150$ W and

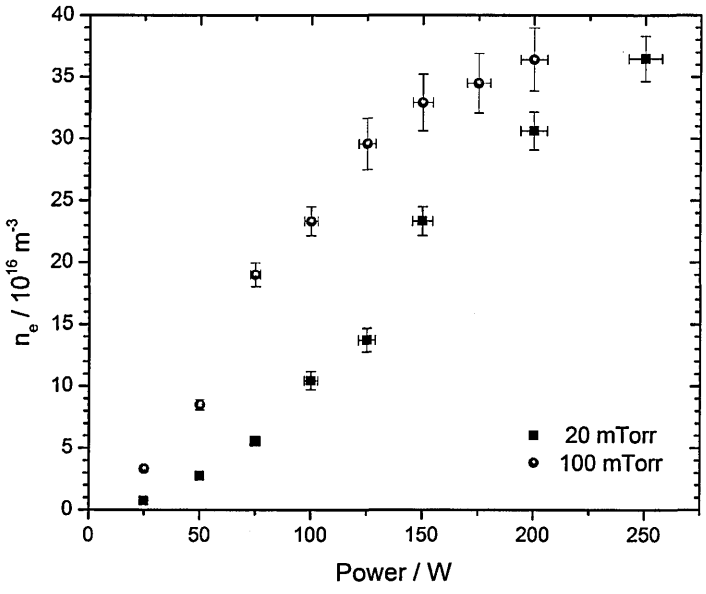

Figure 4.3: Electron density measurement in Ar/Kr/Xe plasma with 8:1:1 mix ratio for 20 and 100 mTorr pressures. The hairpin probe was situated 12 cm above the coil center.

$P = 75$ W for the 20 and 100 mTorr pressures respectively. This step increase could indicate the transition from an E- to a H-mode. A similar step increase was not seen in the pure argon case, fig 4.2, probably because of insufficient input power for the 20 mTorr Ar discharge ($P_{max} = 100$ W). The electron density seems to start saturating for $P > 150$ W in the 100 mTorr case as the error bars start to increase at this power range. This could be attributed to the merge of the probe resonance peak with the background signal, which changes significantly at these powers and electron densities.

Ion density in argon plasma operated at 20 mTorr was measured using a planar

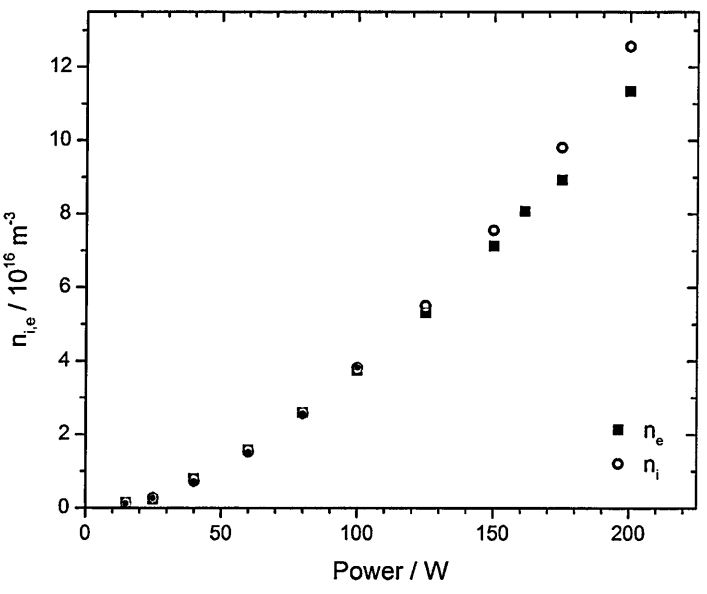

Figure 4.4: Comparison of the electron density measurement using a hairpin probe resonator (black squares) and ion density measurement using a planar Langmuir probe (red circles) in a 20 mTorr pure argon plasma where both probes were situated 15 cm above the coil center.

Langmuir probe. The probe tip consisted of a stainless steel disk with a diameter of 6 mm. The probe was operated in the ion saturation regime and was maintained at a potential of -40 V. The ion saturation equation (2.6), which requires the Bohm speed equation (2.7), was applied to the measured current to calculate the ion density. Details of these equations can be found in section 2.4.2.1.

Figure 4.4 shows a comparison between the electron density measurement and ion density measurement using a hairpin probe and a planar Langmuir probe,respectively, in a 20 mTorr pure argon plasma. Both probes were situated 15 cm above the coil center to enable the measurement of densities at powers

above 100 W. The Bohm speed was estimated to be $u_B = 2688$ m/s assuming that Ar^+ is the dominant ion and the electron temperature was set to 3 eV in order to calculate the ion density from the ion saturation current. The two measurement techniques are in very good agreement.

The design of the planar Langmuir probe is slightly more robust than that of the hairpin probe. With this benchmarking of the two probes, the planar Langmuir probe could be used in cases where it is extremely difficult to extract the resonance from the hairpin probe. The planar Langmuir probe was extensively used in experiments described later in this chapter.

Plasma densities of the order of 10^{17} up to 10^{19} m^{-3} have been reported by various authors in ICP [Godyak *et al.*, 2002; Godyak, 2011; Hori *et al.*, 1998] and ECR [Bowden *et al.*, 1993] sources. The input powers used by these authors was relatively higher ($\sim$ 500 W) than that used in these experiments. However, the dimensions of our system are smaller than those used by Godyak *et al.* [2002]; Godyak [2011]; Hori *et al.* [1998], and we probably reach similar power densities at lower power input values compared with their high input power values.

The electron density will have some profile as a function of the distance from the center of the coil region. This profile was not characterised due to the problems, mentioned earlier, that occur whilst using the probe in the coil center or close to the coil edge. However, the measured density values when the probe is 15 cm above the coil center, for 20 mTorr Ar plasma at 100 W, are almost three times less than what was measured at 10 cm above the coil center, fig 4.2. If one assumes that the density is at least one order of magnitude higher in the center than that measured 10 cm away, the plasma seems to be in the H-mode for a pressure of 20 mTorr with an input power greater than 50 W. The lowest

electron density was found to be for the lowest pressure in both cases, the pure argon and Ar/Kr/Xe plasmas. The electron density increases by a factor varying from 1.5 up to 4.5 with the increase in pressure. This suggests that the plasma is in the H-mode for all the pressures at powers much less than 50 W.

Several attempts to record complete I-V characteristic curves using Langmuir probes, either cylindrical or planar, were carried out for several plasma operational conditions, but there were problems with the data that prevented full analysis of the I-V curve. Floating potentials ($>$ 20 V) and plasma potentials ($>$ 30 V) were measured for pure argon at 20 mTorr with 50 W input power.The electron saturation region rapidly tended to a constant value parallel to the V-axis. These high measured potentials and deviant features in the electron saturation region occurred due to the large distance separating the probe tip from any nearby grounded surface. This led to insufficient return current during the electron saturation regime where too much electrons were withdrawn from the plasma. The plasma potential increased so that it sustains itself and contains the remaining electrons. The electron temperature could not be deduced from the I-V characteristics because of the features of the I-V curve at the electron saturation region. Introducing a grounded surface to a position close to the probe tip could be one solution. However, this required a different probe design, as introducing another electrode requires a different access port. This matter is currently being resolved, but for the results in this thesis the focus was only on the ion saturation region.

Optical emission spectroscopy was carried out to further characterise the PL80 and to attempt to measure the electron temperature. The results of these measurements are presented in the following section.

4.1.2 Spectrally resolved emission measurements and electron temperature estimation

Optical emission spectroscopy is a well-established technique in plasma characterisation. Complicated models, such as collisional radiative models (CRM), have been used by some researchers to extract carefully electron temperatures and densities [Donnelly & Schabel, 2002; Zhu *et al.*, 2012]. Indicative temperatures can be deduced from simpler models, such as ours (section 3.3.2.2). This section describes the OES measurements performed for a wide range of plasma pressures and input powers. These measurements were used to estimate the range of electron temperatures attained in the PL80 ICP source.

A constant total gas flow of 30 sccm was maintained while the pressure was varied from 20 up to 80 mTorr. The plasma was mainly constituted from argon with traces of Kr and Xe with 8:1:1 ratios. Emission lines from each of these species was measured for different input powers.

Figure 4.5 (a), (b) and (c) shows the measured emission lines as a function of the input power for three gas pressures. The emission from argon is divided by 8 to allow direct comparison with the other emission lines. The data was normalised with the highest measured intensity in each case.

It can be seen that the emission from Xe, Kr & Ar increase simultaneously as the power increases for all these pressures. Emission from Kr and Ar increase in a similar manner. For the pressure of 20 mTorr, all the emission lines seem to increase almost linearly as the input power increases. For the pressures of 40 and 80 mTorr, there seems to be a subtle step in the increase of the emissions for 100 W input power, after which the lines seem to linearly increase. This step

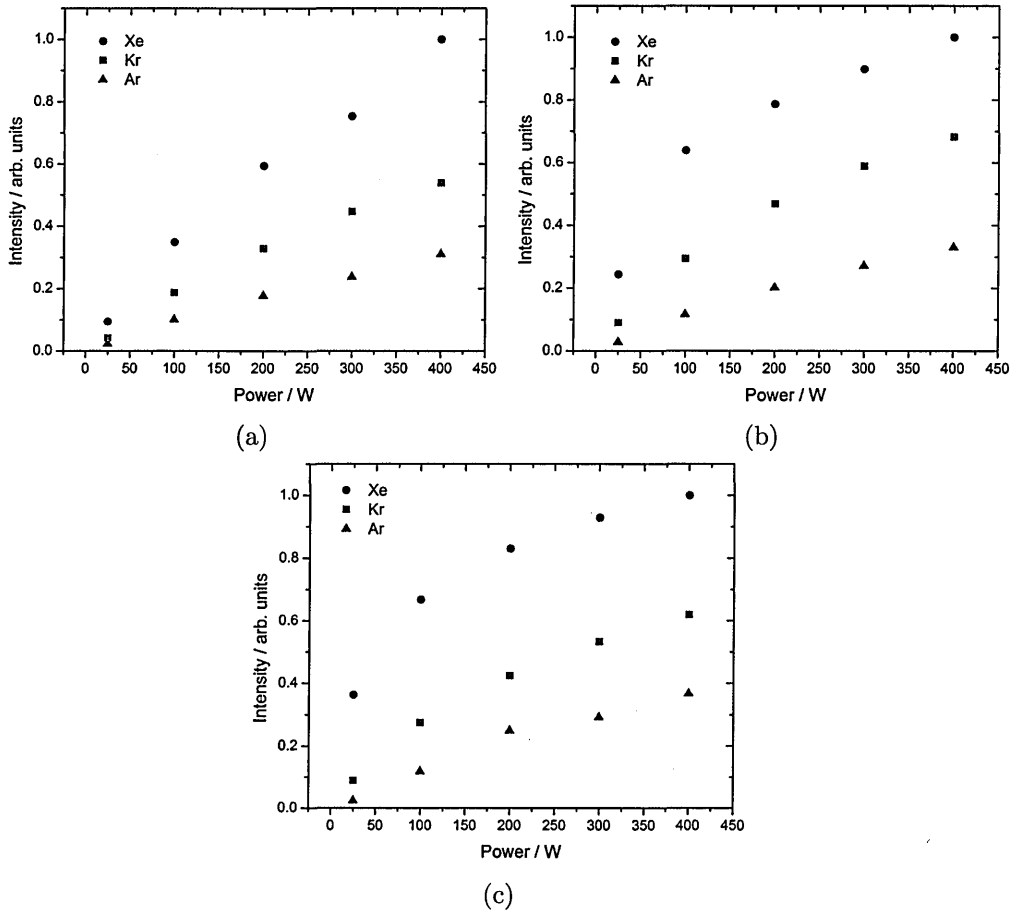

Figure 4.5: Emission lines from Ar, Kr & Xe as a function of input power for (a) 20 mTorr, (b) 40 mTorr and (c) 80 mTorr.

increase is relatively small when compared to the raw measured emission and is magnified due to the normalisation of the scale.

The electron temperature was estimated for these operating conditions from the ratios of the intensities of the emission lines using the model presented in section 3.3.2.2. The EEDFs were also assumed to be Maxwellian-like in the model. It is more likely that the EEDFs are Maxwellian due to the higher electron density

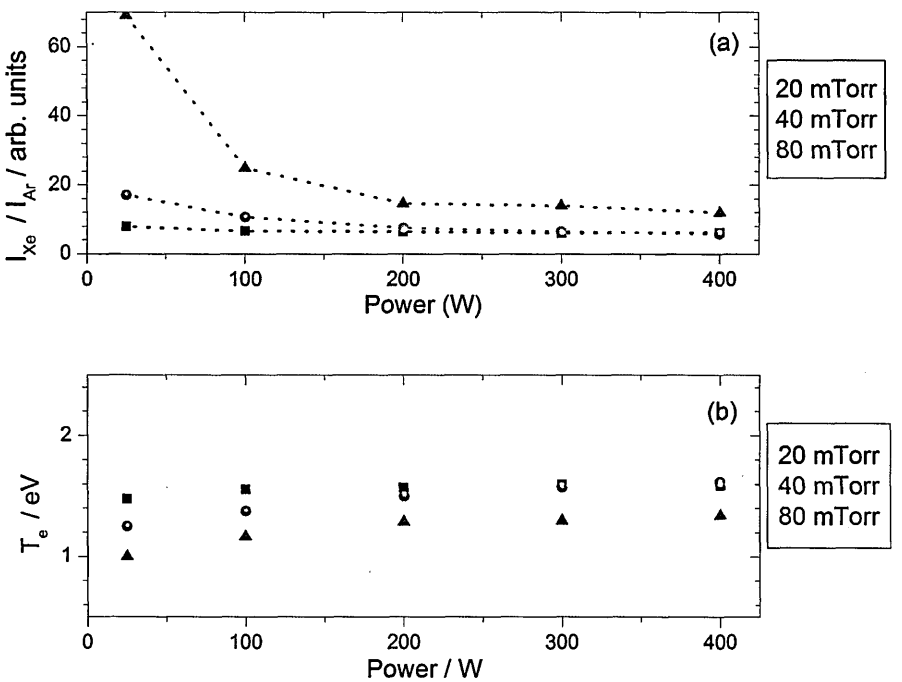

Figure 4.6: (a) shows the ratio of the emission lines only from Xe with respect to Ar for 20, 40 and 80 mTorr and (b) gives the estimated electon temperature for these pressures extracted from the simple analytical model.

(compared to the CCP case), which leads to higher electron-electron collision frequencies, and the absence of large sheath potentials.

Figure 4.6 (a) shows the ratio of emissions from Xe to Ar for 20, 40 and 80 mTorr and (b) the estimated electron temperatures for these conditions extracted from the simple analytical model. Emission ratios of Kr to Ar showed similar trends to those of $I_{Xe/Ar}$ and hence were not included in the graph in order to simplify the presentation of these data. The emission ratio shows a large decrease for the 80 mTorr case as the input power increases from 50 to 200 W and tends to a constant value for higher powers. For the 40 mTorr case, the emission

ratio shows a relatively small decrease as the input power increases and tends to a constant value at an input power of 200 W. The emission ratio for the 20 mTorr case seems to attain a constant value for all the input power range, tending to a similar value of that of the 40 mTorr case for $P \geq 250$ W.

Figure 4.6 (b) shows the estimated electron temperature for these different pressures as a function of the input power. The estimated T_e shows almost no change for the 20 mTorr case, while the estimated T_e increases slightly from 1.2 to 1.5 eV when the power increases from 50 to 200 W for the 40 mTorr case. The estimated T_e, for these two pressure conditions, follows the behavior of the emission ratio and settles at the same value ($\sim$ 1.5 eV) at an input power of 200 W. For the 80 mTorr pressure, the estimated T_e increases from $\sim$ 1 eV, for input power of 50 W, to 1.3 eV for $P \geq 200$ W.

The measured emission was for the line of sight passing through along the axis of the plasma and was not only obtained from the center or peripheries of the plasma region. It is expected that T_e will have a particular profile peaking in the core region of the plasma close to the coil and will decay further away from it. The estimated T_e resembles the line average temperature. This could explain why the estimated temperatures are slightly lower than expected (2.8 eV).

The density measurements suggest that the plasma is operating mostly in the H-mode, i.e. high plasma density, and that adding traces of Kr/Xe gas mixture does not change the plasma density. The spectrally resolved measurements and the simple analytical model suggest that $1.2 \leq T_e \leq 1.5$ eV is the variation of the T_e for these selected pressures and input powers. These operational conditions were selected as they are relevant to the study carried out on the CCP source and to the typical operating conditions of source used for the neutral beam etching

experiments described in the next chapter. Similar measurements were carried out for pulsed input powers for different pressures. These sets of measurements are presented in the following section.

4.2 Plasma behavior for pulsed operation

This section contains a study of the pulsed PL80 ICP source. There are two aims of this study. The first is to characterise our source in the pulsed regime, and the second is to characterise the ignition phase. The studies were performed using a combination of electrical and optical measurement techniques. Total light emission from the plasma was measured for a range of conditions. The simple OES technique, presented in section 3.3.2, with electrical measurements, mostly using a planar Langmuir probe, were used to study the ignition phase of a specific set of pulse conditions.

In initial studies, the discharge was operated using pure argon gas as well as Ar/Kr/Xe gas mixtures with pressures ranging from 20 to 100 mTorr. Pulse frequencies $1 \leq f \leq 5$ kHz with duty cycles ranging from 10 up to 90% were used. The average power was maintained at $P_{av} = 344 \pm 4$ W for all pulse frequencies and duty cycles. The circuit presented in figure 2.4 (b) [page 43] was used generate the pulsed input power. The pulse frequencies and duty cycles were controlled using a function generator. An ENI power supply was used to generate the pulsed RF power. These conditions were used to determine a set of optimised operational conditions for our source.

4.2.1 Parameter space sweep

In this section we probed the parameter space using various pulse frequencies, duty cycles and gas pressures. The parameter space is huge, and probing all possible conditions would take a very long time. Plasma emission, however, is relatively straightforward to measure, and the initial study focused on simply recording emission for a wide range of conditions. Emission strongly depends on electron properties, so this approach enabled us to narrow the range of conditions where more detailed measurements were made. With this approach, a photodiode was used to record the total light emission from the plasmas operated at different pulse conditions.

We have already seen that adding traces of Xe and Kr to an Ar plasma had little effect on the plasma behavior (section 4.1.1). Hence, the emission study was carried out in a pure Ar discharge. The Ar/Kr/Xe gas mixture was used when optical emission spectroscopy and a detailed study of the ignition phase was performed.

Figure 4.7 shows the measured total light emitted from a 20 mTorr Ar plasma operated at a pulse frequency of 1 kHz (a), 2.5 kHz (b) and 5 kHz (c) with 30, 50, 70, 75 and 90% duty cycles. Total light emission was also measured for 40, 60 & 80% duty cycles for pulse frequencies of 1 and 2.5 kHz, and were omitted to increase the clarity of the graphs. The measurements show that the emission clearly depends on the duty cycle. A small time shift in the measured emission can be seen during the early phase of the pulses. This time shift is an artifact resulting from the smoothing and averaging of the digitised signal recorded by the oscilloscope. The smoothing and averaging was necessary for some measurements

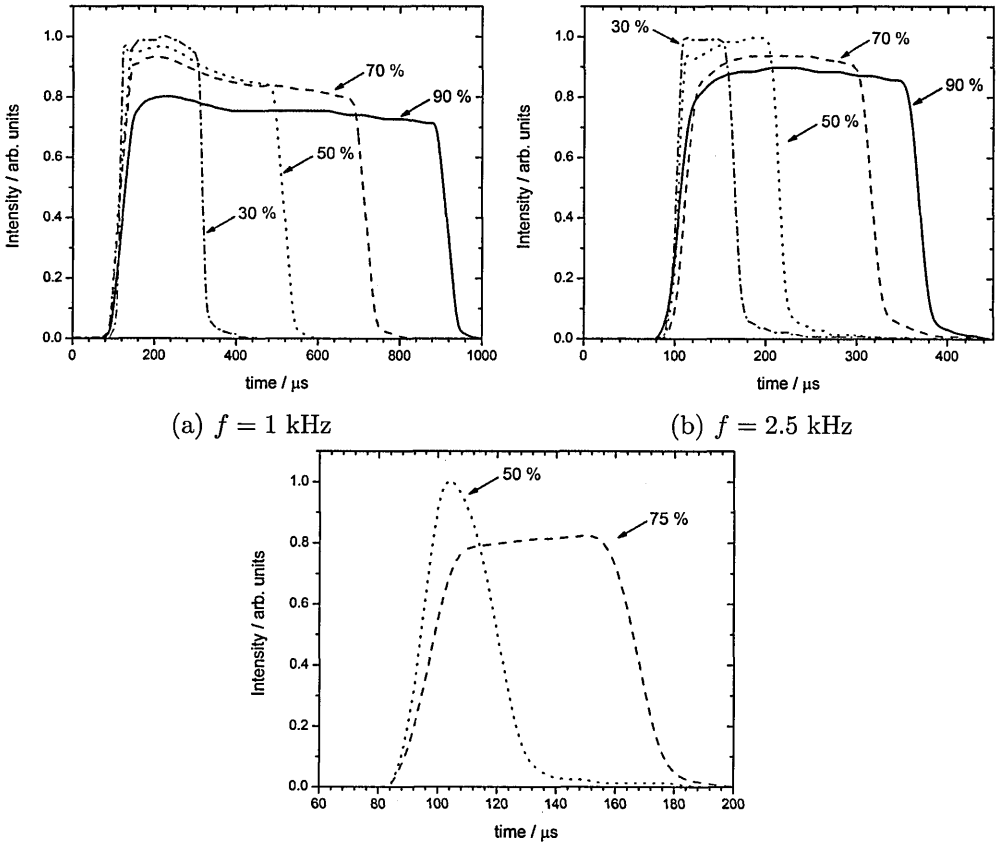

(a) $f = 1$ kHz (b) $f = 2.5$ kHz

(c) $f = 5$ kHz

Figure 4.7: Total light emission from a 20 mTorr argon plasma for different duty cycles, ranging from 30 to 90%, for pulse frequencies of 1 kHz (a), 2.5 kHz (b) and 5 kHz (c).

due to the resolution of the oscilloscope used in these measurements.

No significant peaks were measured for all pulse frequencies and duty cycles. The shortest duty cycles seem to have the highest emission intensity for all frequencies, while the measured intensity decreases as the duty cycle increases. The total light emission seems to converge to a value similar to that attained at the end of the longest duty cycle as the duty cycles increase.

Figure 4.7 (a) shows the total emission measured for several duty cycles for a pulse frequency of 1 kHz ($T = 1$ ms). A relatively small peak in the early part of the pulse can be seen in the emission of the 30 and 50% duty cycles. This peak seems to gradually decrease and eventually disappear as the duty cycle increases, i.e. the duration of the active glow phase increases.

Figure 4.7 (b) shows the total emission measured for several duty cycles for a pulse frequency of 2.5 kHz ($T = 400$ μs). The emission shows similar general behavior as the emission for the 1 kHz pulse. Small peaks can be seen during the early ignition stages in the 30 and 50% duty cycle cases which disappear for longer duty cycles.

Figure 4.7 (c) shows similar data as the previous graphs for a pulse frequency of 5 kHz ($T = 200$ μs). A Gaussian profile was measured for the emission of the 50% duty cycle. This profile is similar to that measured for the ramped input pulse with $f = 1$ kHz and 10% duty cycle in the pulsed-CCP case, figure 3.18 (b) [p 95]. No distinct features in the emission were measured for the 75% duty cycle. It takes the RF power supply about 20 μs to reach the maximum input power and there is an inherit response delay of 80 μs. This explains the Gaussian profile of the emission in figure 4.7 (c). This constrains the length of the active glow and the pulse frequencies that we can operate the system at.

Figure 4.8 shows the measured total light emitted for the same range of conditions, but when the gas pressure was 40 mTorr. A clear peak in the emission is detected in the early phase of each pulse for all the conditions. The intensity of this peak gradually decreases for duty cycle greater than 50%. The total light emission seems to converge to a value similar to that attained at the end of the active glow phase of the longest duty cycle.

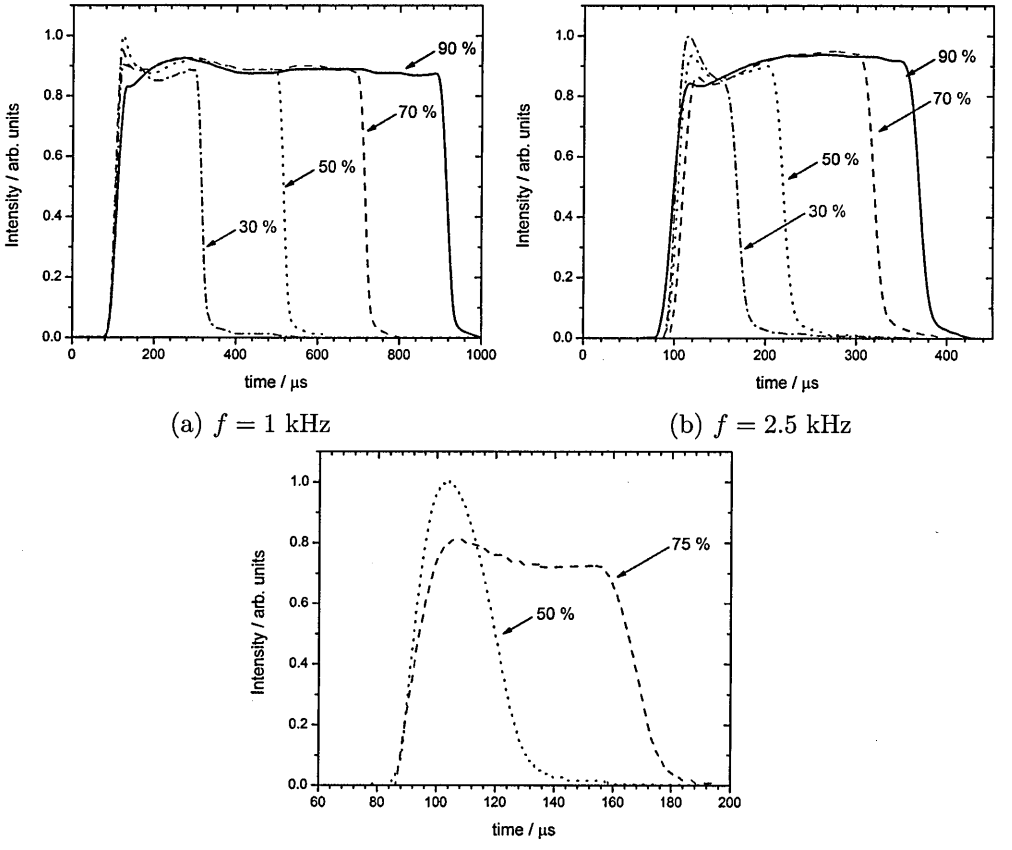

(a) $f = 1$ kHz (b) $f = 2.5$ kHz

(c) $f = 5$ kHz

Figure 4.8: Total light emission from a 40 mTorr argon plasma for different duty cycles, ranging from 30 to 90%, for pulse frequencies of 1 kHz (a), 2.5 kHz (b) and 5 kHz (c).

Figure 4.9 shows the same measurements for the case of $p = 80$ mTorr. The peak in the emission in the early phase of the active glow is even more distinct and is observed for all different pulse frequencies and duty cycles. The intensity of this peak gradually decreases for duty cycle greater than 50%. The total light emission seems to converge to a value similar to that attained at the end of the active glow phase of the longest duty cycle. The difference in the emission profiles

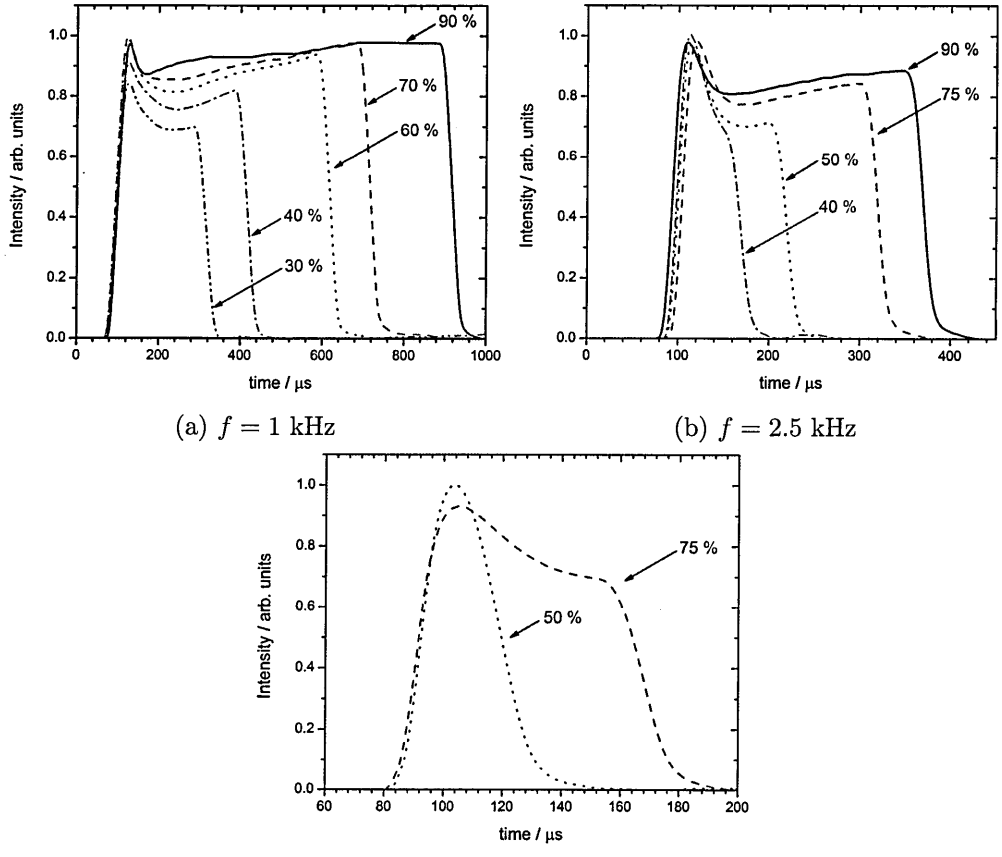

(a) $f = 1$ kHz (b) $f = 2.5$ kHz

(c) $f = 5$ kHz

Figure 4.9: Total light emission from a 80 mTorr argon plasma for different duty cycles, ranging from 30 to 90%, for pulse frequencies of 1 kHz (a), 2.5 kHz (b) and 5 kHz (c).

between the 40 and 80 mTorr cases is due to the different conditions, such as the electron densities, at the end of the afterglow phase.

The modified waveform pulse with 1 kHz frequency and 50% duty cycle was used to change the ignition phase of a 100 mTorr Ar/Kr/Xe plasma; the RF-voltage was the same as that shown in figure 3.2 (b). Figure 4.10 shows the total emitted light for the modified pulse input. The effective active glow phase seems

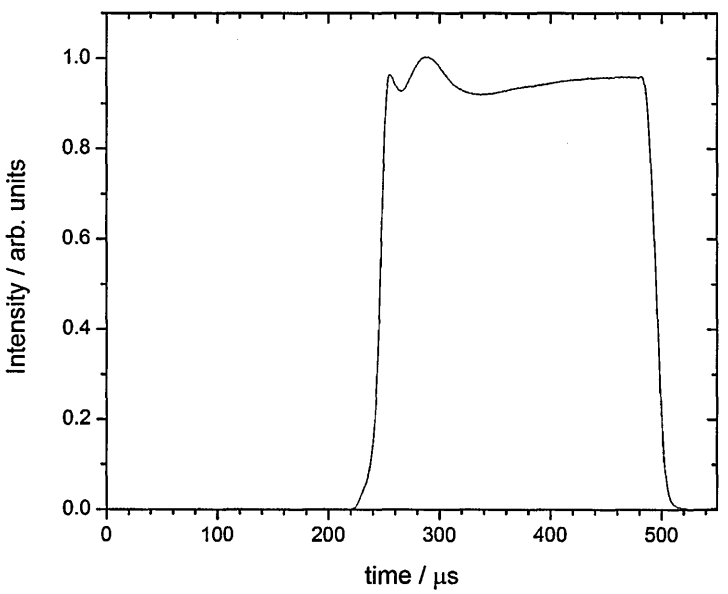

Figure 4.10: Total plasma emission measured for 100 mTorr Ar/Kr/Xe with a ramped input pulse waveform with $f = 1$ kHz and 50% duty cycle.

to be shorter and the plasma ignites around $t = 220$ μs. It can be seen that the emission profile does not follow the profile of the input RF-voltage, as was the case in the pulsed CCP discharge. In fact the emission profile is similar to the profile of the input current. Hence, for the ICP source, proper pulse tailoring requires control of the input current rather than the input voltage. This was not possible with our power supply.

In summary, the total plasma emission measurements show that a peak appears in the early phase of the active glow for pressure $p \geq 40$ mTorr, while almost no peaks appear for $p \leq 30$ mTorr. The intensity of the emission peak in the early phase of the active glow increases as the pressure increases. The duty

cycle and pulse frequency seem to have less of an effect on the intensity of the peak compared to that of the pressure change. Spectrally resolved emission measurements were performed to provide further insight on this behavior and into the associated ignition processes. The results of these measurements are provided in the following section.

4.2.2 Spectrally resolved measurements

Optical emission spectroscopy measurements were performed to probe the ignition phase for the pulsed ICP source. Spectroscopic studies require the addition of Kr and Xe gases, as was done in section 4.1.2 and the research described in chapter 3.

The discharge was operated with a pulse frequency of 1 kHz with 30%, 50% and 90% duty cycles with P_{av} = 344 W. An Ar/Kr/Xe gas mixture, with 8:1:1 flow ratios and a total gas flow of 30 sccm, was used to generate the discharge. The plasma was operated at two different pressures to perform this study: 20 and 100 mTorr. This should show the different ignition behavior observed in the total emission measurements described above. Three emission lines were selected, one from each of the gases. Detailed information about these emission lines can be found in table 3.1 [p. 78].

Figure 4.11 contains the temporally and spectrally resolved measurements for a 20 mTorr Ar/Kr/Xe plasma operated at 1 kHz pulse frequency with 30%, 50% and 90% duty cycles, having P_{av} = 344 W. In each case, the emission intensity was normalised to the maximum value of the xenon emission line, and the emission intensity of the argon line was divided by eight.

Figure 4.11 (a) shows a gradual increase in the intensity of the three emission

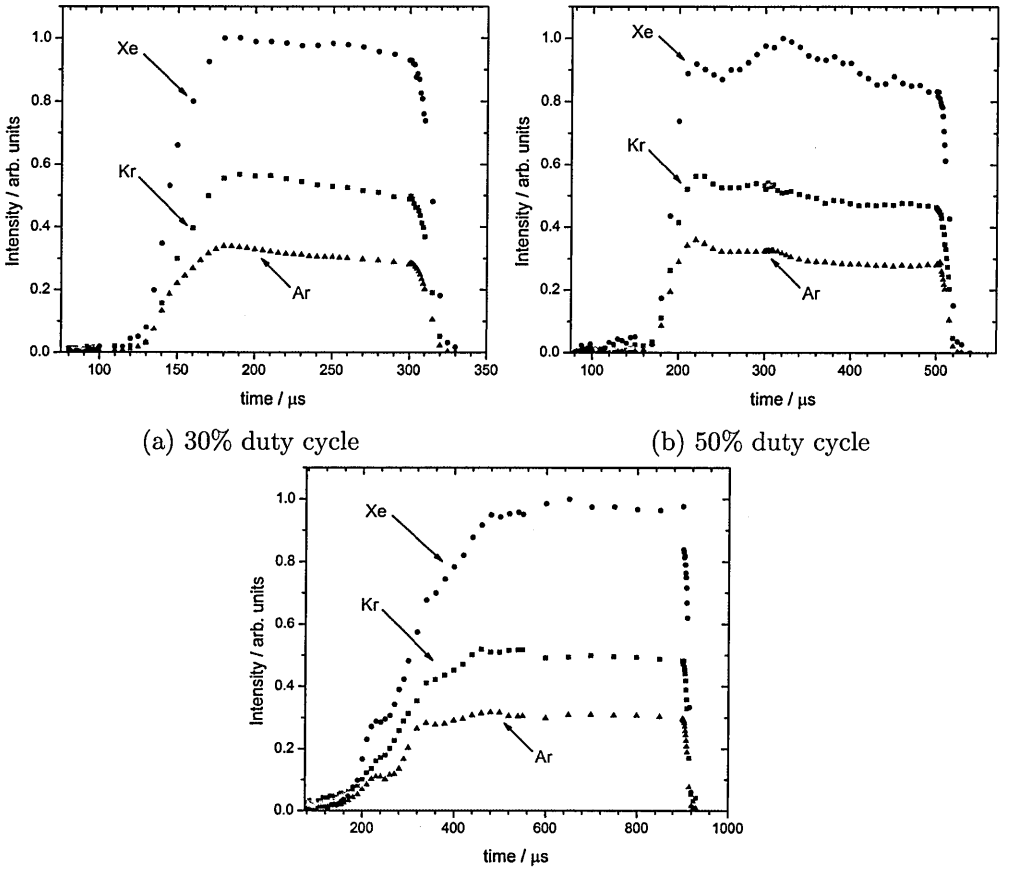

(a) 30% duty cycle

(b) 50% duty cycle

(c) 90% duty cycle

Figure 4.11: Spectral and time resolved emission for 20 mTorr Ar/Kr/Xe plasma operated at 1 kHz pulse frequency with 30% (a), 50% (b) and 90% duty cycles.

lines reaching a maximum value around $t \sim 170$ μs. These emission lines show no peak or any significant features during the early ignition part of the active glow phase.

Figure 4.11 (b) shows a gradual increase of the emission intensities of all the emission lines in a manner similar to that of the 30% duty cycle case. The xenon emission lines shows some fluctuations for $t \geq 250$ μs, while the Kr and

Ar emission lines seem to be almost constant at this time. These fluctuations, ±7%, in the Xe emission line seem to be larger than they actually are due to the normalisation of the data.

The spectrally resolved emission for the 90% duty cycle is included in figure 4.11 (c). The emission gradually increases for all three lines, reaching a maximum value at $t \sim 440$ μs. In fact, the absolute measured values are 30% less than the emission measured for the 50% duty cycle case.

The general profile of these spectrally resolved lines resembles the profiles of the total light measured in figure 4.7 (a) for the same duty cycles.

Figure 4.12 contains the same data for the 100 mTorr case. As was done before, the emission intensities was normalised by the maximum emission intensity of the xenon line, and the argon lines were divided by eight. It can be seen from the graphs that all the emission lines contain peak features in the ignition stages of the active glow phase.

For the 30% duty cycle case, all three emission lines exhibit peak features during the early stage of active glow phase. These peaks are relatively broad compared to the peaks detected in the early phase of the active glow in the pulsed CCP study, figure 3.7 [p 78].The peaks begin at times ranging from 20 to 50 μs. The emission lines from Ar, Kr and Xe tend to a constant value around 125, 145 and 170 μs respectively.

For the 50% duty cycle case, these emission lines show a similar trend to those measured for the 30% duty cycle case. The emission lines also exhibit broad peaks, starting also from 20 up to 40 μs. The emission intensities reach a constant value around 140 μs for all these emission lines.

It can be seen from figure 4.12 (c), for the 90% duty cycle case, that the

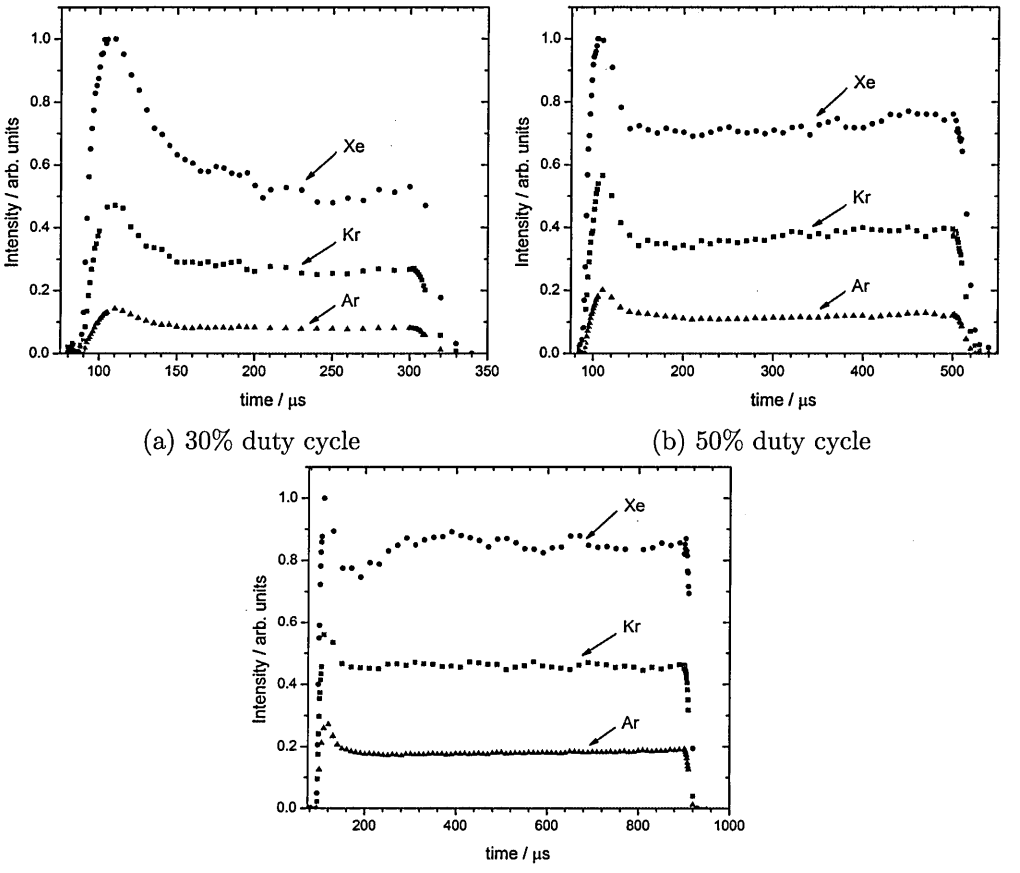

(a) 30% duty cycle

(b) 50% duty cycle

(c) 90% duty cycle

Figure 4.12: Spectral and time resolved emission for 100 mTorr Ar/Kr/Xe plasma operated at 1 kHz pulse frequency with 30% (a), 50% (b) and 90% duty cycles.

emission lines show a similar profile as the previous cases, but with more similarly timed peak increases. For this case, these peaks start at times in the 25 to 30 μs range. All the emission lines seem to reach a steady value around 150 μs.

Figure 4.13 shows the ratio of the emission lines of Xe with respect to Ar for the two pressures 20 and 100 mTorr, for these plasmas with 1 kHz pulse frequency with 30%, 50% and 90% duty cycles. The general profile of Kr/Ar emission lines

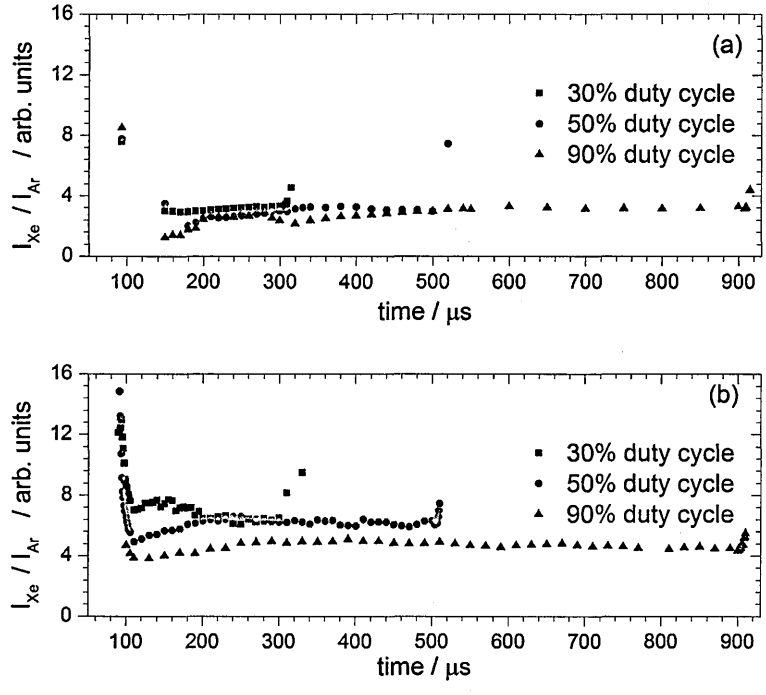

Figure 4.13: Ratio of the Xe emission lines w.r.t Ar (Xe/Ar) for (a) 20 mTorr and (b) 100 mTorr plasma with 1 kHz pulse frequency and 30%, 50% and 90% duty cycles.

ratio is similar to those presented in figure 4.13 and are not shown here to simplify the presentation of the data.

Figure 4.13 (a) shows the Xe/Ar ratio for the 20 mTorr plasma. The ratios seem to rapidly decrease for all duty cycles during the ignition phase and reach a similar value after $\sim$ 100 μs. An overshoot of the ratios can be seen at $t = 320, 520$ and 920 μs indicating the beginning of the afterglow phase for the 30%, 50% and 90% duty cycles respectively. The ratio overshoot at the beginning of the afterglow indicates the rapid cooling down of electron temperature at this phase.

Figure 4.13 (b) shows the ratio for the 100 mTorr plasma. The ratios seem

to rapidly decrease for all duty cycles during the ignition phase and reach a similar value after $\sim$ 240 μs. An overshoot of the ratios is seen at the end of each duty cycle at $t = 320, 520$ and 920 μs for 30%, 50% and 90% duty cycles respectively. The general profile of these ratios is similar to the ratios measured for the 20 mTorr plasma, figure 4.13 (a).

The spectrally resolved emission shows no distinct features during the ignition phase of the 20 mTorr case and a similar profile to that of the total measured emission. The spectrally resolved emission showed broad peaks for all the duty cycles in the 100 mTorr case, which have a similar profile to the measured total emission.

The results can be interpreted as follows. The ignition of the plasma occurs on a time scale of few microseconds, not tens of microseconds. The ignition of the plasma contributes to the emission in these peaks but is not the only factor. Another factor could be that these broad emission peaks are due to a non-Maxwellian EEDF during the early active glow stages. The shape of the EEDFs is decided by the balance between the energy gains of electrons at various energies from the electromagnetic fields and their energy space diffusion. The energy space diffusion is inefficient since the dominant collisions are the electron-neutral collisions at high pressures. The frequency of electron-electron collisions and electron mean free path decrease with higher pressures, especially when the electron density is low during the early ignition phase. However, as the density of electrons builds up the frequency of electron-electron collisions increases, resulting in an efficient thermalisation of the electrons. The increase in electron-electron collisions changes the EEDF into a Maxwellian-like distribution. The apparent time scale for this change is 50, 40 and 30 μs for the 30%, 50% and 90% duty

cycles respectively. The decrease in these time scales is due to the increase in the electron density at the end of the afterglow phase as the duty cycle increases. Similar time scales to such changes were reported previously by Ashida *et al.* [1995].

In summary, spectrally resolved emission measurements were performed for a plasma operated at two pressures with different duty cycles. Differences in the ignition phase were studied for different duty cycles and two different pressures. Spatiotemporal charge density measurements were performed to support this analysis and study. The results of these measurements are presented in the following section.

4.2.3 Spatiotemporal charge density measurements

A planar Langmuir probe was used to perform spatiotemporal measurements of the positive ion current for the same plasma conditions that were presented in section 4.2.2. Hence, measurements were made in an Ar/Kr/Xe plasma operated at two pressures: 20 and 100 mTorr, with 1 kHz pulse frequency and 30%, 50% and 90% duty cycles. The positive ion current was measured on the azimuthal axis of the discharge using a planar Langmuir probe, with the probe potential set at -50 V to collect only positive ions and repel the energetic electrons. The probe was positioned at five positions on the azimuthal axis: +10, +5, 0, -5 and -10 cm. The zero centimeter position is at the centre of the coil region, and the positive direction is upwards from the centre in the direction of the gas inlet.

Figure 4.14 shows the collected current along the azimuthal axis of the discharge as a function of time with respect to the input pulses. The vertical axis

represents the position of the planar Langmuir probe on the azimuthal axis. The zero position on the vertical axis is close to the center of the coil. The current is normalised to the maximum value collected. All the planar Langmuir probe measurements in the following sections are presented in this particular style.

Figure 4.14 (a) shows the spatiotemporal positive ion current measured for 20 mTorr discharges operated with a 30% duty cycle. As can be seen from the graph, the maximum positive current is collected at the center of the discharge (distance = 0 cm) around $t = 170$ μs, $I^+_{max} = 50.1$ mA. The maximum current collected in this case is the highest compared to the peak of the currents measured for the 50% and 90% duty cycle cases. A small positive current was collected after 300 μs, when the discharge power is turned off. This is interpreted as being due to the ambipolar diffusion of positive ions.

Figure 4.14 (b) shows the spatiotemporal positive ion current measured for the same 20 mTorr pressure but with duty cycle of 50%. In this graph, the measured current is normalised to the maximum positive current measured for the 30% duty cycle. It can be seen that the maximum positive current is collected at the center of the discharge around $t = 160$ μs, $I^+_{max} = 47.2$ mA.

Figure 4.14 (c) shows the spatiotemporal positive ion current measured for the 90% duty cycle case. Once again, the measured current is normalised to the maximum positive current measured for the 30% duty cycle. It can be seen that the maximum positive current is collected at the center of the discharge around $t = 150$ μs, $I^+_{max} = 37.8$ mA. As mentioned earlier, the positive current collected after $t = 500$ μs can be attributed to the ambipolar diffusion of positive ions.

Figure 4.15 shows the positive ion current collected on the azimuthal axis for the same plasma conditions except for pressure, which was set to 100 mTorr. For

the 30% duty cycle case, shown in part (a), the maximum collected current is collected at the center of the discharge at $t = 160$ μs, $I^+_{max} = 69.51$ mA.

For the 50% duty cycle, shown in part (b), the maximum collected current is collected at the center of the discharge at $t = 160$ μs, $I^+_{max} = 71.4$ mA.

Finally, for the 90% duty cycle case, shown in (c), the maximum collected current is collected at the center of the discharge at $t = 160$ μs, $I^+_{max} = 66.52$ mA.

These measurements show that the collected current reaches a maximum value after 160 μs for all cases. These measurements give the profile of the temporal evolution of the positive ions on the azimuthal axis of the discharge.

To extract the ion density from these measurements, it is necessary to know the ion mass distribution, which is difficult to know exactly in the Ar/Kr/Xe gas mixture. However, it is possible to estimate a reasonable density by assuming that Xe^+ is the dominant ion constituting approximately 90% of the ion mass distribution. The ionization threshold energy is 12.129, 13.999 and 15.759 eV for Xe^+, Kr^+ and Ar^+ respectively [NIST Atomic Spectra Database].

The maximum ion density can be estimated using assumptions stated earlier and applying the ion saturation current equation (2.6) and calculating the Bohm speed using equation (2.7) [p. 52]. The maximum ion density can be estimated using $I_{Xe^+\ max} = 0.9 I^+_{max}$ and $I^+_{max} = I_{is} = -e n_s u_B A$ where I^+_{max} is the maximum positive collected current, n_s ion density, u_B Bohm speed and A the collection area. The electron temperature can be estimated from the Xe/Ar emission line ratios when steady state conditions are achieved for each of the duty cycles in order to calculate the Bohm speed. The planar Langmuir probe is a disk with diameter $D = 6$ mm, and hence the area of the probe is $A = \pi(\frac{D}{2})^2$. The existence of a sheath around the probe increases the effective collection area, especially in

the ion saturation region. Typically, the effective collection area becomes the sum of the physical area of the probe and the extra area created by the sheath.

Therefore, the effective collection area becomes $A_{eff} = \pi(\frac{D}{2} + 3\lambda_D)^2$. The effect of the sheath becomes minimal as the plasma density increases and the electron temperature decreases. The plasma density and electron temperature measurements in section 4.1.1 and 4.1.2 suggested high plasma densities ($n_e \geq 10^{18}$ m^{-3}) and low electron temperature ($T_e \sim 1.6$ eV). Therefore, we can conclude that the effect of the sheath around the probe can been neglected when estimating the positive ion densities for these cases.

The electron temperature was estimated from the spectroscopy measurements to be 1.6 eV and 1.2 eV for the 20 and 100 mTorr discharges respectively. These electron temperatures are attained throughout the active glow phase when the ratio of the Xe/Ar emission lines reaches a steady value. The Bohm speeds calculated for these electron temperatures are 1085 and 940 m/s for the 20 and 100 mTorr discharges respectively. The ion density can be estimated using assumptions mentioned earlier and these electron temperature and Bohm speeds. Two values of the positive current for each set of operational conditions were used to estimate the ion density during the active glow phase. These two current were the maximum and minimum collected currents during the active glow phase after the ignition of the plasma. Table 4.1 gives the set of estimated ion densities for all the operational conditions of interest. The values of the current used for these calculations were extracted from the center of the discharge, i.e. the center of the coil (d=0 cm).

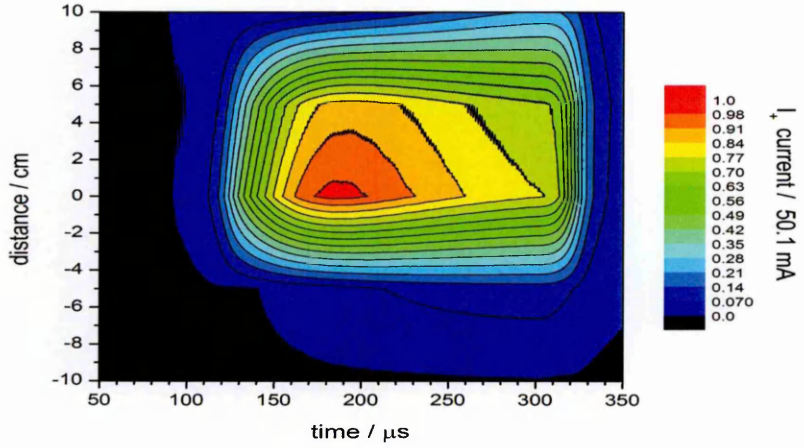

(a) 30% duty cycle

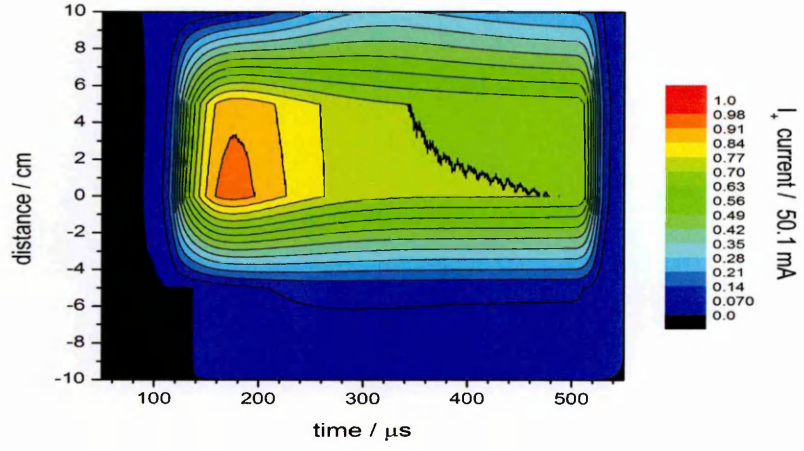

(b) 50% duty cycle

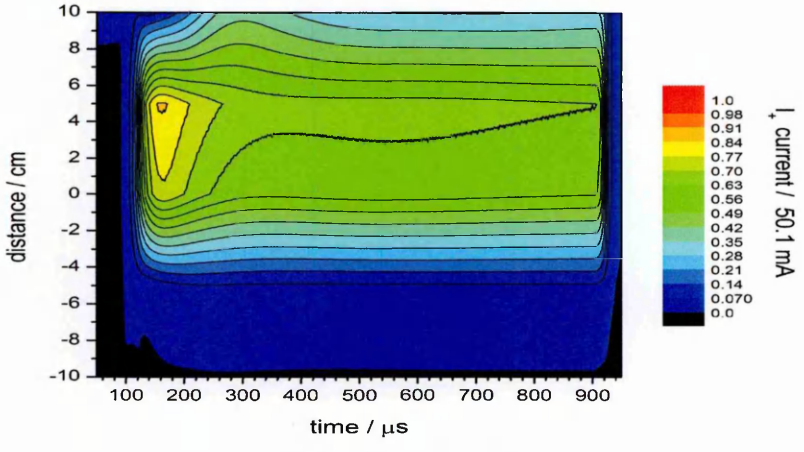

(c) 90% duty cycle

Figure 4.14: Spatiotemporal positive current collected by planar Langmuir probe for 20 mTorr Ar/Kr/Xe plasma operated at 1 kHz pulse frequency with 30% (a), 50% (b) and 90% duty cycles. The values are normalised to 50.1 mA, which is the highest positive current measured for the 30% duty cycle case.

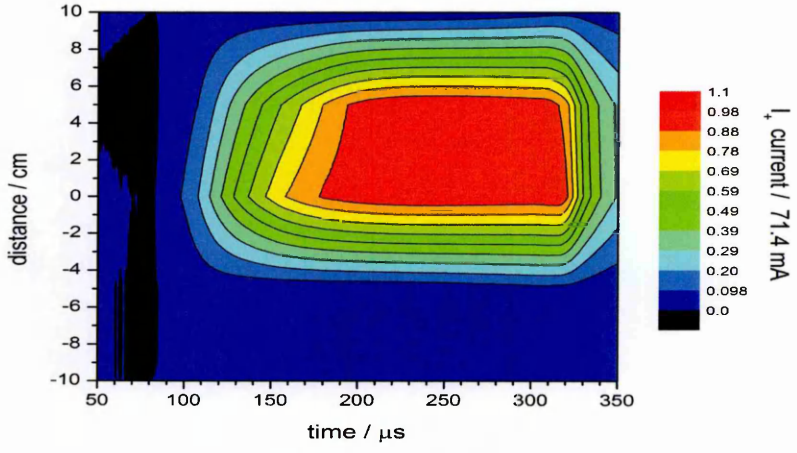

(a) 30% duty cycle

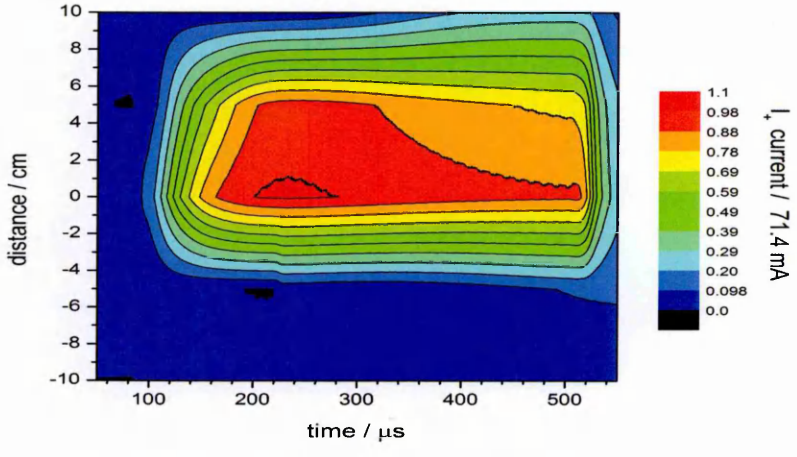

(b) 50% duty cycle

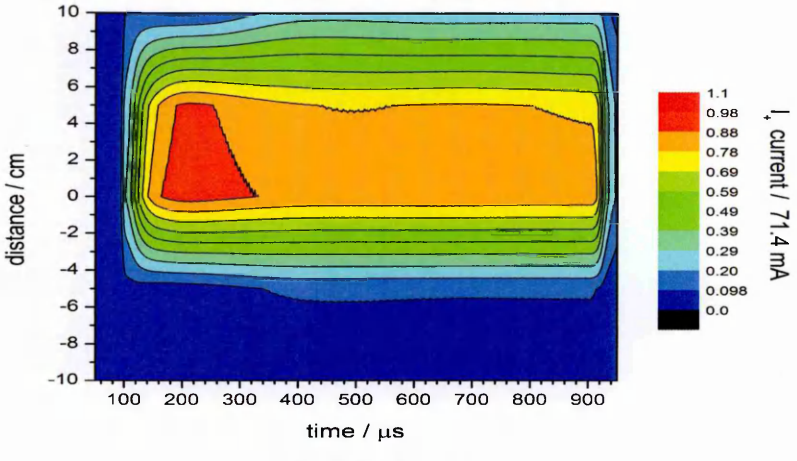

(c) 90% duty cycle

Figure 4.15: Spatiotemporal positive current collected by planar Langmuir probe for 100 mTorr Ar/Kr/Xe plasma operated at 1 kHz pulse frequency with 30% (a), 50% (b) and 90% duty cycles. The values are normalised to 71.4 mA, which is the highest positive current measured for the 50% duty cycle case.

Table 4.1: This table provides the estimated maximum and minimum ion densities attained during the active glow phase for each of the operational conditions.

Ar/Kr/Xe plasma, $f = 1$ kHz					
p/mTorr	dc	$I^{Xe^+}_{max}$/mA	$I^{Xe^+}_{min}$/mA	$n^+_{max}/\mathrm{m}^{-3}$	$n^+_{min}/\mathrm{m}^{-3}$
20	30%	45.09	34.92	5.17×10^{18}	4×10^{18}
	50%	42.53	31.41	4.87×10^{18}	3.6×10^{18}
	90%	34.03	25.47	3.9×10^{18}	2.92×10^{18}
100	30%	62.56	61.47	8.28×10^{18}	8.13×10^{18}
	50%	64.26	57.69	8.50×10^{18}	7.63×10^{18}
	90%	59.87	54.54	7.92×10^{18}	7.22×10^{18}

Table 4.1 includes the calculated ion densities for the 20 and 100 mTorr Ar/Kr/Xe discharges and the different duty cycles. It can be seen from these values that the plasma density is relatively high for all the operational conditions. This also suggests that our discharges, under these pulse conditions, are operated in the H-mode. It is worth noting that the ion density was calculated from the measured ion current under the assumption that Xe^+ constitutes 90% of the ion species. Even if the Xe^+ was chosen to have different percentages, such as 75% or 80%, the measured densities would still be relatively high. However, the measured ion current is in fact high regardless of what ion and percentage was chosen to calculate the density. These ion densities were calculated to give a better feel for the characteristics of the PL80.

4.3 Conclusions

The characterisation of the PL80 ICP source was performed in continuous and pulsed operational conditions. The plasma properties were measured in the coil region of the PL80 ICP source for pure argon and Ar/Kr/Xe plasmas. Opti-

cal emission spectroscopy and charge density measurements were performed to measure the various plasma properties.

In continuous mode, plasma density was measured using a hairpin probe for various pressure and input powers. Ion densities were also measured using a planar Langmuir probe for the same operational conditions. These measurements showed that the plasma density was high, $n_e \geq 10^{17}$ m^{-3}, for low input powers and increased as the pressure increased which suggests that the plasma is operating in the H-mode in all the studied cases.

Optical emission spectroscopy was performed for a range of operational conditions. The electron temperature was estimated from the Xe/Ar ratio using the simple model described in chapter 3. Relatively low electron temperatures were deduced for the operational conditions on the assumption of Maxwellian-like EEDFs.

In pulsed mode, a similar set of measurements was performed. The ignition phase was probed using a combination of the OES and density measurements. Ion density measurements were performed using a planar Langmuir probe. The hairpin probe was not used for electron density measurements, due to the technical problems encountered in the high density source. Hence, the ion density measurements gave the density during the active glow phase only. A new hairpin probe design is being considered to enable the measurement of electron density during the afterglow phase.

Total emission from the plasma was measured for a variety of pulse conditions. Spectrally resolved measurements were performed for two pressures, 20 and 100 mTorr as these pressures had the most distinct features in the early active glow phase, and several pulse conditions. No obvious transient stages from

E- to H-mode were observed from these measurements which suggests that the rise of the plasma density is very rapid.

In summary, measurements in continuous and pulsed modes were successfully performed. Plasma density and electron temperature ranges where extracted from these measurements. These values produced a good understanding of the operating conditions of this ICP plasma source, in conditions similar to those expected to be useful for neutral beam etching. The effect of the neutral beam etching setup on these plasma properties will be studied in the following chapter.

Chapter 5

Neutral beam etching

The previous chapters have presented the pulse tailoring technique and its effect on plasma properties. This chapter describes research in which pulsed plasmas and pulse tailoring techniques are used to carry out neutral beam etching (NBE).

The current status of NBE research was presented in section 1.4. This chapter includes a detailed description of the modifications performed on the PL80 ICP source to transform it into a NBE source. Results of preliminary NBE are presented and challenges facing this research are discussed.

This chapter is divided as follows. Section 5.1 contains a detailed description of the development of the NBE set up. Section 5.2 includes a set of optical and electrical measurements to gauge the effect of the NBE adapter on the plasma properties. Section 5.3 contains measurements of the extracted beam energy and the neutralisation efficiency of the NBE adapter. Section 5.4 includes the preliminary NBE results and etch rate measurements. Finally, section 5.5 contains the conclusions of these preliminary experiments.

5.1 The OU NBE source

The PL80 ICP source is an industrial etching tool and has been described in detail in section 2.2. This industrial etching tool was modified from a typical RIE tool into a NBE tool. The advantage of this is that it meant our NBE source was based on an industrially-relevant apparatus. The disadvantage was that the industrial tool was not configured for easy diagnostic access.

Figure 5.1 is a schematic representation of the Open University NBE source. The plasma volume is confined in the ceramic tube close to the powered coil, while a perforated graphite plate separates the plasma from the wafer and creates a pressure difference between the two regions. The first region is the plasma source region, which was kept typically at a pressure of a few mTorr up to a 100 mTorr. The second region, the processing region where the wafer resides, was kept at a lower pressure - typically 0.3 mTorr. Low pressure in the processing region is necessary to ensure that the extracted energetic neutrals undergo minimal collisions, if any, with background gas particles before reaching the wafer. If the pressure in the processing region is high, the extracted beam will undergo frequent collisions with background gas species, decreasing its energy and directionality. Therefore, keeping the processing region at a low pressure compared to the plasma region is essential.

The extraction and neutralisation adapter consists of a perforated graphite plate, two ceramic pieces, a cylinder and a disk, and electrical connections. The adapter was designed to hold the graphite extraction plates, for ion extraction and neutralisation, and to separate the plasma source from the processing chamber whilst providing the pressure difference required for NBE.

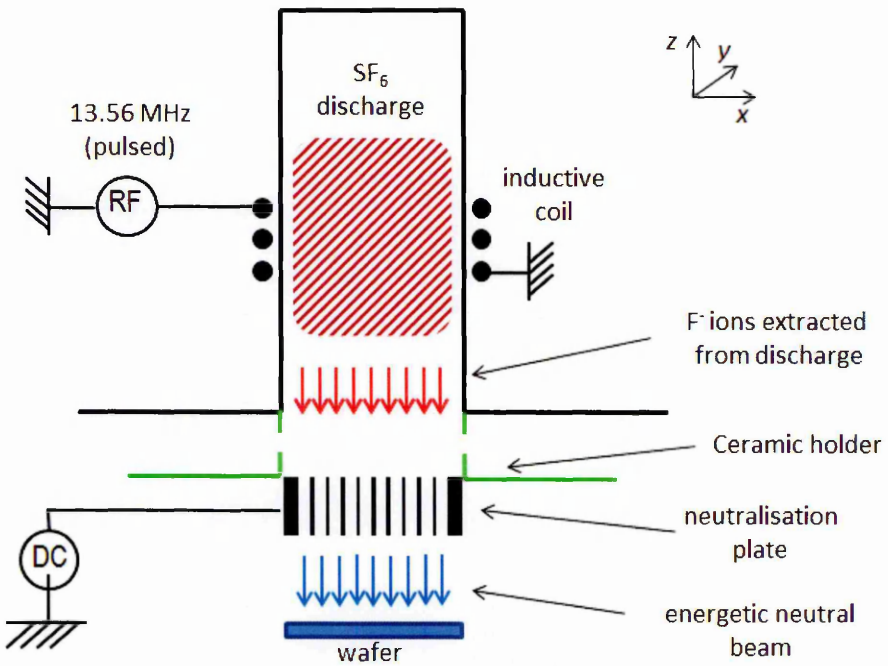

Figure 5.1: A cross-section schematic representation of the OU NBE plasma source.

The adapter consists of a ceramic tube and a ceramic disk, indicated by the green colour in figure 5.1. The ceramic tube separates the carbon plate from the metallic grounded surfaces in the chamber, preventing any arcing. Also, this tube contains four orifices with diameter of 5 mm each. These orifices aid the gas and radicals in the plasma region to diffuse towards the processing chamber and vacuum pump.

Figure 5.2 shows an image of the ceramic holder which is attached to the ICP source inside the PL80. This setup minimises the risk of arcing between the graphite plate and surrounding grounded surfaces especially when it is biased with a few hundred volts. A metallic strip mounted on the lower side of the ceramic disk, shown in figure 5.2, provides electrical contact between the graphite plate

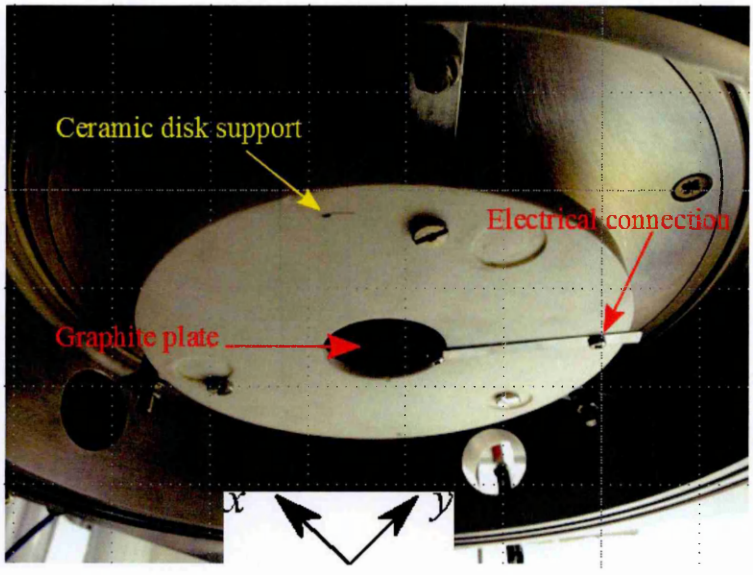

Figure 5.2: An image of the NBE setup inside the PL80 attached to the ICP source. It shows a graphite extractor and the electrical connection used to bias it.

and an external voltage source.

The operating pressure of the plasma source normally ranges from 10 to 100 mTorr, while the processing chamber resides at a pressure varying from 0.1 to 5 mTorr. The extraction grid is situated 10 cm beneath the centre of the coil, and has a 6 cm diameter. The thickness of the extraction carbon plate is 1 cm. In our early tests, it was difficult to run different discharges, especially SF_6 discharges, with gas flow rates above a few sccm when the NBE adapter was put in the chamber. The effective pump rate of the source chamber was generally affected by the neutraliser. Therefore four holes, with 5 mm diameters, were drilled in the ceramic tube, indicated in green in figure 5.1. This higher gas flow enabled discharge operation with about 15 sccm gas flow while still keeping a reasonable pressure difference between the plasma and processing regions. The ceramic disk,

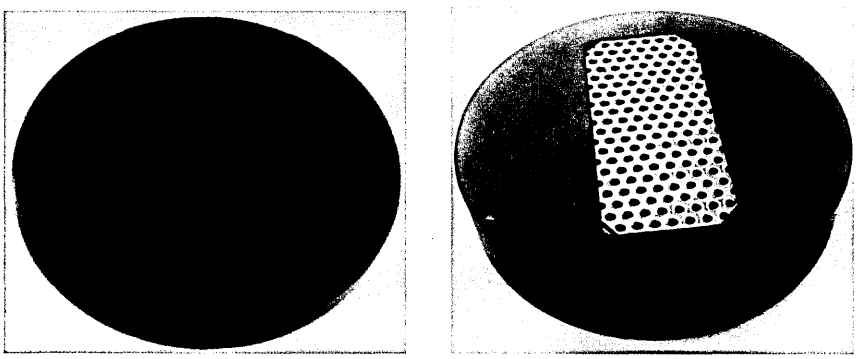

(a) (b)

Figure 5.3: (a) perforated graphite plate with 1 mm hole diameter and is used for extraction and neutralisation of ion beams. (b) graphite plate with a metallic mesh having 1 mm hole diameter. The metallic mesh is 0.8 mm thick and is to extract ion beams only.

figure 5.2, was used to ensure that diffused species from the plasma did not reach the wafer easily.

A second modification of the chamber was the introduction of an additional metal plate, made of perforated aluminium, in the region *above* the plasma. This plate acted as an additional electrode and allowed us to control the potential of the plasma region independently from the graphite plate. Although this enabled much greater control of the extraction process, the presence of the plate blocks diagnostic access to the source plasma.

Several carbon plates with different hole diameters and aspect ratios were tested as neutralisers. The perforated plate shown in figure 5.3 (a) was used for most of the experiments and measurements. There are 224 drilled holes in this plate, each with a 1 mm diameter. The total perforated area is equivalent to $A_h = 176$ mm^2, where A_h is total drilled area. The area of the hole graphite plate is equivalent to $A_G = 2820$ mm^2. Therefore, $\frac{A_h}{A_G} = 6.3\%$ of the entire graphite

plate is perforated. Future experiments are planned for perforated plates with larger total drilled area, however for the experiments presented in this chapter 6.3% is the transparency area of the graphite palate used for extraction and neutralisation of energetic ions.

A metallic perforated plate, of 0.8 mm thickness, containing $\sim$ 150 drilled holes, with 1 mm diameter, was used to extract energetic ions without neutralisation. This plate, positioned over a correspondingly shaped hole in the carbon plate, allows ions to be extracted with minimal contact with surrounding surfaces. The perforated area of the metallic plate is equivalent to $A_m = 120$ mm^2, which gives $\frac{A_m}{A_G} = 4.3\%$.

This particular extractor allowed us to extract ion beams whose IEDF[1] we could then measure. These IEDF were used as one estimation of the energy distribution of neutrals extracted when the carbon neutraliser plate was used. An RFEA[2] was used to measure the IEDF of the extracted species when the plasma was operated in pulsed and continuous mode. The RFEA was positioned on the lower electrode where the wafer normally resides.

A series of optical and electrical measurements were performed to measure the plasma properties when the NBE adapter was installed in the PL80. The plasma properties were then compared to those presented in the chapter 4 which were measured without the NBE adapter in the chamber. These measurements are presented in the following section.

[1]Ion energy distribution function
[2]Retarding field energy analyser, manufactured by Impedans

5.2 Characterisation of the plasma properties with the NBE adapter

The main aim of this research is to perform neutral beam etching by extracting and neutralising negative ions generated in pulsed discharges operated with electronegative gases. There are several methods and approaches to generate negative ions, as described in section 1.4 [p. 21]. Our approach depends on generating negative ions in the afterglow phase of pulsed discharges. The electron temperature decreases drastically in the first few microsecond of the afterglow phase, as was seen in the previous chapters, making the conditions favorable for dissociative electron attachment processes. These processes increase the density of negative ions in the afterglow phase. Therefore, our discharges were operated in pulsed mode throughout most of the experiments presented in this chapter. However, some initial measurements were made with the discharge in continuous mode, in order to gauge the effect of the NBE adapter on the plasma properties.

Argon discharges were used to perform plasma studies and characterise the plasma source. Discharges operated in SF_6 gas were used to carry out neutral beam etching. Other plasma chemistries have been used to perform neutral beam etching, as was discussed in section 1.4. However, SF_6 gas is used instead of other gases, such as chlorine or bromine based gases, because it is more user friendly and conforms to the health and safety regulations of the current set up. It is also a standard etching gas and allows us to characterise the NBE tool.

This section contains a study of the effect of the NBE adapter on the plasma properties. The studies were performed using a combination of optical and electrical measurement techniques. Total light emission from the plasma was measured

for a range of conditions. The simple OES technique, presented in section 3.3.2, with electrical measurements, was used to gauge the effect of the NBE adapter on the plasma properties for specific conditions. These measurements are presented below.

5.2.1 Spectrally resolved measurements

In initial studies, the discharge was operated in pure argon with $11 \leq p \leq 80$ mTorr with total gas flow of ranging from 8 up to 34 sccm with 1, 2.5 and 5 kHz pulse frequencies with duty cycles ranging from 25% up to 90%. Traces of Kr and Xe gases were added when spectrally resolved measurements were performed to estimate the electron temperature. The plasma emission is relatively straightforward to measure and strongly depends on the electron properties. A photodiode was used to measure the plasma emission for a range of conditions when the NBE adapter was included in the PL80, while spectrally resolved measurements were performed for a selected set of conditions.

5.2.1.1 Total plasma emission measurements

Plasma emission was measured for the same operational conditions presented in section 4.2.1 in order to compare the effect of the NBE adapter on the electron properties. The discharge was operated in pure argon at 20, 40 and 80 mTorr with $1 \leq f \leq 5$ kHz pulse frequencies and duty cycles ranging from 30% up to 90%.

Figure 5.4 shows the measured plasma emission when the NBE adapter was in place for a 20 mTorr argon discharge operated with 1 kHz pulse frequency and several different duty cycles. It can be seen from this figure that the plasma

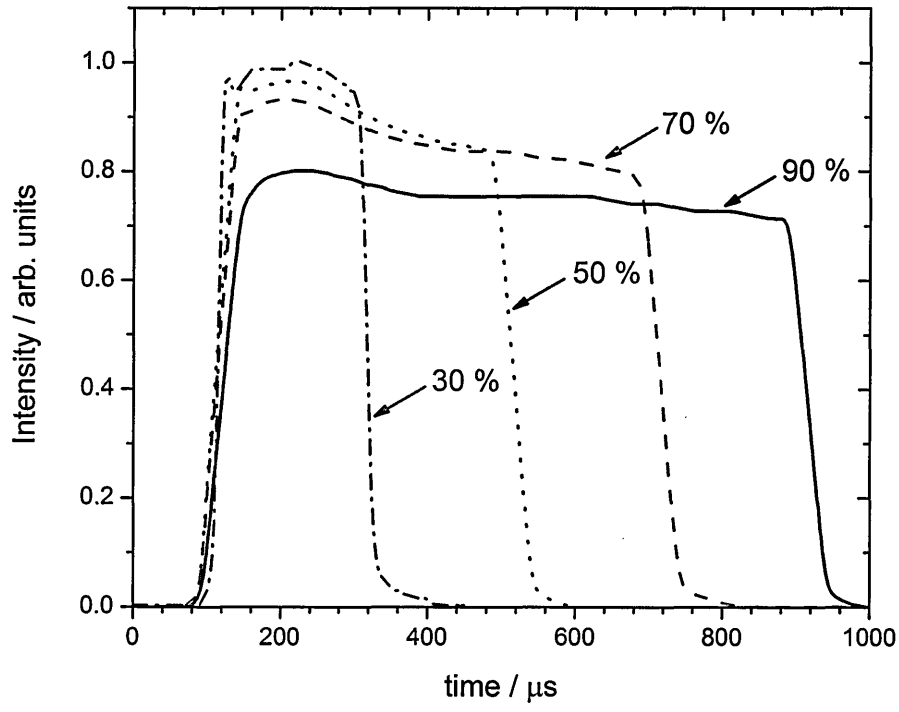

Figure 5.4: Total plasma light emission measured for 20 mTorr argon discharge operated at $f = 1$ kHZ with 30%, 50%, 70% and 90% duty cycles when the NBE adapter was in the PL80.

emission profile changes relatively little compared to the measurements without the NBE adapter, shown in figure 4.7 [p. 119]. The measurements in figure 5.4 are normalised with respect to the maximum measured value. In fact, the absolute measured values are slightly less than those presented in figure 4.7 by a factor of $\sim$ 10%. However, the profiles show relatively little change when the traces are normalised to the maximum measured value. This suggests that the NBE adapter has a relatively small effect on the plasma emission.

Similar plasma emission measurements were performed for the other pulse conditions and gas pressures. These measurements exhibited the same behavior

as the case presented in figure 5.4 with intensities being 10% less than those measured without the NBE adapter and similar profiles when the measurements are normalised. These measurements have not been presented as they all show the same effect of the NBE adapter on the plasma emission.

Spectrally resolved emission measurements were performed to estimate the electron temperature change when NBE adapter was mounted in the PL80 for the same operating conditions used in this section.

5.2.1.2 Electron temperature estimation

The addition of small traces of Xe and Kr gases is required to perform spectrally resolved emission measurements. The electron temperature can then be estimated from the ratio of measured emission lines (Xe/Ar) using the simple model presented in section 3.3.2.2 [p. 81]. This model is suitable for discharges in steady state conditions, not during transient conditions. Also, the plasma emission measurements, in the previous section when the plasma was operated in pulsed mode, showed that the NBE adapter has very little influence on the measured plasma emission. Therefore, the discharge was operated in continuous mode to perform these measurements with $25 \leq P \leq 400$ W input power and maintained at $p = 40$ mTorr with a total gas flow of 15 sccm using Ar/Kr/Xe gas mixture with 8:1:1 ratio.

Figure 5.5 shows the ratio of the measured Xe emission line to that of Ar and the estimated electron temperature for a 40 mTorr Ar/Kr/Xe plasma as a function of the input power. Similar measurements were performed for discharges operated at 20 and 80 mTorr. These measurements showed similar behavior of the electron temperature as that showed in the 40 mTorr case. The $p = 40$ mTorr

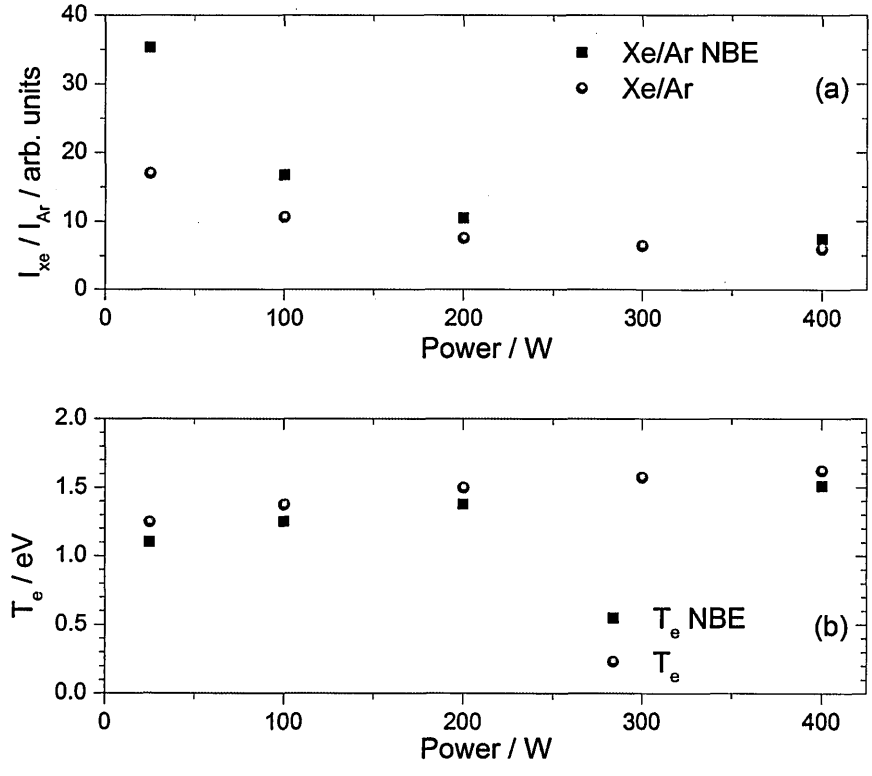

Figure 5.5: (a) Xe/Ar emission ratio measured for a 40 mTorr Ar/Kr/Xe discharge with $25 \leq P \leq 400$ W input power. (b) the estimated electron temperature from the Xe/Ar emission ratios for the same operational conditions. The squares (with NBE in the legend) represent the measurements performed with the NBE adapter, while the circles represent the measurements without the NBE adapter.

measurements were selected as a wide range of parameters were covered and all showed similar behavior.

It can be seen from figure 5.5 that the electron temperature decreases by $\sim$ 0.1 eV throughout the entire input power range when the NBE adapter is added in the PL80. Also, the plasma emission measurements of pulsed discharges showed a decrease of about 10% in the total measured light when the NBE adapter

was used. Hence, it can be assumed that the NBE adapter has the same effect on the discharge when it is operated in both pulsed and continuous modes.

Another set of spectrally resolved measurements was carried out for a discharge operated in an $SF_6/Ar/Kr/Xe$ gas mixture with a 20 sccm total gas flow and 5:3:1:1 ratio. The discharge was operated in pulsed mode with $f = 1$ kHz and 50% duty cycle and maintained at 20, 40, 60 and 80 mTorr. The emission from Xe and Ar was measured only at the end of the active glow phase ($t = 490$ μs), when steady state conditions were achieved. The simple model was used to estimate the electron temperatures for the different operational pressures. This measurement was performed to estimate the electron temperature range during the neutral beam etching process, when access to the plasma is severely limited.

Figure 5.6 shows the ratio of the measured Xe and Ar emission lines and the estimated electron temperature for a $20 \leq p \leq 80$ mTorr $SF_6/Ar/Kr/Xe$ discharge operated with $f = 1$ kHz and 50% duty cycle and $P_{av} = 330$ W. The emission measurements were performed at the end of the active glow phase when steady state conditions are achieved. It can be seen from these measurements that the electron temperature tends to a value of 1.9 eV. Also, T_e slightly decreases as the pressure increases. The estimated electron temperatures are higher than those measured for discharges operated in inert gases, as expected.

In summary, the NBE adapter has relatively small effect on the plasma emission and hence the electron temperature. Charge density measurements were performed to compare with these optical measurements. These measurements are presented in the following section.

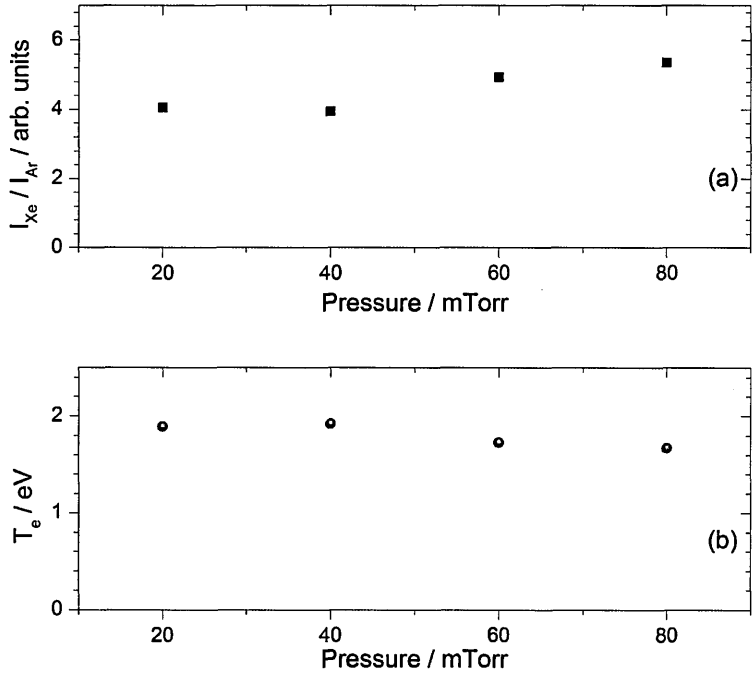

Figure 5.6: (a) Xe/Ar emission ratio measured for a $20 \leq p \leq 80$ mTorr SF_6/Ar/Kr/Xe discharge with $P_{av} = 330$ W input power. (b) the estimated electron temperature from the Xe/Ar emission ratios for the same operational conditions.

5.2.2 Charge species density measurements

As presented in the previous section, several optical measurements showed little effect of the NBE adapter on the source plasma parameters. Electron and ion density measurement for continuous and pulsed discharges were performed to compare with these findings. First, electron density was measured using a hairpin probe for argon discharges operated at different pressures and input powers in continuous mode when the NBE adapter was mounted in the PL80. Positive ion current was then measured using a planar Langmuir probe for discharges operated in pulsed mode using SF_6 gas, also with the NBE adapter in the PL80.

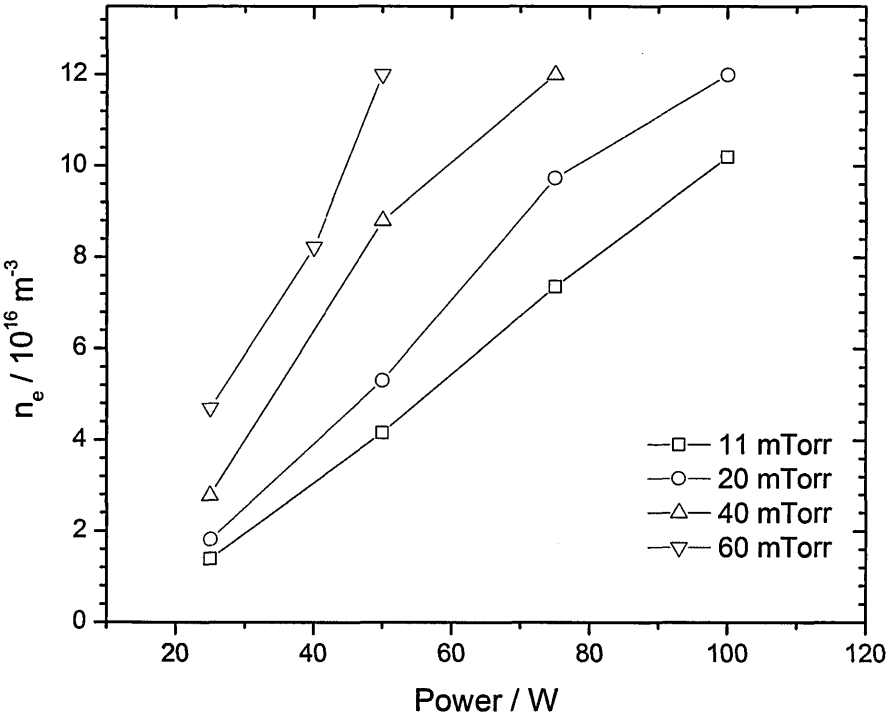

Figure 5.7: Electron density measurements at 10 cm above the coil region for argon discharges operated at $11 \leq p \leq 60$ mTorr with $25 \leq P \leq 100$ W with the NBE adapter mounted in the PL80.

The NBE adapter was installed in the PL80 and a hairpin probe was introduced into the system from the top access port, as shown by the blue arrow in figure 4.1 [p. 106]. The hairpin probe was located 10 cm above the centre of the coil region. Argon gas was used to generate discharges at pressures of 11, 20, 40 and 60 mTorr with total gas flows of 8, 13, 23 and 34 sccm, respectively, with input power $25 \leq P \leq 100$ W. This measurement was performed as an initial test of the effect of the NBE adapter on the plasma density.

Figure 5.7 shows the electron density measurements for different argon pressure and input powers under the conditions described above. Similar measure-

ments were performed for the same operational conditions without the NBE adapter in the PL80, shown in figure 4.2 [p.107]. It can be seen from the comparison between the measured plasma density in both figure 4.2 and 5.7 that there is almost no effect of the NBE adapter on the plasma density. A simple comparison of pulsed Ar discharge was not made, as these are not used for NBE. Instead, positive ion current measurements of pulsed SF_6 discharges were performed using a planar Langmuir probe.

A planar Langmuir probe was used to perform spatiotemporal ion density measurements for pulsed SF_6 discharges. The discharges were maintained at a pressure of 30 mTorr with a total gas flow of 5 sccm and pulse frequencies of 1 and 2 kHz with 30%, 50% and 60% duty cycles. The gas pressure in the plasma region was equal to 19 mTorr when the input power was switched off and 30 mTorr when the input power was on. This pressure increase could be related to an increase in the gas temperatureor to fragmentation/dissociation processes of the SF_6 molecule when the discharge is on. The bias of the planar Langmuir probe was maintained at -50 V throughout these measurements in order to measure the positive ion current, using the same techniques as the measurements presented in figure 4.14 and 4.15.

Figure 5.8 shows the spatio-temporal measured positive ion current for SF_6 discharges operated at a pressure of 30 mTorr, in the plasma region, with $f = 1$ kHz and 50% duty cycle, $f = 2$ kHz and 60% duty cycle and 30% duty cycle. The positive ion current was measured along the axis of the discharge, representing the relative distance from the center of the coil region, which is represented by the zero position on the scale.

(a) $f = 1$ kHz, 50% duty cycle

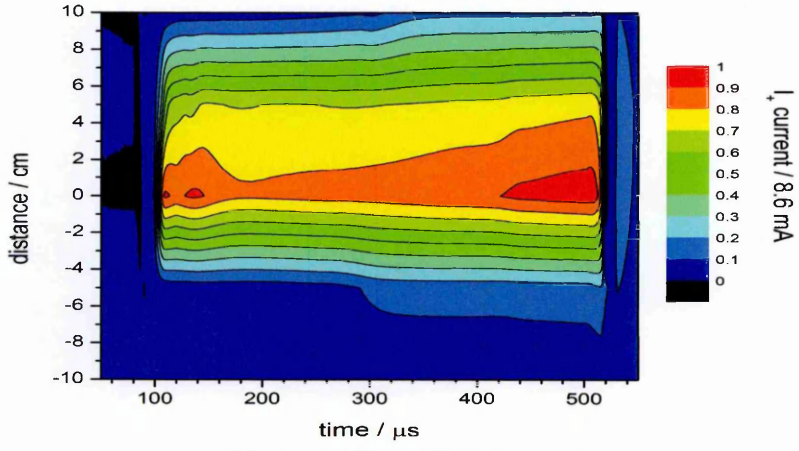

(b) $f = 2$ kHz, 60% duty cycle

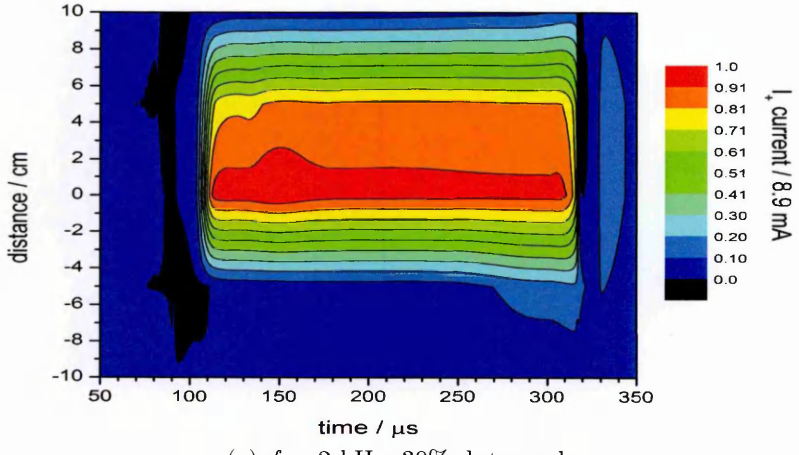

(c) $f = 2$ kHz, 30% duty cycle

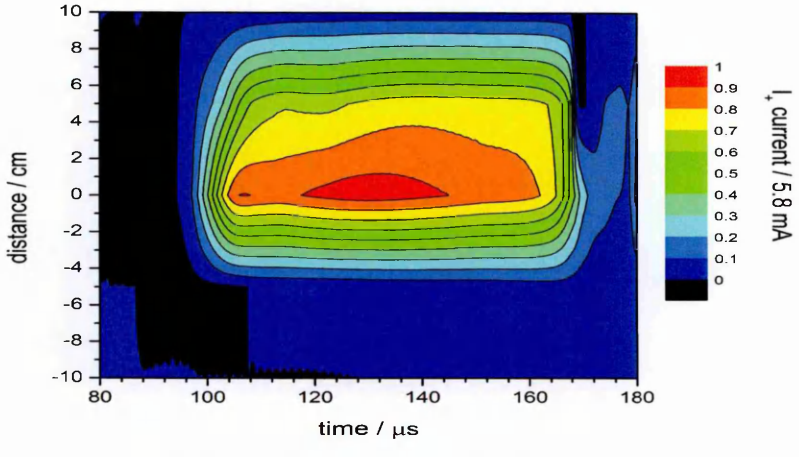

Figure 5.8: Spatiotemporal positive current collected by planar Langmuir probe for 30 mTorr SF_6 plasma operated at 1 kHz pulse frequency with 50% duty cycle (a), 2 kHz 60% (b) and 30% duty cycles. The values are normalised to highest positive current measured for each case.

It can be seen that the highest measured current is at the center of the discharges in all the cases presented in figure 5.8. The maximum measured current is 8.6, 8.9 and 5.8 mA for the cases presented in figure 5.8 (a), (b) and (c) respectively. These measured currents are approximately one order of magnitude smaller than those measured at similar conditions in pure argon discharges, as expected for a molecular discharge.

The maximum ion density of the measured cases can be estimated by the assumption that 90% of the positive ion species is SF_5^+ [Kokkoris *et al.*]. The electron temperature for these operational conditions is estimated to be 1.6 eV, from the OES measurements presented in the previous section. Therefore the Bohm speed for the SF_5^+ ions is calculated to be ~ 1100 m s^{-1}. The maximum ion density can be calculated using $I_{SF_5^+} = 0.9I^+$, where $I_{SF_5^+}$ is the estimated current due to the dominant positive ion and I^+ is the total measured positive ion current. The estimated maximum ion densities are 1.55×10^{16} m^{-3}, 1.6×10^{16} m^{-3} and 1.04×10^{16} m^{-3} for the cases presented in figure 5.8 (a), (b) and (c) respectively.

It can be seen that the density is relatively high for these operational conditions. In fact, the cases presented in (a) and (b) have similar maximum estimated positive ion densities. High plasma density and fast pulses are favorable to perform neutral beam etching. Higher plasma density means higher dissociative electron attachment in the afterglow, which results in more negative ions. Also, faster input pulses mean that the extraction graphite plate can be pulsed more frequently. These two conditions should result in higher extracted fluxes.

Negative ions are neutralised relatively more efficiently than positive ions, as mentioned in section 1.4, and the etch rate depends on the rate of species arriving to the surface. Therefore, the set of conditions used in case (b) was chosen to

be used as the standard operational conditions in the preliminary neutral beam etching experiments, as it is crucial to have high negative ion densities in the afterglow phase and increase the extracted beam fluxes to have faster etch rates.

However, it is very difficult to analyse or measure the energy of the extracted neutral particles. Therefore, measurements using a metallic grid, figure 5.3 (b), were used to extract ion beams without neutralising them. These preliminary measurements are presented in the following section.

5.3 Extracted beam energy measurements

It is necessary to understand the effect of pulse tailoring on the plasma properties in order to have a comprehensive control over these properties according to the desired application, especially increasing the negative ion density for neutral beam etching purposes. Another aspect to be probed is the properties of the extracted species from the plasma source, in particular their relative energies.

So far, we have been measuring the plasma properties in the bulk plasma region, and certain preferable conditions were selected to acquire a high density plasma suitable for negative ion generation. However, we performed a set of measurements to assess the energy of the extracted species from the plasma source, the degree of control that we have over their energies and the neutralisation efficiency of our set up. These preliminary measurements were performed using the perforated graphite plate, figure 5.3 (a), and the graphite plate that contains a stainless steel mesh, figure 5.3 (b). The first graphite plate has 1 mm diameter holes drilled in it. This results in hollow cylinders with 10 mm length (equal to the thickness of the graphite plate) and 1 mm diameters. The extracted ions

are neutralised due to surface grazing collisions in these cylinders. Hence, this graphite plate is used to extract and neutralise ions from the plasma and will be referred to as the neutraliser. The second plate, which contains the metallic mesh, is used to extract ions only without neutralisation and will be referred to as the extractor. These two graphite plates were used with a retarding field energy analyser (RFEA) to measure the total collected ion flux and ion energy distribution function (IEDF).

Ideally, these plates and the RFEA would be used to measure fluxes and IEDFs of negative ions. However, surface charging issues and other challenges made it difficult to measure negative ions extracted from the plasma. For this reason, the properties of positive ion beams were measured to assess the control over the ion energy and neutralisation efficiency in our set up.

In order to measure the energy of extracted positive ion beams, the extractor plate was mounted in the NBE adapter. An argon discharge was operated at a pressure of $\sim$ 20 mTorr with 13 sccm total gas flow and $P = 200$ W. The discharge was not pulsed as these experiments only require a source of ions. The top aluminium perforated electrode, section 5.1, was introduced into the plasma region and was grounded, providing a stable ground potential in the plasma source. The extractor was negatively biased with $-300 \leq V \leq -50$ V. The lower table which holds the RFEA was biased synchronously with the extractor to create a field-free region between the extraction point and detection area.

Figure 5.9 shows the measured IEDF for a 20 mTorr argon discharge for different biasing voltages applied to the extractor and lower table. It can be seen from this graph that the ion energy is proportional to the applied potential on the extractor. Also, it can be seen that the ion flux increases with applied potential

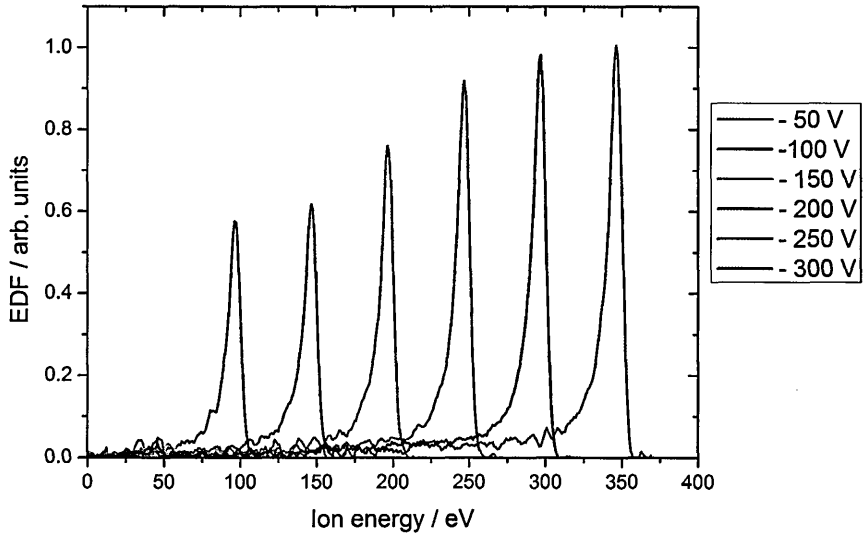

Figure 5.9: IEDF measured for different negative biasing voltages of the extraction grid.

(the area of the IEDF represents the ion flux).

The IEDF was also measured for similar operational conditions and biasing voltages when the neutraliser was installed in the NBE adapter. These measurements are shown in figure 5.10. It can be seen from this graphs the ion energies exhibit a similar dependence on the applied bias as the case when the extractor is used, figure 5.9. However, the relative areas of the IEDFs are smaller from those measured when the extractor was used instead of the neutraliser, especially for low bias voltages. This suggests that the flux of charged species, positive ions in this case, is lower when the neutraliser is installed in the system.

The discharge conditions were kept the same throughout these experiments. The ion fluxes were measured using the RFEA for both cases when the extractor

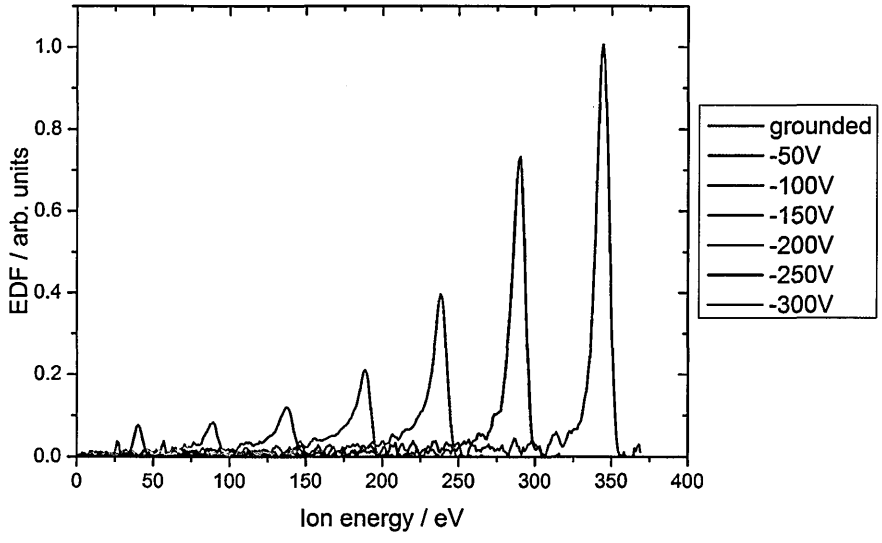

Figure 5.10: IEDF measured for different negative biasing voltages of the neutraliser. The black solid line shows the measured IEDF when no biasing was applied to both the neutraliser and lower table.

and neutraliser were installed in the NBE adapter. Figure 5.11 shows a comparison between the measured ion fluxes as a function of the biasing voltages for the extractor and neutraliser. It can be seen from this graph that the measured flux is higher when the extractor is used. Also, both fluxes increase as a function of the applied bias.

It is assumed that the maximum extracted ion flux is that measured when the extractor is used, as minimal neutralisation, if any, is expected in this case due the very small thickness of the mesh.

The neutralisation efficiency of the setup can be estimated from these measurements. The maximum ion flux is expected to be measured when the extractor is used. Therefore, $\Gamma = \frac{\Phi_N}{\Phi_E}$ where Γ is the neutralisation efficiency and Φ_N and

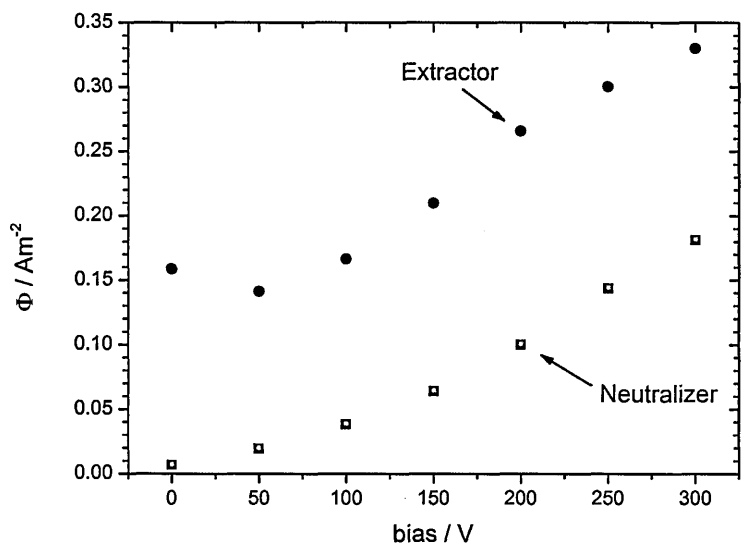

Figure 5.11: This graph shows the measured ion flux from the extractor (blue disks) and neutraliser (red squares) as a function of biasing potential for a 20 mTorr argon discharge operated at 200 W input power.

Φ_E are the measured fluxes from the neutraliser and extractor respectively. Figure 5.12 shows the neutralisation efficiency as a function of the bias voltage on the graphite plates. It can be seen from this graph the neutralisation efficiency decreases as the biasing potential increase, and the highest neutralisation efficiency is around 95% for the lowest biasing potential.

The neutralisation efficiency is in agreement with the flux measurements. The ion flux increases as the biasing potential increases which suggests that higher ion density arrives at the collection area. This increase in the measured flux, in the case of the neutraliser, could be related to the behavior of the sheath in front of the orifices. If the sheath has a curved profile in front of these orifices of the neutraliser, the extracted ions are more likely to collide with the graphite

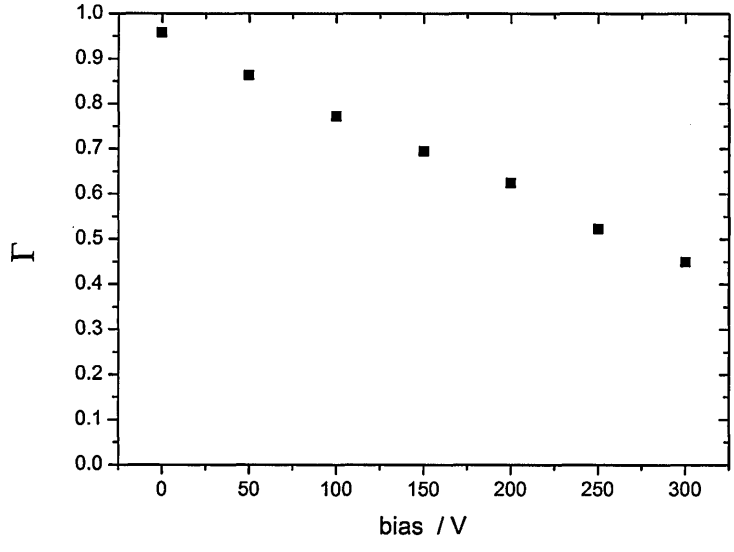

Figure 5.12: This graph shows the neutralisation efficiency, $\Gamma = \frac{\Phi_N}{\Phi_E}$, as a function of the biasing potential.

inner walls of the graphite cylinders as they migrate from the sheath towards the processing region. As the applied potential increases, the sheath should become more parallel to the graphite plate. When this occurs, the ions will propagate in a direction perpendicular to the graphite plate and parallel with the direction of the drilled cylinders, which decreases the probability of ions colliding with the graphite surface and decreases the neutralisation efficiency while the collected ion flux increases. This could be a possible explanation of why the ion flux increases and neutralisation decreases as the biasing potential increases. A second possibility is that the ions spend more time in the neutraliser holes when they have low energy, and hence there is more time for the ions to collect an electron from the graphite in a neutralisation process.

In summary, the effect of the NBE adapter on plasma parameters was studied by performing a set of electrical and optical measurements. The properties of the extracted ion/neutral beams were studied as a function of the potential applied to the extraction/neutraliser plates. The neutralisation efficiency was calculated for a simple argon plasma.

For neutral beam etching, a sufficient particle flux should reach the substrate surfaces with enough energy to provoke etching. Therefore, a bias potential just high enough to extract energetic particles and sufficient flux to carry out neutral beam etching is required. The results presented in this section were used to select a set of plasma parameter and biasing potential to perform preliminary neutral beam etching experiments. This is presented in the following section.

5.4 Preliminary NBE results

In the previous sections, plasma parameters and ion beam properties were measured for a range of conditions. Ion density measurements performed for SF_6 discharges showed that relatively high plasma density is achieved for a pulse frequency of 2 kHz and 60% duty cycle. RFEA measurements showed that the extracted ion energy can be controlled via biasing the neutraliser plate and the neutralisation efficiency decreases as the biasing potential increases. For positive ion neutralisation and a bias potential of -200 V, a neutralisation efficiency of 60% is expected. However, neutralisation efficiency should be relatively higher for negative ions compared with positive ions. Therefore, if a biasing potential of 200 V was selected to extract negative ions, a neutralisation efficiency higher that 60% is expected, with the extracted beams having sufficiently high energies

to perform etching.

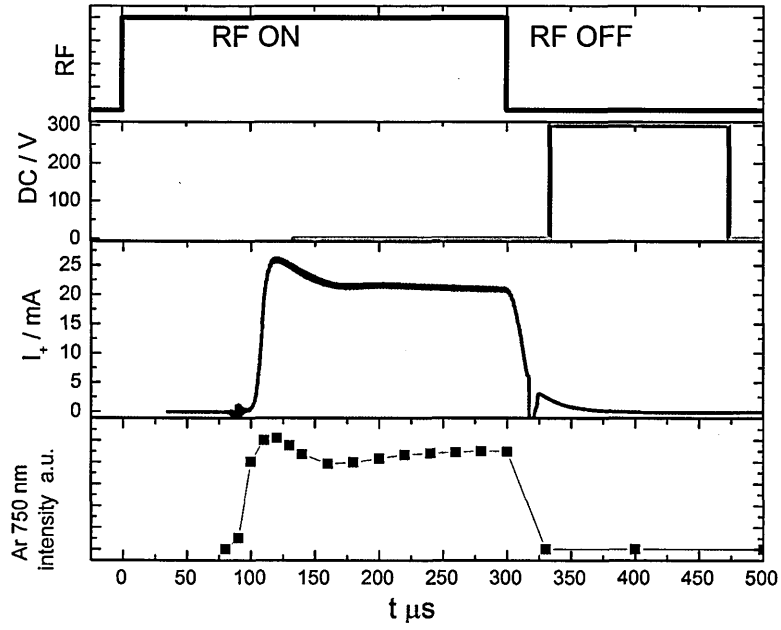

Figure 5.13: This figure shows the typical plasma conditions used to perform neutral beam etching. The biasing of the neutraliser was pulsed 20 μs after the input power was switched off with a maximum voltage of 300 V for a duration of 150 μs. This figure also shows the positive ion density current measured using a planar Langmuir probe, and the emission profile of the Ar line during the active glow of the discharge.

From these plasma characterisation and beam measurements, a set of standard operational conditions was used to perform neutral beam etching. This set of conditions is as follows: SF_6 gas flow of 5 sccm, p = 30 mTorr in the plasma region, p = 0.3 mTorr in the processing region, f = 2 kHz with 60% duty cycle, P_{av} = 330 W. The neutraliser was biased in the afterglow phase of the discharge with a maximum potential of 300 V, and the duration of bias was equal to 150 μs.

Figure 5.13 shows the plasma operational conditions used to perform neutral beam etching. The discharge was maintained at a pressure of 30 mTorr using

SF_6 gas and traces of Ar to measure the emission profile during the active glow. A planar Langmuir probe was used to measure the positive ion current measured in the discharge during the active glow phase. The graphite plate was biased with a delay of 20 μs in the afterglow for a duration of 150 μs, with a maximum voltage of 300 V. The biasing of the graphite was intentionally delayed to allow electrons to cool down and undergo dissociative electron attachment to generate negative ions.

A blank poly-silicon wafer and a patterned wafer were used to perform the preliminary neutral beam etching experiments. The blank wafers were made from a 200 nm thick layer of poly-silicon covering a 400 nm silicon oxide layer, which was deposited on an 800 μm thick recycled silicon substrate. These blank wafers were used to perform several tests, including putting the wafers at different positions with respect to the orifices of the neutraliser. As the thickness of the poly-Si layer changed, the index of refraction changed, creating a colour gradient which was used as crude indicator of etching. The poly-Si and SiO_2 have a pink and dark blue colours respectively.

Figure 5.14 shows three poly-Si samples subjected to the standard neutral beam etching conditions. It can be seen from sample (1), which was subjected to ten minutes of standard neutral beam etching, that the 200 nm of poly-Si is completely etched, since the SiO_2 layer can be seen by the naked eye (dark blue colour). Also, the pattern of the drilled orifices in the neutraliser, figure 5.3 (a), is transferred onto the sample. Sample (2) was exposed to 5 min of neutral beam etching. Evidence of some etching can be seen by the change of the colour in the area subjected to the extracted beams. Sample (3) was exposed also for 10 minutes to the same neutral beam etching conditions without neutraliser bias.

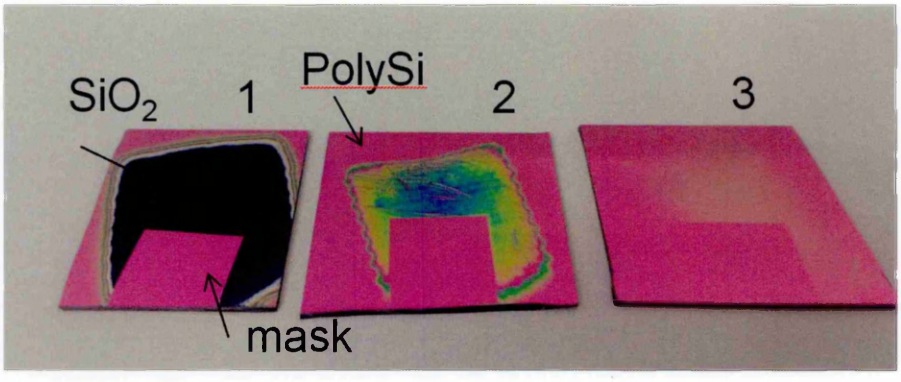

Figure 5.14: Three poly-Si blank tiles subject to standard neutral beam etching conditions. Samples (1) and (2) were exposed to 10 and 5 minutes of neutral beam etching respectively. Sample (3) was subjected to the same plasma conditions for 10 minutes but without any biasing on the neutraliser. A hard mask was used to cover some part of the samples which was exposed to the extracted beam.

This sample barely shows an change in colour which suggests the etching rate was very low compared to when the neutraliser was biased.

In a separate experiment, a poly-Si tile was positioned 5 cm away from the central axis of the neutraliser on the lower table whilst the plasma was operated at the standard conditions. The purpose of this experiment was to gauge if there was any etching due to species diffusing from the ceramic cylinder in the NBE adapter. The tile exhibited no colour change, which suggests that the etching that occurs in the processing chamber is due to species traversing the neutraliser.

A test patterned silicon wafer was used to assess the etch rate and directionality of the neutral beam etching. This patterned sample was supplied by our industrial collaborators, Oxford Instruments (OIPT). An SEM[1] was used to image the etched features of the patterned samples. Figure 5.15 shows an image of the test pattern wafer taken by a SEM. This image shows the different patterns

[1]Scanning electron microscope

and their dimensions.

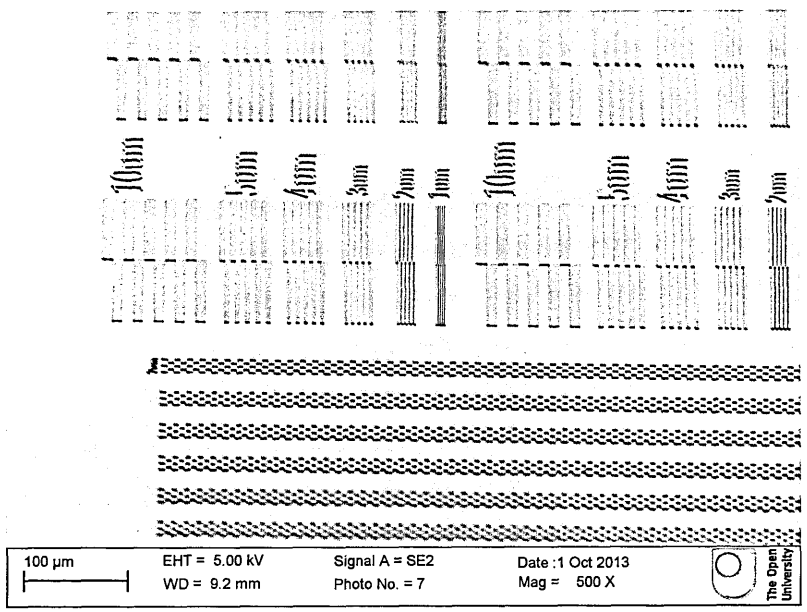

Figure 5.15: An image of the patterned wafer. This image was taken by a SEM and shows the different line ratios and dimensions of the patterns.

Tiles of this test wafer were exposed to the standard neutral beam etching conditions for 5, 10, 15 and 20 minutes. Various SEM images were taken for these samples and are presented in figure 5.16. It can be seen that while there is clear evidence that the neutral beam is etching the surface, the etch is isotropic. Undercut of the resist can be clearly seen. Image (c) shows a lateral etch of 141.5 nm and a depth of 435.9 nm.

Isotropic etching of silicon by fluorine-containing plasmas is a known process [Verdonck *et al.*, 2004]. Studies have shown that under-etching of the silicon layer increases in the presence of ion bombardment, indicating that fluorine surface transport is important for these processes. These studies have concluded that part of the energy of the incoming ions is transferred to the fluorine compounds,

which are on the horizontal surfaces and that ion bombardment enhances the fluorine surface transport [Verdonck *et al.*, 2004].

In our neutral beam etching, we assume the energy of ions is relatively close to that of the applied potential on the neutraliser. Also, we assume that the ions lose a small fraction of their energy through charge exchange surface grazing collisions. We estimated the neutralisation of positive ions close to 60% in a pure argon discharge. The neutralisation efficiency of negative ions is relatively higher than that of positive ions, but the negative ion density is generally lower which results in a lower extracted flux of neutrals. The energy of the extracted beam is assumed to be of few hundred eV, which is still reactively high. However, the flux of particles is less, as in these cases negative ion are being extracted and neutralised, which decreases the etch rate. Nevertheless, with all these estimations, the silicon lateral etching could be explained due to mechanisms dominated by fluorine surface transport similar to that reported by Verdonck *et al.* [2004].

Fluorine radicals are highly reactive even at room temperature. One possible way to decrease the side etch due to surface transport would be to decrease the temperature of the sample to micro Kelvin temperatures using cryogenic cooling. Another approach would be to use plasma chemistries that create a passivation layer on the sidewalls of the etched trenches. Fluorocarbon-based chemistries could be used, but would generate a risk of forming thin coatings on the graphite neutraliser, which would decrease the efficiency of neutralisation. Other chemistries involve adding oxygen to the SF_6 discharges to create an SiO_2 passivation layer on the sidewalls of the trenches. A potential problem is that oxygen might etch the graphite, but if introduced in small traces and the measurements were performed rapidly, this side effect can be avoided.

Hence, another set of samples from the same patterned wafer were exposed to otherwise standard neutral beam etching conditions, with 1 sccm of oxygen added to the discharge. The addition of oxygen increased the pressure in the plasma chamber from 30 up to 40 mTorr, whilst the pressure was 0.9 mTorr in the processing region. Tiles of the patterned samples were exposed to neutral beam etching under this set of conditions for 5, 10, 15 and 20 min. The SEM images for these experiments are shown in figure 5.17.

It can be seen from the SEM images in figure 5.17 that the silicon lateral etching was suppressed by the addition of oxygen for samples etched for 5 and 10 min. The samples shown in images (a) and (b) seem to have been anisotropically etched, which suggests that the addition of oxygen gas has helped the directionality of the etch by perhaps forming a thin passivation layer on the sidewalls of the trenches. However, image (c) shows that lateral etching can still be observed after prolonged etching. Nevertheless, the side etch is relatively less than that shown in the figure 5.16 (c).

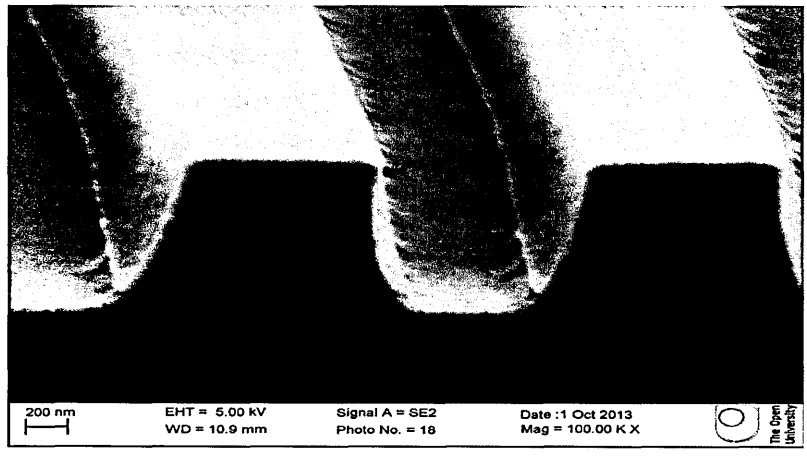

(a)

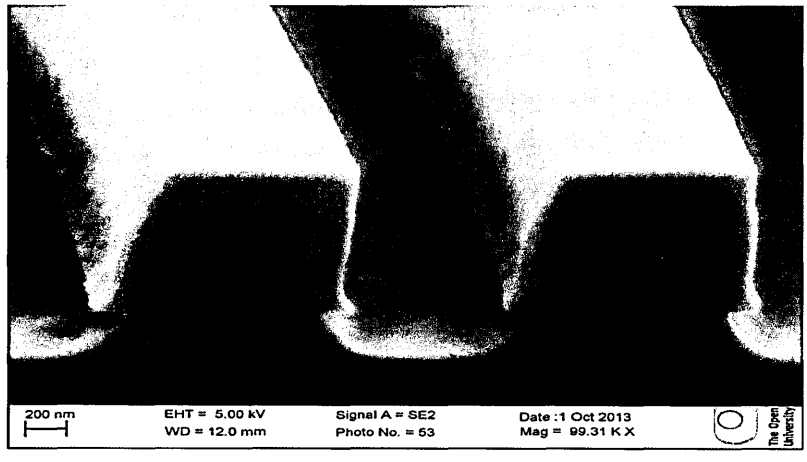

(b)

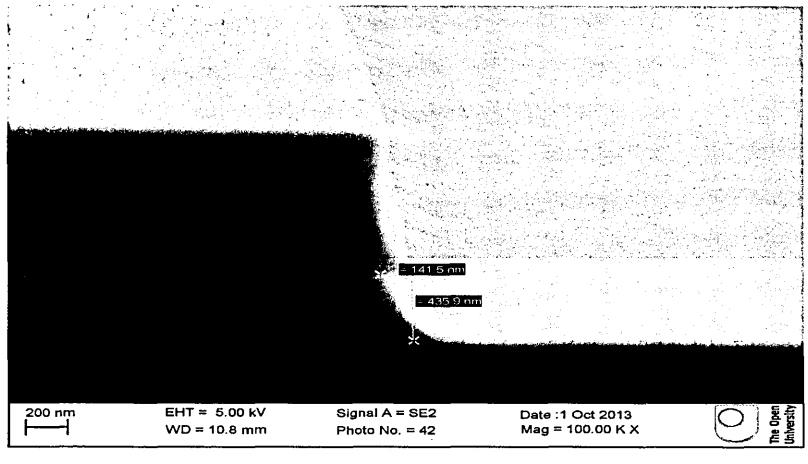

(c)

Figure 5.16: SEM images of patterned tiles exposed to our standard NBE operating conditions in pure SF_6 plasma for 5 minutes (a), 10 minutes (b) and 15 minutes (c). Image (c) shows lateral etch 141.5 nm and 435.9 nm etch depth.

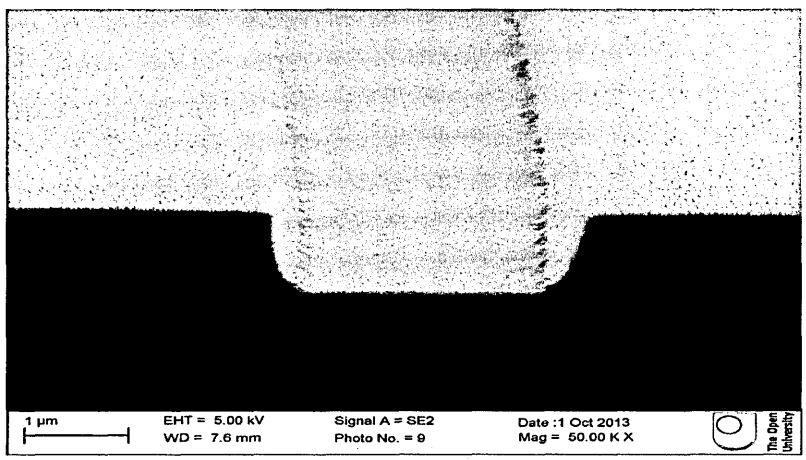

(a)

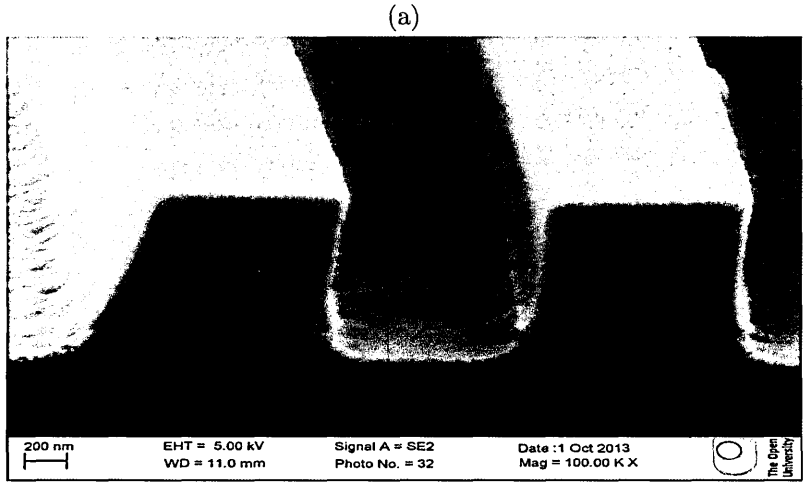

(b)

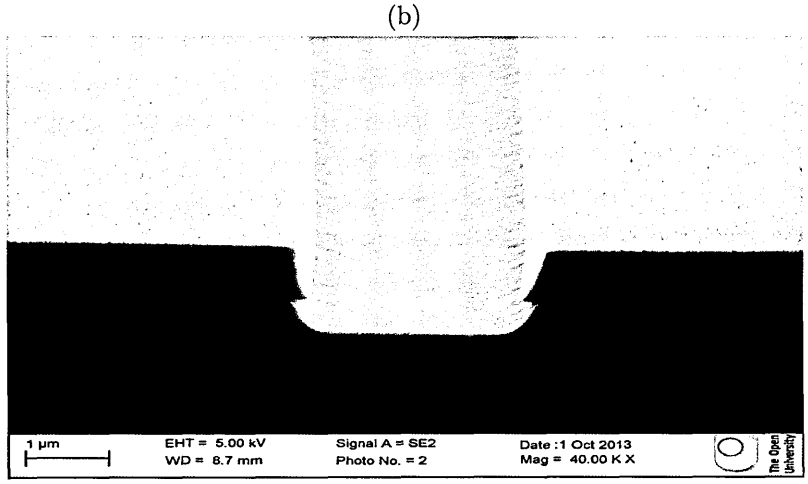

(c)

Figure 5.17: SEM images of patterned tiles exposed to our standard NBE operating conditions in SF_6/O_2 plasma with 8:2 ratio for 5 minutes (a), 10 minutes (b) and 20 minutes (c).

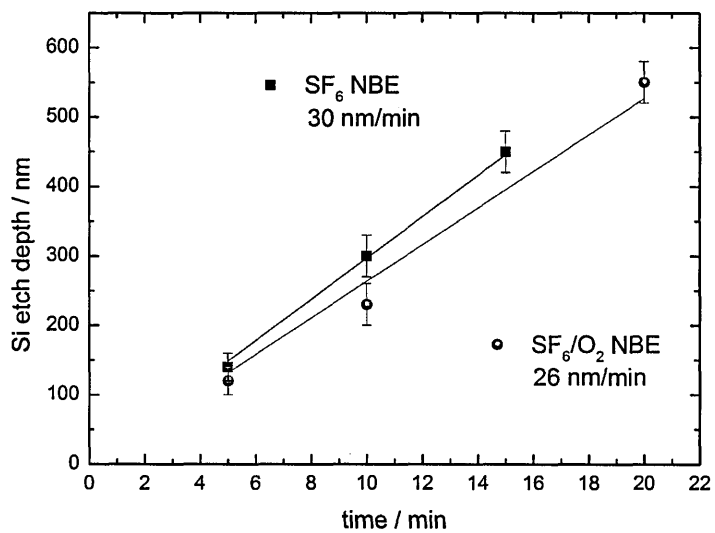

Figure 5.18: The etch rates were estimated from the SEM measurements to be 30 nm/min and 26nm/min for SF_6 NBE (black squares) and SF_6/O_2 NBE (red disks).

The etch rates can be estimated for the SF_6 and SF_6/O_2 neutral beam etching from the SEM measurements of the etched depth for different time exposure. These measurements are presented in figure 5.18. It can be seen from this graph that the etch rate is estimated to be 30 nm/min for neutral beam etching performed in pure SF_6 discharge and 26 nm/min when oxygen is added to the discharge.

This is a low etch rate compared with standard silicon etching techniques, for which rates of 1 μm per minute and above can be achieved. However, our development of NBE is aimed at next stage wafers, containing fine features and thin layers. While some increase in the NBE etch rate is desirable, this preliminary result, with an unoptimised system, is a promising first result. Other chemistries

and plasma operational conditions are planned to be used in experiments in the near future, as this research is still ongoing in our group.

5.5 Conclusions

A setup for neutral beam etching was designed and and successfully tested in the PL80 plasma source to perform neutral beam etching.

The effect on plasma properties of adding the NBE adapter was studied using various optical emission and electrical measurements. No significant effect was observed.

In a second preliminary experiment, a series of measurements was carried out to test the dependence of the extracted beam on the extraction potential. The results showed that the beam energy could be controlled.

Finally, a set of standard plasma operating conditions was used to test neutral beam etching with two plasma chemistries, SF_6 and SF_6/O_2. The plasma operating conditions were selected based on the plasma density measurements and extracted beam measurements that resulted in relatively high neutralisation efficiency and high ion energies. SEM imaging was used to perform etch rate measurements and determine the etch properties of these two chemistries.

The preliminary neutral beam etching results appear to be promising. These measurements show the first anisotropic neutral beam etch reported by our group.

This is ongoing research in our group, and plans to improve the NBE adapter design are being made. Further optimisation of the discharge conditions is expected to lead to improved NBE results, as well as better understanding of the key issues that determine etch quality.

Chapter 6

Development of a novel wafer probe for in-situ measurements

The previous chapter focused on neutral beam etching, which is a possible solution to one of the problems of etching devices with very fine features. Another problem that arises due to the increased number of devices in a single chip is the resistive-capacitive (RC) delay between interconnects. For example, aluminium has been replaced with copper, which has higher conductivity; though that has has required new technologies for its patterning as it is not readily patterned and etched in silicon compatible processing. This chapter focuses on another aspect of this problem.

This metal replacement required a change in the integration sequence, from metal patterning followed by dielectric filling, to dielectric patterning followed by copper filling. To reduce the RC delays one can introduce dielectric materials with low permittivities instead of the traditional material silicon dioxide, SiO_2[1].

[1] SiO_2 has a κ-value of 4.2

These new dielectrics are known as low-κ materials with κ-values as low as 2, almost half that of SiO_2. Plasma processing for low-κ materials has proved to be challenging for many reasons, some of which are discussed in this chapter. The research described in this chapter focuses on the development of a novel method to monitor, in real time and in-situ, the changes induced in low-κ thin films due to plasma exposure. The diagnostic method is relevant to the pulsed plasma theme of the rest of the thesis because the fundamental principle of operation is a pulsed mode that shares a certain amount with the pulsing of plasmas described in Chapters $3-5$.

The chapter is divided as follows. Section 6.1 contains background information about low-κ dielectrics and includes the challenges and motivations behind this research. Section 6.2 consists of two parts; the first describes the design of the wafer probe, and the second introduces the analytical model which was developed to extract plasma parameters and film characteristics from experimental data. Section 6.3 contains a series of experiments performed to benchmark the wafer probe design, the experimental apparatus and the analytical model used in this research. Section 6.4 covers some of the results obtained for different dielectric materials, mainly SiO_2 and low-κ, using the wafer probe. Finally, section 6.5 highlights the milestones achieved and possible extensions to this work.

6.1 Background and motivation

The introduction of new materials to IC fabrication is driven mostly by the necessity to decrease RC delay and power consumption in circuits with nanometre scale components. This drive has led to the replacement of aluminium with copper as

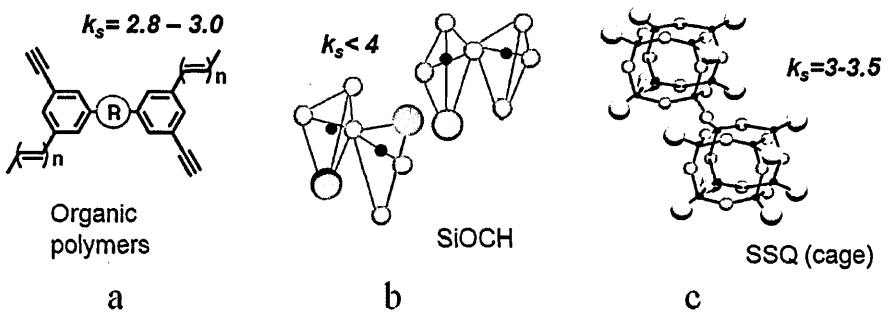

Figure 6.1: This figure shows the different types of low-κ matrix materials and their skeleton κ-value (K_S) [Baklanov *et al.*, 2013].

the metallic conductor and the replacement of the conventional inter-metal dielectric, SiO_2, with new materials that have smaller permitivities. Those materials with low dielectric constants are known as low-κ materials. Using low-κ materials in the integration process introduces new challenges due to the sensitivity of this material to plasma exposure.

Low-κ materials typically use a honeycomb structure to try to approach the ideal vacuum dielectric ($\kappa = 1$), hence they are low mass density materials. Many low-κ materials are composed of SiO_2 molecular units in an open cage structure with additional methyl groups (-CH_3) that form a lining cover of the pores. Other low-κ materials are based on organic polymers, known as organosilicate glasses (OSG or SiOCH). Figure 6.1 shows some different types of low-κ materials and their different κ-values [Baklanov *et al.*, 2013].

The porosity of the structure of these low-κ materials and their low density make them sensitive to plasma exposure. As the porosity of these materials increases, their κ-value decreases and their sensitivity to plasma exposure increases [Verdonck *et al.*, 2013]. Densification and carbon removal are examples of the changes that low-κ materials undergo when exposed to plasmas. How-

ever, the removal of the methyl group from the linings of the pores is the most devastating effect. The methyl group on these linings give the low-κ material a hydrophobic nature. The removal of this methyl group changes the hydrophobic nature of the low-κ into a hydrophilic one. Water (H_2O) has a low frequency κ-value of 80 [Baklanov *et al.*, 2013]. The adsorption of H_2O into the porous structure of the low-κ increases the κ-value way beyond that of SiO_2, making the material useless as an inter-metal dielectric.

Surface analysis techniques such as SEM[1], TEM[2], SIMS[3] and AFM[4] have been extensively used to analyse and characterise the plasma-induced damage on low-κ materials [Baklanov *et al.*, 2013; Verdonck *et al.*, 2013]. Also, FTIR[5] has been used to study changes in the composition of low-κ materials after plasma exposure [Baklanov *et al.*, 2013; Verdonck *et al.*, 2013]. Simulations have also been used to study the effect of plasma induced damage by radicals and VUV photons [Shoeb *et al.*, 2012]. However, it is still unclear at which stage of plasma exposure the low-κ material undergoes the transformation from hydrophobic to hydrophillic, especially in complicated device integration processes. Most of the surface analysis techniques mentioned earlier are ex-situ and require the samples to be transferred to a separate chamber to be analysed, which adds another difficulty in determining where and when the water adsorption takes place. There is a great need for a real time in-situ monitoring technique.

In this chapter, we present a novel technique, based on the concept of the ion flux probe, to monitor changes in film properties induced by plasma exposure

[1]Scanning Electron Microscope
[2]Transmission Electron Microscopy
[3]Secondary Ion Mass Spectroscopy
[4]Atomic Force Microscopy
[5]Fourier Transform Infra Red Spectroscopy

in-situ in real time. This technique is referred to as the *wafer probe* technique. Using a low-κ film, with known thickness and dielectric constant, we aim to track the evolution of the resistivity and capacitance as a function of plasma exposure time. The permittivity can then be deduced by using a simple parallel plane capacitor model.

There are two major aims for this study. The first aim is to assess the usage of a wafer tile to extract information about the plasma, ion flux and electron temperature, as well as the evolution of the film properties as a function of plasma exposure time. This has the long term aim of using the whole wafer as a probing instrument. The second aim is to attempt to find when water adsorption onto the surface takes place. Water adsorption could take place in the plasma chamber, when the sample is exposed to air, or in both situations.

6.2 Probe design & analytical model

A new probe was designed to address the aims of this research. In this chapter this probe is referred to as the *wafer probe*. It uses the same methodology as that of the ion flux probe, presented in section 2.4.2.2 [p. 53]. The difference between the wafer probe and a conventional ion flux probe is that the wafer probe uses a tile from a multi-layer wafer as the probing surface instead of using a section of an existing boundary material.

6.2.1 Probe design

The design of the probe is relatively simple and the external circuit used for the measurements is the same as that for a standard ion flux probe. The probe tile

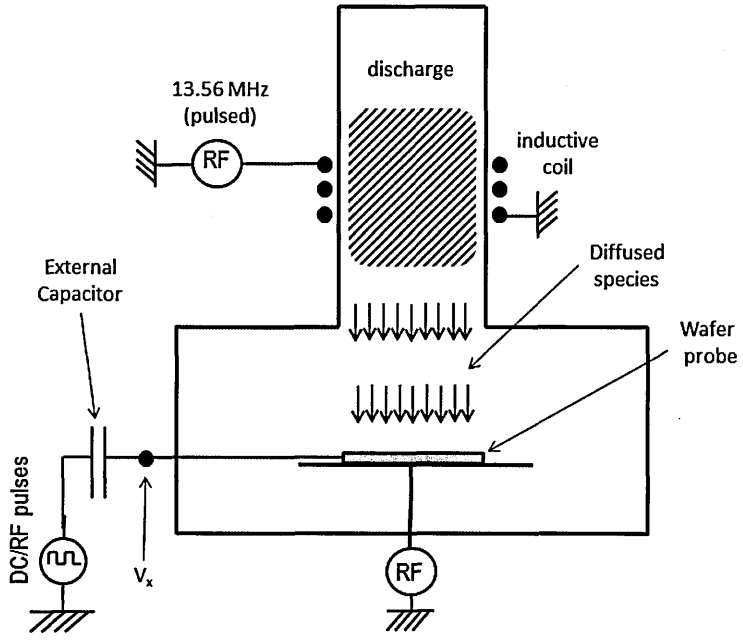

Figure 6.2: A schematic representation showing the position of the wafer probe (in blue) in the PL80 plasma source and the external circuit used for the measurements. V_x indicates where the potential between the plasma-side of the capacitor and ground/bias is measured.

is mounted in a ceramic sample holder and is connected to an external circuit. The external electrical circuit is mainly composed of a voltage source, an external capacitor, and an acquisition card or oscilloscope.

Figure 6.2 shows the position of the wafer probe in the PL80 system and a simplified circuit diagram used in the measurements. The wafer probe is called so not only because it uses a tile of wafer as the probing surface but also because it produces in almost real time in-situ information of the changes in the dielectric properties induced by plasma exposure. In this technique, an external pulsed bias source (RF or DC) is used to charge the external capacitor. A 16-bit acquisition card or an oscilloscope is used to measure the biasing of the capacitor during the

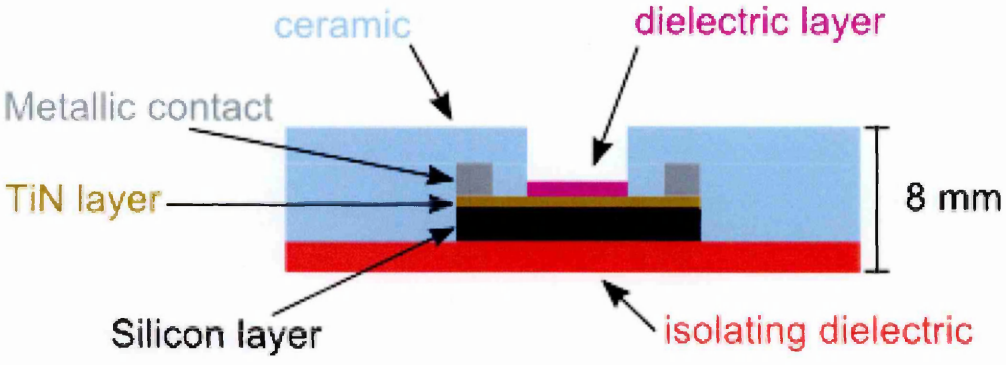

Figure 6.3: A schematic drawing of the cross-section of the wafer probe showing its various components - the sample holder thickness and the multi-layer tile. The vertical scale is not linear so that thinner layers can be more easily seen.

charging and discharging phases, indicated by V_x in figure 6.2. The measurements were performed in the PL80 system where the plasma was generated mostly using the ICP source, and the table supporting the probe was used as a CCP source in other experiments.

Figure 6.3 shows in detail the different parts of the wafer probe that is located in the plasma chamber. It is composed of a ceramic disk which holds the tile. This ceramic disk includes a metallic square frame concealed from the plasma but in contact with a conducting layer in the tile, as can be seen in the figure.

Figure 6.3 shows a cross-section of the wafer probe and shows the ceramic holder (light blue) and the metallic frame (grey) which constitutes the electrical connection between the tile and the external circuit. The tiles are based on a silicon substrate (black), a conducting layer typically made of titanium nitride TiN (gold), the dielectric thin film (magenta) and an external isolating dielectric (red) that centers the wafer tile in the ceramic frame. The isolating dielectric, made from PTFE, is used to isolate the tile from being grounded or biased if the lower electrode was excited externally.

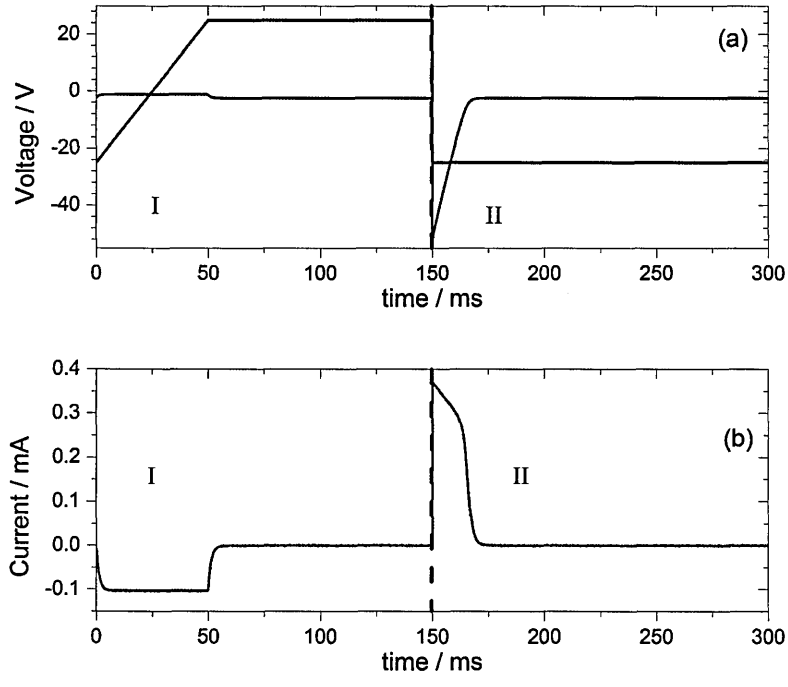

Figure 6.4: The measured voltage (a) and current (b) over one pulse cycle. The black voltage trace in (a) is the applied potential to the probe. (I) and (II) indicate the the charging and discharging phase of the capacitor.

Initial tests were done with a tile of bare aluminium in the ceramic holder. In this configuration the wafer probe functions as a conventional ion flux probe for preliminary tests and measurements. Following this, a multi-layer wafer tile with a titanium nitride (TiN) metallic layer exposed to the plasma was used to perform detailed measurements. Silicon dioxide and two types of low-κ materials were used as the thin film dielectric for these experiments.

During the experiments, data measured from the wafer probe is viewed in the form of current as a function of biasing voltage. However, the data are measured as a function of time. Figure 6.4 shows the measured experimental voltage and current traces as a function of time. Figure 6.4 (a) shows two traces; the applied

potential pulse (black solid line) and measured potential (blue solid line). The red dotted line separates the charging (I) and discharging (II) phases of the capacitor. Figure 6.4 (b) shows the derived experimental current as a function of time. The charging of the capacitor results from the electron flux arriving at the surface of the probe. The discharging occurs mainly due to the positive ion flux. These two phases are described in more detail in section 2.4.2.2 [p. 53].

The experiments were carried out in the Plasma Laboratory at the Open University, while most of the data analysis and ex-situ measurements were carried out with collaborators at IMEC in Belgium. An analytical model was used to analyse the data and extract information about the charged species arriving to the surface of the probe and the changes, if any, of the dielectric properties induced by plasma exposure. This model is presented below.

6.2.2 Analytical model

The analytical model is the same as that used for the typical ion flux probe measurements [Booth *et al.*, 2000; Šamara *et al.*, 2012a]. Figure 6.5 shows the two circuits that are used in the analytical model. The first circuit, figure 6.5 (a), is used when there is no thin film or dielectric covering the metallic layer. The second circuit, figure 6.5 (b), is used when there is a thin film covering the probing surface. The set of equations used in the numerical modelling are:

$$C_b \frac{dV_b}{dt} = I_{probe} + \frac{V_x}{R_x} \tag{6.1}$$

$$C_{film} \frac{dV_{film}}{dt} = I_{probe} + \frac{-V_{film}}{R_{film}} \tag{6.2}$$

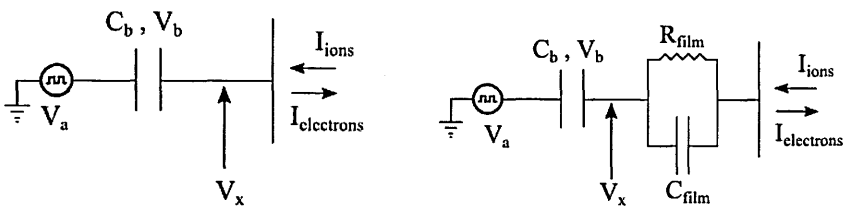

Figure 6.5: (a) is a circuit diagram for a wafer probe without any film covering the surface area, and (b) the circuit diagram in the case of a thin film covering the probing surface. C_b is the external capacitance, V_x the measured voltage, R_{film} and C_{film} the film resistivity and capacitance respectively, and V_a is the applied potential.

$$I_{probe} = I_0[1 - s(V_{probe} - V_f) - \exp(\frac{V_{probe} - V_f}{kT_e})] \tag{6.3}$$

$$V_{probe} = V_a + V_b + V_{film} \tag{6.4}$$

where V_a, V_b and V_x are the applied potential, potential drop across the capacitor and the the measured potential respectively. V_{film}, R_{film} and C_{film} are the potential drop across the film, resistance and capacitance of the film. C_b the external known capacitance and s is a sheath correction factor.

In the system above, V_x is the potential measured by a high impedance voltage probe connected to the acquisition card (represented by an arrow in figure 6.5) and R_x is the total resistance of the voltage probe. The other variables correspond to the elements shown in figure 6.5.

A probe consisting of an aluminium or metalised wafer tile with no thin film (i.e. the metallic layer was exposed directly to the plasma) was used to extract the plasma properties (n_i and T_e) to characterise plasma conditions. These extracted

parameters were then used in the model directly when a sample with a thin film was exposed to the same plasma conditions. This allowed us to minimise the number of fitting parameters used to extract film properties and their evolution, if any, as a function of plasma exposure time. Actually, n_i and T_e can still be obtained even in the case where there is a film covering the probing surface area without previous knowledge of these parameters. However, separately measuring n_i and T_e increases the data processing speed.

6.3 Benchmarking the wafer probe

The ion flux probe is a well established diagnostic technique and is described by a robust analytical model [Booth *et al.*, 1999, 2000; Šamara *et al.*, 2012a]. However, our approach depends on using a multi-layer wafer tile held in a ceramics sample holder as the probing surface, as shown earlier in figure 6.3. The aluminium piece and multi-layer wafer tiles will be referred to as the Al and TiN probes, respectively. The benchmarking of the analytical model and comparison of these two different probe materials are presented in the following sections.

6.3.1 Analytical model vs. measurements

The model benchmarking can be divided into two parts. The first is the simple ion flux probe without any films, figure 6.5 (a), and the second includes a dummy load with parallel R and C mimicking the existence of a film, figure 6.5 (b). Al and TiN probes were subjected to an argon plasma to perform these measurements. The measurements presented in this section were obtained for a 50 mTorr argon plasma operated at $P = 330$ W with 20 sccm gas flow.

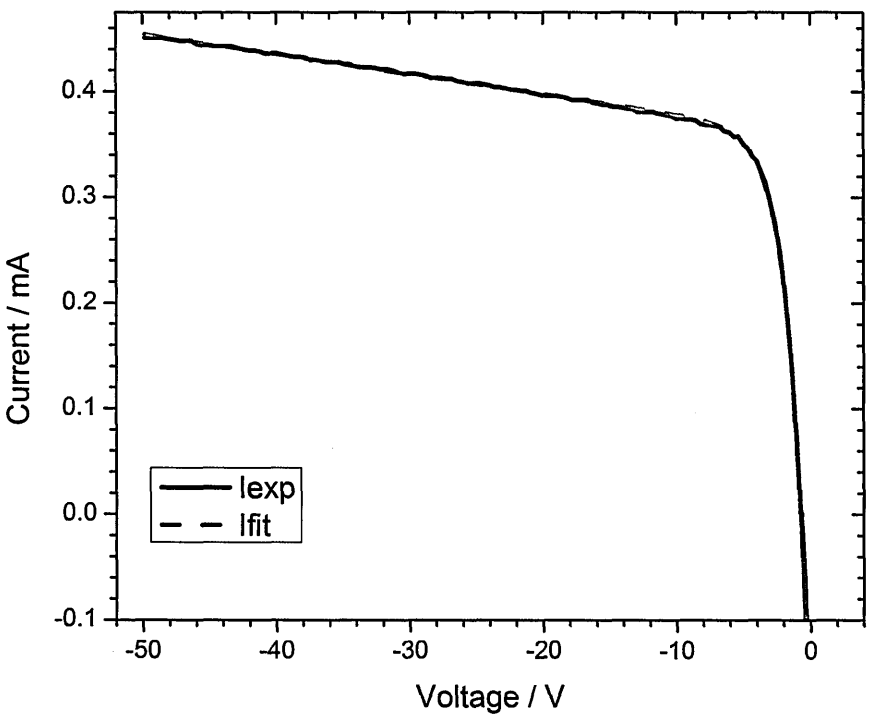

Figure 6.6: This figure shows a typical measured (solid black) *I-V* characteristic of an Al probe and the fitted curve (dashed red) from the model.

Figure 6.6 shows the measured and fitted *I-V* curves obtained from an Al probe. The black solid line shows the measured *I-V* curve and the red dashed line shows the fitted curve. The simple analytical circuit presented in figure 6.5 (a) was used to perform this fitting. It can be seen that a very good agreement between measured and fitted curves is achieved for the case of the Al probe. The plasma properties extracted from this example are as follows: $T_e = 1.4$ eV, $n_i = 4.8 \times 10^{12}$ cm^{-3} and ion flux $\Phi = 8.8 \times 10^{17}$ cm^{-2}s^{-1}. The ion density and flux measurements will be presented in units of cm^3 instead of m^3 in this chapter for convenience.

The same arrangement was used to measure various plasma parameters for

different operating conditions. The measured ion flux and electron temperature were compared with those obtained using an independent ion flux probe that was inserted horizontally, perpendicular to the azimuthal axis of the plasma and parallel to the wafer probe surface. The independent ion flux probe was about 3 cm away from the azimuthal axis and 2 cm above the wafer probe's surface. Measurements obtained using the Al probe were found to be in good agreement with the independent ion flux probe measurements.

The second test is to mimic a thin film on the probe surface by connecting a dummy load in series with the probe. The dummy load consists of a parallel R and C with known values. Convenient values of R and C have to be chosen, as the purpose of these numerical modelling and measurements is to characterise film properties. Calculating the theoretical R and C values of a thin film, low-κ or SiO_2 dielectric, of known thickness and permittivity is relatively simple. The following parallel plate model equations:

$$C = \frac{\epsilon A}{d} \tag{6.5}$$

and

$$R = \frac{\rho d}{A} \tag{6.6}$$

can be used to calculate the expected values for a thin film, where A and d are the area and depth (thickness) of the sample and ϵ and ρ are the permittivity and resistivity of the dielectric. For example, for the case of a 200 nm thick SiO_2, $\epsilon_r = 4.2$ and $\rho = 10^{12}$ Ωm, layer with $A = 2.56$ cm^2, the calculated capacitance value was $C \sim 47$ nF and resistance $R \sim 780$ kΩ.

A series of measurements with $47 \leq C \leq 470$ nF and $R = 220$ kΩ and different

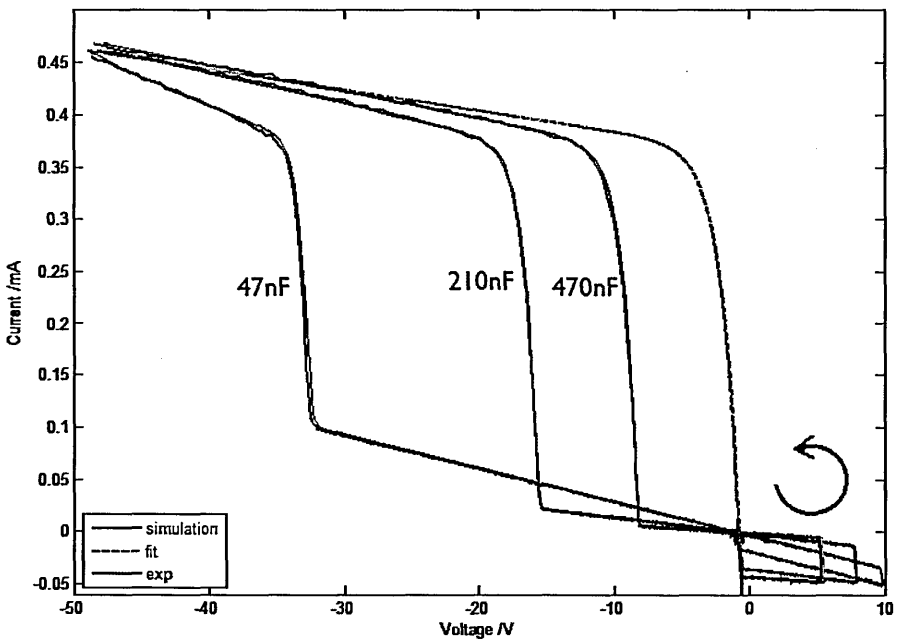

Figure 6.7: shows several I-V curves of a TiN probe with different capacitors exposed to the same plasma conditions. Dummy loads (R & C) were connected in parallel to mimic a thin film. The blue and red solid lines are the measured and modelled I-V characteristics respectively. The fit curve (dashed pink) is the measured I-V characteristic without any dummy loads and was used to extract the plasma properties.

plasma conditions were conducted. The capacitance has a far greater effect on the I-V characteristics than the resistance. Therefore, one resistor with different capacitors was used for these measurements.

Figure 6.7 shows I-V curves for three different capacitors and the same resistor measured under the same plasma conditions. The pink dotted line is the I-V measured curve for these plasma conditions without any resistors or capacitors connected to it. The plasma properties extracted from this measurement were used as the input for the fitting process for the other cases that included R and C. The blue and red lines in the graph are the measured and fitted I-

V curves respectively. It can be seen that very good agreement between the measurements and the modelling is achieved. The loop at $-2 \leq V \leq 10$, on the far right of the graph, depends on the RC values of the film and the electron temperature. The orientation of this hysteresis loop is anticlockwise. The smaller the capacitance the narrower and smaller the loop is. The value of the resistor affects the dimensions of the loop only, while the capacitance affects the loop as well as the region before the floating potential when electrons start to arrive to the surface of the probe.

Excellent agreement between the model and measured data was achieved for both cases, a metallic probe (Al or TiN) and a 'fake film' covering the probe. This indicates that the method developed here for the analysing the probe data is valid, and gives confidence that this approach can be used for other probe materials.

6.3.2 Al Vs TiN probe measurements

An argon discharge was operated at $20 \leq p \leq 100$ mtorr and $50 \leq P \leq 300$ W with 20 sccm total gas flow. The Al probe was used to measure several I-V curves for different plasma conditions and the analytical model was used to extract the plasma parameters. Figure 6.8 shows the measured ion density and electron temperature for a range of argon plasmas. These measured values are consistent with density measured using a planar Langmuir probe for similar conditions, presented in figure 4.14 (c) [p. 134]. The ion density is calculated from the collected ion flux when the ion mass is known, and hence the Bohm speed can be calculated.

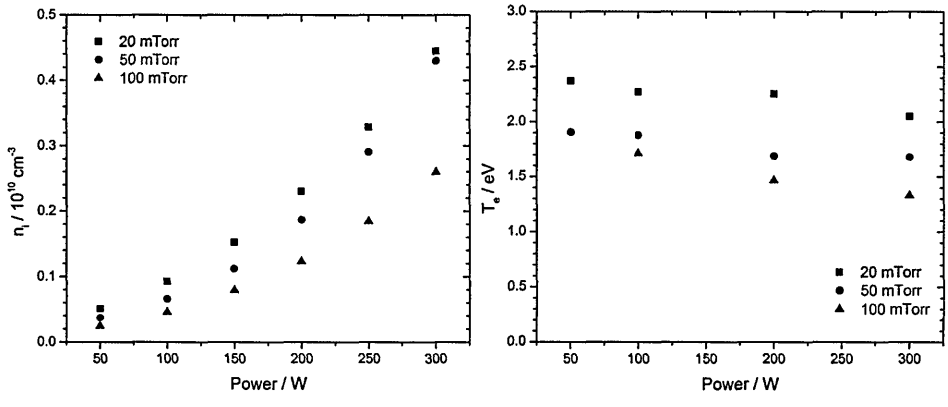

(a) (b)

Figure 6.8: (a) ion density and (b) electron temperature measurements for 20, 50 and 100 mTorr argon plasmas for $50 \leq P \leq 300$ W, using an Al probe. The ion density is presented in cm^{-3} for convenience.

Figure 6.8 (a) shows the ion density increasing as a function of the input power. The electron temperature, figure 6.8 (b), exhibits a weak dependence on the input power, as expected, and is higher for lower pressures, as was estimated from the OES measurements presented in figure 4.6 [p 115].

The ion densities obtained from the Al and TiN probe measurements were compared for discharges maintained at 50 and 100 mTorr with $50 \leq P \leq 300$ W, since the ion density is relatively similar for 20 and 50 mTorr cases (figure 6.8).

Figure 6.9 shows a comparison of the ion density measured for 50 and 100 mTorr argon plasmas using two different probe surfaces. The data shows little difference between the densities measured using these two probes. The ion density measured by both probes seems to be close for $P \leq 250$ W. The ion density measured by the TiN probe is slightly larger than that measured by the Al probe for $P = 300$ W. These relatively small differences could be due to slightly different plasma conditions, or the materials constituting the probe surface. Slightly different plasma

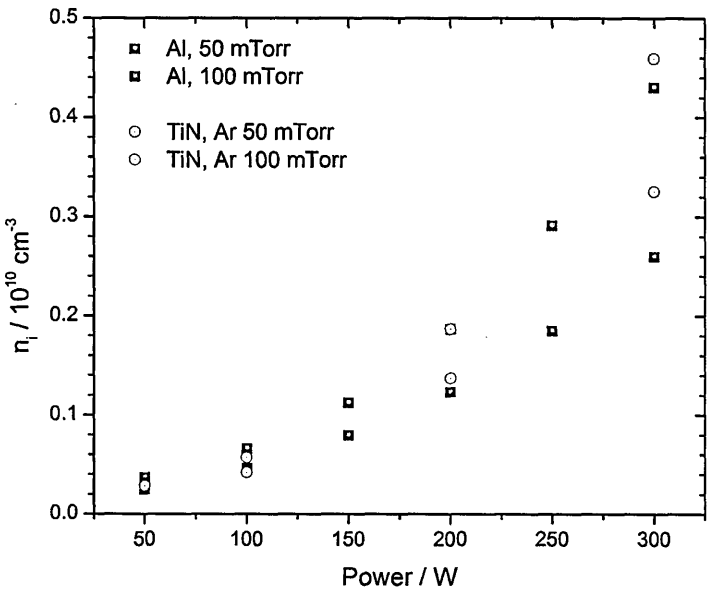

Figure 6.9: Comparison of the ion density measured by the Al (closed squares) and TiN (open circles) probes for a 50 and 100 mTorr Ar plasmas with $50 \leq P \leq 300$ W.

conditions could occur if the PL80 was not evacuated to the same base pressure before conducting these measurements. Also, the measured *I-V* characteristic curves from the TiN probes showed an excellent fit to the extracted *I-V* curves from the model, similar to figure 6.6.

Some processes in ULSI circuit manufacturing require high energy ions which can be achieved by a capacitively coupled electrode operated in contact with the plasma. The lower electrode, or table, in the PL80 can be used as an RF electrode. However, the wafer probe resides on this table. Some experiments were conducted to verify if the probe works when the table beneath it is biased by an RF input power.

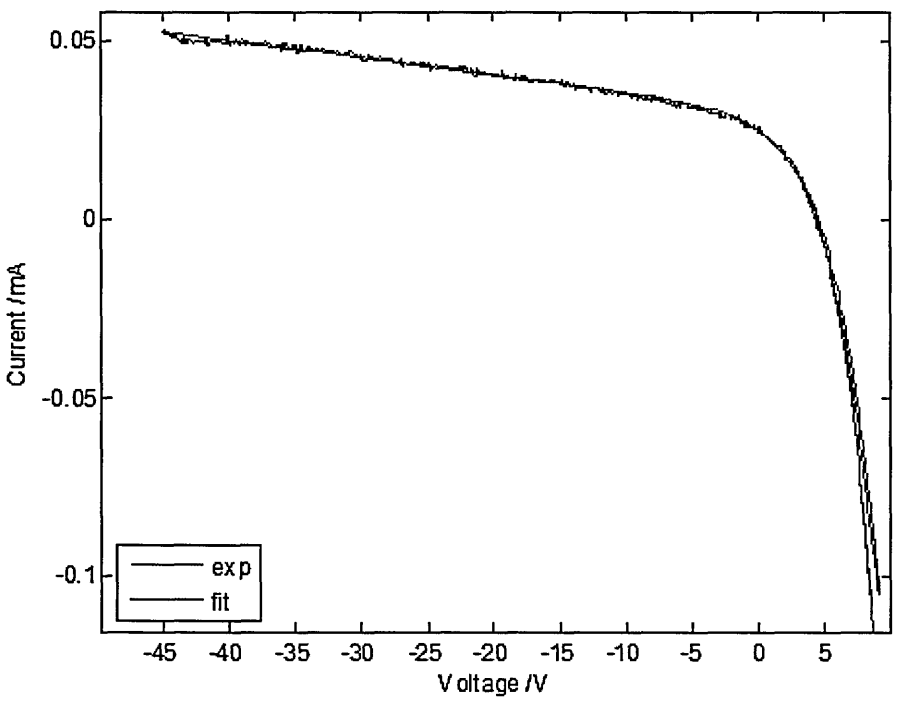

Figure 6.10: Measured and fitted *I-V* curves from a TiN wafer probe when the system was run in CCP mode, i.e. the table was biased, of a 50 mTorr Ar plasma $P_{CCP} = 100$ W.

For this study, an argon discharge was operated at 50 mTorr with an input power of 100 W in capacitively coupled mode. In this case the table was the only source of RF input. Figure 6.10 shows the measured (blue) and fitted (green) *I-V* traces for this discharge. The theocratical curve fits the experimental data excellently. The plasma properties extracted from this measurement are $T_e = 2.63$ eV, $\Phi = 7 \times 10^{16}$ cm^{-3}s^{-1} and $n_i = 2.77 \times 10^{11}$ cm^{-3}.

Other experiments with 50 mTorr argon plasma operated only in CCP mode for $40 \leq P \leq 300$ W were conducted, and similarly clear data was extracted from the wafer probe. The wafer probe was also used to extract plasma properties

when the discharge was operated in both ICP and CCP modes, i.e. RF power was fed independently to both the coil and table. However, the measured data had some periodic oscillation in the voltage which required some filtering or digital smoothing. The oscillations in the measured voltage could be attributed to different RF phases between the CCP and ICP, which on this occasion could not be synchronised or phase locked. Nevertheless, plasma parameters were successfully extracted from these measurements.

In summary, measurements with Al and TiN probes gave good fits and comparable data. The wafer probe detected a small hysteresis loop at the beginning of the Al probe measurement that vanished after few seconds of plasma exposure. This hysteresis loop is caused by the existence of a native Al_2O_3 layer on the Al tile. This highlights the power of the method, since native Al_2O_3 is quite thin, a few nanometers at maximum. The analytical model was found to fit the measured data of the clean probes, i.e. no film, and in the case of a fake film, i.e. external parallel R and C. The wafer probe could function properly even when the table beneath it was operating as the electrode for a CCP source.

This series of measurements shows that the wafer probe could be used for accurate and reliable measurements. Hence, this gives confidence that tiles covered with different dielectric materials could be used in order to assess plasma induced damage to the film materials.

6.4 Wafer probe results with dielectric films

The study was carried out on Ar, H_2 and O_2 plasmas operated at 50 mTorr. Hydrogen plasmas with pressures lower than 50 mTorr could not be sustained,

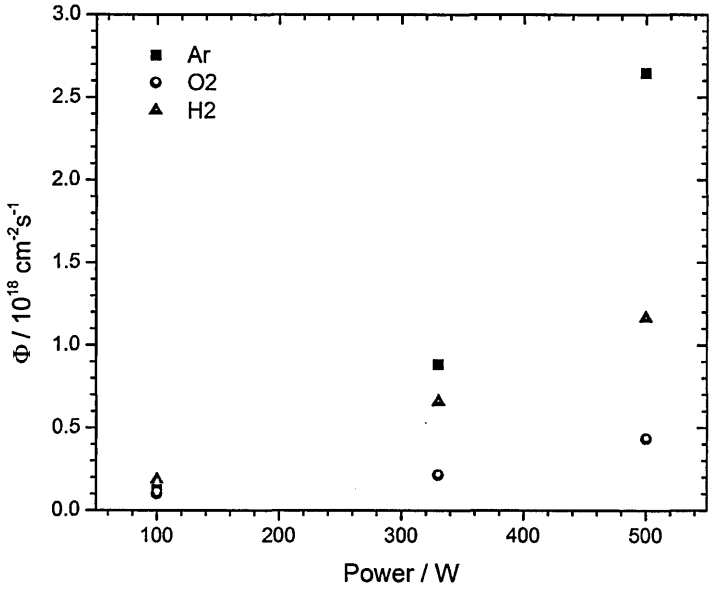

Figure 6.11: Ion flux measurements using a TiN probe for 50 mTorr Ar, H_2 and O_2 plasmas for $100 \leq P \leq 500$ W.

due insufficient pumping capability, and higher pressures produced lower plasma densities in the diffused plasma region where the wafer probe resides.

One of the aims of this research is to assess plasma-induced damage on thin film properties. Therefore, similar ion flux from different plasmas is necessary to compare the effect of different plasma chemistries on thin film properties. A TiN probe was used to measure the ion fluxes of Ar, H_2 and O_2 plasmas operated at 50 mTorr for different input powers.

Figure 6.11 shows the measured ion flux for different discharges operated at 50 mTorr. The lowest ion flux was measured for the oxygen plasma, even for higher powers, compared with argon or hydrogen plasmas. Similar ion fluxes

Table 6.1: Plasma parameters measured by a TiN probe for different discharges and operational conditions.

Plasma properties for $p = 50$ mTorr.			
Gas	P / W	Φ / $10^{17}\text{cm}^{-2}\text{s}^{-1}$	T_e / eV
Ar	100	1.25	1.80
	330	8.82	1.38
	500	26.5	1.11
H_2	100	1.85	4.43
	330	6.60	3.20
	500	11.67	3.23
O_2	100	1.0	2.32
	330	2.13	1.77
	500	4.33	1.75

from argon and hydrogen were obtained for an input power of 330 W.

A summary of the plasma parameters measured for different discharges is given in table 6.1. The standard operating conditions were set to be $p = 50$ mTorr and $P = 330$ W for hydrogen, oxygen and argon discharges for all the results presented in the following section, unless stated otherwise.

Low-κ materials are very sensitive to plasmas and have a complex structure, as mentioned in section 6.1. Therefore, initial wafer probe measurements were carried out on samples with different film thicknesses of SiO_2. These experiments aimed to test the analytical model when a real film is covering the wafer probe, using a relatively simple dielectric with well known properties that are resilient to certain plasma chemistry. The results and measurements of these experiments are presented in the following section.

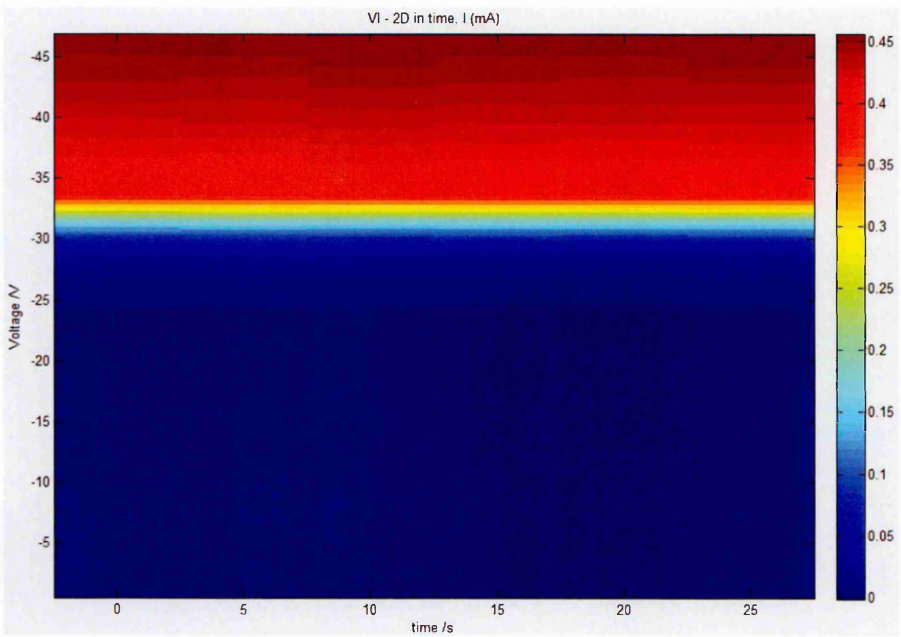

Figure 6.12: 2D colour map for the measured I-V characteristic of a 100 nm SiO_2 coated tile exposed to an argon plasma operated with the standard conditions. The x-axis is the time axis (in seconds), y-axis is the voltage (in volts) and the measured current is represented by the colour scale (in mA).

6.4.1 Silicon dioxide dielectrics

Different tiles coated with silicon dioxide having 100, 200 and 400 nm film thicknesses were exposed to various plasma conditions to test the analytical model when a real film covered the probe surface. These tiles were exposed to Ar, H_2, O_2 and even SF_6 plasmas whilst the I-V characteristics were being recorded.

Silicon dioxide should not be etched, nor its properties changed as function of exposure time to these plasma chemistries. Figure 6.12 shows a 2D colour map for I-V curves measured as a function of plasma exposure time. These measurements were recorded in real time. If any changes in the plasma condition or film properties were to happen, they would have been seen on this 2D map. Different

SiO_2 coated tiles were exposed for longer times (up to 10 minutes) to different plasma chemistries without any changes in the film properties or occurrence of plasma instabilities. *I-V* 2D maps were recorded for these different chemistries and conditions, and the output was similar to that presented in figure 6.12. The importance of these measurements is that they verify the stability of the discharge and the reproducibility of these measurements.

In the next stage of this experiment, SiO_2 coated tiles with different film thicknesses were exposed to an argon plasma. Figure 6.13 shows the measured (black squares) and fitted (red disks) *I-V* curves from an argon plasma for SiO_2 coated tiles with (a) 100, (b) 200 and (c) 400 nm film thicknesses. The fitted and measured *I-V* curves are distinctly different from each other in certain areas. The largest differences between the measured and fitted *I-V* curves are for the 100 nm SiO_2 coated tile, figure 6.13 (a). The differences between the measured and fitted curves decrease as the thickness of the SiO_2 films increases.

The plasma properties, n_i and T_e, measured by a TiN probe were used to fit these curves whilst varying the R and C values to match the hysteresis loop. The *I-V* curves presented in figure 6.13 have the best R and C values that are close to the ones calculated from equation (6.6) and (6.5).

The *I-V* curves have two main regions, as shown in figure 6.4. These two regions are due to the charging and discharging of the capacitors. The charging of the capacitors is the outcome of the electron flux arriving to the surface of the tile, while the discharging phase is due to the ion flux impinging on the probe's surface. However, a third intermediate region could be introduced in the *I-V* curves. This third region is the intermediate region where the surface potential tends to the floating position. These three regions can be clearly seen

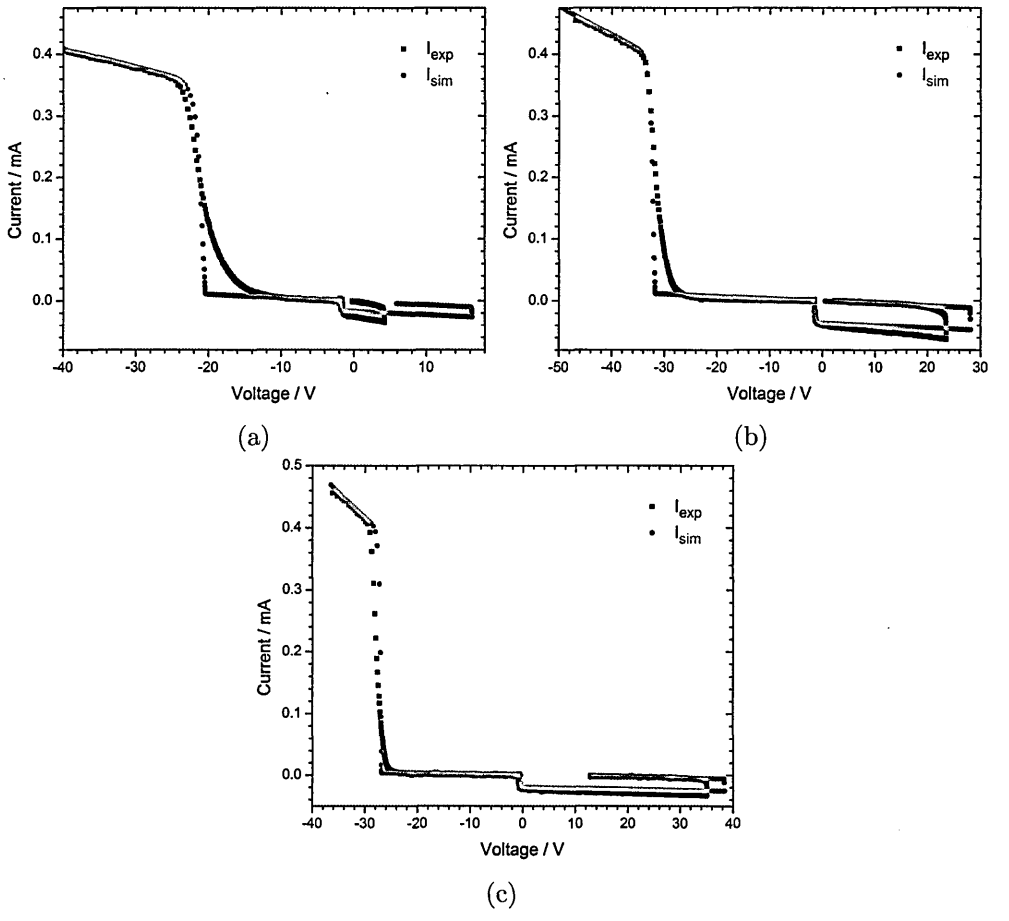

Figure 6.13: *I-V* curves from the wafer probe measurements (black squares) and fitted data (red disks) from the simulation for SiO_2 thin films with (a) 100, (b) 200 and (c) 400 nm thicknesses.

on the *I-V* curves in figure 6.13.

In figure 6.13 (a) these three regions can be discerned as the first region $-40 \leq V \leq -22$, the second region $-10 \leq V \leq 16$ and the third intermediate region for $-22 \leq V \leq -10$. The first region depends on the ion flux, i.e. the linear part $-40 \leq V \leq -28$, while the knee-like feature, $-26 \leq V \leq -22$, depends on both the electron temperature and ion flux. The second region, the

Table 6.2: RC values for different SiO_2 film thicknesses.

Method	Thickness / nm	R / kΩ	C / nF
Modelled	100	1000	90
	200	2000	55
	400	10000	25
Calculated	100	390.6	95.2
	200	781.2	47.6
	400	1562.5	23.8

hysteresis loop $-10 \leq V \leq 16$, strongly depends on the RC characteristics of the thin film and electron temperature. This region is a result of the electron flux collected during the charging phase. The third transient region, $-22 \leq V \leq -10$, depends on the electron temperature and capacitance of the thin film. The third region is referred to as a transient stage because the electron flux starts to increase compared with the ion flux in this region, before the two fluxes equilibrate.

Figures 6.13 (b) and (c) also have these clear three regions. However, as mentioned earlier, the model curves tend to become more comparable with the measured data as the thickness of the films increases. There are still some differences between the measured and fitted curves, but they are by far in better agreement with each other compared with the 100 nm case. However, the fitted curves follow a similar general trend as that measured by the wafer probe for all film thicknesses.

Table 6.2 lists the RC values extracted from the analytical model for the I-V curves presented in figure 6.13 and the values calculated using equations (6.5) and (6.6).

So far the plasma properties, n_i and T_e, were used to fit the data from the model in figure 6.13. This technique could be referred to as an ion flux fitting

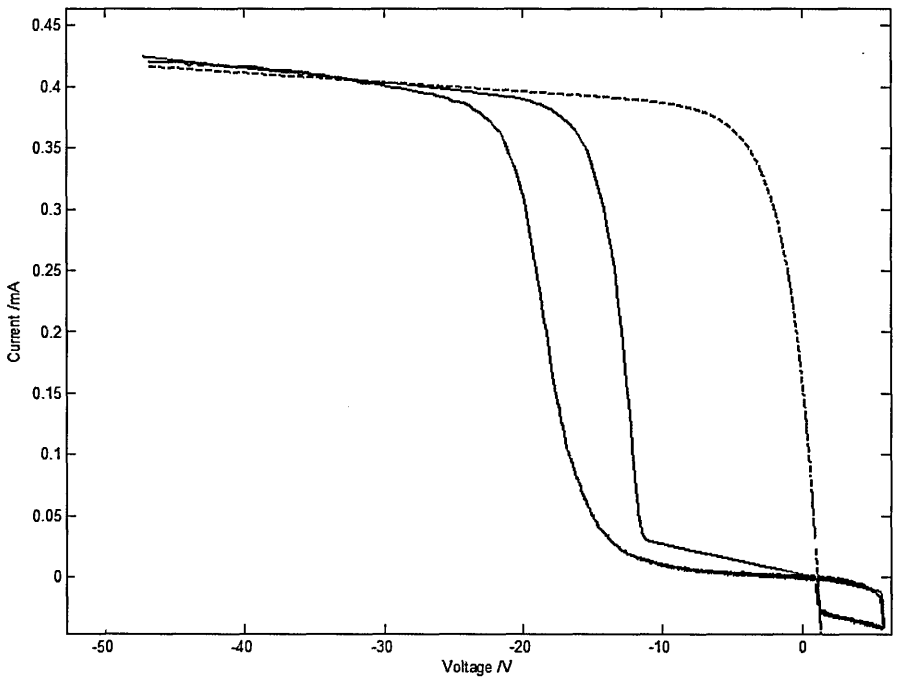

Figure 6.14: This is the same measured data presented in figure 6.13 (a), but the electron flux fitting was used instead of the ion flux fitting technique. This figure shows the experimental data (blue curve), modelled output (red curve) and the data from a TiN probe (dashed pink curve).

approach. As can be seen from these graphs, there is a clear mismatch between the measured and fitted curves, especially for thin SiO_2 films. However, another fitting technique could be used where the electron flux sensitive region could be fitted. This could be achieved by matching the hysteresis loops of the measured and fitted data. However, this technique increases the fitting parameters and decreases the integrity of the output. The electron flux fitting technique was implemented for the measured data presented in figure 6.13 (a) in order to assess if it would result in a better fit.

Figure 6.14 shows *I-V* curves for a 100 nm SiO_2 coated tile exposed to an

argon plasma. The solid blue line is the measured data, the red solid line is the output of the simulation and the dashed pink line is the I-V of a TiN probe exposed to the same plasma conditions. A very good agreement between the model and the measured data is realised on the hysteresis loop, $0 \leq V \leq 10$ as this was the purpose of electron flux fit, while these curves greatly diverge from each other for $-35 \leq V \leq 0$. The differences between these two curves are clear and larger than those reported in figure 6.13 (a). $R = 120$ kΩ and $C = 250$ nF are the RC values extracted from the simulation to produce this hysteresis loop fitting. The resistivity is three times less than the calculated value and one order of magnitude less than that extracted from the ion flux fitting method. However as mentioned previously, the resistivity has a smaller effect on the I-V curves, compared to that of the capacitance, and its effect is localised to the hysteresis loop. The capacitance, on the other hand, has an effect on the transient region in the I-V curves as well as the hysteresis loop. The extracted C value from the electron flux fitting process is about 2.78 times larger than that extracted from the ion flux fitting technique and calculated values (table 6.2). Hence, it seems that the electron flux fitting is not appropriate. This could probably be related to the perturbation of the plasma caused by the collection of the electron flux during this phase.

The wafer probe measurements and the I-V curves extracted from the analytical model qualitatively agree and are comparable. Quantitative measurements of R and C values of SiO_2 dielectrics could be achieved for relatively thick films > 200 nm.

Differences between fitted and measured I-V curves were obvious, especially with the relatively thin 100 nm films. These differences could be attributed to

several factors. For instance, plasma-surface interactions or photoconductivity[1] may cause breakdown in thin films. The plasma-surface interactions could be due to an effect of electrons charging the SiO_2 surface or certain non-linear behavior of the sheath during the transient region. Thin SiO_2 films could become conductive and their resistivity decrease dramatically if they undergo a breakdown due to a photoconductivity phenomena. The breakdown of dielectrics is easier for thinner films. These phenomena are not included in the analytical model.

A better model, which takes into account some of these phenomena, should be devised after assessing the most probable cause of the deviation between the fitted and measured data. Several different experiments could be devised to explore the possible phenomena causing these differences. However, even with these difference it is still possible to use the wafer probe to qualitatively monitor changes in film properties in-situ in real time. Low-κ films are highly sensitive to plasmas; the wafer probe is used to qualitatively monitor the changes in low-κ thin films as they are exposed to different plasmas.

6.4.2 Low-κ dielectrics

Tiles coated with a well-characterised dielectric, SiO_2, were used in the previous section to assess the wafer probe. Interestingly, differences between the well-established analytical model and measured data were detected for several film thicknesses. This analytical model has been used for plasma measurements in depositing/etching environments and reported to extract film properties [Booth *et al.*, 2000; Šamara *et al.*, 2012a]. These differences at the moment limit the

[1]Photoconductivity is an optical and electrical phenomenon in which a material becomes more electrically conductive due to the absorption of electromagnetic radiation which raises electrons across the band gap.

usage of the analytical model to only extract plasma properties and qualitative changes in thin film properties.

Tiles coated with low-κ dielectrics of thickness 50, 100 and 150 nm were exposed to argon and hydrogen plasmas. Two types of low-κ dielectrics, referred to as HiE and LK with κ-values of 2.5 and 3 respectively, were used in this research. The HiE dielectric is more porous and less dense than the LK. The LK dielectric is used as a protecting layer ($\sim$ 20 nm) for the HiE in some cases [Verdonck *et al.*, 2013].

There hve been vastly contradicting reports of the effect of hydrogen plasma on low-κ dielectrics. Some authors reported no effect on low-κ films, others showed hydrogen plasma processing enhances low-κ film properties and others have reported severe film damage [Baklanov *et al.*, 2013]. Oxygen based plasmas on the other hand cause undesirable chemical modification to low-κ dielectrics, such as the removal of the methyl group, figure 6.1. Therefore, in this study low-κ coated tiles are treated with argon and hydrogen plasmas.

Firstly, a TiN probe was used to measure plasma parameters and monitor any changes in the hydrogen plasma. Other plasmas were already known to be highly stable and reproducible, as indicated by figure 6.12. A similar measurement was carried out for a 50 mTorr hydrogen plasma operated at 330 W. The *I-V* curves were recorded as a function of time to monitor plasma behavior. Figure 6.15 shows a 2D colour map of the measured *I-V* as a function of plasma exposure time. The vertical axis is the voltage axis (V), the horizontal is the time axis (s) and the measured current is presented by a colour scale (mA).

The primary goal of this research is to monitor plasma-induced damage on low-κ dielectrics. Another aim is to assess, if possible, at what stage does the

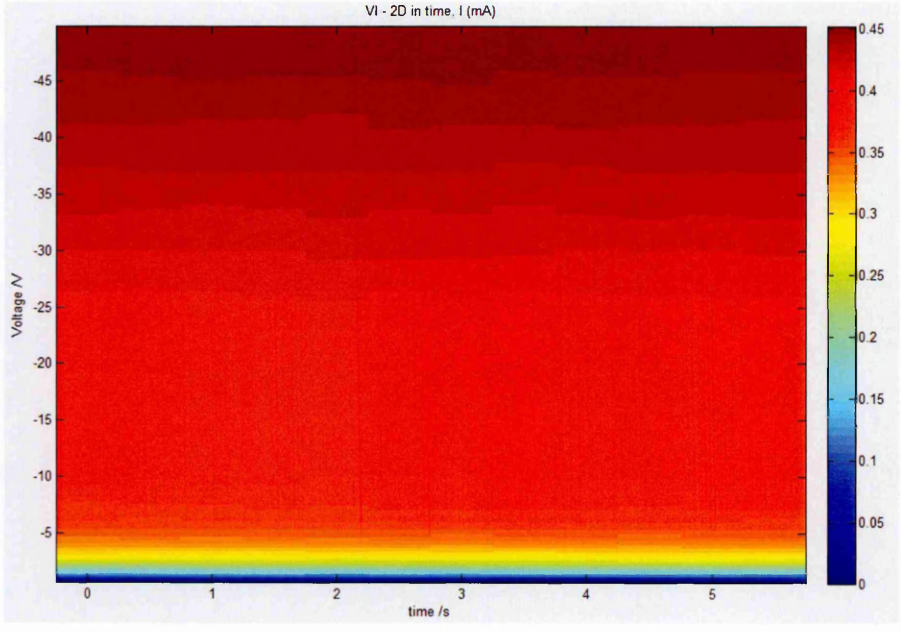

Figure 6.15: 2D colour map of I-V as a function of time for a 50 mTorr 330 W hydrogen plasma. The x-axis is the time access, the y-axis is the voltage axis, and the measured current is represented by the colour scale (in mA).

adsorption of water on low-κ films take place. Therefore, in the following section the effect of argon and hydrogen plasma on low-κ dielectrics will be examined.

6.4.2.1 Low-κ exposed to Ar and H_2 plasmas

Low-κ coated tiles were exposed to argon and hydrogen plasmas, and the evolution of the I-V characteristics as a function of plasma exposure time was recorded.

A tile coated with 100 nm of LK low-κ dielectric was exposed to a 50 mTorr argon plasma operated at 200 W. An identical tile was exposed to a 50 mTorr hydrogen plasma operated at 330 W. The I-V curves for each case were measured after two seconds of plasma exposure time. Figure 6.16 shows the measured I-V curves from a 100 nm low-κ coated tiles exposed to hydrogen (in red) and argon

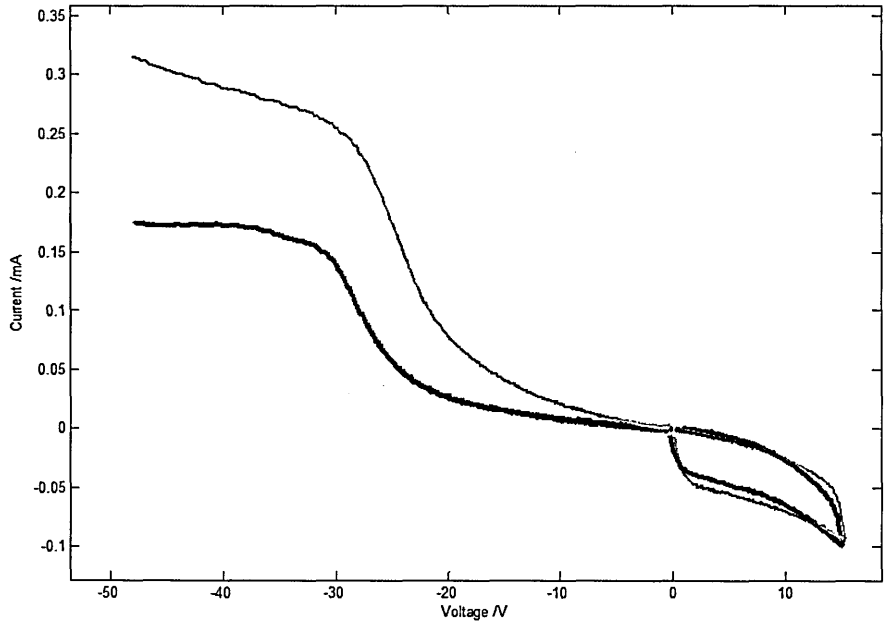

Figure 6.16: *I-V* characteristic measured from a tile coated with 100 nm LK dielectric after two seconds of exposure time to 200 W Ar (blue curve) and 330 W H_2 plasma (red curve), both discharges maintained at $p = 50$ mTorr.

(in blue) plasmas. The hysteresis loops are similar in both cases. These loops depend mostly on the *RC* properties of the thin films. However, the similarity also suggests that almost no changes occurred in the film properties after two seconds of exposure to hydrogen or argon plasmas.

These two tiles were exposed to these plasmas for ten minutes while the *I-V* characteristics were being recorded continuously. Figure 6.17 shows the initial *I-V* curve (in blue) measured after two seconds of Ar plasma exposure and the final measured *I-V* curve (in green) at the end of the experiments, after ten minutes of Ar plasma exposure. There are clear differences between the overall profiles of these two curves. The small change in the hysteresis loop suggests that the *RC* properties of the low-κ film did not significantly change due to ten

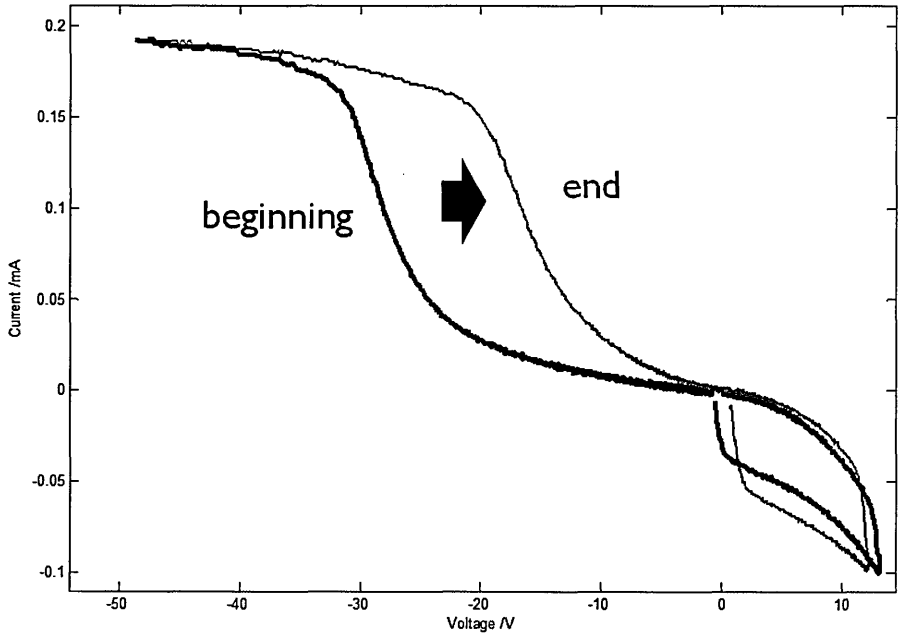

Figure 6.17: Evolution of *I-V* characteristic measured by a tile coated with 100 nm of low-κ dielectric exposed to Ar plasma for two seconds (blue curve) and after ten minutes (green curve).

minutes of argon plasma exposure. However, the hysteresis loop seems to attain a form similar to that of a SiO_2 dielectric, figure 6.13. One possible explanation could be related to the formation of a thin protective layer, with exposure to ion bombardment leading to the densification of a top thin layer of the low-κ dielectric [Baklanov *et al.*, 2013; Verdonck *et al.*, 2011]. Relatively small changes occur to the *RC* properties of the low-κ dielectric as this protective layer forms, which in turn prohibit any further changes in the film properties.

Figure 6.18, on the other hand, shows the *I-V* curves measured after two seconds (blue curve) and ten minutes (green curve) of exposure to a hydrogen plasma. In this case, there are clear changes in the hysteresis loop between the beginning and end of hydrogen plasma exposure. The changes in the hysteresis

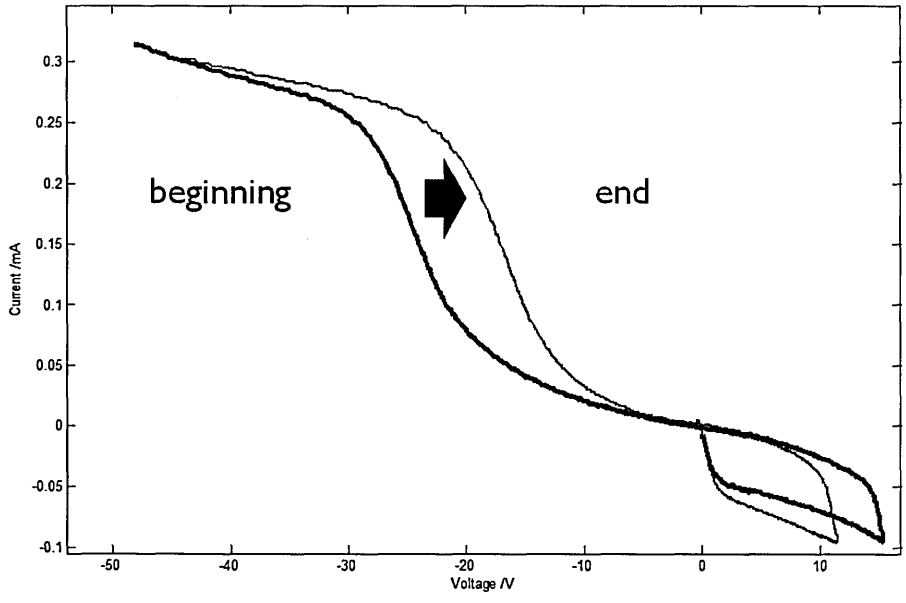

Figure 6.18: Evolution of I-V characteristic measured by a tile coated with 100 nm of low-κ dielectric exposed to hydrogen plasma for two seconds (blue curve) and after ten minutes (green curve).

loop are more evident than that of the film exposed to argon plasma. This change suggests that the RC properties of the low-κ dielectric have been modified. These changes could be induced by hydrogen replacing the methyl groups in the honeycombed structure, forming Si−H bonds or breakage of Si−O−Si into Si−H and Si−OH, forming hydrophilic groups [Baklanov *et al.*, 2013].

Figure 6.18 shows two I-V curves measured at the beginning and end of the experiment, where a low-κ coated tile was exposed to hydrogen plasma. Figure 6.19 shows the temporal evolution of the I-V curves for two minutes, acquired using a fast acquisition card. The changes in the measured current are due to the changes in the RC properties of the low-κ film. The plasma properties are stable during these measurements, as shown in figure 6.12. The low-κ properties are clearly

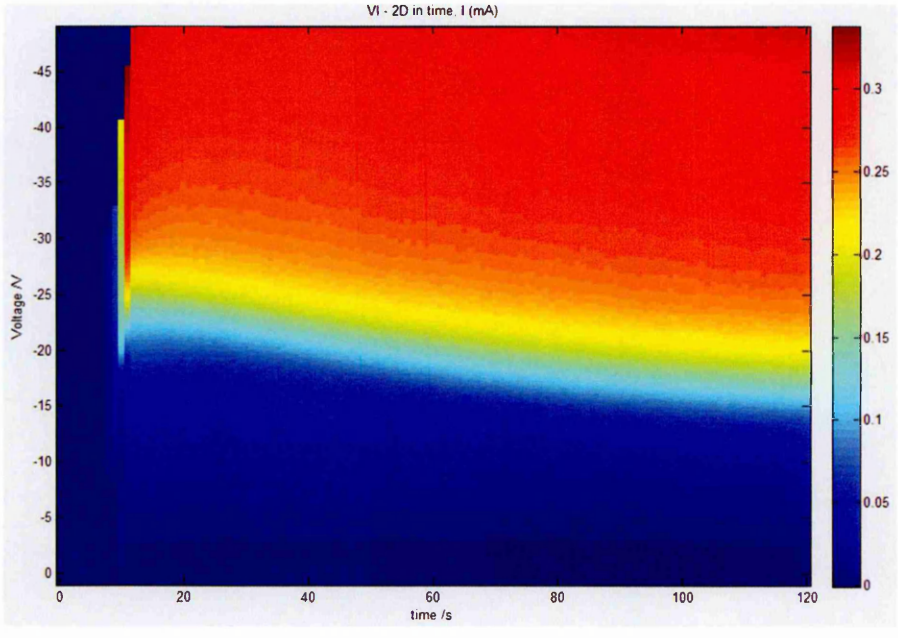

Figure 6.19: 2D map of I-V evolution of low-κ exposed to H_2 plasma for two minutes. The measured current is represented by the colour scale.

changing as the film is exposed to the hydrogen plasma, which is clear from the changes in the colour gradient of the I-V curves. The data acquisition starts before the plasma was ignited, and the ignition of the plasma is evident for $t < 10$ s in figure 6.19. Changes in film properties can be qualitatively recorded in this way. However, further experiments in-situ and ex-situ are required to determine the nature of the actual changes.

Tiles with different low-κ types and thicknesses were exposed to similar plasma conditions. These samples exhibited the same behavior when exposed to argon and hydrogen plasmas. Measured I-V characteristics were compared to the output of the analytical model when the ion flux fitting method was used. The measured and fitted curves deviated from each other, similar to the SiO_2 cases

presented previously in figure 6.13. The measured and fitted curves tend to a similar profile as the thickness of the low-κ material increased (up to 150 nm). The low-κ material has a more complex structure and plasma-surface interaction than the SiO_2, therefore, the analytical model was not used to extract RC values for the low-κ films at this stage of the research.

Next, different plasma chemistries and experimental procedures were performed to qualitatively measure the changes in low-κ properties when exposed to air after plasma treatment. Also, the low-κ coated tiles were exposed to fluorine rich plasmas while I-V characteristic data was being measured. The results of these experiment are presented in the following section.

6.4.2.2 Low-κ qualitative measurements

Water adsorbed in the pores of low-κ dielectrics is one of the main challenges that limit the wide use of these materials at the moment in ULSI circuits. One of the aims of this research is to determine when the water adsorption takes place. Low-κ dielectrics are hydrophobic by nature; however, this nature changes when exposed to copper reducing plasmas, such as those using hydrogen.

In order to assess the water adsorption effect, low-κ coated tiles were treated with hydrogen plasmas for intervals of ten minutes, after which they were exposed to the lab atmosphere for ten minutes. The samples were then plasma treated for another ten minutes. This procedure was carried out for various plasma conditions and low-κ thicknesses. Measurements for standard plasma operating conditions are reported in this section, where $p = 50$ mTorr and $P = 330$ W.

Figure 6.20 shows the measured I-V characteristics for a 100 nm thick low-κ coated tile. The dark and light blue I-V curves were measured at the beginning

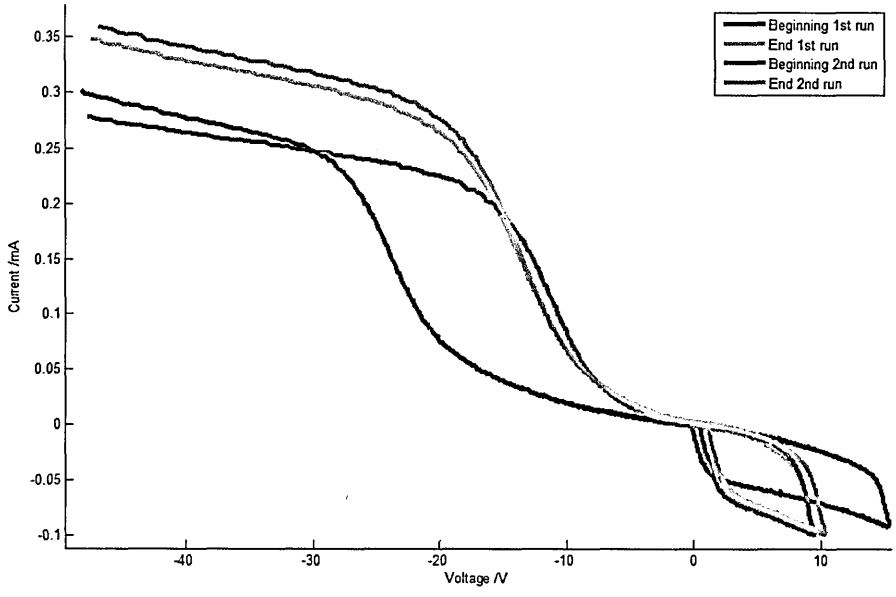

Figure 6.20: I-V curves from a low-κ dielectric coated tile exposed to hydrogen plasma for an interval of ten minutes. The dark blue I-V curve is measured at the beginning of the experiment and the light blue I-V curve is measured at the end of the first ten minute treatment. The sample is treated with hydrogen plasma for another ten minutes after being exposed to the lab atmosphere. The dark red and orange I-V curves are measured at the beginning and end of the second treatment interval, respectively.

and end of the first hydrogen plasma treatment interval, respectively. The sample was exposed to the lab atmosphere for ten minutes before being treated again with hydrogen plasma. The dark red and orange I-V curves were measured at the beginning and end of the second treatment interval, respectively.

Figure 6.20 shows a clear change in the hysteresis loop between the beginning and end of the first plasma treatment (dark and light blue curves). These changes could be related to plasma-induced changes of the low-κ dielectric properties. However, the loop does not seem to be different after the sample was exposed to the lab atmosphere for ten minutes (dark red curve). The dimensions of the

hysteresis loop undergo a slight change after another ten minutes of hydrogen plasma treatment (orange curve).

Relative changes in the film properties can be measured using this technique. However, ex-situ and surface analysis measurements must be performed to determine the physical or chemical changes that the film undergoes after these plasma treatments. Nevertheless, if water was adsorbed on the low-κ film, the capacitance/resistance would have dramatically increased. This increase would have caused the dimensions of the hysteresis loop to increase, which is not the case in these measurements.

Similar experiments with different thicknesses of low-κ dielectrics were performed and showed the same behaviour. Samples treated with argon plasma showed even less change, which could be related to the densification of the top layer of the dielectric. In a sense, it seems that hydrogen is a 'softer' plasma which causes mild changes to the low-κ properties.

The low-κ sample that was treated in hydrogen plasma, figure 6.20, was exposed to the lab atmosphere for eight consecutive weeks before being treated again with the same hydrogen plasma conditions. Figure 6.21 shows the I-V curves measured for ten minutes plasma treatment referred to as the third plasma run. The dark blue and green lines in figure 6.21 are the dark blue and light red I-V curves, respectively, of the sample presented in figure 6.20, which represent the initial and final measured I-V curves of the sample presented in figure 6.20. The red and light blue curves are the measured I-V curves at the beginning and end of the third plasma treatment. The hysteresis loop seems to be different at the beginning of the third plasma treatment (red and light blue curves) and also different from the initial measured hysteresis loop (dark blue). This could be re-

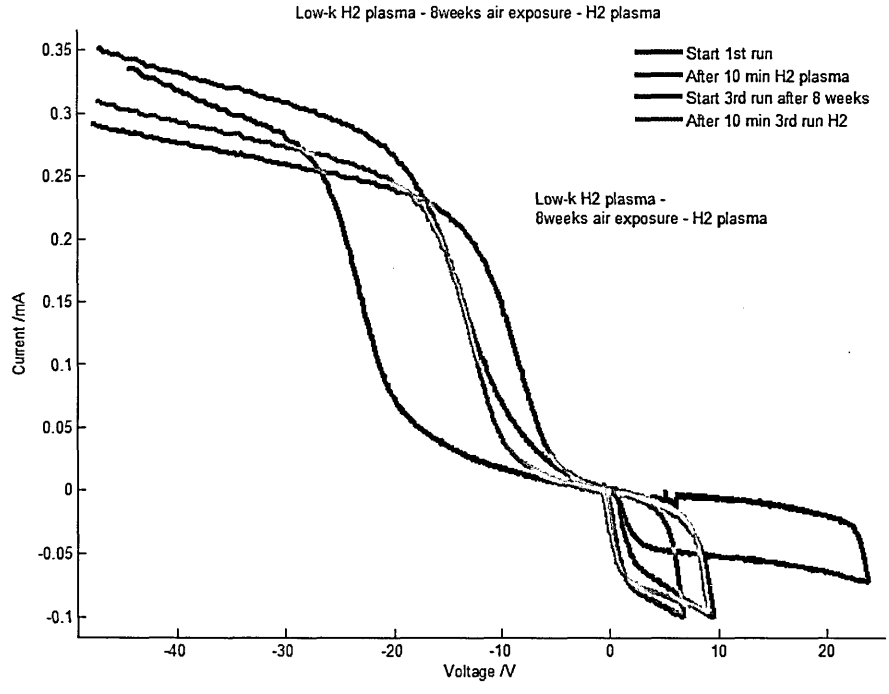

Figure 6.21: Low-κ coated tile exposed to hydrogen plasma for an interval of ten minutes after being exposed to the lab atmosphere for eight weeks. This is the same sample that was treated in figure 6.20.

lated to a number of factors; possibly adsorption of water and/or other molecules on the low-κ films. However, after ten minutes of hydrogen plasma treatment the hysteresis loop seems to attain similar dimensions as when it was treated for the second time with hydrogen plasma, i.e. light blue and green curves.

Finally, the wafer probe was used to monitor the effect of an etching plasma on a low-κ coated tile. A tile coated with 150 nm of HiE low-κ dielectric was exposed to an Ar/SF_6 plasma with a 9:1 flow ratio operated at 50 mTorr with $P = 330$ W. The wafer probe was used to record the evolution of the film properties as a function of plasma exposure time.

Figure 6.22 shows measured I-V curves from this tile. The blue I-V curve

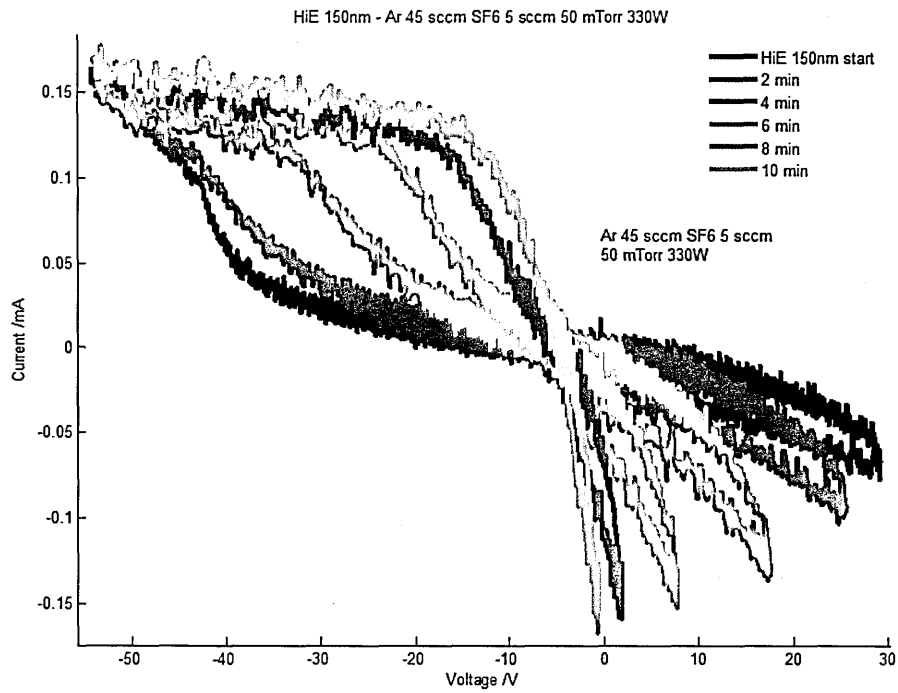

Figure 6.22: The evolution of the HiE 150 nm film I-V characteristic as a function of Ar/SF_6 plasma exposure time. The signal/noise ratio is relatively low as the total collected current was low under these operating conditions. Even so, evident changes in the film properties can be seen from these measurements.

indicates the beginning of the experiment, and the existence of the film is evident from the hysteresis loop. The evolution of the I-V curve is plotted in two minutes time steps. The hysteresis loop seems to gradually shrink, which suggests that the HiE low-κ film is being etched. After ten minutes the thin film is almost etched completely and the I-V curve (mustard) starts to resemble that of a metallic probe, since a TiN layer exists beneath the low-κ film, as shown in figure 6.3.

These preliminary experiments have showed that the wafer probe can be used to extract plasma properties as well as relative changes in film properties, even during highly reactive and etching conditions.

6.5 Conclusions

The main aim in this chapter was to monitor in real time in-situ plasma-induced changes on thin film properties, and the effect of water adsorption on film properties. The latter is still unclear at this stage of the research and further experiments are necessary to resolve this matter. Further experiments are proposed to introduce water molecules and/or other species in a controlled fashion on the low-κ films in the PL80 system. These experiments will enable us to study the effect of the introduced molecules without exposing the sample to the lab atmosphere. However, the wafer probe successfully used multi-layer tiles to measure plasma properties and monitor in real time in-situ plasma-induced changes of the dielectric properties.

TiN probe measurements with an external RC circuit, mimicking thin films, gave I-V curves which could be well fitted, giving almost exact R and C values for the resistors and capacitors connected to the circuit.

For SiO_2 coated tiles, the response is not quite like the ideal test using an external RC circuit. It seems that electron and ion fluxes do not obey the same dynamics and cannot be fitted together. This requires further clarification and more insight into the exact charging mechanisms, which requires optimisation of the model. One possible approach is to use dielectrics sandwiched between two thin metallic layers. The aim of this is to shield the dielectric from direct plasma exposure and transform the tile into a capacitor. This could lead to better understanding of the charging and discharging phases and hence to a better model.

For low-κ coated tiles, measurements with Ar and H_2 discharges were per-

formed. The hysteresis loops measured from different conditions of Ar and H_2 plasmas were very similar, which indicates that this part is relatively independent of the plasma conditions. This hysteresis loop is directly linked to the properties of the dielectric, SiO_2 or low-κ, exposed to the plasma.

Hydrogen plasma treatment of low-κ dielectrics seems to have a gentler effect than argon. This could be related to the densification process that occurs when the low-κ dielectrics are treated with an argon discharge.

Temporally resolved measurements showed relative changes in low-κ film properties when exposed to argon or hydrogen plasmas. Also, low-κ film time resolved etching was observed for an Ar/SF_6 discharge.

Chapter 7

Conclusions & future work

7.1 Summary & conclusions

The objective of this investigation is to explore the use of pulse methods to control and monitor the properties of low pressure electrical discharges for the purpose of optimising such plasmas for neutral beam etching (NBE). The protocol that is envisaged involves a first step in which the etching gas is fragmented by hot electrons followed by a cooling and electron phase during which negative ions are formed. Extraction, acceleration and neutralisation of these negative ions is facilitated during the afterglow period whereas the fragmentation processes occur primarily in the active plasma. The discharges were operated in two systems: a research reactor and an industrial etching tool.

Chapter 3 describes a detailed study of plasma properties, in particular electron dynamics, measured in a pulsed capacitively coupled plasma source. The electron dynamics were studied for a range of pulse tailoring conditions with particular emphasis on the early ignition stages. A simple optical emission spectroscopy technique was developed in order to probe the highly transient ignition phases. This study showed the effect of pulse tailoring on the plasma proper-

ties, in particular EEDFs, for different waveform inputs. It was shown that the EEDF could be controlled by using different input waveforms without greatly effecting other plasma properties, such as the electron density. Controlling the EEDF will enable fine tuning of certain plasma chemistries through the enhancement of some reactions and suppression of others.

Chapter 4 describes optical and electrical measurements performed over a wide range of operational conditions to characterise an inductively coupled source when operated in continuous and pulsed modes. Electron densities were measured using hairpin probes and spatio-temporal ion density measurements were performed using a planar Langmuir probe. The simple optical emission spectroscopy technique was used to estimate electron temperature from plasmas operated in continuous mode and to study the ignition phase of pulsed discharges. Density measurements suggested that the plasma is nearly always operating in the H-mode, i.e. high plasma density. The OES measurements suggested that the plasma almost instantaneously ignites in the H-mode for the operational conditions that were studied.

Chapter 5 contains the description of the OU NBE apparatus and the various measurements that were performed to assess the effectiveness of NBE applied in this way. Initial measurements showed that the NBE adapter almost had no effect on the plasma properties, such as electron temperature and density. Also, the extracted beam energies were controlled up to a few hundred electronvolts, while other groups have reported only a few electron volts. A standard set of plasma conditions was selected based on the diagnostics performed for a range of operating conditions. Preliminary neutral beam etching results showed an etch rate of 30 nm/min when pure SF_6 is used within the discharge when operated

with square wave modulation at 2 kHz. Under these conditions there is also significant lateral etching observed. It was concluded that the lateral etch was most likely due to fluorine surface transport. The addition of small traces of oxygen gas significantly reduced the lateral etching.

Chapter 6 introduces a novel pulsed measurement technique using an in-situ wafer probe. Plasma properties were successfully measured using a tile from a multi-layer wafer. An analytical model was used to extract plasma properties and dielectric properties. It was found that this measuring technique and model can be used to qualitatively monitor plasma induced changes on the dielectric properties in-situ and in real time. Exact quantitative fits could not be obtained due to the model lacking necessary plasma-surface interactions. Future research should solve this problem.

7.2 Future work suggestions

Optical emission spectroscopy: this technique gives high time resolved access to transient phases in pulsed discharges and could be expanded to further interpret the plasma behaviour. Also, the simple OES model used in pulsed CCP could be enhanced by including a variety of non-Maxwellian EEDFs.

Collisional radiative models (CRM) are more complex models that used spectrally resolved emission measurements to extract plasma properties of discharges operated in steady state conditions. A hybrid transient kinetic model in combination with CRM could be used to further analyse the pulsed behavior of discharges using the simple OES presented in this research.

Neutral beam etching: preliminary NBE results, presented in chapter 5, are

encouraging and highlight various opportunities for enhancing the method in terms of effectiveness, anisotropy, selectivity and diverse applications. There are two ways to achieve these opportunities. First, a systematic study of the etch output while probing the space parameter of the pulsed discharge and extraction protocol. This can be achieved by pulse tailoring the discharge in order to optimise the plasma chemistry, as the effectiveness of pulse tailoring on the EEDF was showed in chapters 3 and 4, to achieve conditions more suitable for the extraction of negative ions during the afterglow. Enhancing the conditions for negative ion formation in the afterglow can increase the etch rates of this technique. The second approach is studying the extracted species in the processing region by using a quadrupole mass spectrometer. This will give direct insight on the types of extracted species and what possible etch/depostion processes might take place, besides analysing the energy of the extracted species. This point is of grave importance as the charged species can be measured relatively easy in the discharge, while it is very difficult to acquire information about the extracted neutral species in the processing region. Further enhancements on the apparatus could be achieved by adding magnetics to cool down electrons, possibly enhancing the production of negative ions, and to filter out any electrons from the extraction region, or controlling the temperature of the substrates to few tens of Kelvins limiting the flouring surface transport and its reactivity.

Atomic layer etching (ALE) is an area which could benefit from NBE. Typical ALE techniques depend on chemically enhancing the selective etching of a layer by decreasing its activation energies by using a passivation layer. This passivation layer can be formed by introducing a precursor in the system or alternating gas mixtures whilst operating the discharge. However, this can be avoided by using

a single gas mixture in the plasma and applying NBE. The etching selectivity of these atomic layers depend on the energy threshold differences between the different layers. The energy of the extracted beam can be tailored and fine tuned in accordance with the etch requirements without changing the gas mixtures or introducing any precursors into the system to achieve ALE.

Wafer probe: finally, the wafer probe technique described in chapter 6 could be significantly improved by improving the analytic model. Inclusion of plasma-surface interactions in the model would significantly help the effectiveness of this technique. Additionally, tiles with dielectrics sandwiched between metallic layers can be used to further comprehend those interactions and improve this analytical models. Also, the wafer probe could be used to perform measurements during neutral beam etching. This would give a sense of the extracted/diffused charges and allow to monitor the changes in the dielectric properties of thin films in almost real time. The changes in the dielectric properties can be monitored only if enough charged species arrive to the wafer probe surface. This technique could be used to assess the neutralisation efficiency as well.

References

AHN, T.H., NAKAMURA, K. & SUGAI, H. (1996). Negative ion measurements and etching in a pulsed-power inductively coupled plasma in chlorine. *Plasma Sources Science and Technology*, **5**, 139. 65

ASHIDA, S., LEE, C. & LIEBERMAN, M.A. (1995). Spatially averaged (global) model of time modulated high density argon plasmas. *Journal of Vacuum Science & Technology A: Vacuum, Surfaces, and Films*, **13**, 2498–2507. 64, 73, 104, 130

ASHIDA, S., SHIM, M. & LIEBERMAN, M. (1996). Measurements of pulsed-power modulated argon plasmas in an inductively coupled plasma source. *Journal of Vacuum Science & Technology A: Vacuum, Surfaces, and Films*, **14**, 391–397. 104

BAKLANOV, M.R., DE MARNEFFE, J.F., SHAMIRYAN, D., URBANOWICZ, A.M., SHI, H., RAKHIMOVA, T.V., HUANG, H. & HO, P.S. (2013). Plasma processing of low-k dielectrics. *Journal of Applied Physics*, **113**, 041101. xvii, 175, 176, 201, 204, 205

BANNA, S., AGARWAL, A., CUNGE, G., DARNON, M., PARGON, E. & JOUBERT, O. (2012). Pulsed high-density plasmas for advanced dry etching processes. *Journal of Vacuum Science & Technology A: Vacuum, Surfaces, and Films*, **30**, 040801. 62, 64, 104, 105

BI, Z.H., LIU, Y.X., JIANG, W., XU, X. & WANG, Y.N. (2011). A brief review of dual-frequency capacitively coupled discharges. *Current Applied Physics*, 1–7. 64

BOOTH, J.P. & CUNGE, G. (1997). The transition from symmetric to asymmetric discharges in pulsed 13.56 mhz. *Journal of Applied Physics*, **82**, 552. 64, 65

BOOTH, J.P., CUNGE, G., NEUILLY, F. & SADEGHI, N. (1998). Absolute radical densities in etching plasmas determined by broad-band UV absorption spectroscopy. *Plasma Sources Sci. Technol.*, **7**, 423–430. 66

BOOTH, J.P., BRAITHWAITE, N.S.J., GOODYEAR, A., NEUILLY, F. & FRANCOU, J.M. (1999). Ion flux and electron temperature measurements with an insulator-covered planar electrostatic probe. In *Frontiers in Low Temperature Plasma Diagnostics III*, Saillon, Switzerland. 57, 183

BOOTH, J.P., BRAITHWAITE, N.S.J., GOODYEAR, A. & BARROY, P. (2000). Measurements of characteristic transients of planar electrostatic probes in cold plasmas. *Review of Scientific Instruments*, **71**, 2722–2727. 49, 55, 56, 57, 181, 183, 200

BOOTH, J.P., AZAMOUM, Y., SIRSE, N. & CHABERT, P. (2012). Absolute atomic chlorine densities in a Cl 2 inductively coupled plasma determined by two-photon laser-induced fluorescence with a new calibration method. *Journal of Physics D: Applied Physics*, **45**, 195201. 66

BOWDEN, M.D., OKAMOTO, T., KIMURA, F., MUTA, H., UCHINO, K., MURAOKA, K., SAKODA, T., MAEDA, M., MANABE, Y., KITAGAWA, M. *et al.* (1993). Thomson scattering measurements of electron temperature and density in an electron cyclotron resonance plasma. *Journal of applied physics*, **73**, 2732–2738. 111

BOYLE, P.C., ELLINGBOE, A.R. & TURNER, M.M. (2004). Independent control of ion current and ion impact energy onto electrodes in dual frequency plasma devices. *Journal of Physics D: Applied Physics*, **37**, 697–701. 64

BRAITHWAITE, N.S.J. (1997). Internal and external electrical diagnostics of rf plasmas. *Plasma Sources Science and Technology*, **6**, 133. 45

BRAITHWAITE, N.S.J., BOOTH, J.P. & CUNGE, G. (1996). A novel electrostatic probe method for ion flux measurements. *Plasma Sources Sci. Technol.*, **5**, 677–684. 49, 53, 57

BRIHOUM, M., CUNGE, G., DARNON, M., GAHAN, D., JOUBERT, O. & BRAITHWAITE, N.S.J. (2013). Ion flux and ion distribution function measurements in synchronously pulsed inductively coupled plasmas. *Journal of Vacuum Science & Technology A: Vacuum, Surfaces, and Films*, **31**, 020604–020604. 62, 105

CHABERT, P. & BRAITHWAITE, N.S.J. (2011). *Physics of Radio-Frequency Plasmas*. Cambridge University Press, Cambridge. 2, 46, 49, 53, 56, 57

CHAPMAN, B.N. (1980). *Glow discharge processes : sputtering and plasma etching*. Wiley. 5

CHEN, F.F. (2009). Langmuir probes in RF plasma: surprising validity of OML theory. *Plasma Sources Science and Technology*, **18**, 035012. 49, 53, 66

CHEN, Z., DONNELLY, V.M., ECONOMOU, D.J., CHEN, L., FUNK, M. & SUNDARARAJAN, R. (2009). Measurement of electron temperatures and electron energy distribution functions in dual frequency capacitively coupled CF[sub 4]/O[sub 2] plasmas using trace rare gases optical emission spectroscopy. *Journal of Vacuum Science & Technology A: Vacuum, Surfaces, and Films*, **27**, 1159–1165. 66, 67, 71

CHILTON, J., BOFFARD, J., SCHAPPE, R. & LIN, C. (1998). Measurement of electron-impact excitation into the 3p^{5}4p levels of argon using Fourier-transform spectroscopy. *Physical Review A*, **57**, 267–277. xii, 67, 77, 78, 83

CHILTON, J.E., STEWART, M.D. & LIN, C.C. (2000). Cross sections for electron-impact excitation of Krypton. *Physical Review A*, **62**, 1–13. xii, 67, 77, 78, 83

DONNELLY, V.M. (2004). Plasma electron temperatures and electron energy distributions measured by trace rare gases optical emission spectroscopy. *Journal of Physics D: Applied Physics*, **37**, R217–R236. 66, 71

DONNELLY, V.M. (2013). *Private communication*. 71

DONNELLY, V.M. & SCHABEL, M.J. (2002). Spatially resolved electron temperatures, species concentrations, and electron energy distributions in inductively coupled chlorine plasmas, measured by trace-rare gases optical emission spectroscopy. *Journal of Applied Physics*, **91**, 6288. 66, 71, 113

ECCLES, A.J., VAN DEN BERG, J.A., BROWN, A. & VICKERMAN, J.C. (1986). Evidence of a charge induced contribution to the sputtering yield of insulating and semiconducting materials. *Applied Physics Letters*, **49**, 188–190. 22

ECONOMOU, D.J. (2008). Fast (tens to hundreds of ev) neutral beams for materials processing. *Journal of Physics D: Applied Physics*, **41**, 024001. 31

FONS, J. & LIN, C. (1998). Measurement of the cross sections for electron-impact excitation into the 5p^{5}6p levels of xenon. *Physical Review A*, **58**, 4603–4615. xii, 67, 77, 78, 83

GAHAN, D., DANIELS, S., HAYDEN, C., SULLIVAN, D.O. & HOPKINS, M.B. (2012). Characterization of an asymmetric parallel plate radio-frequency discharge using a retarding field energy analyzer. *Plasma Sources Science and Technology*, **21**, 015002. 64

GANS, T., SCHULZ-VON DER GATHEN, V. & DÖBELE, H.F. (2004). Prospects of Phase Resolved Optical Emission Spectroscopy as a Powerful Diagnostic Tool for RF-Discharges. *Contributions to Plasma Physics*, **44**, 523–528. 66

GODYAK, V., PIEJAK, R. & ALEXANDROVICH, B. (2002). Electron energy distribution function measurements and plasma parameters in inductively coupled argon plasma. *Plasma Sources Science and Technology*, **11**, 525. 111

GODYAK, V.A. (2011). Electrical and plasma parameters of icp with high coupling efficiency. *Plasma Sources Science and Technology*, **20**, 025004. 111

GODYAK, V.A., PIEJAK, R.B. & ALEXANDROVICH, B.M. (1992). Measurements of electron energy distribution in low-pressure rf-discharges. *Plasma Sources Science and Technology*, **1**, 36–58. 49, 53

HORI, T., KOGANO, M., BOWDEN, M.D., UCHINO, K. & MURAOKA, K. (1998). A study of electron energy distributions in an inductively coupled plasma by laser thomson scattering. *Journal of applied physics*, **83**, 1909–1916. 111

HORIKOSHI, S. & HIDAKA, H. (2002). Environmental remediation by an integrated microwave/uv illumination technique.3. a microwave-powered plasma light source and photoreactor to degrade pollutants in aqueous dispersions of tio_2 illuminated by the emitted uv/visible radiation. *Environmental Science Technology*, **36**, 5229–5237. 14

KOKKORIS, G., PANAGIOTOPOULOS, A., GOODYEAR, A., COOKE, M. & GOGOLIDES, E. (????). 155

KUBOTA, T., BABA, T., SAMUKAWA, S., KAWASHIMA, H., URAOKA, Y., FUYUKI, T. & YAMASHITA, I. (2004). A 7-nm nanocolumn structure fabricated by using a ferritin iron-core mask and low-energy cl neutral beams. *Applied Physics Letters*, **84**, 1555–1557. 29

KUBOTA, T., NUKAGA, O., UEKI, S., SUGIYAMA, M., INAMOTO, Y., OHTAKE, H. & SAMUKAWA, S. (2010). 200-mm-diameter neutral beam source based on inductively coupled plasma etcher and silicon etching. *Journal of Vacuum Science & Technology A: Vacuum, Surfaces, and Films*, **28**, 1169–1174. 29

LANGMUIR, I. (1928). Oscillations in ionized gases . *Proceedings of The National Academy of Sciences of The United States of America*, **14**, 627–637. 2, 53

LI, J., LIU, F.X., ZHU, X.M. & PU, Y.K. (2011a). The spatially resolved measurements of the atomic densities in argon Paschen 1s levels by OES in a capacitively coupled plasma. *Journal of Physics D: Applied Physics*, **44**, 292001–292006. 66, 71

LI, J., ZHU, X.M. & PU, Y.K. (2011b). A novel method of using the OES line ratio to determine the spatially resolved atomic density in low-temperature plasmas and its application in carbon and aluminium atoms in capacitively coupled plasmas. *Journal of Physics D: Applied Physics*, **44**, 455203. 71

LIEBERMAN, M.A. & ASHIDA, S. (1996). Global models of pulse-power-modulated high-density, low-pressure discharges. *Plasma Sources Science and Technology*, **5**, 145. 65

LIEBERMAN, M.A. & LICHTENBERG, A.J. (1994). *Principles of Plasma Discharges and Materials Processing*. Wiley-Interscience publication, John Wiley & Sons. 52, 53, 62

MAHONY, C.M.O. & GRAHAM, W.G. (1999). Heating Modes in Capacitively Coupled RF Plasmas Observed with Emission Spectroscopy. *IEEE TRANSACTIONS ON PLASMA SCIENCE*, **27**, 72–73. 66

MIZUTANI, T. & NISHIMATSU, S. (1988). Sputtering yield and radiation damage by neutral beam bombardment. *Journal of Vacuum Science & Technology A: Vacuum, Surfaces, and Films*, **6**, 1417–1420. x, 20, 22, 23, 25

NIST ATOMIC SPECTRA DATABASE (????). Ionization energies form. 132

NODA, S., NISHIMORI, H., IDA, T., ARIKADO, T., ICHIKI, K., OZAKI, T. & SAMUKAWA, S. (2004). 50 nm gate electrode patterning using a neutral-beam etching system. *Journal of Vacuum Science & Technology A: Vacuum, Surfaces, and Films*, **22**, 1506–1512. 25, 29

OLTHOFF, J.K. & GREENBERG, K.E. (1995). The Gaseous Electronics Conference RF Reference Cell ï£¡ An Introduction. *Journal Of Research Of The National Institute Of Standards And Technology*, **100**, 327–339. 67

OVERZET, L.J. & LEONG-ROUSEY, F.Y. (1995). Time-resolved power and impedance measurements of pulsed radiofrequency discharges. *Plasma Sources Science and Technology*, **4**, 432. 104

OXFORD INSTRUMENTS PLASMA TECHNOLOGY (2002). Silicon etching for mems applications. ix, 15

PANDA, S., ECONOMOU, D.J. & CHEN, L. (2001). Anisotropic etching of polymer films by high energy (~100s of ev) oxygen atom neutral beams. *Journal of Vacuum Science & Technology A: Vacuum, Surfaces, and Films*, **19**, 398–404. x, 25, 26, 27, 28

PEARTON, S.J. & NORTON, D.P. (2005). Dry etching of electronic oxides, polymers, and semiconductors. *Plasma Processes and Polymers*, **2**, 16–37. 16, 18, 19

PERRET, A., CHABERT, P., JOLLY, J. & BOOTH, J.P. (2005). Ion energy uniformity in high-frequency capacitive discharges. *Applied Physics Letters*, **86**, 021501. 64

PIEJAK, R.B., GODYAK, V.A., GARNER, R., ALEXANDROVICH, B.M. & STERNBERG, N. (2004). The hairpin resonator: A plasma density measuring technique revisited. *Journal of Applied Physics*, **95**, 3785–3791. xii, 49, 73, 74

PIEJAK, R.B., AL-KUZEE, J. & BRAITHWAITE, N.S.J. (2005). Hairpin resonator probe measurements in rf plasmas. *Plasma Sources Science and Technology*, **14**, 734. 46, 66

PTASINSKA, S., BAHNEV, B., STYPCZYNSKA, A., BOWDEN, M., MASON, N.J. & BRAITHWAITE, N.S.J. (2010). Dna strand scission induced by a non-thermal atmospheric pressure plasma jet. *Phys. Chem. Chem. Phys.*, **12**, 7779–7781. 13

SAMUKAWA, S. (2006). Ultimate top-down etching processes for future nanoscale devices: Advanced neutral-beam etching. *Japanese Journal of Applied Physics*, **45**, 2395–2407. 25, 27, 29

SAMUKAWA, S. (2007). High-performance and damage-free neutral-beam etching processes using negative ions in pulse-time-modulated plasma. *Applied Surface Science*, **253**, 6681 – 6689. 29, 65

SAMUKAWA, S. & MIENO, T. (1996). Pulse-time modulated plasma discharge for highly selective, highly anisotropic and charge-free etching. *Plasma Sources Science and Technology*, **5**, 132. 1, 14, 19, 64

SAMUKAWA, S., SAKAMOTO, K. & ICHIKI, K. (2002). Generating high-efficiency neutral beams by using negative ions in an inductively coupled plasma source. *Journal of Vacuum Science & Technology A: Vacuum, Surfaces, and Films*, **20**, 1566–1573. x, 19, 20, 27, 28, 43

SAMUKAWA, S., KUBOTA, T., HUANG, C.H., HASHIMOTO, T., IGARASHI, M., NISHIOKA, K., TAKEGUCHI, M., URAOKA, Y., FUYUKI, T. & YAMASHITA, I. (2008). A new silicon quantum-well structure with controlled diameter and thickness fabricated with ferritin iron core mask and chlorine neutral beam etching. *Applied Physics Express*, **1**, 074002. 29

SCHULZE, J., SCHÜNGEL, E., DONKÓ, Z., LUGGENHÖLSCHER, D. & CZARNETZKI, U. (2010). Phase resolved optical emission spectroscopy: a non-intrusive diagnostic to study electron dynamics in capacitive radio frequency discharges. *Journal of Physics D: Applied Physics*, **43**, 124016–124024. 66

SHIMOKAWA, F. & KUWANO, H. (1994). New high-power fast atom beam source. *Journal of Vacuum Science & Technology A: Vacuum, Surfaces, and Films*, **12**, 2739–2744. x, 22, 24, 27

SHOEB, J., WANG, M.M. & KUSHNER, M. (2012). Damage by radicals and photons during plasma cleaning of porous low-k sioch. i. ar/o2 and he/h2 plasmas. *Journal of Vacuum Science Technology A: Vacuum, Surfaces, and Films*, **30**, 041303–041303–15. 176

STAVA, E.K. (1993). A new, low-spatter arc welding machin. *Welding Journal*, **72**, 25–29. 14

STENZEL, R. (1976). Microwave resonator probe for localized density measurements in weakly magnetized plasmas. *Review of Scientific Instruments*, **47**, 603–607. 46

VERDONCK, P., GOODYEAR, A. & BRAITHWAITE, N.S.J. (2004). The influence of diffusion of fluorine compounds for silicon lateral etching. *Thin Solid Films*, **459**, 141 – 144. 166, 167

VERDONCK, P., SAMARA, V., GOODYEAR, A., FERCHICHI, A., BESIEN, E.V., BAKLANOV, M.R. & BRAITHWAITE, N. (2011). Influence of the ion bombardment of o_2 plasmas on low-k materials. *Thin Solid Films*, **520**, 464 – 468. 204

VERDONCK, P., MAHESHWARI, A., SWERTS, J., DELABIE, A., WITTERS, T., TIELENS, H., DEWILDE, S., FRANQUET, A., MEERSSCHAUT, J., CONARD, T., PRADO, J.L., ARMINI, S., BAKLANOV, M.R., VAN ELSHOCHT, S., UEDONO, A., HUANCA, D.R., DOS SANTOS FILHO, S.G. & KELLERMAN, G. (2013). *ECS Journal of Solid State Science & Technology*, **2**, N103–N109. 175, 176, 201

ŠAMARA, V., BOWDEN, M.D. & BRAITHWAITE, N.S.J. (2010). Effect of power modulation on properties of pulsed capacitively coupled radiofrequency discharges. *Journal of Physics D: Applied Physics*, **43**, 124017. 62, 64, 65, 73, 105

ŠAMARA, V., BOOTH, J.P., MARNEFFE, J.F.D., MILENIN, P., BROURI, M. & BOULLART, W. (2012a). A dc-pulsed capacitively coupled planar Langmuir probe for plasma process diagnostics and monitoring. *Plasma Sources Science and Technology*, **21**, 065004. 49, 53, 57, 181, 183, 200

ŠAMARA, V., BOWDEN, M.D. & BRAITHWAITE, N.S.J. (2012b). Modulation of microwave resonance probes. *Plasma Sources Science and Technology*, **21**, 024011. 46, 48, 66

WAGENAARS, E., GANS, T., O'CONNELL, D. & NIEMI, K. (2012). Two-photon absorption laser-induced fluorescence measurements of atomic nitrogen in a radio-frequency atmospheric-pressure plasma jet. *Plasma Sources Science and Technology*, **21**, 042002. 5

WIKIPIDEA IMAGES (2010). Plasma physics. ix, 3

ZHU, X.M. & PU, Y.K. (2010). Optical emission spectroscopy in low-temperature plasmas containing argon and nitrogen: determination of the electron temperature and density by the line-ratio method. *Journal of Physics D: Applied Physics*, **43**, 403001. 66, 71

ZHU, X.M., PU, Y.K., CELIK, Y., SIEPA, S., SCHÜNGEL, E., LUGGENHÖLSCHER, D. & CZARNETZKI, U. (2012). Possibilities of determining non-Maxwellian EEDFs from the OES line-ratios in low-pressure capacitive and inductive plasmas containing argon and krypton. *Plasma Sources Science and Technology*, **21**, 024003. 66, 71, 113